

ADVERTIMENT. L'accés als continguts d'aquesta tesi queda condicionat a l'acceptació de les condicions d'ús establertes per la següent llicència Creative Commons:  <https://creativecommons.org/licenses/?lang=ca>

ADVERTENCIA. El acceso a los contenidos de esta tesis queda condicionado a la aceptación de las condiciones de uso establecidas por la siguiente licencia Creative Commons:  <https://creativecommons.org/licenses/?lang=es>

WARNING. The access to the contents of this doctoral thesis it is limited to the acceptance of the use conditions set by the following Creative Commons license:  <https://creativecommons.org/licenses/?lang=en>



OPTIMIZING MAGNETO-IONICS: TOWARDS BRAIN-INSPIRED FUNCTIONALITIES

by

Zhengwei Tan

Doctoral Thesis

Doctoral Program in Materials Science

Jordi Sort Viñas (Director and Tutor)

Enric Menéndez Dalmau (Director)

Department of Physics

Faculty of Sciences

2023



Memòria presentada per aspirar al Grau de Doctor

per

Zhengwei Tan

Vist i plau

Dr. Jordi Sort Viñas

(Director i tutor)

Dr. Enric Menéndez Dalmau

(Director)

Bellaterra, 20 de octubre de 2023



El **Dr. Jordi Sort Viñas**, professor ICREA del Departament de Física de la Universitat Autònoma de Barcelona,

i el **Dr. Enric Menéndez Dalmau**, professor lector Serra Húnter del Departament de Física de la Universitat Autònoma de Barcelona,

CERTIFIQUEN:

Que **Zhengwei Tan** ha realitzat sota la seva direcció el treball d'investigació que s'exposa a la memòria titulada "OPTIMIZING MAGNETO-IONICS: TOWARDS BRAIN-INSPIRED FUNCTIONALITIES" per optar al grau de **Doctor per la Universitat Autònoma de Barcelona**.

Que el disseny dels experiments, síntesi de mostres, llur caracterització, l'anàlisi dels resultats, la redacció dels articles i d'aquesta memòria són fruit del treball d'investigació realitzat per Zhengwei Tan.

I perquè així consti, signen el present certificat,

Dr. Jordi Sort Viñas

Dr. Enric Menéndez Dalmau

Bellaterra, 20 de octubre de 2023

Acknowledgements

I have reached the end of my PhD, a short yet enjoyable and unforgettable journey that started in October 2020. This achievement wouldn't have been possible without the constant support, guidance, and encouragement of many individuals and institutions. I want to express my heartfelt thanks to those who played essential roles throughout my entire Ph.D.

First and foremost, I want to thank my thesis advisors, Jordi Sort and Enric Menéndez. They have been dedicated, wise, and expert guides throughout my research journey. Their consistent support has significantly influenced my academic path. Also, thanks to the support from Eva Pellicer and Santiago Suriñach. I'm grateful to the Group of Smart Nanoengineered Materials, Nanomechanics, and Nanomagnetism for providing me with the necessary resources, facilities, and academic atmosphere for my research. Their contributions have been invaluable in my pursuit of knowledge. I'd also like to thank Jordi Malapeira for his consistently valuable information and professional help with my documentation-related matters.

I also want to express my gratitude to all the members of our research group who have been a part of this academic journey. Special mentions go to: Konrad, who has shown remarkable patience in assisting with various matters, from helping me with English studies initially to guiding me through thesis-related challenges; Michael, who has been my go-to person for resolving issues related to Spanish-written content, making my adaptation to this environment much smoother; Pau and Ma, who have been indispensable in the experimental aspects of my work and have added an element of fun to our office life; Aleksandra, whose patience and willingness to answer my questions and provide assistance at any time have been truly appreciated. Your presence has made the long hours spent in the lab and office more enjoyable, and it has enriched my overall experience. I'd also like to express my gratitude for the friendship and companionship of Sofia, Nicolau, Aitor, Roger, and Irena.

I must acknowledge the financial support I received from BeMagic, one of the European Union's Horizon 2020 research and innovation programs under the Marie Skłodowska-Curie grant agreement number 861145. I'm thankful to everyone who has been involved in BeMagic, that it is you who allowed me to enjoy each organized workshop.

I owe an immense debt of gratitude to my family for their steadfast belief in me and their endless encouragement. To my parents, your sacrifices and unwavering support have been the foundation of my academic pursuits. To my wife, Xueting (雪婷), words cannot fully convey

my love and appreciation for you. Thank you for being a continuous source of inspiration, for sharing both my joys and challenges. You've been by my side throughout every step of my academic journey. Regardless of the difficulties I faced, your constant presence, encouragement, and innovative solutions have been my greatest sources of strength and motivation. Additionally, I must mention my best friends, especially You, Jianxia (尤建峡) and Lin, Tao (林涛), who have consistently supported me since our youth. One person I must acknowledge is Fan, Zhen (樊贞), who sparked my interest in scientific research and provided guidance at each critical stage of my career.

This thesis is not the result of individual effort but rather a collective endeavor. To all those whose names may not appear in this acknowledgment but have, in various ways, touched my life during this journey, I extend my heartfelt appreciation. This work serves as evidence of the transformative power of collaboration, mentorship, and the enduring support of loved ones. My fervent hope is that the knowledge contained within these pages contributes in some small way to the betterment of our world.

Abstract

Magneto-ionics, a field focused on using voltage-induced ion migration to control magnetic properties, has substantial potential for developing energy-efficient spintronic devices. Nevertheless, realization of this is hindered by notable challenges, such as achieving effective tuning or sufficiently fast effects at room temperature, maintaining material stability, and achieving scalable fabrication. Employing structural-ion systems like Co_3O_4 or CoN films (i.e., materials in which the ion to be moved with voltage is included in their structure) appears promising in addressing some of these challenges. These innovative systems, inherently hosting migrating oxygen or nitrogen ions, facilitate the generation of pronounced ferromagnetism via voltage-driven motion of O^{2-} or N^{3-} ions at ambient temperature and are also compatible with existing semiconductor technology. These features open doors to explore applications in emerging brain-inspired memory functionalities. However, attaining fast switching and high cyclability currently remain a challenge, highlighting the need for further research in this field.

In this Thesis, three innovative strategies are proposed to propel the field of magneto-ionics forward. The first one validates the adaptability of magneto-ionics for neuromorphic functionalities. Specifically, by diminishing the thickness of CoN films from 200 to 5 nm, a significant enhancement, approximately 7.4-fold, in ion motion rate and a sub-1s magneto-ionic response have been achieved. This underscores the feasibility of our approach as a foundational framework for developing artificial synapses. Crucially, with sufficiently thin CoN films and moderately high voltage actuation frequencies (i.e., up to 100 Hz), we demonstrate a voltage-controllable N ion accumulation effect at the outer surface of CoN films adjacent to a liquid electrolyte. This phenomenon allows the modulation of magnetic properties, both during and subsequently after the voltage pulse actuation, expanding the horizon for new functionalities in neuromorphic computing, such as post-stimulated neural learning under a deep sleep.

Next, we show that the introduction of suitable transition-metal elements to binary nitride compounds can substantially enhance magneto-ionics. By incorporating 10 at. % Mn in substitution for Co in CoN thin films, we achieve remarkable improvements in magneto-ionic effects, including saturation magnetization, toggling speeds, and cyclability. These results are underpinned by transformations from metallic to semiconducting behaviors and from

nanocrystalline to amorphous-like structures, leading to increased N-ion transport channels. *Ab initio* calculations provide valuable insights into the lower formation energy for CoMn-N compared to Co-N, elucidating the fundamental role of Mn addition in voltage-driven magnetic effects. This represents a significant step towards improved voltage control of magnetism through electric field-driven ion motion.

Finally, we propose a nanoscale-engineered magneto-ionic architecture, featuring a thin solid electrolyte in contact with a liquid electrolyte, to drastically enhance cyclability while maintaining sufficiently high electric fields for ion motion. While liquid electrolytes avoid problems related to electric pinholes, the insertion of a highly nanostructured Ta layer between a magneto-ionic target material (Co_3O_4) and the liquid electrolyte dramatically increases magneto-ionic cyclability, from less than 30 cycles to over 800 cycles. This enhancement is attributed to the role of the Ta layer as a solid electrolyte, effectively trapping oxygen and hindering O^{2-} ions from migrating into the liquid electrolyte. The combined benefits of solid and liquid electrolytes in this synergetic approach offer a promising strategy for boosting magneto-ionics.

Collectively, the results of this Thesis represent a significant advancement in the field of magneto-ionics, opening new avenues for its application in neuromorphic computing and energy-efficient spintronics while addressing key challenges in tunability, speed, and reversibility of magneto-ionic phenomena.

Resumen

La magnetoiónica, un campo de investigación centrado en utilizar la migración de iones inducida por voltaje para controlar las propiedades magnéticas, tiene un gran potencial para desarrollar dispositivos espintrónicos energéticamente eficientes. Sin embargo, la constatación de este potencial se ve obstaculizada por importantes desafíos científicos, como el de lograr velocidades de movimiento de iones suficientemente rápidas a temperatura ambiente, manteniendo la estabilidad del material y permitiendo una fabricación escalable. Emplear sistemas con iones estructurales como capas de Co_3O_4 o CoN (donde los iones que se pretenden mover con voltaje están contenidos en la estructura de estos materiales) es prometedor para abordar algunos de estos desafíos. Estos sistemas, que intrínsecamente albergan oxígeno o nitrógeno, facilitan la generación de ferromagnetismo a través del movimiento impulsado por voltaje de los iones O^{2-} o N^{3-} a temperatura ambiente y, además, son compatibles con la tecnología de semiconductores existente. Estas características hacen que la magnetoiónica pueda hasta llegar a tener aplicaciones en el desarrollo de funcionalidades inspiradas en el cerebro. Sin embargo, lograr velocidades de iones rápidas y una alta ciclabilidad representan, destacando la necesidad de investigación en esta dirección.

En esta Tesis, se proponen tres estrategias innovadoras para impulsar el campo de la magnetoiónica. La primera estudia la adaptabilidad de la magnetoiónica para ser usada en aplicaciones neuromórficas. Específicamente, al disminuir el grosor de las películas de CoN de 200 a 5 nm, se ha logrado un aumento muy significativo, de aproximadamente 7.4 veces, en la velocidad de movimiento de iones, y una respuesta magnetoiónica sub-1s. Esto subraya la viabilidad de nuestro enfoque como una tecnología que podría emular sinapsis artificiales. Con capas de CoN lo suficientemente delgadas y frecuencias de actuación de voltaje de hasta 100 Hz, demostramos un efecto acumulativo de iones de N controlable por voltaje en la superficie externa de las películas de CoN adyacente al electrolito líquido. Este fenómeno potencia la modulación de propiedades magnetoiónicas, tanto durante como después de la actuación con pulsos de voltaje, expandiendo el horizonte de funcionalidades en computación neuromórficas, como el aprendizaje neuronal postestimulado bajo un sueño profundo.

Además, mostramos que la introducción de elementos metálicos de transición adecuados en capas de CoN es una buena estrategia para mejorar sustancialmente la magnetoiónica. Al substituir un 10% atómico de Mn por Co, logramos mejoras en los efectos magnetoiónicos, por

ejemplo en los valores de magnetización de saturación, las velocidades de movimiento iónico y la ciclabilidad. Esto se debe a que la incorporación de Mn da lugar a un cambio de comportamiento metálico a semiconductor y a una estructura muy cercana a la de materiales amorfos, haciendo que haya un mayor número de canales para el transporte de iones N. Los cálculos *ab initio* proporcionan información sobre energía para la formación de enlaces con nitrógeno, que resulta ser más baja para CoMn-N que para Co-N, esclareciendo el papel fundamental de la adición de Mn en los efectos magneto-iónicos inducidos por voltaje. Esto representa un paso significativo hacia un mejor control del magnetismo a través del movimiento de iones mediado por campos eléctricos.

Finalmente, proponemos una arquitectura magnetoiónica diseñada a la nanoescala, que consiste en un electrolito sólido delgado en contacto con un electrolito líquido, para mejorar drásticamente la ciclabilidad mientras se mantienen campos eléctricos lo suficientemente altos para el movimiento de iones. Mientras que la presencia del dieléctrico líquido evita los problemas derivados de cortocircuitos eléctricos, la inserción de una capa de Ta altamente nanoestructurada entre un material magnetoiónico (Co_3O_4) y el electrolito líquido aumenta drásticamente la ciclabilidad magnetoiónica, de menos de 30 ciclos a más de 800 ciclos. Este aumento se atribuye al papel de la capa de Ta como electrolito sólido, atrapando eficazmente el oxígeno e impidiendo que los iones O^{2-} migren al electrolito líquido. Los beneficios combinados de electrolitos sólidos y líquidos en este enfoque sinérgico ofrecen una estrategia prometedora para impulsar la magnetoiónica.

Colectivamente, estos resultados representan un avance significativo en el campo de la magnetoiónica, abriendo nuevas vías para su aplicación en computación neuromórfica y espintrónica energéticamente eficiente mientras se abordan los desafíos clave en sintonización, velocidad y reversibilidad de los fenómenos magnetoiónicos.

Resum

La magnetoionica, un camp de recerca centrat en utilitzar la migració d'ions induïda per voltatge per controlar les propietats magnètiques, té un gran potencial per desenvolupar dispositius espintrònics energèticament eficients. Tot i això, la constatació d'aquest potencial es veu obstaculitzada per importants reptes científics, com el d'aconseguir velocitats de moviment d'ions suficientment ràpides a temperatura ambient, mantenint l'estabilitat del material i permetent una fabricació escalable. Emprar sistemes amb ions estructurals com capes de Co_3O_4 o CoN (on els ions que es pretenen moure amb voltatge estan continguts a l'estructura d'aquests materials) és prometedor per abordar alguns d'aquests desafiaments. Aquests sistemes, que intrínsecament allotgen oxigen o nitrogen, faciliten la generació de ferromagnetisme a través del moviment impulsat per voltatge dels ions O^{2-} o N^{3-} a temperatura ambient i, a més, són compatibles amb la tecnologia de semiconductors existent. Aquestes característiques fan que la magnetoionica pugui arribar a tenir aplicacions en el desenvolupament de funcionalitats inspirades en el cervell. Tot i això, aconseguir velocitats d'ions ràpides i una alta ciclabilitat representen reptes científics importants, destacant la necessitat de recerca i innovació en aquest camp.

En aquesta Tesi, es proposen tres estratègies innovadores per impulsar el camp de la magnetoionica. La primera estudia l'adaptabilitat de la magnetoionica per a aplicacions neuromòrfiques. Específicament, en disminuir el gruix de les capes de CoN de 200 a 5 nm, s'ha aconseguit un augment substancial, d'aproximadament 7.4 vegades, de la velocitat de moviment d'ions, i una resposta magnetoionica sub-1s. Això subratlla la viabilitat del nostre enfocament com un marc fonamental per desenvolupar sinapsis artificials. Amb capes de CoN prou primes i freqüències d'actuació de voltatge de fins a 100 Hz, demostrem un efecte acumulatiu d'ions de N controlable per voltatge a la superfície externa de les pel·lícules de CoN adjacent a l'electròlit líquid. Aquest fenomen potencia la modulació de propietats magnetoioniques, tant durant com després de l'actuació amb polsos de voltatge, expandint l'horitzó per a funcionalitats neuromòrfiques, com l'aprenentatge neural postestimulat sota un somni profund.

A més, mostrem que la introducció d'elements metàl·lics de transició adequats a capes de CoN és una bona estratègia per millorar substancialment la magnetoionica. En incorporar un 10% atòmic de Mn en substitució de Co, aconseguim millores en els efectes magnetoionics, per

exemple en els valors de magnetització de saturació, les velocitats de moviment iònic i la ciclabilitat. Això és perquè la incorporació de Mn dona lloc a un canvi de comportament metàl·lic a semiconductor i a una estructura molt propera a la de materials amorfs, fent que hi hagi un major nombre de canals per al transport d'ions N. Els càlculs *ab initio* proporcionen informació sobre l'energia per a la formació d'enllaços amb nitrogen, que és més baixa per a CoMn-N en comparació amb Co-N, aclarint el paper fonamental de l'addició de Mn en els efectes magneto-iònics induïts per voltatge. Això representa un pas significatiu cap a un millor control del magnetisme a través del moviment d'ions intervingut per camps elèctrics.

Finalment, proposem una arquitectura magneto-iònica dissenyada a la nanoescala, que consisteix en un electròlit sòlid prim en contacte amb un electròlit líquid, per millorar dràsticament la ciclabilitat mentre es mantenen camps elèctrics prou alts per al moviment d'ions. Mentre que la presència del dielèctric líquid evita els problemes derivats de curtcircuits elèctrics, la inserció d'una capa de Ta altament nanoestructurada entre un material magneto-iònic (Co_3O_4) i l'electròlit líquid augmenta dràsticament la ciclabilitat magneto-iònica, de menys de 30 cicles a més de 800 cicles. Aquest augment s'atribueix al paper de la capa de Ta com a electròlit sòlid, atrapant eficaçment l'oxigen i impedingint que els ions O^{2-} migren a l'electròlit líquid. Els beneficis combinats d'electròlits sòlids i líquids en aquest enfocament sinèrgic ofereixen una estratègia prometedora per impulsar la magneto-iònica.

Col·lectivament, aquests resultats representen un avenç significatiu en el camp de la magneto-iònica, obrint noves vies per a la seva aplicació en aplicacions neuromòrfiques i espintrònica energèticament eficient mentre s'aborden els reptes clau en sintonització, velocitat i reversibilitat dels fenòmens magneto-iònics.

Glossary

AHE	Anomalous Hall Effect
AFM	Antiferromagnetic Material
AI	Artificial Intelligence
B	Magnetic Induction
CGS	Centimeter-Gram-Second
CMOS	Complementary Metal-Oxide-Semiconductor
DB-VEPAS	Doppler Broadening Variable Energy Positron Annihilation Spectroscopy
DMI	Dzyaloshinskii–Moriya Interaction
η_k	Magneto-optical Kerr ellipticity
EB	Exchange Bias
E	Electric Field
EDL	Electric Double Layer
ELBE	Electron Linac for Beams with High Brilliance and Low Emittance
EELS	Electron Energy Loss Spectroscopy
ERD	Elastic Recoil Detection
FM	Ferromagnetic Material
FET	Field Effect Transistor
FFT	Fast Fourier Transformation
GMR	Giant Magnetoresistance
H_{applied}	Applied Magnetic Field
H_c	Coercivity
HDD	Hard Disk Drives
IoTs	The Internet of Things
I_s	Current-Induced Spin Currents
LFM	Lorentz force microscopy
LiPON	Lithium Phosphorus Oxynitride
M	Magnetization
M_R	Remanent Magnetization
ME	Magnetoelectric Effect
MESO	Metal-Insulator-Semiconductor-Metal

ML	Machine Learning
MFM	Magnetic Force Microscopy
MOKE	Magneto-Optical Kerr Rotation
MOSFET	Metal-Oxide-Semiconductor Field Effect Transistors
MRAM	Magnetoresistive Random-Access Memory
MTJ	Magnetic Tunnel Junctions
NM	Nonmagnetic Material
PAS	Positron Annihilation Spectroscopy
PC	Propylene Carbonate
PFM	Piezoelectric Force Microscopy
RBS	Rutherford Backscattering
SOT	Spin–Orbit Torque
STT	Spin–Transfer Torque
T_C	Curie Temperature
T_N	Néel Temperature
VEPALS	Variable Energy Positron Annihilation Lifetime Spectroscopy
VCM	Voltage Control of Magnetism
VSM	Vibrating Sample Magnetometer
XMCD	X-Ray Magnetic Circular Dichroism
XAS	X-Ray Absorption Spectroscopy
XRD	X-Ray Diffraction
XRR	X-Ray Reflectivity
YIG	Yttrium Iron Garnet

Preface

This Thesis is structured into the following chapters:

- 1. Introduction** This chapter provides a concise overview of the research motivation, emphasizing its significance in both fundamental and industrial contexts. It subsequently outlines the primary objectives driving the pursuit of this work.

- 2. Experimental** This section meticulously records the fabrication processes and comprehensive characterizations conducted throughout this Thesis.

- 3. Results** This part is presented as a compilation of published articles.

- 4. General discussion** This section encompasses a comprehensive and wide-ranging discussion of the results obtained throughout this Thesis.

- 5. Conclusion** The most important conclusions derived from this research are succinctly outlined in a point-by-point manner.

- 6. Outlook** In looking ahead, this section outlines several aspects that can be further explored and tracked in future research, built upon the foundation laid by this work.

- 7. Curriculum vitae** The Curriculum vitae is included at the end of the dissertation.

Table of Contents

ABSTRACT	IX
RESUMEN	XI
RESUM	XIII
GLOSSARY	XV
PREFACE	XVII
TABLE OF CONTENTS	XIX
1 INTRODUCTION	1
1.1 Motivation	1
1.2 The development of spintronic devices	3
1.3 Basis of magnetism	8
1.4 Voltage control of magnetism	15
1.5 Magneto-ionics	27
1.6 The "structural-ion" approach in magneto-ionics	42
1.7 Objectives	44
2 EXPERIMENTAL	46
2.1 Sample fabrication	46
2.2 Magnetoelectric characterization	48
2.3 Structural and compositional measurements	50
2.4 Transport measurements	59
2.5 Ab initio Calculations	61
BIBLIOGRAPHY	63
3 RESULTS	80
3.1 Frequency-dependent stimulated and post-stimulated voltage control of magnetism in transition metal nitrides: towards brain-inspired magneto-ionics	81
3.2 From binary to ternary transition-metal nitrides: a boost toward nitrogen magneto-ionics	99
3.3 Regulating oxygen ion transport at the nanoscale to enable highly cyclable magneto-ionic control of magnetism	117
4 GENERAL DISCUSSION	133
5 CONCLUSIONS	139
6 OUTLOOK	141
CURRICULUM VITAE	143

1 Introduction

1.1 Motivation

We currently live in the information age, an era characterized by the widespread use of digital technology and rapid access to information. This digital revolution has brought about significant changes in numerous aspects of human life, transforming communication, commerce, education, healthcare, entertainment, and governance. With the emergence of global phenomena such as the Internet of Things (IoTs), artificial intelligence (AI), machine learning (ML), and Big Data, there is a surging demand for highly functional and energy-efficient miniaturized microelectronic components. These components play a crucial role in driving the advancements of next-generation nanoelectronics, offering improved memory and information processing capabilities.^{1,2}

Functionally, the ubiquitous von Neumann architecture, which is commonly found in computers, excels at performing sequential tasks with great speed. However, it encounters challenges when it comes to complex tasks like pattern recognition on large, imprecise, or incomplete data sets. In contrast, the human brain demonstrates remarkable efficiency in handling such tasks, serving as an inspiration for neuromorphic computing.³ This paradigm mimics the structural organization of the biological brain by decentralizing responsibilities, moving away from single-task units, and redistributing memory and computation functions across a vast network of interconnected neurons and synapses. To achieve such brain-like structures, a shift is required from volatile hardware units to hardware capable of analog tuning of properties based on the provided stimulus. This enables functionalities such as "learning" and "forgetting," among others.⁴ By mimicking the brain's processing abilities, neuromorphic computing offers the potential for significant advancements in tasks requiring pattern recognition and processing uncertain data, paving the way for adaptive and self-learning systems with applications in artificial intelligence, robotics, and data analysis.⁵

In terms of energy efficiency, spintronic systems, which operate using electric currents through spin-transfer torque (STT)^{6,7} or spin-orbit torque (SOT) effects,^{8,9} have emerged as key elements in the field of microelectronics. Nevertheless, the magnetization switching process that involves in electric current-based operations generates undesirable Joule heating effect, leading to compromised energy efficiency. To address this issue, researchers have been exploring a fascinating alternative approach known as voltage control of magnetism (VCM).¹⁰

By modulating magnetic properties using electric fields instead of electric currents, the power dissipation can be minimized, leading to improved energy efficiency in microelectronic systems.

Among various VCM mechanisms, magneto-ionics¹¹⁻¹³ stands out as a promising approach. It involves manipulating magnetic properties by driving ion migration through voltage application, utilizing ions like O^{2-} ,^{11,14,15} H^+ ,^{13,16,17} Li^+ ,^{18,19} F^- ,²⁰ or N^{3-} .^{21,22} This technique holds significant promise for developing low-power memory applications. Recent advancements have focused on improving ion motion rates and endurance, overcoming key challenges in fully exploiting magneto-ionics at room temperature. One interesting case is the utilization of structural oxygen or nitrogen as self-contained moving ions within target materials, such as Co_3O_4 ¹⁵ or CoN ²² films. These target materials, which are compatible with complementary metal-oxide-semiconductor (CMOS) technology, exhibit an initially fully OFF (i.e., paramagnetic) state and provide “ready-prepared” lattice sites for ion diffusion, allowing for net magneto-ionic generation of ferromagnetism by voltage-triggered O^{2-} or N^{3-} ion motion from the films toward an adjacent electrolyte. However, achieving fast switching and high magneto-ionic cyclability in these materials remains a challenge. Improvements in these aspects are of utmost importance to enhance the performance and practicality of magneto-ionics, enabling its widespread adoption in emerging spintronic applications and novel computation paradigms, such as neuromorphic systems.^{12,23}

1.2 The development of spintronic devices

In today's data-driven world, the processing, transmission, and secure storage of digital information are vital for the functioning of modern society. As the demand for high-density information processing and storage continues to grow, it becomes increasingly crucial to address the performance and energy efficiency challenges faced by current electronic technologies. While the development of microchips has followed Moore's Law over the past five decades, which was predicated by Gordon E. Moore in 1965,²⁴ that the number of transistor on a microchip doubles approximately every 18–24 months, sustaining this trend has become more challenging. The downscaling of CMOS devices through advanced fabrication technology has boosted computational capability. However, the relentless pursuit of scaling CMOS devices to ever smaller dimensions face mounting challenges. As critical dimensions of modern transistors rapidly approach sub-10 nm sizes,²⁵ the emergence of quantum effects becomes increasingly pronounced, exacerbating issues such as increased leakage currents due to quantum tunneling.²⁶ Consequently, current CMOS-based components find themselves struggling in maintaining efficiency at atomic-scale dimensions, limiting the further miniaturization of traditional electronic devices and sparking a search for life after Moore's Law.^{27–29}

Spintronics is considered as one of the most promising technologies for the future microelectronic industries, particularly in the anticipated post-CMOS era.^{6,7,30} Unlike conventional electronics that primarily exploit the charge property of electrons for information transmission and storage, spintronic devices offer the opportunity to utilize both the charge and spin properties of electrons. **Figure 1.1** depicts the significant milestones in spintronics research, highlighting the key junctures that have propelled the field forward. The concept of spin was initially proposed in 1925,⁶ and since then, the field of spintronics has seen significant development, fueled by various intriguing phenomena and breakthroughs. These include the spin Hall effect, which involves the separation of spin-up and spin-down electrons due to their different velocities in a material; the discovery of tunnelling magnetoresistance,³¹ a phenomenon where the resistance of magnetic tunnel junction changes based on the relative orientation of the magnetizations and the demonstration of inverse giant magnetoresistance (GMR),³² where a change in where a change in electrical resistance occurs due to the rotation of the magnetization in a magnetic multilayer structure. Furthermore, the invention of magnetic

tunnel junctions (MTJ) has revolutionized the field by providing a versatile platform for exploiting spin-based effects.²⁹ These remarkable phenomena and advancements have paved the way for the development of magnetism-based information memory and processing technologies, which have the potential to revolutionize the field of electronics.

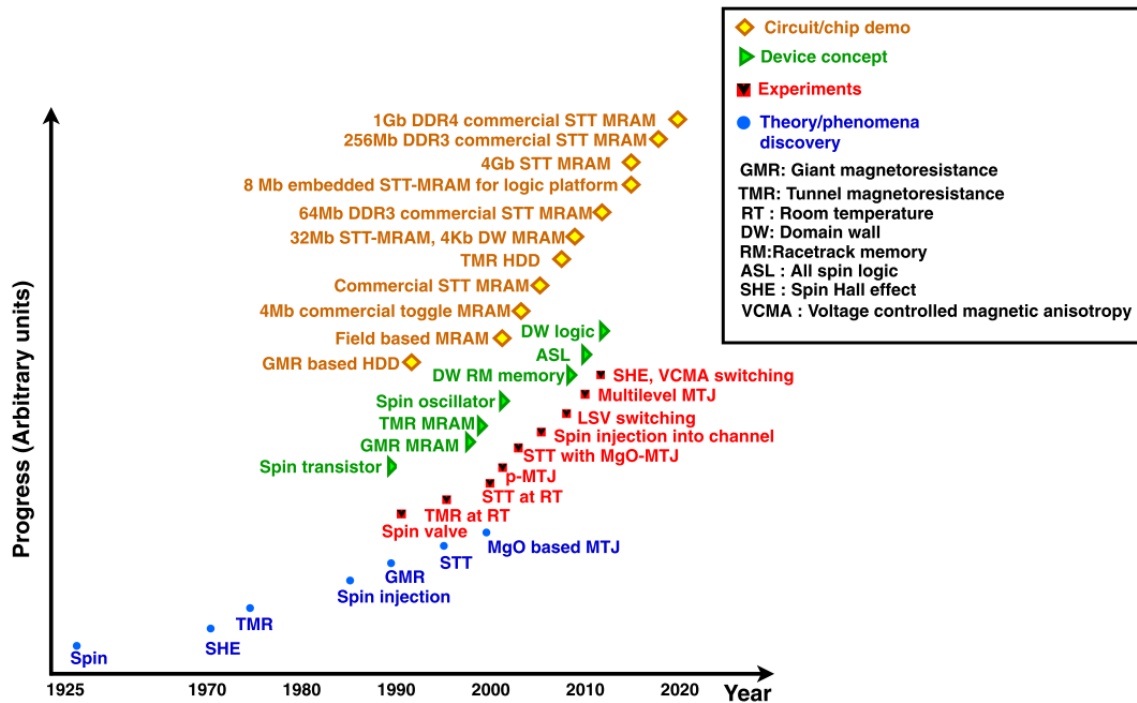


Figure 1.1. Historical developments in spintronics research, adapted from reference 29.²⁹

Hard disk drives (HDDs) have emerged as one of the most popular magnetic storage technologies, playing a pivotal role in the early days of spin-based devices. Since their introduction in 1954, HDDs have significantly contributed to the advancement of high-density information storage technologies. In an HDD, as shown in **Figure 1.2a**, information is stored in many binary digital magnetic units (called “bits”) and these bits can have dipole moment “up” or “down” which is represented in the binary code as \odot =Up and \otimes =Down.³³ Notably, the storage density in HDDs has followed a trajectory similar to Moore's law in the semiconductor industry, exhibiting an impressive increase of eight orders of magnitude in areal storage density over the past 50 years. Magnetoresistive random-access memory (MRAM) is another spintronic technology that has been developed for nonvolatile information storage, first proposed in the 1960s and currently utilized in specialized applications. Relying on magnetic anisotropy for storage and magnetoresistance for retrieval, early MRAMs utilized the GMR effect, whereas newer versions use the TMR effect. With its nonvolatility, speed, endurance,

efficiency, and scalability, MRAM emerges as a leading memory solution for embedded systems, IoTs, and high-performance computing. However, the conventional approach to write information in HDD and MRAM devices, involving the application of external magnetic fields using large magnets or current-carrying coils, leads to substantial energy consumption and spatial requirements, posing critical challenges for device design and operation.³⁴

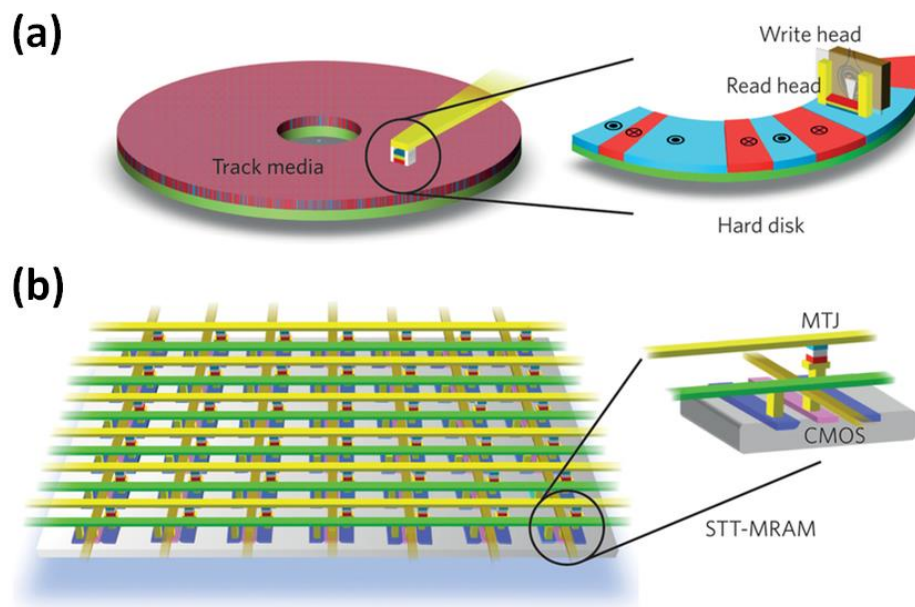


Figure 1.2. Two magnetic memory (storage) devices. (a) Schematic of the mechanical movement of a recording head across the magnetic hard disk drive (HDD) surface. (b) Schematic diagram of a typical magnetoresistive random access memory (MRAM), featuring a magnetic tunnel junction (MTJ) and a transistor access device. The source and drain are denoted by dark blue color; the gate is shown in pink; the bit lines are highlighted using yellow and green; the gate control lines are depicted in dark yellow. STT, spin-transfer torque; CMOS, complementary metal-oxide-semiconductor. Adapted from reference 33.³³

In response to these problems, STT based switching for MRAM was proposed, sparking renewed interest in research and business. As illustrated in **Figure 1.2b**, STT-MRAM contains a MTJ element embedded in a CMOS platform, where the switching of magnetizations is induced by sending a current through the device STT method rather than any external magnetic field, improving the device in terms of energy-efficiency and scalability.³³ STT occurs in spin valve structures consisting of two ferromagnetic material (FM) layers separated by a non-magnetic conductor or insulator, in which the magnetization configuration is controlled by a perpendicular spin-polarized current (j_c) that mediates the transfer of angular momentum between the fixed and free FM layers (**Figure 1.3a**).³⁵ When an electric current passes through a thick magnetic layer (referred to as the fixed or hard layer), it becomes spin-polarized. If this

spin-polarized current is directed to a second, thin magnetic layer (referred to as the free or soft layer), it will interact with the magnetic moment in the free layer, by spin-dependent scattering, resulting in the transfer of a torque to the magnetic moment, causing it to precess. If the torque is large enough, the orientation of the magnetic moment in the free layer can be reversed, in the absence of an external magnetic field. Although STT is currently the main way of writing information in commercial MRAM, writing speed and power consumption are not satisfactory.³⁴ Furthermore, a high current density needs to directly pass through the very thin insulating tunnel barrier in the writing process, which will strongly reduce the endurance of the device.

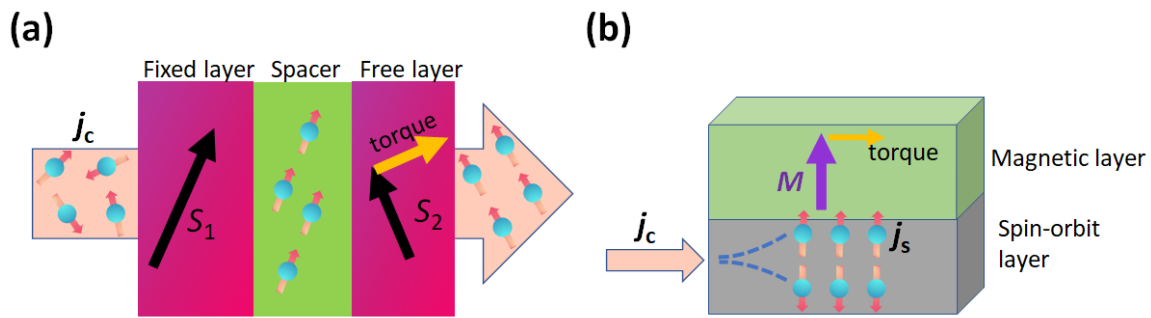


Figure 1.3. Diagram of the mechanisms of spin-transfer torque (STT) and spin-orbit torque (SOT). (a) Schematic of a spin-transfer torque structure consisting of fixed and free ferromagnetic layers sandwiching a nonmagnetic spacer. The unpolarized conduction electrons (j_c) are polarized in the direction of S_1 when passing through the fixed layer, and this polarized current continues to go across the nonmagnetic space layer and the free layer, becoming parallel to the direction of S_2 because of the spin-torque. (b) Schematic illustration of a typical SOT heterostructure composed of a nonmagnetic spin-orbit layer and a magnetic layer. A charge current flow (j_c) passing through the spin-orbit layer induces a transverse spin current (j_s) due to the strong spin-orbit coupling of the nonmagnetic layer. This spin current flows into the ferromagnetic layer and exerts a torque on the local magnetization (M) of the ferromagnetic layer for magnetization switching.

Recently, as an alternative to STT, SOT has attracted considerable attention due to its typical features of non-volatility, reversibility, high speed, and good compatibility with the conventional semiconductor industry.⁸ As shown in **Figure 1.3b**, SOTs in nonmagnetic metal (NM)/FM bilayers arise from in-plane current-induced spin currents (I_s), which are mainly generated by the bulk spin Hall effect and the interfacial Rashba-Edelstein effect. Current-induced SOT mediates the transfer of angular momentum from the lattice to the magnetic layer(s), leading to sustained magnetic oscillations or switching of magnetization (M). Despite of its great potential for next-generation spintronic applications, the requirement of large

writing current and even a static magnetic field in some configuration involves an undesirable Joule heating effect, which is detrimental to energy efficiency.^{36,37}

VCM is a promising alternative to minimize the power dissipation caused in current-based magnetic devices.¹⁰ By utilizing electric fields instead of spin-polarized current or magnetic fields generated by electromagnets, it is possible to achieve a substantial reduction in energy consumption, potentially by several orders of magnitude. For example, in STT-based memory devices, a large current is required to generate a sufficient spin torque for moving domain walls or switching magnetization. Each electron carries a moment of $1 \mu_B$, so the estimated energy consumption for this process, in a device with nominal dimensions of 10×10 nm, is on the order of a few fJ (10^{-15} J). In contrast, a capacitive device that utilizes an electric field to modulate charge can generate large fields of about 10 kV/cm with just about an aJ of energy (10^{-18} J) in a similar 10×10 nm device with a dielectric constant of ~ 100 (which is reasonable for ferroelectrics).³⁸ Since replacing current with voltage on such a small device saves energy by three orders of magnitude, let alone a practical application involving thousands of such small devices. While the physics of this phenomenon may seem straightforward, it can have significant implications for spintronic devices, especially in the development of low-power, high-performance computing devices.³⁶

Among VCM mechanisms, magneto-ionics is notable for inducing substantial changes in magnetic properties at room temperature using small bias voltages, highlighting its potential for low-power spin technologies. To fully exploit its potential, understanding its core principles and improving its performance, especially in temperature operation, switching speed, and reversibility, are crucial. These advancements can drive transformative technological breakthroughs, ultimately shaping the future landscape of spintronics and computing.

1.3 Basis of magnetism

1.3.1 Origin of magnetism and types of magnetic materials

Magnetism is a fascinating and important aspect of the physical world, with far-reaching implications for both basic science and practical applications. Note that vectorial magnitudes are represented in bold throughout this Thesis. The magnetic properties of materials are largely determined by the magnitude and arrangement of their magnetic moments (\mathbf{m}).³⁹ In atomic systems, \mathbf{m} is generated by the combination of two distinct contributions: the spin angular momentum of electrons, which results in a spin magnetic moment, and the orbital angular momentum of electrons, which results in an orbital magnetic moment. Magnetic materials, including iron, cobalt, nickel and their alloys manifest a prevalence of \mathbf{m} in the same direction and this alignment imparts strong magnetic properties to the atoms in these materials. Thus, understanding the response of \mathbf{m} to magnetic fields is a fundamental aspect of the studies related with magnetism, which allows us to comprehend the behavior of magnetic materials in the presence of magnetic fields and enables the development of various magnetic technologies.
40,41

When an applied magnetic field ($\mathbf{H}_{\text{applied}}$) is present, all materials respond to it in some way. For an individual electron, its m can be expressed as:

$$\mathbf{m} = -\frac{\mu_B}{\hbar} (\mathbf{I} + 2\mathbf{s}) \quad (\text{Eq.1.1})$$

Here, s represents the intrinsic spin, \mathbf{I} denotes the orbital angular momentum, μ_B is the Bohr magneton ($\mu_B = 9.27 \times 10^{-24} \text{ JT}^{-1}$), and \hbar is the reduced Planck constant ($\hbar = 1.055 \times 10^{-34} \text{ Js}$). In the case of an atom within a solid material, the net magnetic moment depends on the electron configuration and the interactions between the surrounded electrons. The net magnetic moment per unit volume is referred to as magnetization (\mathbf{M}). When an $\mathbf{H}_{\text{applied}}$ is present, materials can undergo a reorganization or reorientation of spins, resulting in the generation of an induced magnetic field called "magnetic induction" (\mathbf{B}). In free space, these two fields are related as follows:

$$\mathbf{B} = \mu_0 \mathbf{H}_{\text{applied}} \quad (\text{Eq. 1.2})$$

where μ_0 is the permeability of free space ($\mu_0 = 4\pi \times 10^{-7} \text{ N A}^{-2}$ in the international system or $\mu_0 = 1$ in the Centimeter-Gram-Second (CGS) system). However, when dealing with materials, the relationship slightly changes. The equation becomes:

$$\mathbf{B} = \mu_0 (\mathbf{H} + \mathbf{M}) \quad (\text{Eq. 1.3})$$

Here, \mathbf{B} is a function of \mathbf{H} (not $\mathbf{H}_{\text{applied}}$). In the CGS system, Eq. 1.3 is expressed as:

$$\mathbf{B} = \mu_0(\mathbf{H} + 4\pi\mathbf{M}) \quad (\text{Eq. 1.4})$$

By applying the relationship:

$$\mathbf{M} = \chi\mathbf{H} \quad (\text{Eq. 1.5})$$

where χ is the magnetic susceptibility, Eq. 1.4 can be simplified to:

$$\mathbf{B} = \mu_0(\mathbf{H} + \mathbf{M}) = \mu_0\mathbf{H} + \mu_0\chi\mathbf{H} = \mu_0(1 + \chi)\mathbf{H} = \mu_0\mu_r\mathbf{H} = \mu\mathbf{H} \quad (\text{Eq. 1.6})$$

In this equation, μ is the relative permeability. It's important to note that when dealing with materials, \mathbf{H} is no longer equal to $\mathbf{H}_{\text{applied}}$. Instead, it can be expressed as:

$$\mathbf{H} = \mathbf{H}_{\text{applied}} + \mathbf{H}_d \quad (\text{Eq. 1.7})$$

The origin of \mathbf{H} lies in the magnetic redistribution within the material, resulting in an internal magnetic field that strongly depends on the sample shape. This internal field is known as the demagnetizing field (\mathbf{H}_d).

All substances exhibit some type of magnetism, and they exhibit various responses to $\mathbf{H}_{\text{applied}}$. Based on this response, they can be divided into five categories: diamagnetic, paramagnetic, ferromagnetic, antiferromagnetic, and ferrimagnetic, which are summarized diagrammatically wherein magnetic moments are represented by arrows (**Figure 1.4a**). In addition, As shown in **Figure 1.4b**, the various types of materials exhibit different magnetic hysteresis loops, which are obtained by recording m vs. $\mathbf{H}_{\text{applied}}$. The response is related with how the magnetic moments are arranged in the material (Figure 1.4a).

- **Diamagnetism.** Diamagnetism originates from changes in the electron orbital motion (Larmor precession) in an atom in the presence of $\mathbf{H}_{\text{applied}}$, resulting in the generation of a small negative moment that tends to oppose the $\mathbf{H}_{\text{applied}}$ (Figure 1.4a). Thus, a linear relationship between m and $\mathbf{H}_{\text{applied}}$ with a negative slope is observed (Figure 1.4b). As all materials have bound electrons, they exhibit a diamagnetic response to $\mathbf{H}_{\text{applied}}$, although this signal can be overshadowed by stronger contributions such as ferromagnetism or paramagnetism. Diamagnetic materials are normally composed of elements with completed orbital shells that lack unpaired electrons, resulting in a net zero magnetic moment. Consequently, diamagnetism disappears when the external magnetic field is removed (Figure 1.4a).
- **Paramagnetism.** Paramagnetic materials have magnetic moments that are not coupled to each other, as thermal fluctuations overcome the interaction between spins (exchange

interaction), resulting in randomly oriented magnetic moments in the absence of H_{applied} (Figure 1.4a). However, upon the application of H_{applied} , the magnetic moments tend to align themselves in the direction of the field, leading to a linear relationship with a positive slope between m and H_{applied} (Figure 1.4b). When H_{applied} is removed, the magnetic moments become misaligned, causing the disappearance of net magnetization in paramagnetic materials.

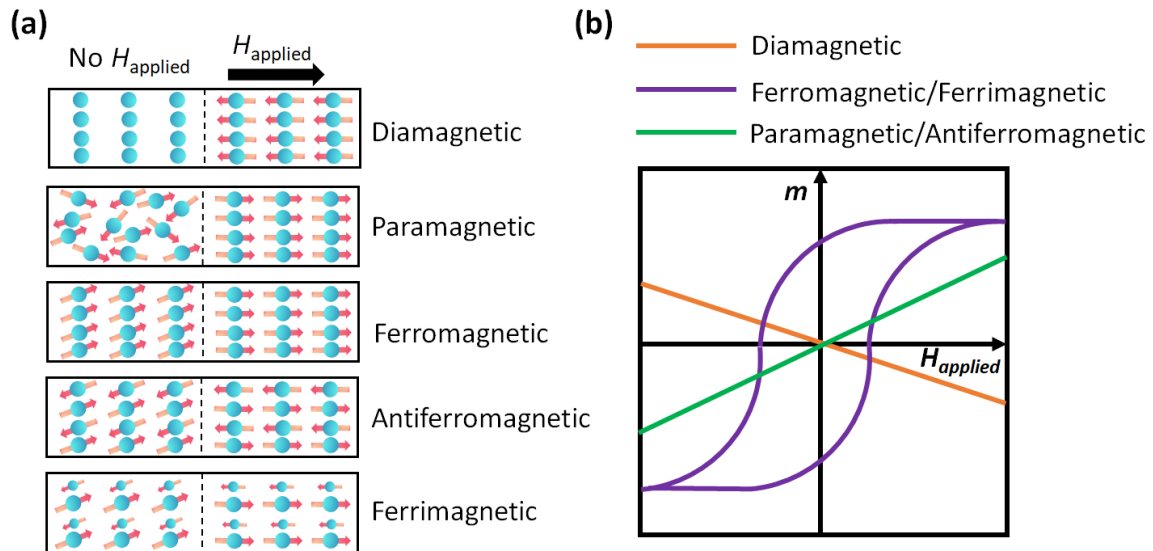


Figure 1.4. (a) Schematic illustration of the arrangement of magnetic moments for different types of materials: diamagnetic, paramagnetic, ferromagnetic, ferrimagnetic, and antiferromagnetic; (b) Cartoon of the recorded magnetic moment m of materials in response to a strong applied magnetic field H_{applied} . The representation of the different behaviors is not scaled.

- **Ferromagnetism.** The ferromagnetic material exhibits a positive and strong exchange interaction between the spins of neighboring atoms. When H_{applied} is applied, the magnetic moments tend to align along the field direction (Figure 1.4a), resulting in the retention of some alignment (spontaneous magnetization) even when the field is removed, displaying a hysteresis behavior. Ferromagnetic materials become paramagnetic when they exceed the Curie temperature (T_C).
- **Antiferromagnetic.** The antiferromagnetic material (AFM) is characterized by negative exchange interactions between adjacent magnetic moments, which causes them to align antiparallel to one another (Figure 1.4a). As a result, there is a complete absence of macroscopic net magnetization in the absence of H_{applied} . However, when the H_{applied} is applied, the magnetization of antiferromagnetic materials exhibits a

positive linear behavior similar to that of paramagnetic materials (Figure 1.4b). Above the Néel temperature (T_N), antiferromagnetic materials become paramagnetic, implying that they lose their antiferromagnetic order.

- **Ferrimagnetism.** Similar to antiferromagnetic materials, the negative exchange interaction in ferrimagnetic materials leads to the antiparallel alignment of magnetic moments. However, the two spin sublattices have different strengths, resulting in non-zero magnetization in the absence of an external magnetic field (Figure 1.4a). Upon the application of H_{applied} , ferrimagnetic materials exhibit hysteresis loops that are similar to those of ferromagnetic materials, as can be seen in Figure 1.4b.

Among all these magnetic materials, FMs are the most widely used in industrial applications and modern technologies, due to their strong magnetism, energy efficiency, versatility, magnetic field manipulation capabilities, role in magnetic storage, and cost-effectiveness. Ferromagnetism arises from the spins of electrons in partially filled outer atom shells, particularly in the $3d$ and $4f$ electronic bands, which possess a net magnetic moment.^{41,42} These electron spins align parallel to each other over small regions called magnetic domains due to a positive exchange interaction between neighboring electrons (**Figure 1.5a**). The size of these domains, which are separated by walls, depends on the material's anisotropy and exchange interaction and can range from several to hundreds of nanometers. **Figure 1.5b** shows the magnetic hysteresis loop, specifically the evolution of M with H_{applied} , which is a well-known macroscopic characteristic exhibited by FM materials. To obtain M , the measured total magnetic moment of a material is typically normalized by the volume of the magnetic material. This hysteresis loop provides valuable insights into the behavior of FM, showcasing their response to changes in H_{applied} and their ability to retain magnetization even in the absence of H_{applied} . As shown in **Figure 1.5bi**, in the absence of H_{applied} , the magnetic domains are randomly oriented to each other, resulting in an unmagnetized material. Upon application of a magnetic field, the magnetic moments of different domains tend to align along the direction of the applied field, causing domain walls to propagate and promoting the growth of magnetic domains aligned with the field at the expense of others (**Figure 1.5bii**). This process continues until the ferromagnetic material macroscopically becomes a single domain state, aligned parallel to the applied field and reaching the maximum possible magnetization, known as saturation magnetization (M_s), as depicted in **Figure 1.5biii**. When the applied field is reduced to zero, the magnetization decreases with a slower rate, without retracing the initial

magnetization curve from a zero-field value, resulting in the hysteresis effect. This effect occurs because the aligned magnetic domains have reached a lower energy configuration, and the domain walls exhibit a certain resistance in response to the field reversal. As a result, even after the removal of the applied field, a portion of the magnetization is retained, which is called remanent magnetization (M_R). Coercivity (H_C), which is the magnetic field required to suppress the net remaining magnetization in the material, is reached as the applied field is increased in the reverse direction, and eventually, saturation is achieved in the reverse direction.

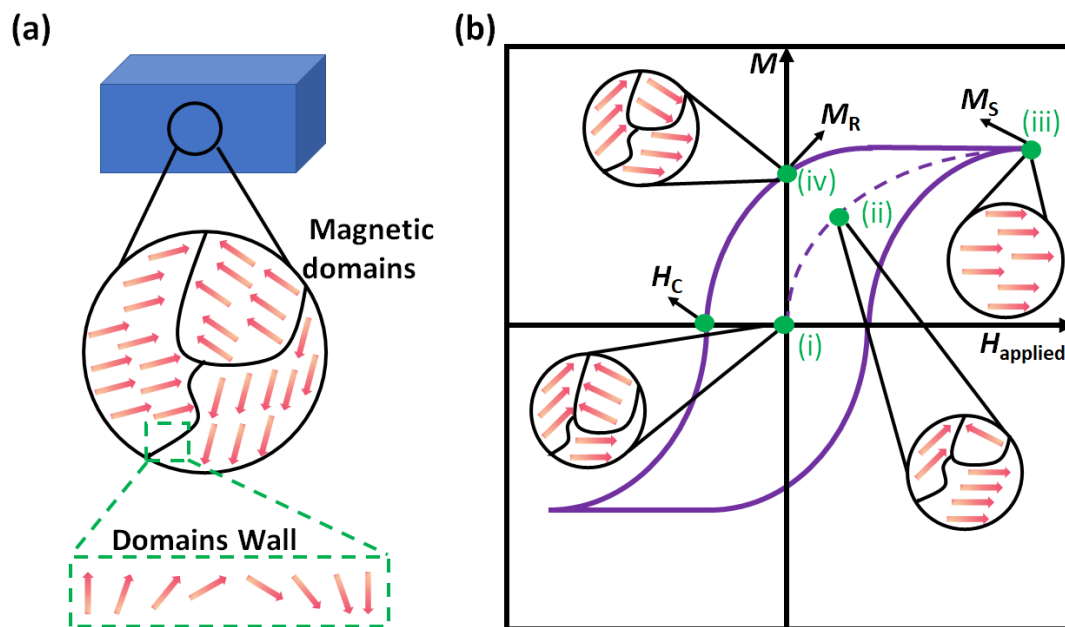


Figure 1.5 (a) A diagram showcasing the magnetic domains and domain walls on a ferromagnetic material (FM). (b) A depiction of the magnetic hysteresis loop, detailing the transformation of magnetic domains in a FM as a magnetic field is applied (H_{applied}). Key magnetic parameters like M_S , M_R and H_C are highlighted across stages i-iv.

The magnetic properties of magnetic materials are influenced by a multitude of factors, such as the crystal structure, composition, particle shape, orientation, crystallite size, exchange energy, and magnetocrystalline anisotropy, among others. Understanding and exploring these factors are crucial in the pursuit of viable strategies to manipulate magnetism. In section 1.3.2, we will delve into a comprehensive examination of diverse methods employed for controlling magnetism, providing detailed insights into this field of study.

1.3.2 Control of magnetism

The manipulation of magnetic states plays a pivotal role in achieving various functions in information technologies, as it corresponds to the switching between fundamental "0" and "1" signals in logic devices.⁸ Typically, specific magnetic properties required for the individual

applications are irreversibly set through the design of phase, composition, microstructure, and shape during the fabrication process. Thus, there is a substantial demand for exploring alternative methodologies that enable the post-fabrication tuning of magnetism in magnetic materials. To address this imperative, extensive efforts have been devoted to using various external stimuli, such as magnetic fields,⁶ spin-polarized currents,^{35,43} strain,^{44–46} ultrafast laser pulses,^{47,48} thermal excitation,⁴⁹ and voltage,¹⁰ with the aim of exerting control over the magnetic behavior. **Figure 1.6** illustrates the potential revolution of these magnetic properties in response to the external stimulation, including (i) M_S ; (ii) H_C ; (iii) Exchange bias (E_B): a phenomenon observed at the interface of ferromagnetic and antiferromagnetic layers, presented as a shift in the hysteresis loop of the ferromagnetic layer; (iv) magnetic anisotropy, referring to the directional dependence of a material's magnetic properties, such as magnetization, susceptibility, or coercivity, which determine its preferred magnetization orientation and stability; (v) T_C and spin textures, such as (vi) skyrmions and (vii) domain walls.

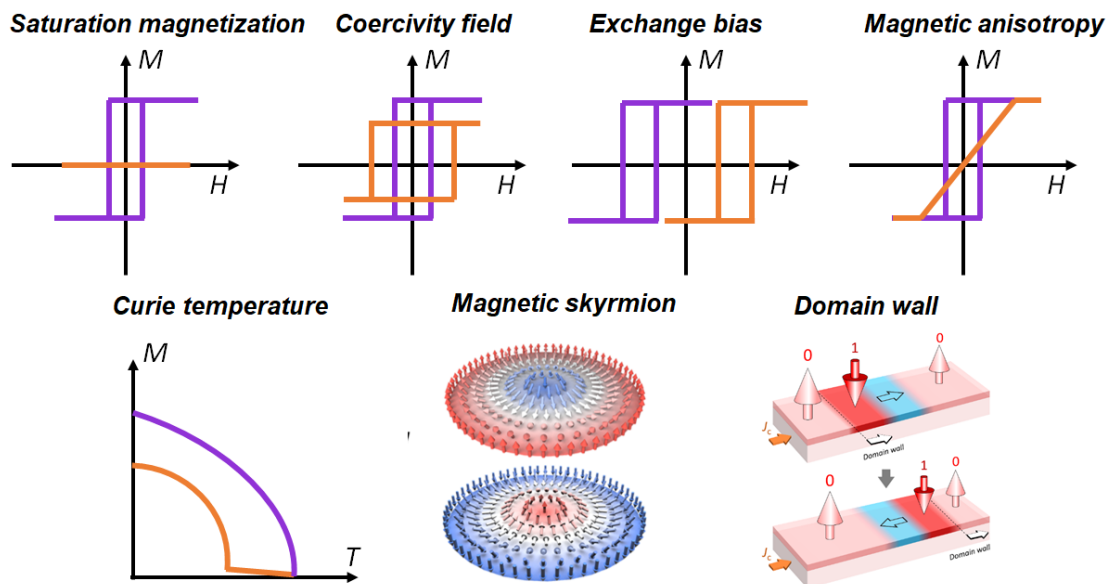


Figure 1.6. Sketch of some magnetic parameters which may be tuned in a magnetic system, including saturation magnetization, coercive field, exchange bias, magnetic anisotropy, curie Temperature, magnetic skyrmions and domain wall (Adapted from reference 50).⁵⁰ The pink and orange-colored shapes represent two distinct magnetic states.

Among all these methods, the advantage of controlling magnetism using voltage as an external stimulus lies in its ability to offer non-invasive and energy-efficient manipulation of magnetic properties. It allows for precise and localized control of magnetism without the need for bulky and power-consuming equipment. Additionally, it provides fast and reversible modulation of

magnetic states, enabling rapid switching and reconfigurability of magnetic devices. Furthermore, voltage control can be integrated with existing electronic circuits and technologies, facilitating the development of compact and multifunctional spintronic devices. Overall, VCM offers significant advantages in terms of efficiency, precision, speed, and compatibility, making it a promising approach for future spin-based information processing and storage technologies.^{36,51}

1.4 Voltage control of magnetism

This strategy of VCM is mainly based on the converse magnetoelectric effect (ME), which denotes the variation of magnetization in response to the application of an electric field E . The first example of such an effect was discussed by Wilhelm Röntgen in 1888,⁵² who found that a dielectric material moving through an electric field would become magnetized. The possibility of an intrinsic magnetoelectric effect in a (non-moving) material was conjectured by P. Curie⁵³ in 1894, while the term "magnetoelectric" was coined by P. Debye⁵⁴ in 1926. Later, Landau and Lifshitz proposed a mathematical formulation of a linear ME effect and its symmetries.⁵⁵ The presence of this effect in Cr_2O_3 was further predicted by Dzyaloshinskii,⁵⁶ followed by its confirmation through experimental observations.⁵⁷⁻⁵⁹ These findings laid the foundation for investigating ME effects in single-phase multiferroics, a category of materials that exhibit multiple types of ferroic order.⁶⁰⁻⁶² However, the intrinsic requirements for a material to possess both ferroelectric and ferromagnetic order make multiferroics uncommon, especially at room temperature, necessitating research efforts beyond single-phase materials.

To address the limitations associated with single-phase multiferroics, extensive experimental and theoretical investigations have been conducted on composite multiferroics. As shown in **Figure 1.7**, these studies encompass a range of mechanisms, including strain effects, modulation of carriers, exchange coupling, orbital reconstruction and the electrochemical effect. Particularly noteworthy in recent years is the emergence of a novel mechanism termed magneto-ionics (**Figure 1.7e**), which has garnered substantial attention owing to its envisioned potential in the realms of nonvolatile memory, logic devices, and neuromorphic computing. **Figure 1.8** shows these mechanisms more intuitively, with some important milestones presented in a timeline, especially recent developments in magneto-ionics.²³ A deeper understanding of these mechanisms can pave the way for the development of new materials with optimized magnetic properties and enhanced control over magnetization, enabling the creation of faster, smaller, and more energy-efficient spintronic devices.

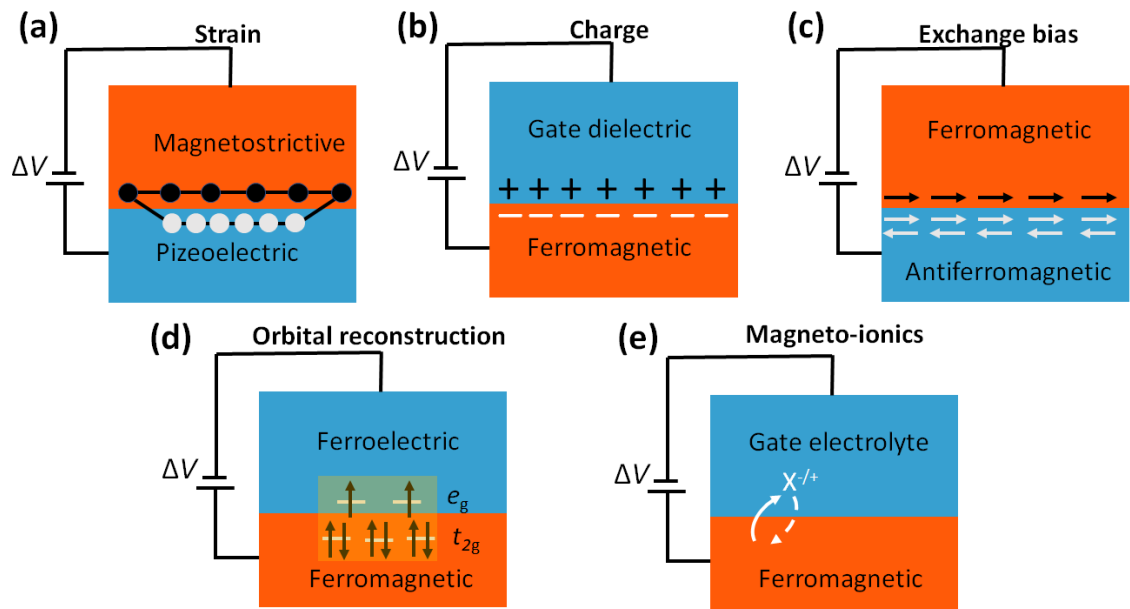


Figure 1.7. Schematic of main mechanisms responsible for voltage control of magnetism (VCM). (a) strain-mediated magneto-electric effect (ME); (b) charge-density-mediated ME effect; (c) Exchange bias-mediated ME effect; (d) Orbital reconstruction-based ME effect; (e) magneto-ionics.

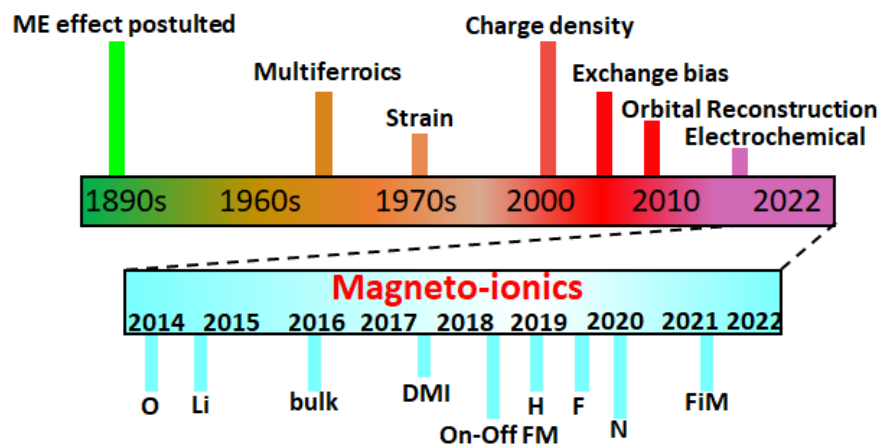


Figure 1.8. Timeline noting representative milestones in voltage control of magnetism and recent developments in magneto-ionics.

1.4.1 Strain

The strain-mediated ME effect is a significant phenomenon for controlling magnetism with the advantage of nonvolatile tuning, high sensitivity, reversibility and compatibility with traditional CMOS devices. The ME systems based on strain-mediated mechanism normally consist of ferromagnetic metals or oxides prepared on a piezoelectric layer or substrates. This

effect mainly involves three dynamic processes: (i) the modulation of lattice or shape in piezoelectric layer induced by an applied voltage through an inverse piezoelectric effect, (ii) the generation of strains arising from the deformation of the piezoelectric layer and (iii) the strain-driven modulation of magnetism in the magnet mediated by the inverse magnetostrictive effect. As a result, the ME coupling is given by:

$$\text{ME effect} = \frac{\text{Magnetic}}{\text{Mechanical}} \times \frac{\text{Mechanical}}{\text{Electric}} \quad (\text{Eq. 1.8})$$

In this case, ferroelectric phase with large piezoelectricity (e.g., PMN-PT, PZT, and BTO) and magnetic phase with large magnetostriction (e.g., Fe, Ni, Co metals, Fe-Ni, FeAl or FeGa alloys or ferrite/ magnetite oxides) are normally selected to obtain high ME coupling coefficients.

The phenomenon of strain-mediated ME coupling was initially investigated in the 1970s on a eutectic composite consisting of a piezoelectric BaTiO₃ and a ferromagnetic magnetostrictive CoFe₂O₄.⁶³ Since then, such a type of VCM mechanism has been widely demonstrated in a large number of systems such as Fe/BTO,^{64,65} CoFeB/PMN-PT,⁶⁶⁻⁶⁸ Co/PMN-PT,^{67,69} CoPd/PZT,⁷⁰ LSMO/BTO⁷¹ and Fe₃O₄/PMN-PT.⁷² As a result, modulations of various magnetic properties, such as m ,^{66,73,74} H_C ,^{64,75} and magnetic anisotropy^{65,68,76} have been realized under this mechanism. Recently, strain-mediated strain effect has been used to control various topological and quantum phenomena, such as interfacial Dzyaloshinskii-Moriya interaction (DMI),^{77,78} magnetic skyrmions,^{79,80} topological Hall effect^{81,82} as well as in atomically thin van der Waals magnets (e.g., Fe₃GeTe₂, CrI₃).^{83,84}

Indirect evidence of strain-mediated ME coupling can be observed through deviations from the expected behavior in the temperature-dependent magnetization curve of layered thin films when they undergo a structural transition at the piezoelectric phase's transition temperature.⁸⁵⁻⁸⁷ Furthermore, the impact of strain on magnetization can be demonstrated by modifying the magnetization hysteresis loop under an applied electric field.^{88,89} Direct visualization of strain-induced magnetization reversal can be achieved by employing various optical imaging techniques, such as magnetic force microscopy (MFM), magneto-optical Kerr rotation (MOKE) in conjunction with piezoelectric force microscopy (PFM), Lorentz force microscopy (LFM), and X-ray magnetic circular dichroism (XMCD) photoelectron microscopy.^{44,90,91}

Despite the remarkable results obtained in the examples above, the practical implementation of the strain-mediated ME effect faces several significant challenges. A critical factor in achieving efficient strain coupling is the establishment of a high-quality interface. The lattice

mismatch between materials and the characteristic of the ferroelectric counterpart plays a critical role in this aspect. Moreover, most ferroelectric substrates are oxide-based, leading to the inevitable oxidation of the ferromagnetic counterpart during deposition. This oxidation process negatively affects the interface and, consequently, the strain coupling mechanism, which becomes weakened.^{92,93} Another drawback is the clamping effect, which significantly restricts the transmission of voltage-induced strain from a piezoelectric counterpart grown as a thin film on a rigid substrate to the magnetic component. The limited ability to transfer strain hinders the effectiveness of the ME effect in such systems. Furthermore, the endurance of strain-based devices is inherently limited due to mechanical fatigue resulting from long-term usage. Contact loosening, cracking, and sparking are common issues that arise over time and adversely affect the device's performance.⁹⁴

1.4.2 Carrier density

The doping level of carriers in heterostructures is a crucial parameter that can significantly impact their magnetic characteristics. The potential to modify carrier density through the application of an electric field provides a promising avenue for manipulating the magnetic properties of diverse magnetic systems, such as semiconductors, ultrathin metals, and oxides. This carrier density-mediated ME effect represents an active research area with the potential to enable advancements in the design and development of magnetic materials for a broad range of applications. In 2000, Ohno et al.⁹⁵ demonstrated this effect in diluted magnetic semiconductors (DMS). Specifically, the authors successfully tuned magnetic moments and Curie temperature in a thin film of (In, Mn)As by utilizing voltage-induced modulation of the hole density. Subsequently, people from the same group were able to induce magnetization reversal in similar (In, Mn)As films by exploiting the change in coercive field induced by charge accumulation.⁹⁶ This behavior has also been observed in other DMS systems, such as (Ga, Mn)As,⁹⁷ (In, Fe)Sb,⁹⁸ and Mn_{0.05}Ge_{0.95}.⁹⁹ Interestingly, the hole density-mediated mechanism has also been utilized to control magnetic anisotropy in (Ga, Mn)As film, which is extensively used in information storage.¹⁰⁰ However, the low-temperature ferromagnetism of magnetic semiconductors limits their practical applications, and only a few studies have successfully demonstrated effective manipulation of the magnetic properties of diluted semiconductors, such as Co-doped TiO₂,⁹⁶ with Curie temperatures above room temperature.

Alternatively, ferromagnetic metals and metallic alloys, such as Fe, Co, NiFe-Pt, Fe-Pd, Co-Pt, and Co-Pd, can be used. However, the screening effect in metals limits the strength and depth of the electric field within the bulk, presenting challenges in control of their magnetism. One solution is to utilize the electrostatic effect, which involves the modulation of magnetic properties through the accumulation of charge at the interface between a dielectric layer and a magnetic medium. This effect has been conventionally been utilized in metal-oxide-semiconductor field effect transistors (MOSFETs), which serve as the fundamental building blocks of modern microelectronics.¹⁰¹ In a MOSFET, a voltage is applied between the metal gate and a semiconducting channel across a thin dielectric oxide.¹⁰² This voltage modulation of the metal gate induces the formation of carriers (electrons or holes) in the channel, creating a two-dimensional sheet due to the electric field's screening at the dielectric-semiconductor interface. This process, known as electrostatic doping, has been highly successful in achieving transistor functionality.¹⁰³ However, when it comes to tuning the magnetic properties of materials, a significantly higher charge density is often required compared to MOSFETs. The charge accumulated in a capacitor can be determined using the equation:

$$Q = \Delta V C \quad (\text{Eq. 1.9})$$

Here, Q represents the charge, ΔV is the applied voltage, and C is the capacitance. The capacitance, in turn, is calculated using the formula:

$$C = \frac{\epsilon_r \epsilon_0 A}{d} \quad (\text{Eq. 1.10})$$

In this equation, ϵ_r denotes the relative permittivity, ϵ_0 is the vacuum permittivity, A represents the area of the capacitor plates, and d is the thickness of the dielectric layer. Therefore, the expression for the accumulated charge in a capacitor, considering the material properties and applied voltage, can be written as

$$Q = \Delta V \frac{\epsilon_r \epsilon_0 A}{d} \quad (\text{Eq. 1.11})$$

To achieve a higher value of Q , traditional dielectric oxides would require relatively large voltages to be applied, sometimes on the order of tens or hundreds of volts. For instance, inducing a variation of only 1 K in the Curie temperature of the semiconducting (Ir, Mn) As system necessitates a high electric field of approximately 1.6 MV/m under a voltage of 125 V.¹⁰⁴ Such high voltage applications are impractical and also cause breakdown of dielectric materials. One possible solution is to employ ultra-thin dielectric layers (e.g., 1–2 nm thick Al_2O_3 , SiO_2 , HfO_2 , or MgO)^{105–107}. However, the preparation of such thin layer with high-quality (e.g., being homogeneous and free of pinholes) remains challenging in practice.

Advanced methods have been pursued to address these challenges, with several yielding impressive advances, most notably the replacement of the MOSFET dielectric with liquid electrolytes. The liquid electrolyte is an ionic medium which contains a balanced number of positive and negative ions with high levels of mobility.¹⁰⁸ As illustrated in **Figure 1.9**, when a voltage (positive, for example) is applied to the gate electrode, anions in the electrolyte will move towards the interface between the electrolyte and the gate electrode to balance the charge introduced by the gate electrode. On the other hand, cations will migrate and accumulate at the interface between the electrolyte and the target material. To compensate for the resulting charge imbalance at the interface between the electrolyte and target material, negative charge will accumulate within the target material. The presence of these two oppositely charged layers at the electrolyte/target material interface gives rise to the formation of an ultra-thin electric double layer (EDL).^{109,110} The EDL is essentially a nanogap parallel-plate capacitor. In such a voltage-gated capacitor, the relation between the electric field E and the applied gate voltage V is given by

$$E = \frac{V}{d} \quad (\text{Eq. 12})$$

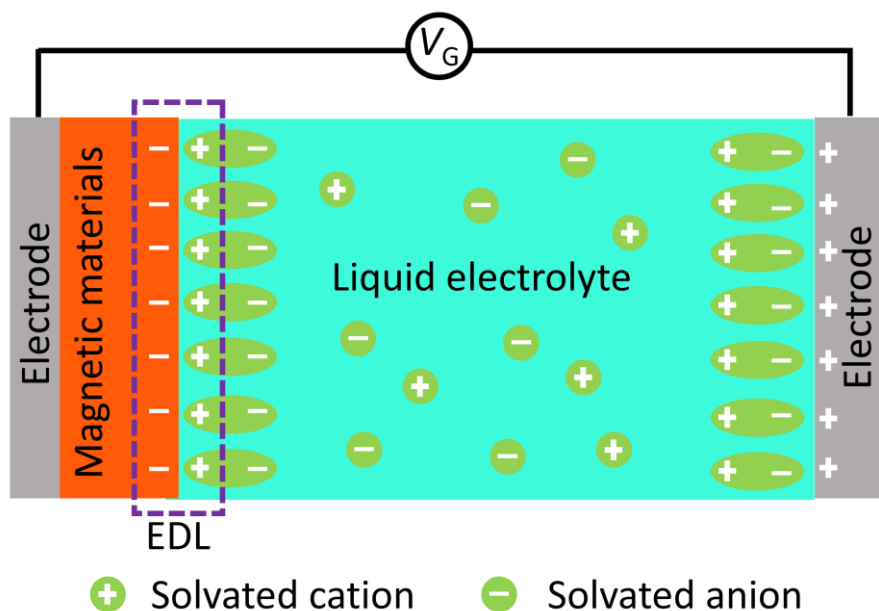


Figure 1.9. Illustration of a capacitor-like geometry employing liquid electrolyte-gating as a method to induce an electric field (E). This setup utilizes the electric double layer (EDL) formed by solvated ions in the electrolyte and induced carriers at the surface of magnetic materials to generate an electric field.

where d denotes the effective thickness of the capacitor. Due to the small d (typically just ≈ 1 nm) of the EDL, a large electric field (≈ 10 – 100 MV/cm) under a gate voltage of just a few

volts can be achieved.¹⁰⁸ Importantly, the capacitance in electrolyte gating is dictated by the EDL, not the electrolyte thickness, enabling the use of thick, low-leakage layers, as well as convenient side-gate geometries. These advantages make liquid electrolytes-gating an appealing approach to induce magnetic changes, promoting the development of magnetoelectric devices. In 2007, Weisheit et al.¹⁰⁴ reported the first observation of the electrostatic ionic effect-induced modulation of magnetism in an ultrathin metal, where they demonstrated a modification of 4.5% and 1% in H_C of Fe-Pt and Fe-Pd ultrathin films (≈ 2 nm), respectively. These changes were attributed to the modification of magnetocrystalline anisotropy and the corresponding energy via the variation in the number of $3d$ electrons, which was subsequently confirmed by density functional calculations for these systems as well as Co-Pt, Co-Pd,¹¹¹ and Cu-Ni.³⁷ Theoretical studies indicated that changes in MAE in response to the electric field are associated with the modulation of unpaired d electrons near the Fermi level and spin-dependent E-field surface screening in ferromagnetic transition metals (e.g., Fe, Ni, and Co).^{112–114} These findings have led to further investigations into these systems, including Fe and CoFeB, for which electric-field-induced changes in H_C have also been reported.^{115,116} Recent research has investigated the electric field manipulation of various magnetic parameters beyond the coercive field. For example, Shimamura et al.¹¹⁷ demonstrated significant tuning of T_C in Co ultrathin films by applying +2 V using an ionic liquid, with a maximum tuning of up to 100 K. Magnetic anisotropy control through the electric field has also been studied, and Maruyama et al. reported up to a 40% change in the magnetic anisotropy of a few atomic layers of Fe metal. This effect resulted from the modulation of Fe electron occupancy by the electric field, in conjunction with the strong spin-orbit coupling between Au and Fe.¹¹⁸ Furthermore, the electric control of spin textures (i.e., skyrmions, domain wall)^{119–122} has been investigated in multiple theoretical works and experimentally demonstrated. Notably, Givord et al.¹²³ achieved effective control of skyrmions in Pt/Co/oxide trilayers via an applied electric field at room temperature. However, these modulations only occur within a few nm from the surface of magnetic metals, restricting the effect to ultrathin films, which can be difficult to be integrated in real devices.

One effective strategy is the utilization of nanoporous materials, intentionally synthesized to enhance the surface-to-volume ratio, thereby promoting a significant enhancement of magnetoelectric effects. In a recent study conducted by Quintana et al.,¹²⁴ intrinsic magnetoelectric effects were investigated in nanoporous Cu-Ni films synthesized through micelle-assisted electrodeposition. The researchers demonstrated that applying voltage across

an EDL using a nonaqueous liquid electrolyte could lead to a drastic reduction in coercivity within the nanoporous metallic alloy, characterized by very narrow pore walls. The nanoporous morphology of the material allowed for a much greater accumulation of surface electric charges compared to fully dense films. The observed purely magnetoelectric effects in Cu-Ni were attributed, based on ab initio calculations, to changes in the magnetic anisotropy energy resulting from electric field-induced, spin-dependent modifications of the magnetic density of states at the surface.

1.4.3 Exchange bias

The exchange bias-mediated ME effect is another mechanism that might be controlled by electric means. It refers to the phenomenon in which the magnetic properties of a ferromagnetic material are influenced by the proximity of an adjacent antiferromagnetic material. This is characterized by a shift in the center of magnetic hysteresis loop from its normal position at $H = 0$ to $H_E \neq 0$ (Figure 1.7).^{125–127} By applying a voltage to a device containing ferromagnetic and antiferromagnetic materials, it becomes possible to manipulate the direction and strength of EB, thereby altering the magnetic properties of the ferromagnetic material. The electric field-controlled exchange bias was initially observed in the Co/Pt multilayers the inclusion of Cr_2O_3 .^{128,129} In this setup, Cr_2O_3 facilitates the formation of AFM single domain through the electric field-assisted cooling process below $T_N = 307$ K and allows for adjustment of the sign of the EB field. Subsequently, He et al.¹³⁰ demonstrated an obvious perpendicular EB effect in [Co/Pd]/ Cr_2O_3 multilayers, in which reversible and room-temperature isothermal switching of the EB field could be achieved by applying voltage pulses in the presence of an auxiliary magnetic field.

Multiferroic materials, such as Cr_2O_3 , YMnO_3 ,¹³¹ LuMnO_3 ,¹³² and BiFeO_3 ^{133–135}, play a significant role in EB-based ME effect. Recently, significant advances have been made in BFO-based heterostructures, including BFO/LSMO interfacial engineering, analysis of spin cycloid BFO, modeling of BFO/CoFe heterojunction and novel ME effect in BFO/two dimensional CrI_3 .^{136–140} After accumulating decades of research into voltage control of EB, Intel has proposed a metal-insulator-semiconductor-metal (MESO) device prototype, which might replace the current CMOS logic device due to its lower energy consumption and higher logic density.¹⁴¹

In addition to multiferroics/FM heterostructure, EB-based ME coupling has been demonstrated in AFM/FM/FE multilayers.^{142–144} In such configurations, similar to the mechanical spring for force transfer, the IrMn exchange spring transfers the influence of the electric field to the interface of the magnetic Co/Pt and AFM IrMn, thereby modulating the magnetism. For example, applying positive and negative voltage to [Co/Pt]/IrMn multilayers increases and suppresses the interfacial exchange interaction, respectively, leading to the modulation of H_{EB} and H_C .¹⁴² The electric field effect on exchange coupling is expected to be prominent within the length of the exchange spring (6 nm for IrMn).

Despite the promising nature of the EB-mediated ME effect for the manipulation of magnetic properties through electric fields, its practical applications are currently limited due to various factors. These encompass temperature sensitivity, relatively weak effect magnitudes, limitations imposed by available material systems, restricted controllability, and scalability issues.

1.4.4 Orbital reconstruction

As clarified above, voltage control of magnetic performance can be achieved through three classic mechanisms: modification of carrier density, strain transfer effect, and exchange coupling. These mechanisms operate by electrically modulating the lattice, charge, and spin, which are the three well-known degrees of freedom in strongly correlated electron systems. However, the fourth degree of freedom, orbital, has received little attention despite its significant importance in physics. Orbital reconstruction refers to the phenomenon whereby the electronic configuration of atoms within a material undergoes changes consequent to modifications in the crystal structure.¹⁴⁵ The occupation of orbitals in a material has a profound impact on the interatomic electron-transfer interaction, influencing both its magnitude and anisotropy, and consequently determining the electronic structure and magnetic ordering.¹⁴⁶ Therefore, the capacity to manipulate the occupancy of orbitals electrically presents a potent mechanism for regulating the electronic structure and magnetism of a material.

One case is the interfacial covalent bond based on orbital reconstruction at the interface between FM metals and dielectric/ferroelectric oxides, in which the magnetism of the FM metals can be manipulated through the electric field applied via the oxides.^{45,118,147} For example, the perpendicular anisotropy of Fe undergoes significant changes in heterostructures of MgO (10 nm)/Fe (0.48 nm), as indicated by the representative magnetic hysteresis loops

observed when applying bias voltages of ± 200 V, which were obtained through Kerr ellipticity (η_K) measurements (shown in **Figure 1.10a**).¹¹⁸ The observed modulation of magnetic anisotropy can be attributed to the changes in electron occupancy induced by the electric field. Specifically, when an electric field of 200 V is applied, there is a change in electron filling of 2×10^{-3} electrons per Fe atoms at the surface, which is significant enough to cause a noticeable alteration in the anisotropy energy of 4 meV per surface Fe atom. This alteration leads to an increase in the energy associated with the $3z^2-r^2$ ($m_z = 0$) orbital (**Figure 1.10b**), which contributes to the MA enhancement. In addition, numerous theoretical and experimental works have demonstrated the orbital reconstruction ME effect via the ferroelectric polarization in ultrathin FM metal/FE oxides heterostructures, such as Fe/BTO, Co/BTO, Co₂MnSi/BTO.¹⁴⁸⁻¹⁵³ Unfortunately, in metal systems, the orbital occupancy of the FM layer is difficult to directly characterize, which places a limit on further insights.

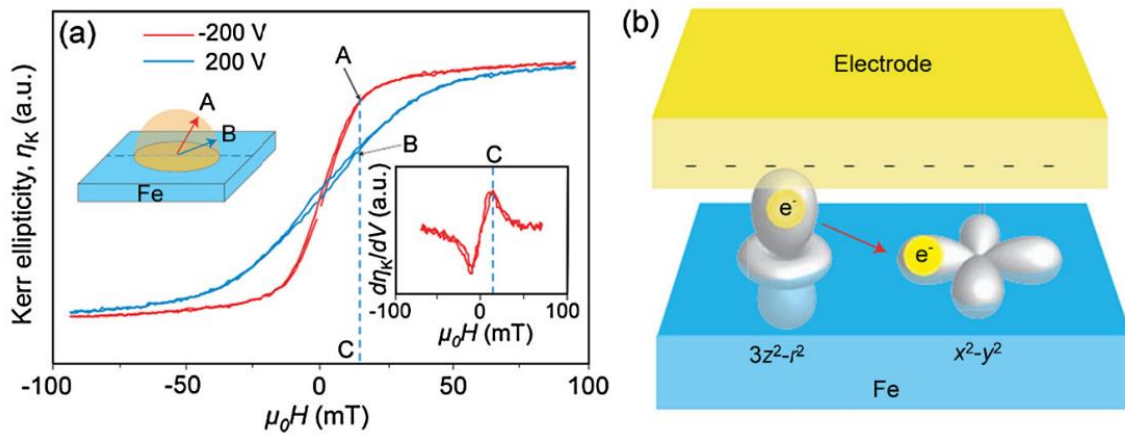


Figure 1.10. (a) Magneto-optical Kerr ellipticity η_K for MgO/Fe under different gate voltages. (b) Sketch of the influence of the external voltage on the orbital occupancy of Fe. Adapted from reference 118.¹¹⁸

1.4.5 Electrochemical processes

Over the past decade, significant progress has been achieved in the field of modulating magnetic properties through voltage-driven electrochemical processes.¹⁵⁴ As depicted in **Figure 1.11**, unlike the sole "charge doping" mechanism seen in magnetoelectric systems based on electrostatic ionic effects (as discussed in section 1.4.2), electrochemical processes involve structural or compositional modifications within a magnetic material. This can occur through surface redox reactions^{155,156} or even ion migration, known as magneto-ionics.^{11,12,22,157} By

utilizing these electrochemical processes, the magnetic properties of the material can be effectively controlled in a nonvolatile manner, independent of the electric field screening length. This presents exciting prospects for achieving dynamic magnetic control with potential applications in areas such as spintronics, magnetic memory devices, and other emerging technologies.

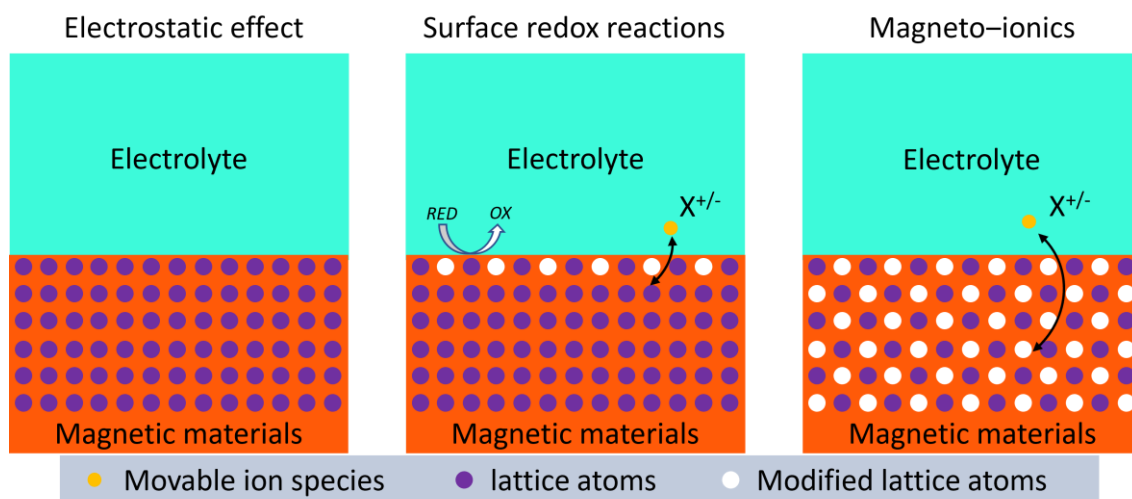


Figure 1. 11. Schematic illustration of possible interactions between ionic species and a magnetic material.

While surface redox reactions are sometimes encompassed within the term "magneto-ionics" in the literature,^{12,106} it is important to note that in this Thesis, these mechanisms will be discussed and introduced separately. This approach capitalizes on the oxidation-reduction reactions of magnetic metallic or metal oxide materials in the presence of an aqueous alkaline electrolyte, commonly using KOH or NaOH. By applying an electrical voltage, a charge-transfer reaction occurs between the electrolyte and the material, leading to a change in its oxidation state and subsequently modulating its magnetic properties.

Among the studied materials, iron-based systems have received significant attention in voltage-controlled magnetism through surface redox reactions. For instance, Leistner et al.¹⁵⁵ achieved a significant variation of M_S up to 20% in a 10 nm thick Fe film immersed in KOH, where the oxidation-reduction processes of a 2 nm Fe layer upon voltage application were attributed to the observed changes. Similar control over magnetization, magnetoresistance (MR), and perpendicular magnetic anisotropy (PMA) has been demonstrated by the same group in $\text{Fe}_3\text{O}_4/\text{Fe}/(001)$ L10 Fe-Pt trilayers and FeO_x/Fe nanoislands using 1 M KOH as the alkaline electrolyte.^{155,156} Besides iron-based systems, voltage-induced magnetoelectric effects via redox reactions have been investigated in Pd-Ni, Co, and Cu-Ni systems.¹⁰⁶ For instance, the

magnetic anisotropy of Co ultrathin films was increased by $0.36 \text{ erg}\cdot\text{cm}^{-2}$ by oxidizing the Co surface in 0.01 M KOH, attributed to the formation of a Co-OH layer from the initially reduced Co-H state. Additionally, Quintana et al.¹²⁴ reported intriguing findings in Cu-Ni alloy films, where subjecting the films to voltage in the presence of NaOH aqueous electrolyte resulted in an increase of up to 33% in M_S . This effect was attributed to a selective electrochemical redox reaction, where the oxidation of the Cu-Ni film affected only the Cu component, leading to an enrichment of Ni content in the Cu-Ni film and subsequently an increase in M_S . These findings underscore the significant potential of voltage-induced electrochemical redox reactions for precise control of magnetic properties in a range of materials.

In contrast, magneto-ionics involves the reversible control of magnetic properties through the back-and-forth motion of ions between the magnetic materials and the electrolytes, often accompanied by structural or compositional modifications in the host material.¹¹⁻¹³ This intriguing field has garnered significant attention due to its potential for next-generation spintronics and recently proposed neuromorphic computing applications. To provide a comprehensive understanding of this area, a detailed discussion will be presented in the subsequent Section 1.5.

1.5 Magneto-ionics

Magneto-ionic control of magnetic materials presents a promising and innovative approach within the realm of magnetoelectricity. A significant advantage of magneto-ionics, distinguishing it from other magnetoelectric strategies, is its nonvolatile operation at room temperature and low voltage. However, despite its potential, there remains a gap between the exploration of fundamental phenomena and the realization of specific applications. This gap arises due to limitations in terms of switching speed, reversibility, and endurance. To bridge this gap effectively, it is essential to deepen our understanding of the underlying principles and advancements within this field, thereby enabling the proposal of effective strategies to enhance performance and enable practical applications.

In this perspective, this chapter aims to provide a comprehensive overview of device architectures utilized in magneto-ionics. Subsequently, it offers a concise summary of recent developments in the field, focusing on various ions and their respective contributions. Finally, the latter portion of this chapter explores the potential of magneto-ionics in the exciting realm of neuromorphic computing.

1.5.1 Device architectures

A typical magneto-ionic device consists of a gate electrolyte in contact with a FM,²³ where the application of an external voltage induces ionic motion and electrochemical reactions. Consequently, reversible modifications in the magnetic material's performance can be achieved. In magneto-ionic studies, the whole device architectures are fabricated differently based on techniques used for magnetoelectric characterization and voltage actuation.

For magnetoelectric characterization, two common configurations are widely used: field effect transistor (FET) and condenser-like structures. As depicted in **Figure 1.12a**, a FET geometry consists of a source electrode, a drain electrode and a gate electrode. This structure is primarily designed for magnetoelectric measurements employing the anomalous Hall Effect (AHE). By applying a voltage to the gate electrode across the insulator, changes in magnetization can be induced. These changes can be tracked by measuring the current flowing between the source and the drain electrodes since there is an inherent connection between the collected electrical data and magnetic information. In this way, the magnetic properties of the material, such as magnetic moment or magnetic field sensitivity, can be determined. The second configuration

involves a condenser-like structure, as illustrated in **Figure 1.12b**. It utilizes a heterostructure composed of magnetic materials and an insulator positioned between two electrodes. When a voltage is applied between these two electrodes across the film and insulator, it can lead to modulation of magnetism. This modulation can be directly monitored using magnetic detection equipment such as vibrating sample magnetometer (VSM), MOKE, superconducting quantum interference device (SQUID) magnetometers.

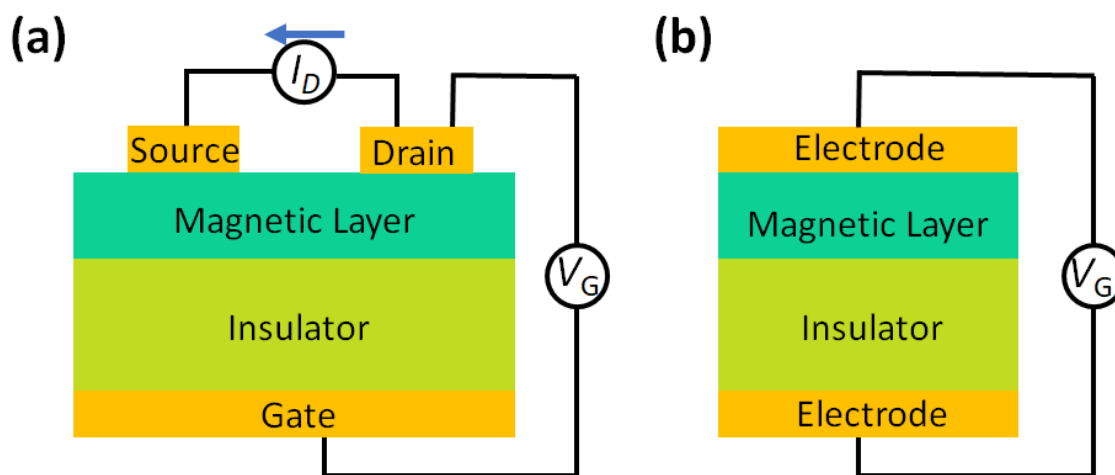


Figure 1.12. Schematic diagrams of two different geometries used for magnetoelectric characterization on magnetic materials: (a) the field-effect transistor (FET) and (b) the capacitor. V_G represents the applied gate voltage that induces an electric field, while I_D represents the current flow used to indirectly detect magnetic changes (the arrow depicts the direction of I_D).

In the field of magneto-ionics, the choice of architecture between solid/liquid or all-solid-state configurations (as shown in **Figure 1.13**) allows for flexibility based on the utilization of either liquid or solid electrolytes. These electrolytes play a crucial role as dielectrics, facilitating the generation of an effective electric field for magnetic actuation, while also serving as ion reservoirs, ensuring the reversible ion transport within the system.

Liquid electrolyte. Various liquid electrolytes have been explored in magneto-ionic studies and they involve three main types: (i) polar aprotic organic solvents, such as propylene carbonate (PC), (ii) ionic liquids, such as LiPF_6 dissolved in ethylene carbonate or KClO_4^- polyethylene oxide and (iii) aqueous electrolytes with dissolved KOH or NaOH. These liquid electrolytes are popularly employed in magneto-ionics for several reasons:

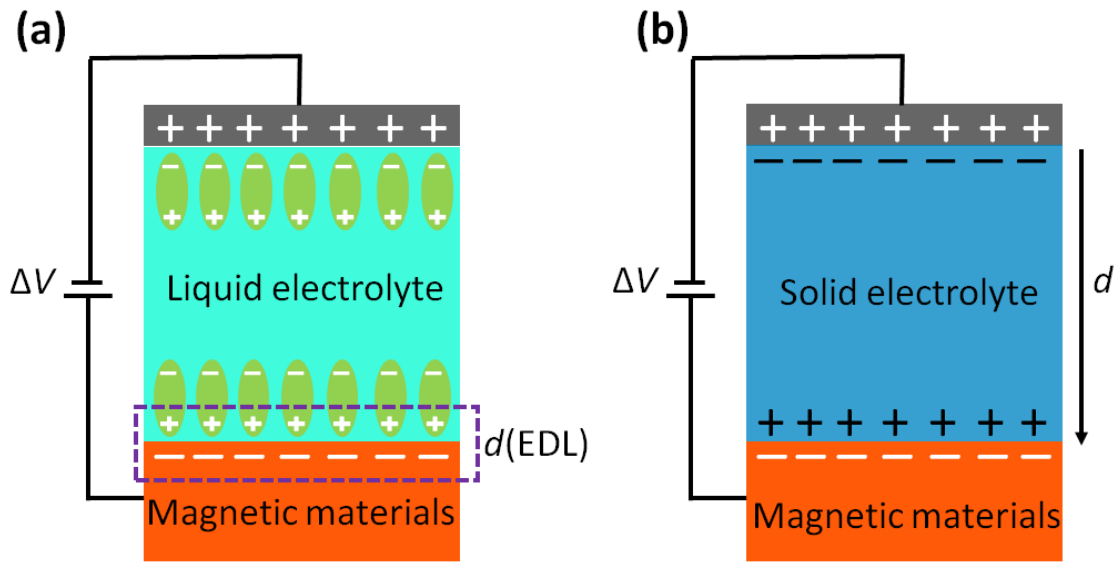


Figure 1.13. Two magneto-ionic configurations for voltage actuation. Schematic of (a) Solid/liquid configuration; (b) all-solid-state configuration. EDL stands for electric double layer and d denotes the effective thickness of the capacitor used to calculate the electric field.

- i) High ionic conductivity: Liquid electrolytes exhibit high ionic conductivity, allowing for efficient ion transport within the system. This enables rapid and reversible changes in the magnetic properties of materials.
- ii) Enhanced charge density: Liquid electrolytes can accumulate a higher charge density compared to solid ones due to the formation of EDL (the effective thickness $d \approx 1$ nm). This higher charge density enables stronger electric fields and larger modulation of the magnetic properties (This has been discussed in detail in **section 1.4.2**).
- iii) Easy ion exchange: Liquid electrolytes provide a favorable environment for ion exchange and diffusion. This facilitates the manipulation of ion concentrations, allowing for precise tuning of the magnetic properties.
- iv) Versatility: Liquid electrolytes offer flexibility in terms of composition, allowing for customization of the ionic species and solvents used. This versatility enables optimization of the electrolyte properties to suit specific magneto-ionics requirements.

However, liquid electrolytes also have limitations that need to be considered:

- i) Evaporation and leakage: Liquid electrolytes are prone to evaporation and can leak from the device, leading to degradation in performance and potential safety hazards,

which require special attention to ensure proper sealing and containment of the liquid electrolytes.

- ii) **Stability:** Some liquid electrolytes may exhibit limited stability, particularly under high voltages or extended operation. This can lead to degradation of the electrolyte and reduced device performance over time.
- iii) **Compatibility:** The choice of liquid electrolyte must consider compatibility with the other materials used in the magneto-ionics device. Some liquid electrolytes may interact or react with the device components, leading to undesired effects or device failure.
- iv) **Environmental impact:** certain liquid electrolytes may contain hazardous or environmentally harmful materials. Proper handling, disposal, and consideration of eco-friendly alternatives are essential to minimize environmental impact.

Solid-state electrolyte. A solid-state electrolyte is a type of electrolyte that is in a solid-state rather than a liquid or gel form. It conducts ions while remaining solid, which plays a crucial role in enabling the movement of ions for magnetization manipulation in a solid-state system. Early success in using solid-state electrolytes for magneto-ionics has been achieved by Bauer et al.¹¹ in a Co/GdO_x bilayer, wherein GdO_x serves as a solid electrolyte and a reservoir for oxygen ion. The authors demonstrates that this solid electrolyte gating of the interfacial oxidation allows for voltage control of magnetic properties to an unprecedented level never achieved through conventional ME mechanisms. Other solid-state electrolytes such as HfO_x,^{158,159} Lithium phosphorus oxynitride (LiPON) and Yttrium iron garnet (YIG)¹⁶⁰ have also attracted great appeal in this field. Solid-state electrolytes hold several advantages compared with liquid counterparts, including:

- i) **Enhanced Stability:** solid-state electrolytes offer improved chemical and electrochemical stability so that they can withstand higher voltages, resist degradation, and maintain their functionality over extended periods, making them suitable for long-term device operation.
- ii) **Lower leakage and evaporation:** solid-state electrolytes eliminate the concerns of leakage and evaporation associated with liquid electrolytes. This enhances the safety and reliability of magneto-ionics devices, particularly in applications where sealing and containment are challenging.

- iii) Compatibility with solid-state materials: solid-state electrolytes can be more compatible with other solid-state materials, such as magnetic thin films or electrodes. This compatibility facilitates better integration and interface properties, leading to improved device performance and functionality.
- iv) High ionic conductivity: although solid-state electrolytes generally have lower ionic conductivity compared to liquid counterparts, significant advancements have been made in developing solid-state electrolytes with high ionic conductivity. These materials enable efficient ion transport and facilitate rapid modulation of the magnetic properties.

However, solid-state electrolytes also have certain limitations that need to be considered:

- i) Limited ionic conductivity: despite recent progress, the ionic conductivity of solid-state electrolytes is typically lower than that of liquid electrolytes. This can impose constraints on the speed and efficiency of ion transport, potentially impacting the dynamic control of the magnetic properties.
- ii) Fabrication challenges: the preparation and fabrication of high-quality solid-state electrolytes can be complex and require specialized techniques. Ensuring homogeneity, uniformity, and absence of defects or impurities in the solid-state electrolyte layer can be challenging, which can affect device performance.
- iii) Interface compatibility: Achieving good interface compatibility between the solid-state electrolyte and the adjacent materials is crucial. Mismatched properties or chemical reactions at the interfaces can hinder ion transport and introduce additional resistance, limiting the overall performance of the magneto-ionics device.

Until now, extensive research has been conducted on both liquid electrolytes and solid-state electrolytes in magneto-ionics. The choice between the two depends on the specific requirements of the application. Ongoing research endeavors to overcome these limitations and advance both types of electrolytes, ultimately leading to the development of innovative magneto-ionics devices with enhanced performance and functionality.

Solid electrolytes, though lacking the ability of forming the EDL, provide advantage over traditional dielectric layers in terms of mobile ions. This feature greatly appeals for all-solid-state magnetic devices, especially in the field of magneto-ionics, which mainly depends on the voltage-driven ions motion (This will be discussed in detail in the coming section 1.5.2). Thus,

the use of electrolytes, either liquid or solid, significantly advances the field of VCM and provides an opportunity for relatively low-voltage operation of magnetoelectric devices.

1.5.2 Recent advances

The first reports realizing magneto-ionic control of magnetism in ultrathin metal films dealt with oxygen-based interfacial reduction/oxidation and associated changes in magnetic anisotropy and coercivity.¹¹ Since then, numerous ionic systems, such as Li^+ ,¹⁶¹ F^- ,^{162,163} H^+ ^{13,16,17} and N^{3-} ^{22,164,165} species, have been investigated. Consequently, this field has witnessed remarkable advancements, particularly in the areas of operating at room temperature, enhancing switching speed, achieving reversibility, and expanding the scope of magneto-ionic tunability to encompass various magnetic phenomena and functional materials. The following discussion will primarily center around significant breakthroughs in this emerging discipline, with particular emphasis on the employed ions.

1.5.2.1 Oxygen ion

A typical oxygen-based magneto-ionic system comprises a FM (metal or oxide) /electrolyte (solid or liquid) heterostructure, in which the magnetism relies sensitively on oxygen stoichiometry and defect structure of target materials. The capability of voltage-driven oxygen transport to tune composition and structure presents a powerful means to electrically control material properties in these systems. Bauer et al.¹¹ made a ground-breaking discovery by directly observing the voltage-induced migration of O^{2-} in Co/GdO_x bilayers. In this case, the PMA in this system can only be derived from an optimally oxidized Co interface and the oxygen state can be modified by the voltage-triggered removal and insertion of oxygen ions at the Co/oxide interface. Consequently, this solid-state electrochemical switching of the interfacial oxidation state can completely remove and restore PMA of a thin Co layer. Importantly, the oxidation state remains unchanged even in the absence of voltage, which highlights the potential of magneto-ionic approaches in the design of nonvolatile spintronic devices. Subsequently, Gilbert et al.¹⁴ revealed how the depth-dependent oxygen diffusion affects the magnetic properties of a 15 nm-thick Co adjacent to AlO_x/GdO_x layers through their structural and magnetic depth profile analysis, which was recorded by the polarized neutron reflectometry (PNR) technique. Specifically, the authors demonstrated that magnetization was tailored along the first 10 nm and that the process was reversible up to a 92%. O^{2-} ion migration and subsequent interfacial oxidation/reduction reactions are also discussed for voltage-induced

magnetic changes in ultrathin Co, Fe, and Co/ Ni films adjacent to HfO_x, AlO_x, MgO or SrCoO_{2.5} barrier layers.¹⁵⁴ As a result, various magnetic properties, such as the easy axis,¹⁶⁶ T_C ,¹⁶⁷ M_s ,¹⁶⁸ H_C ,¹⁶⁹ exchange bias^{170,171} have been successfully controlled via oxygen-based magneto-ionics. Besides these basic magnetic properties, the Dzyaloshinskiie-Moriya constant,¹⁷² which plays a significant role in stabilizing spin textures, such as skyrmions,¹⁷³ chiral domain walls,¹⁷⁴ and spin spirals,¹⁷⁵ have been shown to be tuneable using magneto-ionics in a Pt/Co(0.6 nm)/HfO_x/ionic liquid system. However, the use of magneto-ionic systems that rely on the insertion of O²⁻ ions from an external electrolyte to a target FM material is often hampered by slow dynamics at room temperature, irreversible compositional and structural changes in the FM phase, and poor cyclability. Furthermore, achieving a fully OFF magnetic state with voltage for relatively thick films can be difficult due to the limited penetration of external ions towards the interior of the FM target layers.

To overcome these issues, Quintana *et al.*¹⁵ proposed an alternative “structural-oxygen” approach, that is, utilizing materials that are already oxidized and contain migrating oxygen ions in their as-deposited state. In their study, 100 nm-thick Co₃O₄ films, prepared by plasma-enhanced atomic layer deposition onto SiO₂, were immersed in PC electrolyte containing solvated Na⁺ ions, which is a polar, anhydrous liquid electrolyte capable of generating a significant electric field with low voltage due to the formation of an EDL. By applying a negative voltage, the Co₃O₄ was reduced to Co metal phase, leading to the emergence of ferromagnetism. Conversely, a positive bias reversed the process, resulting in the oxidation of Co back to Co₃O₄ and the disappearance of ferromagnetism. This ON-OFF switch relies on gate-induced O and Co migrations that were driven by mixed vacancy clusters, evidenced by Positron annihilation spectroscopy. Additionally, the ionic transport was found to be promoted at grain boundaries and facilitated by the formation of diffusion channels that contained high levels of oxygen, as observed by high-angle annular dark-field scanning transmission electron microscopy (HDAAF-STEM) and electron energy loss spectroscopy (EELS). Most notably, the process was self-sustaining and did not require an external source or sink of oxygen.

Despite significant advances in the development of oxygen ion-based magneto-ionic systems, the kinetics of the oxidation/reduction reactions are limited by the diffusion of O²⁻. Although sub-millisecond to second modulation has been achieved for thin films up to a few nanometres thick,^{11,176,177} thicker materials typically require minutes to hours for switching.^{14,15,178,179} However, comparisons with resistive switching mechanisms suggest that faster switching

times, potentially on the sub-100 nanosecond timescale, may be achievable through engineering of the ion transport pathways in oxygen-based magneto-ionic reactions.

1.5.2.2 Lithium and fluoride ion

Taking over electrochemical concepts from batteries and supercapacitors, the use of lithium as the mobile ion in magnetoelectric studies has attracted great interest due to their small size, the capacity for reversible intercalation, and fast diffusion kinetics.^{18,19,106,180} The majority of research in this area has centred around intercalation and deintercalation of lithium ions, which are provided by either liquid (e.g., non-aqueous organic liquids containing LiPF_6)^{18,161,181,182} or solid electrolytes (e.g., LiPON).^{183,184} resulting in significant changes in magnetization through bulk electrochemical processes. Thus, reversible changes in the room-temperature magnetization, e.g., in various iron oxides^{18,161,183–185} and ferrites,^{182,186} are realized due to associated valence change and redistribution of transition metal ions (e.g., $\text{Fe}^{2+}/\text{Fe}^{3+}$). For example, Dasgupta et al.¹⁶¹ demonstrated that the magnetic properties of maghemite ($\gamma\text{-Fe}_2\text{O}_3$) can be precisely controlled in a reversible manner by voltage-induced Li insertion or extraction. Similarly, Zhang et al.¹⁸ showed that nanoscale $\alpha\text{-Fe}_2\text{O}_3$ -based batteries can be electrically tuned to exhibit strong ferromagnetism by driving lithiation (magnetic moment enhancement) or delithiation (magnetic moment suppression). The voltage-driven Li^+ ion intercalation has also been demonstrated to be effective in tuning the magnetic moment values of nanoporous $\text{Co}_{0.5}\text{Ni}_{0.5}\text{Fe}_2\text{O}_4$ and CoFe_2O_4 in a reversible manner using an electrolyte of 20 wt.% LiTFSI dissolved in EMIM-TFSI electrolyte within a potential window of 1.5-3.3 V. The potential window can be extended to 1.1-3.4 V for larger variations in magnetic moment values, but the effects become highly irreversible. In addition, researchers have investigated the use of LiTFSI in EMIM-TFSI electrolyte for Li^+ intercalation in $\alpha\text{-LiFe}_5\text{O}_8$ mesoporous thin films.¹⁸⁷ These spinel ferrites were found to have a reversible Li^+ storage potential between 3.2 and 1.4 V, with electrochemical reactions proceeding topotactically. This allowed for control and tuning of M at room temperature in a reversible manner, with up to 4% change. Furthermore, oxygen-deficient $\text{LiFe}_5\text{O}_{8-x}$ was used as a ferrimagnetic material whose magnetic properties could be tailored by voltage in the solid state at the nanoscale, thanks to the oxide's low activation energy for Li^+ ion migration.¹⁸² Recently, Ameziane et. al.^{188–190} have made groundbreaking strides in integrating solid-state Li-ion batteries and supercapacitors with magnetic systems, targeting the modulation of their magnetic performance via voltage-driven Li-ion movement. Some of the notable magnetic properties they have been able to control include perpendicular magnetization

switching in Co/Pt bilayer, dynamics of magnetic skyrmions in the Pt/CoFeB/Pt system and the Ruderman-Kittel-Kasuya-Yosida (RKKY) interlayer interaction in a perpendicularly magnetized [Co/Pt]N/Ru wedge/Pt/Co/Pt multilayer. Impressively, these modulations are executed using small voltage, demonstrating high efficiency, substantial durability and fast response, all under ambient conditions.

The reversible manipulation of ferromagnetic metals with high magnetization is also possible using Li-electrochemistry. For instance, in amorphous $\text{Co}_{40}\text{Fe}_{40}\text{B}_{20}$ films, the (de)lithiation using a solid-state electrolyte yields reversible control of magnetization and magnetic anisotropy via a conversion reaction with Li^+ .¹⁹¹ Also, Li-based electrolytes are beneficial to facilitate the reducibility of iron oxide to iron at RT for the voltage control of magnetization, anisotropy, and exchange bias in iron oxide/iron and FeO_x/FePt films.^{176,192,193}

Apart from lithium ions, the use of fluoride-ion based magneto-ionics offers unique advantages, as they can be intercalated into or deintercalated from suitable host structures.^{162,163} This allows for the use of materials that are inaccessible to Li^+ , such as perovskite-related structures,^{20,194–197} like the $\text{A}_{n+1}\text{B}_n\text{O}_{3n+1}$ Ruddlesden-Popper (RP) system. This structure is particularly interesting as it consists of perovskite blocks separated by rock salt layers which can host additional anions such as fluoride. Recent research has demonstrated reversible magnetization tuning of the ferromagnetic RP manganite $\text{La}_{1-2x}\text{Sr}_{1+2x}\text{Mn}_2\text{O}_7$ through electrochemical F-ion (de)intercalation in an all-solid-state system.¹⁶³ This represents a significant achievement, as a 67% change in relative magnetization was observed with a low operating potential of <1 V, negligible capacity fading, and high Coulombic efficiency. The fluoride-ion based magneto-ionics offers exciting possibilities for the development of novel materials and spintronics with high energy efficiency.

Overall, voltage-induced transport of Li and F ions has been shown to result in significant changes in magnetic properties and offers potential advantages in terms of high electrical efficiency and non-volatility. However, the use of these approaches is currently incompatible with CMOS technology, which limits their viability for practical applications.

1.5.2.3 Hydrogen ion

The utilization of hydrogen ions in magnetoelectric systems has been motivated by gas-phase experiments, which have demonstrated considerable reversible magnetic changes upon (de)hydrogenation of metals.¹⁹⁸ Electrochemical hydrogenation of metals proceeds via the

voltage-controlled reduction of H^+ to atomic H, followed by its absorption into the metal. Hydrogen ion, which is relatively innocuous, and is at the same time the smallest possible ion, can easily diffuse through interstitial sites in metals with a high mobility at room temperature.¹⁹⁹ This feature making it ideal for inducing rapid electric-field-driven property changes in solid-state structures.

Hydrogen ion-based magneto-ionics is a promising field of research that has attracted significant attention in recent years. One of the key breakthroughs in this area was made by Tan et al.,¹³ who observed a voltage-induced spin reorientation in an all-solid layer stack of Au/GdOx/Co(0.9 nm)/Pt under ambient conditions. The authors explained this phenomenon as resulting from a modification of the interface magnetic anisotropy due to electric field-moderated hydrogen migration through layers and electrochemical reactions at the GdOx/Co interface. Specifically, they proposed that the mobile hydrogen ions were generated by water splitting at the top Au electrode, followed by their being pumped through the GdOx layer, and the reduction of H^+ to atomic H at the Co metal interface. By applying the reverse voltage, interstitial water and hydroxides in the Gd_2O_3 release oxygen, which reacts with the Co, and hydrogen, which is ejected. Importantly, it was found that inserting a thin Pd layer at the Co/GdOx interface allowed for a larger voltage range to be applied and faster switching to occur, as the Pd layer protected the Co layer from oxidation. Notably, this hydrogen ion-based magneto-ionic device was demonstrated to be reversible for more than 2000 cycles, with only a slight decay in device functionality and magnetization switching at a relatively high speed of 100 m s^{-1} . This work provides important insights into the fundamental mechanisms underlying hydrogen ion-based magneto-ionics and highlights the potential for this technology to be used in next-generation spintronic devices.

The discovery of voltage-triggered hydrogen migration has led to the development of controllable magnetic properties and materials. As a result, large changes in properties such as magnetic anisotropy,^{200,201} magnetization,²⁰² coercivity field,¹⁷ magnetic order^{203,204} and control of spin textures,^{16,205,206} have been observed. Huang et al.²⁰² have utilized solid-state hydrogen gating to demonstrate deterministic reversal of Néel and magnetization vectors in the ferrimagnet GdCo under ambient conditions. The heterostructure studied comprises a gold gate electrode, a GdOx layer as a proton injector and a perpendicularly magnetized amorphous GdCo ferrimagnetic layer. Element-specific XMCD analysis was used to confirm that the Gd and Co moments exhibit different responses to hydrogen loading in GdCo. Consequently, a

gate voltage can be applied to reversibly adjust the Gd moments from dominating the Co moments to being dominated by them, leading to a change in the total magnetization from Gd-dominated to Co-dominated in the ferrimagnetic layer. This process enables the selection of the dominant magnetic sublattice, as well as independent inversion of Néel and magnetization vectors. Remarkably, in racetrack devices, ferrimagnetic spin textures such as domain walls and skyrmions can be efficiently generated using hydrogen gating within a brief gating time of just 50 μs , maintaining durability for over 10,000 cycles. Recently, Ye et al.¹⁷ showcased the ability to reversibly charge and discharge bulk-sized SmCo_5 powder with hydrogen atoms using minimal voltages. Impressively, this method allows for the tuning of SmCo_5 powder's coercivity by approximately 1 T—a leap that's more than two orders of magnitude greater than what was previously achieved in ultrathin films through charge doping and magneto-ionics. This breakthrough facilitates voltage-assisted magnetization reversal in high-anisotropy SmCo_5 at ambient temperatures.

Besides control of magnetism in metal structures, hydrogen-based magneto-ionic control is also demonstrated for oxide films. In $\text{SrCoO}_{3-\delta}$ films, the voltage-induced insertion of hydrogen ions by ionic liquid gating leads to the formation of $\text{HSrCoO}_{2.5}$, accompanied by a change of magnetic state.²⁰⁷ Furthermore, A novel phase transformation from ferrimagnetic metallic into antiferromagnetic insulating is achieved by protonation of NiCo_2O_4 films via ionic liquid gating at elevated temperatures.²⁰⁸

The opportunities presented by hydrogen ion-based techniques include high scalability, nonvolatility and energy efficiency, going straight to the heart of today's most critical technological challenges. Whereas several challenges come to mind, the first being that the improved mobility of hydrogen is partly arising from weaker bonding, which makes it difficult to retain hydrogen at elevated temperatures (most consumer devices are designed to operate at up to 70 °C, and sometimes much hotter), leading to limitations on the long-term stability of such devices. A second issue with this ionic technology is that the read/write times need to be further improved is to compete with modern hard drives or STT-MRAM, with 10-ms and 10-ns latencies, respectively. Finally, the hydrogenation reaction could induce a large lattice expansion which has been previously identified as a failure mechanism.²⁰⁹

1.5.2.4 Nitrogen ion

As discussed in section 1.5.1, the “structure-oxygen” approach,¹⁵ which incorporates the migrating oxygens into a single layer transition-metal oxide during its deposition, creates a

crystal structure that has more local vacancies and larger ionic pathways. This kind of target material facilitates ion movement in and out of the target material with reduced structural distortion. To further extend the potential of this approach, an examination of the functionality of ions beyond oxygen in magneto-ionic target materials would likely prove fruitful.

Indeed, nitrogen ion-based magneto-ionics (e.g., the structure nitrogen approach) has been proposed by de Rojas *et al.*,²² with significant advantages, both energetically and functionally, over their oxygen-based counterparts. To clarify this superiority, the authors deposited polycrystalline CoN and Co₃O₄ films with the same thickness on identical substrates. Then the samples were electrolyte-gated at –50 V using PC with solvated Na⁺ ions, while their M vs H loops and M_s as a function of time were recorded. It was observed that M_s increases with time, asymptotically, reaching 588 emu cm⁻³ for Co₃O₄ and 637 emu cm⁻³ for CoN. The linear magnetization rate of CoN is calculated to be 722 memu cm⁻³ s⁻¹, a fivefold enhancement over sputtered Co₃O₄. Also, CoN films were found to have better onset voltage and endurance than Co₃O₄ films. The enhancement of these properties was attributed to the lower activation energy for ion diffusion and the lower electronegativity of nitrogen compared to oxygen. Perhaps the most interesting feature of nitrogen magneto-ionics, beyond the increased magneto-ionic rates, is the exact way in which the ions are transported from the film. As characterized by HAADF-STEM and EELS, nitrogen transport occurs uniformly creating a plane-wave-like migration front, unlike the formation of diffusion channels for oxygen migration. Subsequently, nitrogen-based magnetoionics has also been reported in FeN films.¹⁶⁴ Iron nitride films show a larger increase in coercive field, H_C , up to ≈ 100 Oe, compared with ≈ 10 Oe in cobalt nitride, indicative of relatively smaller activated magnetic regions, comprising single- or few- domain structures in mostly denitrided regions. This suggests that FeN, while slower, may be more useful for magnetic memory applications.

Recently, Jensen *et al.*²¹ have reported an interesting study on the reversible manipulation of exchange bias in CoFe/MnN heterostructures by using nitrogen-based magneto-ionics. In this study, the researchers found that the application of a magnetic field during cooling leads to the diffusion of nitrogen ions from the MnN layer into the Ta capping layer. This process results in a significant exchange bias, with values of 618 Oe at 300 K and 1484 Oe at 10 K. Moreover, the researchers observed that the exchange bias can be further enhanced by applying a voltage conditioning, leading to a 5% and 19% increase at 300 K and 10 K, respectively. Importantly, this enhancement can be reversed by applying a voltage with an opposite polarity. The

researchers attribute the enhancement in exchange bias to the nitrogen migration within the MnN layer and its diffusion into the Ta capping layer, which is supported by the results of polarized neutron reflectometry studies.

Overall, nitrogen ion-based magneto-ionics represents a promising avenue for low-energy-dissipation spintronics. One significant advantage of this approach is its potential to overcome the limitations associated with room temperature ionic migration and irreversibility commonly observed in certain oxygen-based magneto-ionic systems. Moreover, this method has demonstrated faster ionic motion and is compatible with current CMOS technology. However, there is still considerable room for improvement in the optimization of structural ion materials with respect to switching speeds and cyclability before they can be considered competitive with other magneto-ionic approaches. Currently, the switching states in structural ion systems require 10^2 - 10^3 seconds at room temperature, which falls well behind H^+ ¹³ or heat-assisted O^{2-} systems.¹¹ To advance this approach towards device applicability, additional work must be done, such as defect engineering through ion irradiation, regulation of ion transport at the nanoscale, and the selection of better electrolytes.

1.5.3 Brain-inspired magneto-ionics

Magneto-ionics, relying on the control of magnetic properties through voltage-driven ion migration, holds significant potential for the development of low-power memory applications. In recent years, significant progress has been made in improving ion motion rates and endurance, which are the two main bottlenecks to exploit the full potential of magneto-ionics at room temperature. This has been achieved by proper selection of the moving ion species, target materials, heterostructure designs, electrolytes, and voltage actuation protocols. Thanks to these advancements, it is now possible to suggest that magneto-ionic materials may serve as suitable candidates for not just spintronic applications, but also for newly proposed neuromorphic computing paradigms that draw inspiration from the brain.

Over the last two decades, significant progress has been made in brain-inspired algorithms, such as artificial neural networks. These advances have been driven by improvements in computational power, access to big data, and breakthroughs in training methods. However, the implementation of these algorithms on digital computers is becoming increasingly limited by the von-Neumann architecture, which separates processing and memory units and constrains memory bandwidth, slowing down processing and increasing energy consumption. As a result, there is a growing body of research aimed at developing alternative computing paradigms inspired by biological principles. One such approach is neuromorphic computing, which aims to create hardware that mimics the functioning of the brain in order to perform sophisticated tasks in an energy-efficient manner.

To advance the field of neuromorphic computing and engineering, the exploration of novel physics and materials will be of key relevance creating artificial nanoneurons and synapses, connecting them together in huge numbers, organizing them in complex systems and computing with them efficiently. Early successes in neuromorphic computing have relied heavily on conventional electronic materials, particularly silicon-based CMOS spiking neural networks. Prominent examples include the TrueNorth chip from IBM that can recognize disparate objects from video feeds in real-time and the SpiNNaker Project within the European Union Human Brain Program that can execute cognitive tasks. However, Since CMOS chips suffer from energy inefficient synaptic operations based on volatile random-access memory, significant effort has been devoted to nonvolatile memory as a foundation for neuromorphic computing. To date, a number of systems have shown promise in this regard, based on resistive-switching oxides, phase-change compounds, spintronic multilayers. Among them, magneto-

ionics is particularly appealing due to the potential improvement of energy efficiency, envisaging ultra-low power hardware with minimized Joule heating effects. In addition, magneto-ionics could exploit the extra degree of freedom provided by the vector nature of magnetization which may allow synapses to be directly programmed with positive and negative synaptic weights without need of additional electronics. For example, Mishira et al.²¹⁰ have successfully developed an energy-efficient three-terminal artificial synapse at the nanoscale, utilizing magneto-ionic principles. This device incorporates distinct pathways for reading and writing operations and relies on the magnetic properties of Cobalt (Co) to enable the generation of both positive and negative synaptic outputs. By utilizing voltage-actuated oxygen movement into and out of the Co layer, the magnetization of Co, which represents the synaptic weight, can be precisely manipulated. Moreover, they have effectively demonstrated the realization of a wide range of synaptic functions, including synaptic potentiation and depression, modulation of spike magnitude, rate, and timing-dependent plasticity, as well as the transition from short-term to long-term plasticity. This comprehensive demonstration underscores the versatility and potential of the proposed brain-inspired magneto-ionic technologies.

However, while the weight (e.g., resistance, magnetization) update in most current nonvolatile technologies can be manipulated by changing the input electric signal (value and sign), the post-stimulated (without input) states are usually not controllable due to system-inherent relaxation effects. This post-stimulus uncontrollability greatly limits the emulation of some important brain-inspired functions, such as maintaining learning efficiency even during deep sleep. Therefore, procedures capable of controlling post-stimulated evolution while maintaining good tunability in modulation of weight update are highly desired.

1.6 The "structural-ion" approach in magneto-ionics

The manipulation of magnetic states through magneto-ionics plays a pivotal role in enabling a multitude of functions in information technologies, as it facilitates the essential switching between fundamental "0" and "1" signals in logic devices. A drastic ON-OFF switching of ferromagnetism via voltage-driven ionic movement has been highly pursued for the realization of information memory and processing. For instance, researchers have used high-temperature voltage-assisted oxidation of ultrathin (0.7 nm) Co layers in contact with GdO_x underlayers to suppress magnetization.¹¹ Additionally, ON-OFF ferromagnetism at low temperatures has been achieved in $\text{La}_{0.74}\text{Sr}_{0.26}\text{MnO}_3$ films by electrochemical (pseudocapacitance) doping.¹⁵ Despite these advancements, these approaches suffer from a weak tuning effect at room temperature, limiting their widespread application. Although the use of light ions, such as H^+ and Li^+ , allows for magnetization changes at room temperature, achieving a total OFF state remains problematic due to difficulties in fully oxidizing or reducing the target material.

This Thesis explores the use of "structural-ion" approaches (as discussed in sections 1.5.2.1 and 1.5.2.4) to address certain challenges and achieve room-temperature ON-OFF switching of magnetism effectively. The proposed magneto-ionic device is housed within a home-made capacitor-like configuration, which is simplified in **Figure 1.13a** and the ON-OFF switching of magnetism is demonstrated in **Figure 1.13b**. The as-grown sample displays paramagnetic properties, representing the OFF state. By applying a negative voltage ($-V$), oxygen or nitrogen ions migrate into the liquid electrolyte, leaving behind ferromagnetic Co metal within the target material, transitioning to the ON state. Conversely, a positive voltage ($+V$) drives the ions back into the target materials from the liquid electrolyte, reducing Co metals to their corresponding oxides, and leading to the OFF state again. This reversible manipulation of the magnetic state allows for precise control and promising applications in magneto-ionic devices.

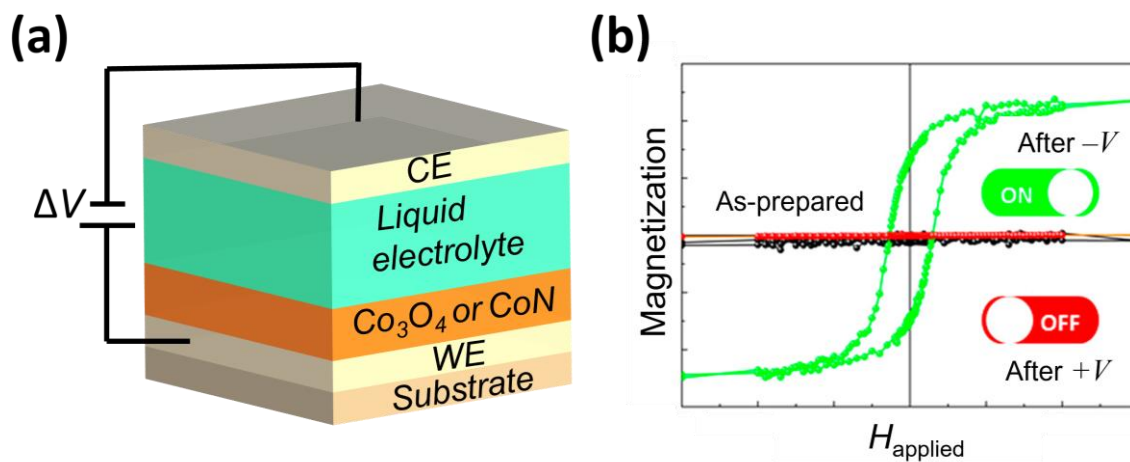


Figure 1.13. Reversible ON-OFF switching of magnetism enabled by "structural-ion" approaches. (a) A schematic representation of the electrolyte-gating process, specifically applied to Co_3O_4 or CoN films. (b) The demonstration of reversible ON-OFF switching of magnetism. This is carried out by recording the magnetic hysteresis loop of a pristine sample, followed by treatment at negative bias ($-V$) and subsequent recovery upon applying positive bias ($+V$).

1.7 Objectives

The primary goal of this Thesis is to harness the potential of “structural-ion” approaches to enable magneto-ionics for technological applications, such as neuromorphic computing. In pursuit of this overarching aim, the following specific objectives are presented below:

- **Feasibility assessment of employing the magneto-ionic system in neuromorphic computing.**
 - The growth of CoN films with thicknesses ranging from 5 to 200 nm using reactive sputtering while using liquid electrolyte gating, for the investigation of the effect of film thickness reduction on ion mobility.
 - Magnetoelectric characterization in CoN films, especially the evolution of magnetization with time (M vs. t), both during (stimulated) and after (post-stimulated) electric voltage application.
 - The exploration of the interplay between ion motion rates and stimulus frequency on M vs. t ; the former is modulated by adjusting film thickness, and the latter by altering the frequency of voltage pulses.
 - The emulation of critical neuromorphic functions, such as information processing, memory retention, recovery, and the potential for self-evolution by maturity (i.e., magnetization updating even when a voltage is no longer applied).
- **Enhancement of magneto-ionics performance in ternary nitride films.**
 - The fabrication of CoN films and CoMnN films, with a 10 at. % substitution of Co by Mn, on identical substrates under uniform growth conditions.
 - The conduction of structural, compositional and electrical measurements on as-prepared CoN and CoMnN films to investigate the influence of Mn introduction on nanostructures and electric transport properties.
 - The comparison of electrolyte-gated evolution of magnetic hysteresis loops and M vs. t in CoN and CoMnN films, to demonstrate the impact of Mn substitution on key magneto-ionic performances, such as the minimum threshold voltage required to initiate magneto-ionic effects and cyclability.
- **Improvement of magneto-ionics cyclability by synergistically combining the advantages of solid and liquid electrolytes.**

- The introduction of an amorphous-like Ta layer as a solid electrolyte between a magneto-ionic target material (specifically, Co_3O_4) and the liquid electrolyte.
- The measurement of the magneto-ionic response and cyclability of Co_3O_4 films varying the thickness of Ta protective layers over a range from 0 to 50 nm, aimed at evaluating the optimal Ta thickness that drastically enhances cyclability while preserving sufficiently high electric fields to trigger ion motion.
- **In-depth exploration of voltage-driven ionic transport mechanisms.**
 - The exploration of voltage-driven ion transport mechanisms behind the observed magneto-ionic phenomena by employing advanced structural and compositional measurement techniques on samples before and after voltage actuation. These techniques include $\theta/2\theta$ X-ray diffraction (XRD), HAADF-STEM, EELS, X-ray absorption spectroscopy (XAS), and elastic recoil detection (ERD) analysis.

2 Experimental

This chapter presents the experimental details employed in this Thesis, along with an overview of the main techniques utilized throughout the study. While theoretical concepts related to conventional techniques are not provided here, as they can be found in advanced textbooks, we aim to offer insights into the fundamentals of less common techniques. This chapter ensures that unfamiliar readers can grasp key concepts essential for understanding our research.

2.1 Sample fabrication

2.1.1 Types of working electrode/substrates

(i) *Si/Ti/Cu*. This substrate is used for magnetoelectric characterization in all studies conducted within this Thesis. For the growth of continuous films, non-doped (100) oriented Si wafers (0.5 mm thick) were previously coated with a 20 nm-thick titanium and 60 nm-thick copper seed layers by reactive sputtering in a high-vacuum chamber (with a base pressure $< 8 \times 10^{-8}$ Torr). **Figure 2.1a** shows the image of the sputtering system used in our lab for sample fabrication. The Ti layer acts as an adhesion layer.²¹¹ As shown in **Figure 2.1b**, the Ti and Cu layers were partly masked to avoid the film deposition of target materials and later served as working electrodes.

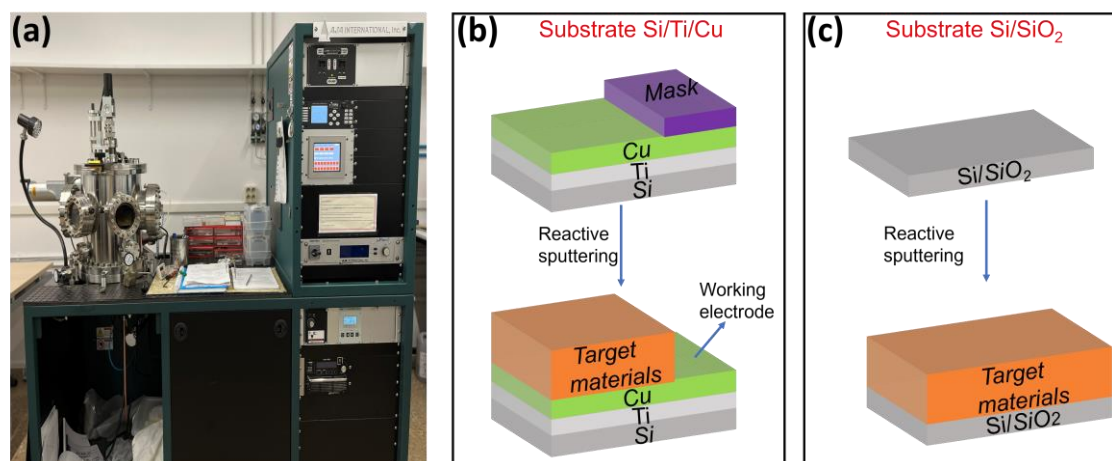


Figure 2.1 (a) Pictures of the sputtering system used in our lab for sample fabrication (AJA International ATC 2400). Schematic diagram of target material growth on substrate (b) Si/Ti/Cu and (c) Si/SiO₂.

(ii) *Si/SiO₂*. Employing this substrate (with thickness of the SiO₂ of around 1 micrometer) for depositing target materials enables the execution of X-ray reflectivity (XRR) and transport measurements. XRR is a powerful tool for the in-depth characterization of multilayer properties (roughness, thickness, and density distribution). However, the exact extraction of the

parameters of stack layers is difficult and complex because the XRR scans acquire an entangled signal from all layers. In this Thesis, a single layer is directly grown on the substrate to avoid this problem and enhance thickness test result precision. In addition, resistivity as a function of temperature is measured for electronic transport analysis. In this case, a high-resistivity SiO₂ layer on the surface of Si substrate serves to provide a stable and uniform background for the sample. Consequently, the occurrence of undesired current flow and voltage drops can be largely avoided, thereby ensuring precise characterization of the sample's electrical properties.

2.1.2 Target materials deposition

The materials of interest investigated in this Thesis encompass Co₃O₄, CoN, and CoMnN films. Preceding their deposition, two distinct substrates, namely Si/Ti/Cu (**Figure 2.1b**) and Si/SiO₂ (**Figure 2.1c**), were positioned on the substrate holder. This arrangement ensures the uniform deposition of the target materials onto these two substrates under identical conditions. These films were grown in a reactive sputtering system with a base pressure in the 10⁻⁸ Torr range. Ultra-high vacuum enables minimization of oxygen contamination and, thus, to rule out traces of oxygen magneto-ionics. The distance between the substrate and targets was around 10 cm, and the growth rate was approximately 0.6 Å s⁻¹. At a total working pressure of 3 × 10⁻³ Torr, Co₃O₄ was grown in a 50% O₂/50% Ar (in gas flow ratios), while CoN and CoMnN were deposited in a 50% N₂/50% Ar atmosphere. For the deposition of CoMnN pure Co and Mn targets were co-sputtered and rates were calibrated to obtain a Co/Mn ratio of 9:1. In addition, the Co₃O₄ films were subsequently coated with Ta protective layers of variable thickness (ranging from 5 to 50 nm), which also show an important role as solid ionic conductor to improve magneto-ionics cyclability. The gun power to grow Ta was 100 W.

2.2 Magnetolectric characterization

For the implementation of the magnetolectric characterization, the samples were mounted in a homemade electrolytic cell filled with anhydrous PC with Na^+ solvated species (5-25 ppm), as displayed in **Figure 2.2a**. Magnetic properties were recorded by performing vibrating sample magnetometer (VSM) while electrolyte gating the films in a capacitor configuration (i.g., Pt/electrolyte/magnetic materials/Cu/Ti/Si) at room-temperature.

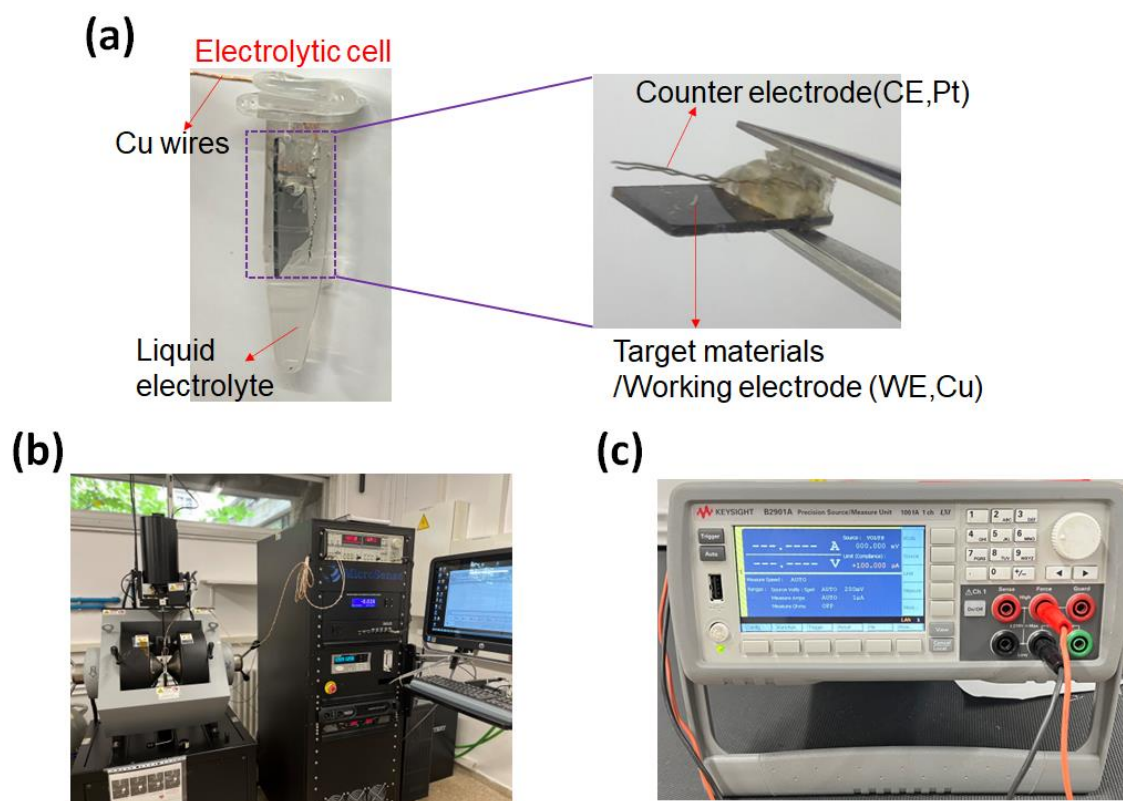


Figure 2.2 (a) Schematic of the homemade electrolyte cell used for magnetolectric measurement while electrolyte gating the films. Pictures of (b) a magnetometer from Micro Sense (LOT-Quantum Design) and (c) an Agilent B2902A power supply.

As shown in **Figure 2.2b**, a VSM from Micro Sense (LOT-Quantum Design), with a maximum applied magnetic field of 2 T, was used. The magnetic properties were measured along the film plane upon applying different voltages, using an external Agilent B2902A power supply (**Figure 2.2c**), between the Cu working electrode and the counter-electrode (Pt wire). The sign of voltage was such that negative charges accumulate at the working electrode when negative voltage was applied (and vice versa for positive voltages). The Na^+ solvated species in the electrolyte are aimed at improving conductivity.^{22,106} The magnetic signal is normalized to the

volume of the sample exposed to the electrolyte. Note that the hysteresis loops were background-corrected using the signal at high fields (i.e., fields always far above saturation fields) to eliminate linear contributions.

2.3 Structural and compositional measurements

2.3.1 $\theta/2\theta$ XRD

$\theta/2\theta$ X-Ray diffraction analysis (XRD) patterns were measured on a Materials Research Diffractometer from Malvern PANalytical, equipped with a PIXcel1D detector, using Cu K_α radiation (**Figure 2.3a**). As shown in **Figure 2.3b**, this technique involves directing X-rays at a crystalline sample at a specific angle (θ) and measuring the resulting diffraction pattern at twice that angle (2θ). When the X-rays strike the crystal lattice of the sample, they interact with the electrons surrounding the atoms. This interaction leads to constructive interference of the X-rays that satisfy Bragg's law,²¹² which is given by:

$$n\lambda = 2d \sin(\theta) \quad (\text{Eq. 2.1})$$

Where n is the order of the diffraction peak (1 for the first-order peak, 2 for the second-order, and so on), λ is the wavelength of the X-rays, d is the interplanar spacing of the crystal lattice. By varying the angle 2θ and measuring the intensity of the diffracted X-rays, a diffraction pattern is obtained. This pattern consists of a series of peaks corresponding to the different crystallographic planes present in the sample. The positions and intensities of the diffraction peaks provide valuable information about the crystal lattice parameters, crystal symmetry, and arrangement of atoms in the material. This information can be used to determine the crystal structure, crystal phase, and other structural properties. Overall, $\theta/2\theta$ XRD is a powerful technique for characterizing the atomic arrangement in crystalline materials, aiding in the identification and analysis of various types of samples.

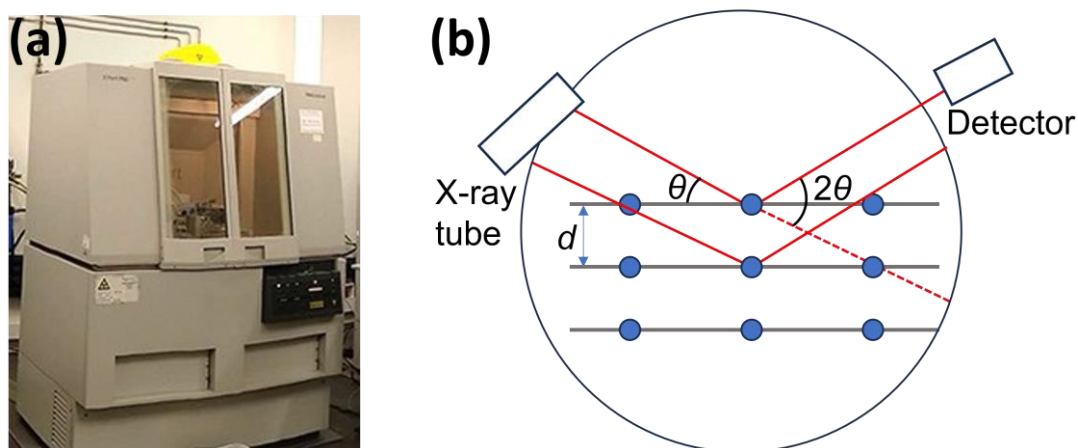


Figure 2.3 (a) Picture of XRD equipment from Malvern PANalytical. (b) Schematic of Bragg's diffraction.

2.3.2 HAADF-STEM and EELS

High-angle annular dark-field scanning transmission electron microscopy (HAADF-STEM), and electron energy loss spectroscopy (EELS) were performed on a TECNAI F20 HRTEM/STEM microscope operated at 200 kV (**Figure 2.3a**). These advanced techniques, integral to materials science and nanotechnology, enable the comprehensive characterization and study of nanoscale material properties.¹⁴⁹ As depicted in **Figure 2.3b**, HAADF-STEM, a specialized variant of STEM, involves the controlled scanning of a focused electron beam across a thin film. The transmitted electrons are captured by a detector positioned at a specific angle. This interaction between the electron beam and the sample's atoms yields high-resolution images, unveiling intricate atomic arrangements. Consequently, scientists can explore crystal lattices, defects, and nanoscale features with exceptional precision.

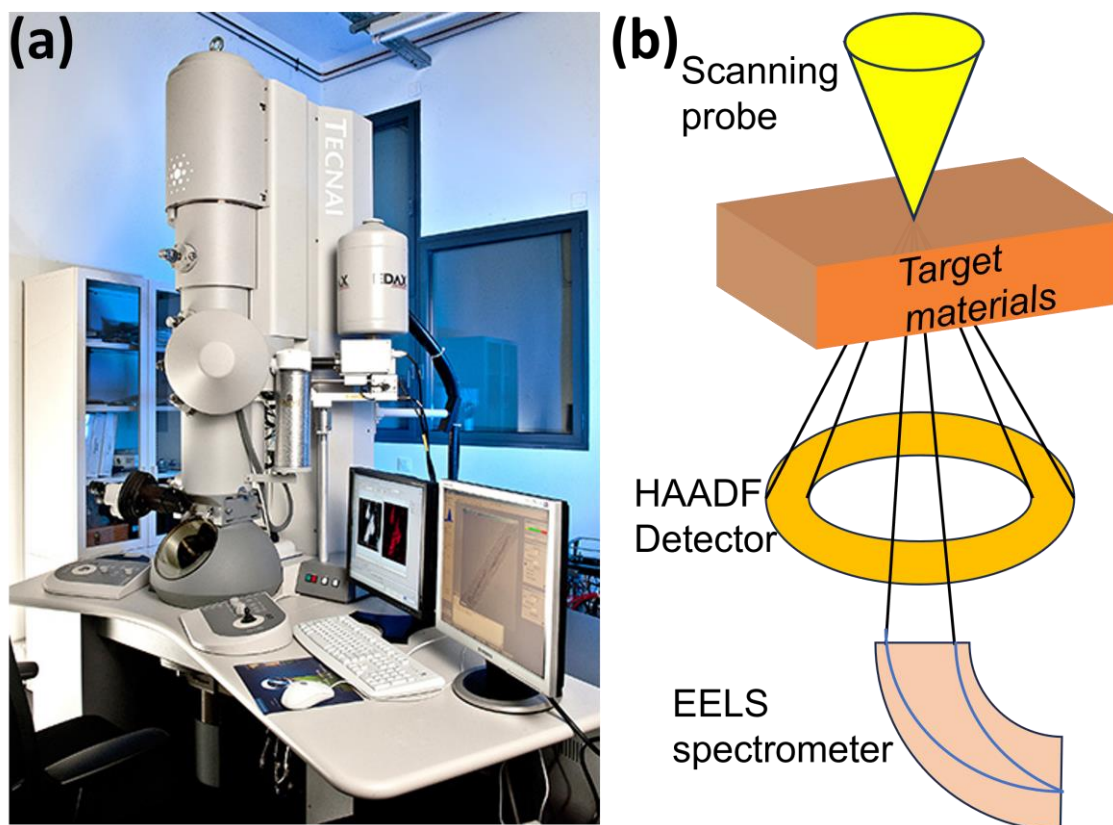


Figure 2.4 (a) Picture of a TECNAI F20 HRTEM/STEM microscope. (b) Schematic of imaging principles of HRTEM and EELS.

Complementary to HAADF-STEM, EELS offers insight into energy variations of electrons upon interaction with the sample. Through the focused electron beam's interaction with a confined region of the specimen, certain electrons undergo energy loss due to diverse

processes, encompassing inelastic scattering, plasmon excitation, and core-level ionization. An energy analyzer then segregates these energy-loss electrons based on their distinct energies. The collected electrons are subsequently subjected to meticulous analysis, culminating in an energy loss spectrum replete with discernible peaks and edges. These features correlate with specific elements within the sample. The subsequent generation of EELS mappings, represented in distinct colors, allows for the visualization of target elements within the designated scanning area. This capability holds significant relevance in research associated with ionic dynamics, as these mappings offer direct evidence of ion distribution and movement. Note that before HAADF-STEM and EELS characterization, the cross-sectional lamellae were prepared by focused ion beam and placed onto a Cu transmission electron microscopy grid.

In this Thesis, the synergistic utilization of HAADF-STEM and EELS techniques emerges as a robust strategy for investigating ion transport mechanisms, with the former providing cross-sectional film images and the latter offering elemental mappings. Enhanced by Fast Fourier Transformation (FFT), crystal phase information is obtained, complementing XRD techniques. Notably, EELS mappings vividly depict localized migration and redistribution of studied ions within the target layer, serving as direct evidence of ion movement and enabling a more coherent interpretation of observed magnetic phenomena. Collectively, these integrated approaches advance our understanding of ion transport and associated magnetic behaviors, offering a comprehensive framework for insightful material analysis.

2.3.3 XAS

X-ray absorption spectroscopy (XAS) measurements were conducted using the BL29-BOREAS beamline at ALBA Synchrotron Light Source (Barcelona, Spain).²¹³ The dichroism end-station consists of a cryomagnetic designed for ultra-high vacuum (UHV) compatibility, manufactured by Scientific Magnetics Ltd. The samples are situated within a UHV environment boasting a base pressure below 1×10^{-10} mbar, and mount on a sample holder connected to the cold finger of a variable temperature cryostat spanning from 3 K to 350 K. To facilitate drain current measurements, the sample insert is electrically insulated. Additionally, the sample holder features four supplementary electrical contacts for 4-probe assessments. Cryomagnetic is constituted of a triad of orthogonal superconducting split-coils, enabling the generation of horizontal magnetic fields of up to 6 T along the beam axis, with a sweep rate of 2 T/minute. Simultaneous activation of these coils encompasses a sphere of 2 T, progressing at

a sweep rate of 0.4 T/minute. Moreover, a 3-chamber sample preparation and insertion system expedite swift sample interchange, accommodating up to four samples concurrently. The preparatory chamber situated beneath the magnet encompasses standard surface preparation tools such as a cleaver, scraper, molecular beam epitaxy-evaporators for metals and organic molecules, an e-beam heating stage, and an ion sputtering gun. The experimental spectra were acquired utilizing the total electron yield (TEY) mode, thus ensuring meticulous and precise data acquisition.

XAS serves as a robust technique employed to explore the electronic structure and local surroundings of atoms within a material.²¹⁴ This approach offers valuable insights into energy levels, bonding characteristics, and the coordination environment of specific elements in each sample. The underlying principle of XAS involves interaction between incident X-rays and the sample, followed by the collection and analysis of the resulting absorption data. This process involves generating X-ray radiation with a defined energy range using either a synchrotron light source or an X-ray tube, specifically adjusted to match the energy levels associated with core electrons of elements within the sample. As X-rays traverse the material, their intensity is attenuated (illustrated in **Figure 2.5a**). This attenuation is described by Beer's law,²¹⁵ quantified through the absorption coefficient, as indicated in Eq. 2.2:

$$I_t = I_0 e^{-\mu(E)t} \quad (\text{Eq. 2.2})$$

where I_0 represents the incident X-ray intensity, I_t denotes the transmitted X-ray intensity, t signifies the sample thickness, and E is the absorption coefficient that is dependent on the photon energy. XAS discerns the energy-dependent fine structure of the X-ray absorption coefficient. When the incident X-ray energy is lower than the binding energy of the electron in the element's orbital (e.g., s orbital), the electrons remain unexcited, leading to a flat region (depicted in **Figure 2.5b**).²¹⁶ However, certain less-favored transitions like $1s$ to $3d$ in transition metals manifest as a pre-edge peak. As the X-ray energies increase, exciting core electrons to the unoccupied state (**Figure 2.5c**), incident X-rays engage inner atoms, inducing partial energy absorption by core electrons, propelling them from a core level (e.g., E_1) to higher energy states (e.g., E_2 or E_3), and causing core hole formation.

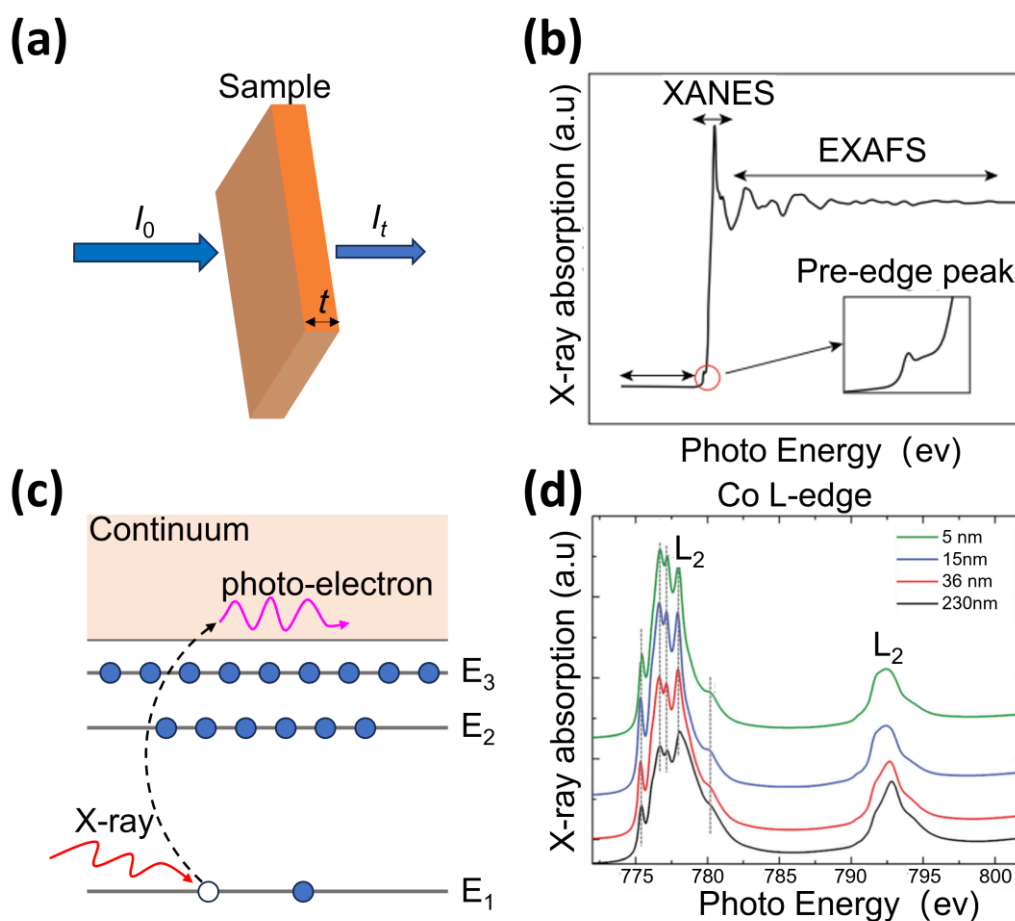


Figure 2.5 (a) Schematic of incident and transmitted X-ray beam. (b) Illustration of the X-ray absorption process and electron excited process. Scheme adapted from reference 216.²¹⁶ (c) Schematic of XAS including the pre-edge, XANES, and EXAFS regions (d) Example of Co $L_{2,3}$ -edge XAS of the 5, 15, 36 and 230 nm thick cobalt oxide films. Scheme adapted from reference 217.²¹⁷

Post-energy absorption, any excess energy from the X-ray transfers to the ejected photo-electron, resulting in a notable jump in the spectrum termed the X-ray absorption near edge structure (XANES) (**Figure 2.5b**). This region holds sensitivity to the oxidization state and electronic structure of the detected elements, as the core electron energy is influenced by the electron distribution within the valence state. With further escalation of X-ray energies, core electrons are propelled to continuum state (**Figure 2.5c**), generating outgoing and scattering wave interference with neighboring atoms. These interferences, whether constructive or destructive, give rise to oscillations in the extended X-ray absorption fine structure (EXAFS) region (Figure 2.5b), providing insights into the local atomic structure encompassing parameters like bond distance and coordination number. By further comparing the

experimental spectrum to reference spectra or theoretical calculations, researchers can deduce the specific chemical and structural properties of the target material.

The target materials investigated in this Thesis are *3d* transition metal nitrides or oxides, whose edge energies position, branching ratios and structures have been widely studied by analyzing their electronic structure (i.e., oxidation state) using L-edge XAS (**Figure 2.5d**). This method helps understand the phase transition of the target material, thereby facilitating an in-depth exploration of the fundamental mechanisms that underlie the observed magnetoionic phenomena.

2.3.4 ERD analysis

Elastic Recoil Detection (ERD) is a surface analysis technique used to characterize the composition and depth profile of materials, particularly for light elements. In this Thesis, an impinging ion beam of 9.6 MeV $^{79}\text{Br}^{5+}$ particles was used.²¹⁸ The end station for ERD experiments is illustrated in **Figure 2.6a**. The scattering process occurs within a vacuum chamber with a diameter of 100 mm, maintained at a pressure below 1.0×10^{-7} mbar. The samples are affixed to a sample holder and the positioning of the sample is facilitated by the motorized vertical translation stage, achieving a precise control over sample tilt with an accuracy of 0.02 degrees.

The fundamental working principle of ERD involves the interaction of high-energy ions with the sample, causing the ejection of atoms from the sample's surface. Subsequently, these ejected atoms are then detected and analyzed to provide information about the elemental composition and concentration, which vary as a function of depth. In the ERD process, as shown in **Figure 2.6b**, a beam of heavy ions with high energy, typically composed of Cl, He or Br ions, is directed onto the surface of the sample being analyzed. Consequently, elastic collisions occur between the incident ions and some of the target atoms, causing that part of incident ions backscatter on the sample and are recorded for their energy with an energy-sensitive detector I, and that target atoms are scattered out of the sample (i.e., the recoil light ions, such as H or N ions) and subsequently detected in forward direction by detector II. An absorber is set in forward direction used to prevent forward scattered heavy ions, which allows the direct and independent determination of the mass, charge or energy of recoil ions. Adjusting the energy of the incident ions enables precise control over the depth at which the recoiled atoms originate, where lower-energy ions yield shallower profiles and higher-energy ions

probe deeper material layers. In this way, quantitative depth profiles of multiple elements are obtained simultaneously.

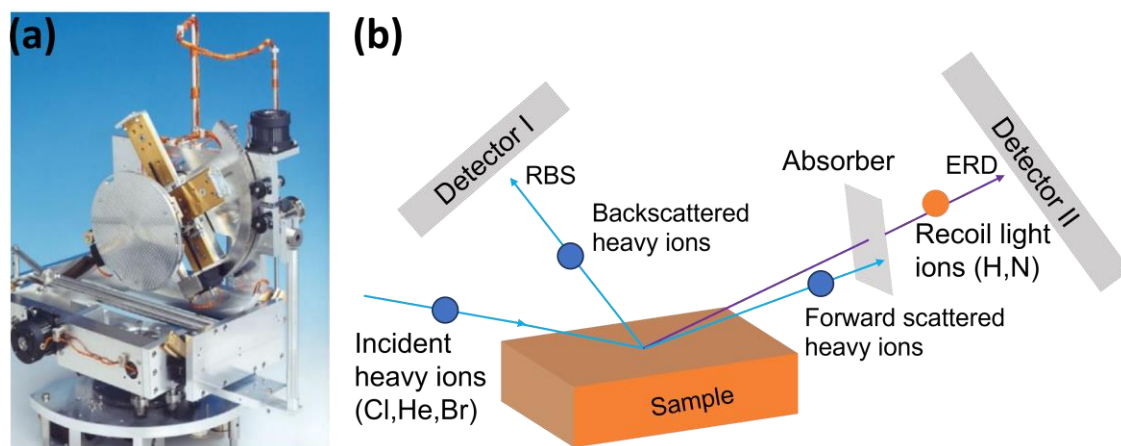


Figure 2.6 (a) Picture of the end station for elastic recoil detection (ERD) analysis. This schematic representation has been adapted from reference.²¹⁸ (b) Schematic of the fundamental principles of Rutherford backscattering (RBS) and Elastic Recoil Detection (ERD). In RBS, the energy of the backscattered ions is detected by detector I, while in ERD, the mass and/or charge and energy of recoil ions are detected by detector II.

In this Thesis, the utilization of ERD holds great significance due to its ability in analyzing light elements in a non-destructive manner, which are difficult to detect using other X-ray-based techniques like HRTEM and XAS. By using this technique, the depth distribution of N^{3-} at the interface between the film and the electrolyte can be obtained, providing direct evidence of some surface phenomenon, such as the ion accumulation effect, enabling the exploration of new mechanism underlying the observed magneto-ionic behaviors.

2.3.5 PAS measurements

This Thesis encompasses Positron annihilation spectroscopy (PAS) measurements conducted at the monoenergetic positron source (MePS) beamline, which is an end station of the radiation source ELBE (Electron Linac for beams with high Brilliance and low Emittance) at Helmholtz-Zentrum Dresden-Rossendorf (Germany),²¹⁹ with the picture of this system shown in **Figure 2.7a**. PAS stands as a versatile method for investigating atomic-scale phenomena and material properties. This advanced technique primarily capitalizes on the intricate interplay between positrons and electrons intrinsic to a given material, encompassing the phenomenon of positron annihilation. This facilitates the investigation of material defects with high sensitivity, even at low concentrations. As shown in **Figure 2.7b**, magnetically guided positrons from a ^{22}Na source of predetermined energies E (30 eV-36 keV) are implanted at depths of up to a few

micrometer into the sample.²²⁰ Then, the positrons reduce their energy within a few picoseconds due to thermalization and diffuse through the lattice (10-100 nm depending on trapping defects) until they are trapped in a defect and annihilate with an electron. This annihilation process will result in the complete conversion of their mass into energy, manifesting as electromagnetic radiation, typically in the form of gamma-ray photons (γ). Various defects, such as dislocations, grain boundaries, vacancies (single or clustered), and voids, cause distinct momentum distributions and concentrations of annihilating electrons, consequently engendering distinctive alterations in the emitted photon energy spectrum and positron lifetime. Thus, by detecting these emitted gamma-ray photons and subsequently subjecting them to analytical scrutiny, researchers can furnish insights into atomic-scale material defects, compositional attributes, and structural characteristics. Notably, the absence of positively charged atomic nuclei in defects creates a localized repulsive potential for positrons, thereby entrapping them at neutral or negatively charged defect sites. This distinct process allows for the scrutiny of minuscule defect concentrations and nanometer-scale defect dimensions. Taking advantage of all these features, PAS has emerged as a well-established tool in the study of metals, semiconductors, polymers, and porous materials.

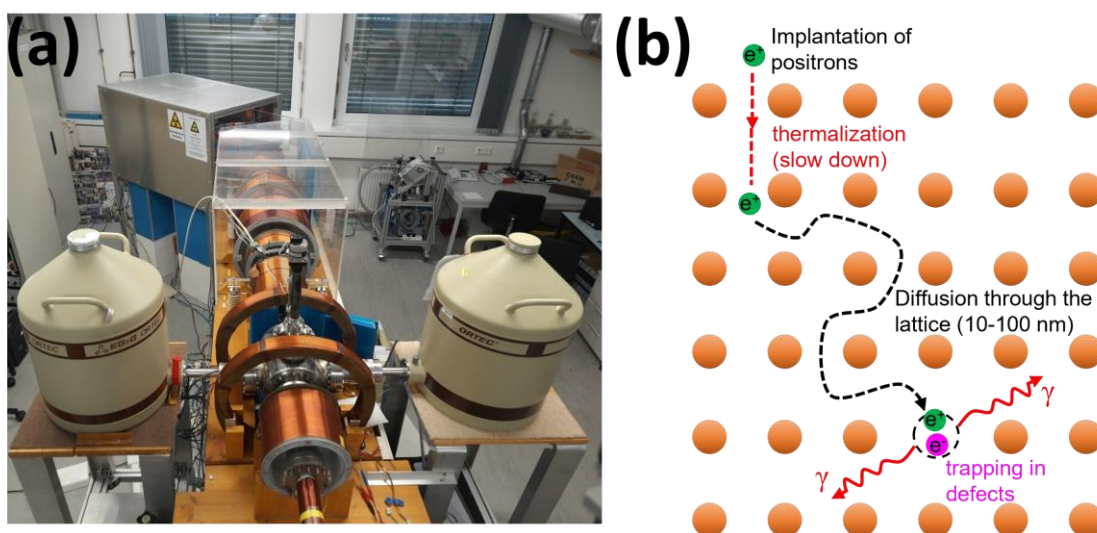


Figure 2.7 (a) Picture of an end station of the radiation source ELBE (Electron Linac for beams with high Brilliance and low Emittance) at Helmholtz-Zentrum Dresden-Rossendorf (HZDR, Germany). (b) Schematically illustrating the process from the implantation of positrons to their trapping in defects.

In this Thesis, to investigate the phenomenon of magneto-ionics concerning the evolution of defects, two PAS-based techniques are being employed:

- **Variable Energy Positron Annihilation Lifetime Spectroscopy (VEPALS)** quantify the time span from positron implantation within a material to the subsequent emission of annihilation radiation.²²¹ Positrons are trapped preferentially within atomic defects, characterized by localized reductions in electron density that in turn lead to prolonged positron lifetimes. Consequently, the VEPALS technique serves as a sensitive means to deduce sizes and concentrations of vacancy-type defects, such as nano-cavities. The positron annihilation lifetime is distinctly characteristic across elemental materials and defects. For instance, defect-free iron exhibits a positron lifetime of 108 ps, while a single-atom vacancy register 175 ps.
- **Doppler Broadening Variable Energy Positron Annihilation Spectroscopy (DB-VEPAS)** utilizes the energy-momentum conservation during positron annihilation.²¹⁹ The momentum of the electron-positron pair before annihilation is transferred to the annihilation quanta. In the case of two-photon annihilation the 511 keV photons experience a slight but notable energy shift in the laboratory frame, resembling the Doppler-effect. Since the primary contribution to the electron-positron momentum arises from the electron's orbital momentum, DB-VEPAS emerges as a discerning tool for examining the local chemical environment around defects. Both the introduction of impurity atoms to defect sites and the formation of material precipitates in alloys can be investigated using this technique.

Through the integration of these two methodologies, we can acquire precise quantitative insights into the dynamic changes in sizes and concentrations of different defects, as they occur during the process of voltage-induced migration of ions. In this way, the intricate mechanisms underpinning phenomena associated with magneto-ionics can be unraveled from the point of structural defects.

2.4 Transport measurements

To investigate the electrical properties of the materials under study, transport measurements were conducted using the 4-contact van der Pauw configuration within a controlled cooling system.²²² Consequently, a comprehensive range of resistivity values was recorded as a function of temperature. Prior to conducting resistivity measurements, the samples, designated for resistivity analysis, were deposited onto high-resistivity Si/SiO₂ substrates of uniform thickness (as depicted in Figure 2.1c). To facilitate electrical connections, four electrodes were patterned and evenly distributed at edges and these contacts are labeled A, B, C, and D, as shown in **Figure 2.8**. The measurement setup involves passing a small electrical current through two of the contacts (e.g., A and B) and measuring the voltage across the other two contacts (e.g., C and D). It is noteworthy that the selected levels of current and voltage were judiciously determined to ensure measurement precision, while mitigating potential thermal effects. The key principle underlying the van der Pauw method is the reciprocity theorem, which states that if the current is injected at contacts A and B, the voltage distribution at contacts C and D is independent of the positions of A and B but only depends on the sample's resistivity distribution. This is crucial because it allows for a wide range of configurations and simplifies the measurements. The resistivity determination involves the measurement of the voltage spanning contacts C and D, coupled with knowledge of the applied current. The utilization of the van der Pauw formula, entailing intricate manipulation of voltage and current values, enables the computation of the material's resistivity.

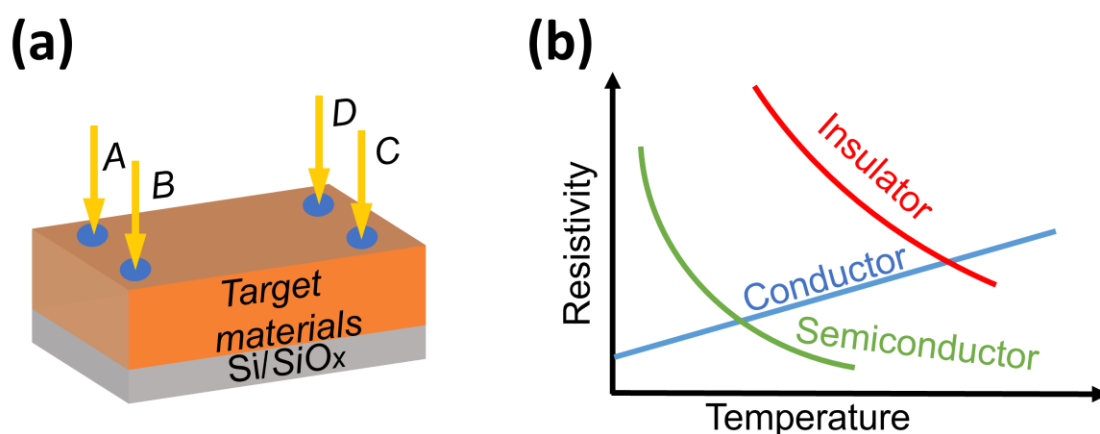


Figure 2.8 (a) Experimental setup for Van-der-Pauw measurement. (b) Schematic diagram of variation of conductivity of conductor, insulator and semiconductor with temperature.

Figure 2.8b presents a graph depicting the temperature-dependent resistivity of conductors, semiconductors, and insulators, shedding light on the distinct electronic properties of each material. For conductors, the loosely bound valence electrons facilitate easy movement under electric current. Yet, as temperature increases, heightened vibrations in metal ions cause more frequent electron collisions, thereby reducing their average velocity and increasing the material's resistivity. Conversely, semiconductors possess a narrower forbidden gap between their conduction and valence bands compared to pure conductors. A minor temperature elevation supplies enough energy for electrons to transition to the conduction band, enhancing the semiconductor's conductivity and lowering its resistivity. In the case of insulators, though they share some temperature-dependent resistivity characteristics with semiconductors, their broader energy gap and partially filled valence band make electron movement more challenging. As a result, insulators consistently maintain a higher resistivity than semiconductors.¹⁶⁵

For the purposes of probing temperature-dependent resistivities, in our case spanning from 30 to 300 K, the samples were encapsulated within a closed helium (He) refrigeration system. By systematically varying the temperature through this system, a graph depicting resistivity as a function of temperature can be generated. A comparative analysis of these electronic properties before and after magneto-ionic processing allows for the identification of inherent changes in atomic bonding, the density of local charge carriers, and structural defects, promoting a refined understanding of the observed magneto-ionic phenomena within the realm of electrical performance.

2.5 *Ab initio* calculations

Ab initio calculations provide foundational theoretical insights to interpret observed magneto-ionic behaviors. Central to magneto-ionics is the energy required to modify the bonding between magnetic metal and movable ions. This Thesis employs the projector-augmented wave (PAW) method, facilitated by the VASP package using the generalized gradient approximation, to estimate the energy barrier for ion diffusion.²²³ Prior research has validated this methodology, particularly in contrasting Co-O and Co-N formation energies across various crystal structures.²² As depicted in Figure 2.9, the minimum energy paths were charted as oxygen or nitrogen ions integrated into a Co slab, relative to a cobalt reference layer's displacement. The formation energies were then deduced by comparing the two lowest energy points. Consequently, the energies were calculated as 1.54 (1.85) and 1.14 (1.37) eV/atom for oxygen and nitrogen insertion into HCP (FCC) Co surfaces, respectively. This indicates that nitrogen's integration into cobalt requires less energy than oxygen, aligning with experimental findings where CoN exhibits superior magneto-ionic properties compared to Co_3O_4 . Such theoretical techniques deepen our understanding of magneto-ionic processes at the quantum scale.

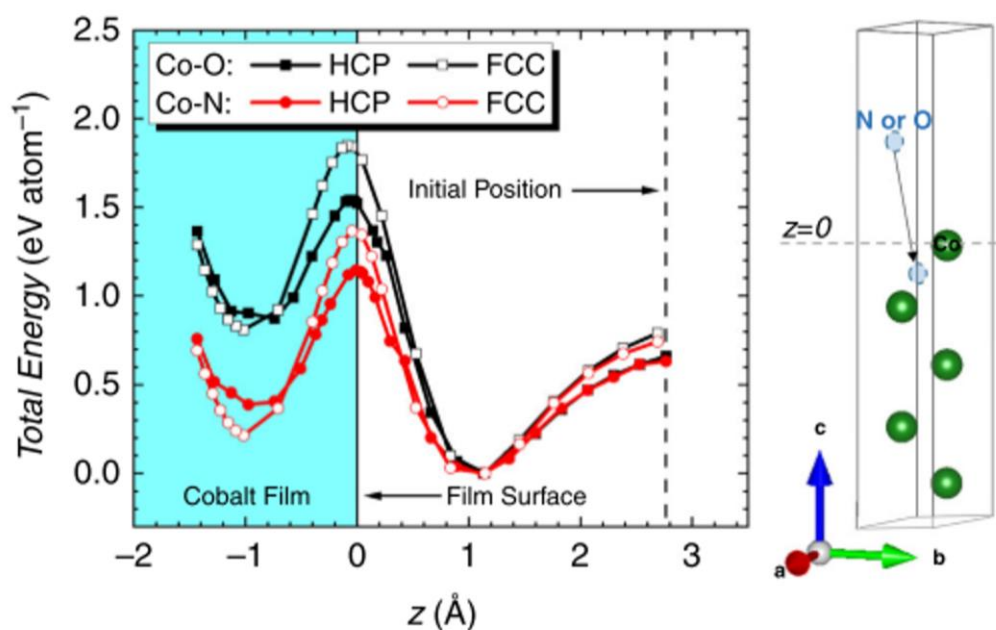


Figure 2.9. *Ab initio* calculations: Co-O vs. Co-N formation energy. Adapted from ref. 22.²²

In this Thesis, we adopt this specific method with the primary aim of determining the formation energies of Co-N and CoMn-N bonds. Through this comparison, the influence of Mn

substitution on magneto-ionic behaviors can be comprehensively understood from an atomic energy standpoint. To achieve this, we employed (4×2) supercells, featuring a thickness of four monolayers, for both Co (90%)-Mn (10%) and pure Co. This allowed us to represent and analyze Mn-doped Co in contrast to undoped Co. To calculate the energy barrier that a nitrogen atom must surpass to merge with the material's surface, we employed the nudged elastic band method (NEB)^{224,225} was used on the nitrogen pathway. Throughout the process, atomic coordinates were consistently adjusted until the exerted forces were minimized to $1 \text{ meV } \text{\AA}^{-1}$. We set a kinetic energy limit of 500 eV for the plane-wave basis, utilizing $25 \times 25 \times 1$ k-point meshes. This theoretical approach not only enhances our atomic-level understanding of magneto-ionic systems but also paves the way for more informed material design and optimization in future applications.

Bibliography

- (1) Grollier, J. et al. Neuromorphic spintronics. *Nat. Electron* **3**, 360-370 (2020).
- (2) Sangwan, V. K. & Hersam, M. C. Neuromorphic nanoelectronic materials. *Nat. Nanotechnol.* **15**, 517-528 (2020).
- (3) Strukov, D. ;, Indiveri, G. ;, Grollier, J. ; & Fusi, S. Building brain-inspired computing. *Nat. Commun.* **10**, 4838 (2019).
- (4) LeCun, Y., Bengio, Y. & Hinton, G. Deep learning. *Nature* **521**, 436-444 (2015).
- (5) Christensen, D. V. et al. Roadmap on neuromorphic computing and engineering. *Neural. Comput. Appl.* **2**, 022501 (2022).
- (6) Žutić, I., Fabian, J. & Sarma, S. das. Spintronics: Fundamentals and applications. *Rev. Mod. Phys.* **76**, 323 (2004).
- (7) Hirohata, A. et al. Review on spintronics: Principles and device applications. *J Magn. Mater.* **509**, 166711 (2020).
- (8) Song, C. et al. Spin-orbit torques: Materials, mechanisms, performances, and potential applications. *Prog. Mater. Sci.* **118**, 100761 (2021).
- (9) Ryu, J., Lee, S., Lee, K. J. & Park, B. G. Current-Induced Spin-Orbit Torques for Spintronic Applications. *Adv. Mater.* **32**, 1907148 (2020).
- (10) Song, C., Cui, B., Li, F., Zhou, X. & Pan, F. Recent progress in voltage control of magnetism: Materials, mechanisms, and performance. *Prog. Mater. Sci.* **87**, 33-82 (2017).
- (11) Bauer, U. et al. Magneto-ionic control of interfacial magnetism. *Nat. Mater.* **14**, 174-181 (2015).
- (12) Nichterwitz, M. et al. Advances in magneto-ionic materials and perspectives for their application. *APL Mater.* **9**, 030903 (2021).
- (13) Tan, A. J. et al. Magneto-ionic control of magnetism using a solid-state proton pump. *Nat. Mater.* **18**, 35-41 (2019).
- (14) Gilbert, D. A. et al. Structural and magnetic depth profiles of magneto-ionic heterostructures beyond the interface limit. *Nat. Commun.* **7**, 12264 (2016).
- (15) Quintana, A. et al. Voltage-controlled ON-OFF ferromagnetism at room temperature in a single metal oxide film. *ACS Nano* **12**, 10291-10300 (2018).
- (16) Chen, G. et al. Reversible writing/deleting of magnetic skyrmions through hydrogen adsorption/desorption. *Nat. Commun.* **13**, 1350 (2022).

- (17) Ye, X. et al. Giant voltage-induced modification of magnetism in micron-scale ferromagnetic metals by hydrogen charging. *Nat. Commun.* **11**, 4849 (2020).
- (18) Zhang, Q. et al. Lithium-ion battery cycling for magnetism control. *Nano Lett* **16**, 583-587 (2016).
- (19) Ameziane, M. et al. Lithium-ion battery technology for voltage control of perpendicular magnetization. *Adv. Funct. Mater.* **29**, 2113118 (2022).
- (20) Wissel, K. et al. Developing intercalation based anode materials for fluoride-ion batteries: topochemical reduction of $\text{Sr}_2\text{TiO}_3\text{F}_2$ via a hydride based defluorination process. *J. Mater. Chem. A* **6**, 22013-22026 (2018).
- (21) Jensen, C. J. et al. Nitrogen-Based Magneto-ionic Manipulation of Exchange Bias in CoFe/MnN Heterostructures. *ACS Nano* **17**, 6745-6753 (2023).
- (22) de Rojas, J. et al. Voltage-driven motion of nitrogen ions: a new paradigm for magneto-ionics. *Nat. Commun.* **11**, 5871 (2020).
- (23) Rojas, J. de et al. Voltage control of magnetism with magneto-ionic approaches: Beyond voltage-driven oxygen ion migration. *Appl. Phys. Lett.* **120**, 070501 (2022).
- (24) Mishra, R., Kumar, D. & Yang, H. Oxygen-Migration-Based Spintronic Device Emulating a Biological Synapse. *Phys. Rev. Appl.* **11**, 054065 (2019).
- (25) Moore, G. Cramming more components onto integrated circuits. *Electronics*, **38**, 8 (1965).
- (26) Waldrop, M. M. The chips are down for Moore's law. *Nature* **530**, 144-147 (2016).
- (27) Shalf, J. The future of computing beyond Moore's Law. *Phil. Trans. R. Soc. A.* **378**, 20190061 (2020).
- (28) Manipatruni, S., Nikonov, D. E. & Young, I. A. Beyond CMOS computing with spin and polarization. *Nature Phys.* **14**, 338-343 (2018).
- (29) Barla, P., Joshi, V. K. & Bhat, S. Spintronic devices: a promising alternative to CMOS devices. *J. Comput. Electron.* **20**, 805-837 (2021).
- (30) Wolf, S. A. et al. Spintronics: A spin-based electronics vision for the future. *Science* **294**, 1488-1495 (2001).
- (31) Bhatti, S. et al. Spintronics based random access memory: a review. *Mater. Today* **20**, 530-548 (2017).
- (32) Baibich, M. N. et al. Giant magnetoresistance of (001) Fe/ (001) Cr magnetic superlattices. *Phys. Rev. Lett.* **61**, 2472-2475 (1988).

- (33) Parkin, S. & Yang, S. H. Memory on the racetrack. *Nat. Nanotechnol.* **10**, 195-198 (2015).
- (34) Tang, W., Liu, H., Li, Z., Pan, A. & Zeng, Y. J. Spin-Orbit Torque in Van der Waals-Layered Materials and Heterostructures. *Adv. Sci.* **8**, 2100847 (2021).
- (35) Kawahara, T., Ito, K., Takemura, R. & Ohno, H. Spin-transfer torque RAM technology: Review and prospect. *Microelectron. Reliab.* **52**, 613-627 (2012).
- (36) Yoda, H. et al. Voltage-control spintronics memory (VoCSM) having potentials of ultra-low energy-consumption and high-density. In *2016 IEEE Int. Electron Devices Meeting (IEDM)* 27.6.1-27.6.4 (IEEE, 2016).
- (37) Quintana, A. et al. Voltage-Induced Coercivity Reduction in Nanoporous Alloy Films: A Boost toward Energy-Efficient Magnetic Actuation. *Adv. Funct. Mater.* **27**, 1701904 (2017).
- (38) Ramesh, R., Manipatruni, S. & Young, I. Electric-field control of magnetism. *MRS Bull.* **44**, 288-294 (2019).
- (39) Hellman, F. et al. Interface-induced phenomena in magnetism. *Rev. Mod. Phys.* **89**, 025006 (2017).
- (40) Jiles, D. C. Recent advances and future directions in magnetic materials. *Acta Mater.* **51**, 5907-5939 (2003).
- (41) Spaldin, N. *Magnetic materials: fundamentals and applications*. Cambridge university press, 2010.
- (42) Cullity, B. D., and Chad Graham, C. D. *Introduction to magnetic materials*. John Wiley & Sons, 2011.
- (43) Li, Y., Edmonds, W. K. & Wang, K. Spin-Orbit Torque (SOT) Materials and Devices. *Spintronics: Materials, Devices and Applications*, 113-138 (2022).
- (44) Xu, H. et al. Strain-mediated converse magnetoelectric coupling in $\text{La}_{0.7}\text{Sr}_{0.3}\text{MnO}_3/\text{Pb}(\text{Mg}_{1/3}\text{Nb}_{2/3})\text{O}_3\text{-PbTiO}_3$ multiferroic heterostructures. *Cryst. Growth Des.* **18**, 5934-5939 (2018).
- (45) Feng, C. et al. Significant Strain-induced orbital reconstruction and strong interfacial magnetism in $\text{TiNi}(\text{Nb})/\text{Ferromagnet}/\text{Oxide}$ heterostructures via oxygen manipulation. *Adv. Funct. Mater.* **28**, 1803335 (2018).
- (46) Peng, R. C. et al. Fast 180° magnetization switching in a strain-mediated multiferroic heterostructure driven by a voltage. *Sci. Rep.* **6**, 27561 (2016).

- (47) Matsubara, M. et al. Ultrafast optical tuning of ferromagnetism via the carrier density. *Nat. Commun.* **6**, 6724 (2015).
- (48) Afanasiev, D. et al. Ultrafast control of magnetic interactions via light-driven phonons. *Nat. Mater.* **20**, 607-611 (2021).
- (49) Sato, O., Tao, J. & Zhang, Y. Z. Control of Magnetic Properties through External Stimuli. *Angew. Chem. Int. Ed. Engl.* **46**, 2152-2187 (2007).
- (50) Luo, Z. et al. Current-driven magnetic domain-wall logic. *Nature* **579**, 214–218 (2020).
- (51) Nozaki, T. et al. Recent progress in the voltage-controlled magnetic anisotropy effect and the challenges faced in developing voltage-torque MRAM. *Micromachines* **10**, 327 (2019).
- (52) Röntgen, W. C. Ueber die durch Bewegung eines im homogenen electrischen Felde befindlichen Dielectricums hervorgerufene electrodynamische Kraft. *Ann. Phys.* **271**, 264-270 (1888).
- (53) Curie, P. Sur la symétrie dans les phénomènes physiques, symétrie d'un champ électrique et d'un champ magnétique. *J. Phys. Theor. Appl.* **3**, 393-415 (1894).
- (54) Debye, P. Bemerkung zu einigen neuen Versuchen über einen magneto-elektrischen Richteffekt. *Z. Med. Phys.* **36**, 300-301 (1926).
- (55) Landau, L. D., & Lifshits, E. M. Electrodynamics of continuous media. *Oxford: Pergamon press*, 1946.
- (56) Dzyaloshinskii, I. E. On the magneto-electrical effects in antiferromagnets. *Sov. phys. JETP* **10**, 628-629 (1960).
- (57) Folen, V. J., Rado, G. T. & Stalder, E. W. Anisotropy of the magnetoelectric effect in Cr₂O₃. *Phys. Rev. Lett.* **6**, 607-608 (1961).
- (58) Astrov, D. N. The magnetoelectric effect in antiferromagnetics. *Sov. Phys. JETP* **11**, 984-985 (1960).
- (59) Astrov, D. N. Magnetoelectric effect in chromium oxide. *Sov. Phys. JETP* **11**, 729-733 (1961).
- (60) Bibes, M. & Barthélémy, A. Towards a magnetoelectric memory. *Nat. Mater.* **7**, 425-426 (2008).
- (61) Ramesh, R. & Spaldin, N. Multiferroics: progress and prospects in thin films. *Nat. Mater.* **6**, 21-29 (2007).

- (62) Spaldin, N.A. & Ramesh, R. Advances in magnetoelectric multiferroics. *Nat. Mater.* **18**, 203-212 (2019).
- (63) Van Den Boomgaard, J., Van Run, A. M. J. G. & Van Suchtelen, J. Magnetoelectricity in piezoelectric-magnetostrictive composites. *Ferroelectrics*, **10**, 295-298 (1976).
- (64) Sahoo, S. et al. Ferroelectric control of magnetism in heterostructures via interface strain coupling. *Phys. Rev. B* **76**, 092108 (2007).
- (65) Shirahata, Y. et al. Switching of the symmetry of magnetic anisotropy in Fe/BaTiO₃ heterostructures. *Appl. Phys. Lett.* **99**, 022501 (2011).
- (66) Zhang, S. et al. Electric-field control of nonvolatile magnetization in Co₄₀Fe₄₀B₂₀/Pb(Mg_{1/3}Nb_{2/3})_{0.7}Ti_{0.3}O₃ structure at room temperature. *Phys. Rev. Lett.* **108**, 137203 (2012).
- (67) Li, P. et al. Electric Field Manipulation of Magnetization Rotation and Tunneling Magnetoresistance of Magnetic Tunnel Junctions at Room Temperature. *Adv. Mater.* **26**, 4320-4325 (2014).
- (68) Lou, J. et al. Giant electric field tuning of magnetism in novel multiferroic FeGaB/Lead Zinc Niobate-Lead Titanate (PZN-PT) heterostructures. *Adv. Mater.* **21**, 4711-4715 (2009).
- (69) Yang, S. W. et al. Nonvolatile 180 magnetization reversal by an electric field in multiferroic heterostructures. *Adv. Mater.* **26**, 7091-7095 (2014).
- (70) Lee, J. W., Shin, S. C. & Kim, S. K. Spin engineering of CoPd alloy films via the inverse piezoelectric effect. *Appl. Phys. Lett.* **82**, 2458 (2003).
- (71) Eerenstein, W., Wiora, M., Prieto, J., Scott, J. F. & Mathur, N. D. Giant sharp and persistent converse magnetoelectric effects in multiferroic epitaxial heterostructures. *Nat. Mater.* **6**, 348-351 (2007).
- (72) Liu, M. et al. Giant Electric Field Tuning of Magnetic Properties in Multiferroic Ferrite/Ferroelectric Heterostructures. *Adv. Funct. Mater.* **19**, 1826-1831 (2009).
- (73) Taniyama, T., Akasaka, K., Fu, D., & Itoh, M. Artificially controlled magnetic domain structures in ferromagnetic dots/ferroelectric heterostructures. *J. Appl. Phys.* **105**, 07D901 (2009).

- (74) Taniyama, T. et al. Electrical voltage manipulation of ferromagnetic microdomain structures in a ferromagnetic/ferroelectric hybrid structure. *J. Appl. Phys.* **101**, 09F512 (2007).
- (75) Wang, J. et al. Switchable voltage control of the magnetic coercive field via magnetoelectric effect. *J. Appl. Phys.* **110**, 043919 (2011).
- (76) Sun, Y. et al. Electric-Field Modulation of Interface Magnetic Anisotropy and Spin Reorientation Transition in (Co/Pt)₃/PMN-PT Heterostructure. *ACS Appl. Mater. Interfaces* **9**, 10855-10864 (2017).
- (77) Gusev, N. S., Sadovnikov, A. V., Nikitov, S. A., Sapozhnikov, M. V. & Udalov, O. G. Manipulation of the Dzyaloshinskii-Moriya Interaction in Co/Pt Multilayers with Strain. *Phys. Rev. Lett.* **124**, 157202 (2020).
- (78) Zhu, M. et al. Theoretical routes for current-free magnetization switching induced by joint effects of strain and Dzyaloshinskii-Moriya interaction. *Appl Phys. Lett.* **121**, 032402 (2022).
- (79) Ba, Y. et al. Electric-field control of skyrmions in multiferroic heterostructure via magnetoelectric coupling. *Nat. Commun.* **12**, 322 (2021).
- (80) Hou, Z. et al. Controlled Switching of the Number of Skyrmions in a Magnetic Nanodot by Electric Fields. *Adv. Mater.* **34**, 2107908 (2022).
- (81) Lu, Q. et al. Giant tunable spin Hall angle in sputtered Bi₂Se₃ controlled by an electric field. *Nat. Commun.* **13**, 1650 (2022).
- (82) Liu, Z. Q. et al. Electrical switching of the topological anomalous Hall effect in a non-collinear antiferromagnet above room temperature. *Nat. Electron.* **1**, 172-177 (2018).
- (83) Qi, Y. et al. Recent Progress in Strain Engineering on Van der Waals 2D Materials: Tunable Electrical, Electrochemical, Magnetic, and Optical Properties. *Adv. Mater.* **35**, 2205714 (2023).
- (84) Choi, E. M., Sim, K. I., Burch, K. S. & Lee, Y. H. Emergent Multifunctional Magnetic Proximity in van der Waals Layered Heterostructures. *Adv. Sci.* **9**, 2200186 (2022).
- (85) Gupta, R., Shah, J., Chaudhary, S., Singh, S. & Kotnala, R. K. Magnetoelectric coupling-induced anisotropy in multiferroic nanocomposite (1-x)BiFeO₃-xBaTiO₃. *J. Nanopart. Res.* **15**, 2004 (2013).

- (86) Venkataiah, G., Shirahata, Y., Itoh, M. & Taniyama, T. Manipulation of magnetic coercivity of Fe film in Fe/BaTiO₃ heterostructure by electric field. *Appl. Phys. Lett.* **99**, 102506 (2011).
- (87) Fang, L. *et al.* Experimental and theoretical evidence of enhanced ferromagnetism in sonochemical synthesized BiFeO₃ nanoparticles. *Appl. Phys. Lett.* **97**, 242501 (2010).
- (88) Geprägs, S., Brandlmaier, A., Opel, M., Gross, R. & Goennenwein, S. T. B. Electric field controlled manipulation of the magnetization in Ni/BaTiO₃ hybrid structures. *Appl. Phys. Lett.* **96**, 142509 (2010).
- (89) Liu, M., Lou, J., Li, S. & Sun, N. X. E-field control of exchange bias and deterministic magnetization switching in AFM/FM/FE multiferroic heterostructures. *Adv. Funct. Mater.* **21**, 2593-2598 (2011).
- (90) Gao, Y., Hu, J. M., Wu, L. & Nan, C. W. Dynamic in situ visualization of voltage-driven magnetic domain evolution in multiferroic heterostructures. *J. Phys.: Condens. Matter* **27**, 504005 (2015).
- (91) Wu, H. *et al.* Chain formation mechanism of magnetic particles in magnetorheological elastomers during pre-structure. *J. Magn. Magn. Mater.* **527**, 167693 (2021).
- (92) Regan, T. *et al.* Chemical effects at metal/oxide interfaces studied by x-ray-absorption spectroscopy. *Phys. Rev. B* **64**, 214422 (2001).
- (93) Bisht, M. *et al.* Electric Polarity-Dependent Modification of the Fe/BaTiO₃ Interface. *Adv Mater Interfaces* **3**, 1500433 (2016).
- (94) Eerenstein, W. *et al.* Giant sharp and persistent converse magnetoelectric effects in multiferroic epitaxial heterostructures. *Nat. Mater.* **6**, 348-351 (2007).
- (95) Ohno, H. *et al.* Electric-field control of ferromagnetism. *Nature* **408**, 944-946 (2000).
- (96) Chiba, D., Yamanouchi, H., Hatsukura, F. & Ohno, H. Electrical manipulation of magnetization reversal in a ferromagnetic semiconductor. *Science* **301**, 943-945 (2003).
- (97) Liu, X. *et al.* Perpendicular magnetization reversal, magnetic anisotropy, multistep spin switching, and domain nucleation and expansion in Ga_{1-x}Mn_xAs films. *J. Appl. Phys.* **98**, 063904 (2005).

- (98) Tu, N. T., Hai, P. N., Anh, L. D. & Tanaka, M. Electrical control of ferromagnetism in the n-type ferromagnetic semiconductor (In, Fe) Sb with high Curie temperature. *Appl. Phys. Lett.* **112**, 122409 (2018).
- (99) Xiu, F. *et al.* Electric-field-controlled ferromagnetism in high-Curie-temperature Mn_{0.05}Ge_{0.95} quantum dots. *Nat. Mater.* **9**, 337-344 (2010).
- (100) Chiba, D. *et al.* Anomalous Hall effect in field-effect structures of (Ga, Mn) As. *Phys. Rev. Lett.* **104**, 106601 (2009).
- (101) Dennard, R. H. *et al.* Design of ion-implanted MOSFET's with very small physical dimensions. *IEEE J. SOLID-STATE CIRC.* **9**, 256-268 (1974).
- (102) Mehonic, A. *et al.* Silicon Oxide (SiO_x): A promising material for resistance switching? *Adv. Mater.* **30**, 1801187 (2018).
- (103) Ahn, C. H. *et al.* Electrostatic modification of novel materials. *Rev. Mod. Phys.* **78**, 1185-1212 (2006).
- (104) Weisheit, M. *et al.* Electric field-induced modification of magnetism in thin-film ferromagnets. *Science* **315**, 349-351 (2007).
- (105) Guan, Y., Han, H., Li, F., Li, G. & Parkin, S. S. P. Ionic gating for tuning electronic and magnetic properties. *Annu. Rev. Mater. Res.* **53**, 25-51(2023).
- (106) Navarro-Senent, C., Quintana, A., Menéndez, E., Pellicer, E. & Sort, J. Electrolyte-gated magnetoelectric actuation: Phenomenology, materials, mechanisms, and prospective applications. *APL Mater.* **7**, 030701(2019).
- (107) Leighton, C., Birol, T. & Walter, J. What controls electrostatic vs electrochemical response in electrolyte-gated materials? A perspective on critical materials factors. *APL Mater.* **10**, 040901 (2022).
- (108) Leighton, C. Electrolyte-based ionic control of functional oxides. *Nat. Mater.* **18**, 13-18 (2019).
- (109) Kudoh, Y. & Nishino, A. Recent development in electrolytic capacitors and electric double layer capacitors. *Electrochemistry* **69**, 397-406 (2001).
- (110) Shin, S. J. *et al.* On the importance of the electric double layer structure in aqueous electrocatalysis. *Nat. Commun.* **13**, 174 (2022).
- (111) Zhang, H. *et al.* Electric-field control of surface magnetic anisotropy: a density functional approach. *New J. Phys.* **11**, 043007 (2009).

- (112) Duan, C. -G. et al. Surface magnetoelectric effect in ferromagnetic metal films. *Phys. Rev. Lett.* **101**, 137201 (2008).
- (113) Nakamura, K. *et al.* Giant modification of the magnetocrystalline anisotropy in transition-metal monolayers by an external electric field. *Phys. Rev. Lett.* **102**, 187201 (2009).
- (114) Tsujikawa, M. & Oda, T. Finite Electric Field Effects in the Large Perpendicular Magnetic Anisotropy Surface Pt/Fe/Pt (001). *Phys. Rev. Lett.* **102**, 247203 (2009).
- (115) Bauer, U., Przybylski, M., Kirschner, J., letters, & G. B. -N. Magnetoelectric charge trap memory. *Nano Lett.* **12**, 1437-1442 (2012).
- (116) Liu, Y. T. *et al.* Ionic-liquid gating of perpendicularly magnetised CoFeB/MgO thin films. *J. Appl. Phys.* **120**, 023901 (2016).
- (117) Shimamura, K. *et al.* Electrical control of Curie temperature in cobalt using an ionic liquid film. *Appl. Phys. Lett.* **100**, 122402 (2012).
- (118) Maruyama, T. *et al.* Large voltage-induced magnetic anisotropy change in a few atomic layers of iron. *Nat. Nanotech.* **4**, 158-161 (2009).
- (119) Nakatani, Y., Hayashi, M., Kanai, S., Fukami, S. & Ohno, H. Electric field control of Skyrmions in magnetic nanodisks. *Appl. Phys. Lett.* **108**, 152403 (2016).
- (120) Fook, H., Gan, W., reports, W. L. -S. & 2016, undefined. Gateable skyrmion transport via field-induced potential barrier modulation. *Sci. Rep.* **6**, 21099 (2016).
- (121) Kang, W. *et al.* Voltage controlled magnetic skyrmion motion for racetrack memory. *Sci. Rep.* **6**, 23164 (2016).
- (122) Hsu, P. *et al.* Electric-field-driven switching of individual magnetic skyrmions. *Nat. Nanotech.* **12**, 123-126 (2017).
- (123) Schott, M. *et al.* The skyrmion switch: turning magnetic skyrmion bubbles on and off with an electric Field. *Nano Lett.* **17**, 3006-3012 (2017).
- (124) Quintana, A. *et al.* Voltage-induced coercivity reduction in nanoporous alloy films: a boost toward energy-efficient magnetic actuation. *Adv. Funct. Mater.* **27**, 1701904 (2017).
- (125) Nogués, J. & Schuller, I. K. Exchange bias. *J. Magn. Magn. Mater.* **192**, 203-232 (1999).
- (126) Stamps, R. L. Mechanisms for exchange bias. *J. Phys. D: Appl. Phys.* **33**, R247 (2000).

- (127) Kiwi, M. Exchange bias theory. *J. Magn. Magn. Mater.* **234**, 584-595 (2001).
- (128) Borisov, P. *et al.* Magnetoelectric switching of exchange bias. *Phys. Rev. Lett.* **94**, 117203 (2005).
- (129) Binek, C. *et al.* Electrically controlled exchange bias for spintronic applications. *J. Appl. Phys.* **97**, 10C514 (2005).
- (130) K. B. *et al.* Robust isothermal electric control of exchange bias at room temperature. *Nat. Mater.* **9**, 579-585 (2010).
- (131) Laukhin, V. *et al.* Electric-field control of exchange bias in multiferroic epitaxial heterostructures. *Phys. Rev. Lett.* **97**, 227201 (2006).
- (132) Skumryev, V. *et al.* Magnetization reversal by electric-field decoupling of magnetic and ferroelectric domain walls in multiferroic-based heterostructures. *Phys. Rev. Lett.* **106**, 057206 (2011).
- (133) Wu, S. M. *et al.* Full electric control of exchange bias. *Phys. Rev. Lett.* **110**, 067202 (2013).
- (134) Chu, Y. H. *et al.* Electric-field control of local ferromagnetism using a magnetoelectric multiferroic. *Nat. Mater.* **7**, 478-482 (2008).
- (135) Wu, S. *et al.* Reversible electric control of exchange bias in a multiferroic field-effect device. *Nat. Mater.* **9**, 756-761 (2010).
- (136) Burns, S. R. *et al.* Expansion of the spin cycloid in multiferroic BiFeO₃ thin films. *npj Quantum Mater.* **4**, 18 (2019).
- (137) Burns, S. R., Paull, O., Juraszek, J., Nagarajan, V. & Sando, D. The experimentalist's guide to the cycloid, or noncollinear antiferromagnetism in epitaxial BiFeO₃. *Adv. Mater.* **32**, 2003711 (2020).
- (138) Liao, Y. C. *et al.* Understanding the switching mechanisms of the antiferromagnet/ferromagnet heterojunction. *Nano Lett* **20**, 7919-7926 (2020).
- (139) Yi, D. *et al.* Tailoring magnetoelectric coupling in BiFeO₃/La_{0.7}Sr_{0.3}MnO₃ heterostructure through the interface engineering. *Adv. Mater.* **31**, 1806335 (2019).
- (140) Li, P., Zhou, X.-S., Guo, Z.-X. Intriguing magnetoelectric effect in two-dimensional ferromagnetic/perovskite oxide ferroelectric heterostructure. *npj Comput Mater* **8**, 20 (2022).
- (141) Manipatruni, S. *et al.* Scalable energy-efficient magnetoelectric spin-orbit logic. *Nature* **565**, 35-42 (2019).

- (142) Wang, Y. *et al.* Room-temperature perpendicular exchange coupling and tunneling anisotropic magnetoresistance in an antiferromagnet-based tunnel junction. *Phys. Rev. Lett.* **109**, 137201(2012).
- (143) Wang, Y. *et al.* Electrical control of the exchange spring in antiferromagnetic metals. *Adv. Mater.* **27**, 3196-3201 (2015).
- (144) Zhang, P. *et al.* Electrical control of antiferromagnetic metal up to 15 nm. *SCI. CHINA. PHYS. MECH.* **59**, 687511 (2016).
- (145) Cui, B. *et al.* Magnetoelectric coupling induced by interfacial orbital reconstruction. *Adv. Mater.* **27**, 6651-6656 (2015).
- (146) Tokura, Y. & Nagaosa, N. Orbital physics in transition-metal oxides. *Science* **288**, 462-468 (2000).
- (147) Wang, S. *et al.* Nitrogen tuned charge redistribution and orbital reconfiguration in Fe/MgO interface for significant interfacial magnetism tunability. *Adv. Funct. Mater.* **29**, 1806677 (2019).
- (148) Duan, C. G., Jaswal, S. S. & Tsymbal, E. Y. Predicted magnetoelectric effect in Fe/BaTiO₃ multilayers: Ferroelectric control of magnetism. *Phys. Rev. Lett.* **97**, 047201 (2006).
- (149) Serin, V. *et al.* TEM and EELS measurements of interface roughness in epitaxial Fe/MgO/Fe magnetic tunnel junctions. *Phys. Rev. B* **79**, 144413 (2009).
- (150) Pan, Y., Jin-song, Z., Jai-Yeoul, L. & Hee, Y.L. Thin film processing and multiferroic properties of Fe-BaTiO₃ hybrid composite. *T. NONFERR. METAL. SOC.* **21**, 92-95 (2011).
- (151) Dai, J., Zhang, H., & Song Y.-M. Interfacial electronic structure and magnetoelectric effect in M/BaTiO₃ (M= Ni, Fe) superlattices. *J. Magn. Magn. Mater.* **324**, 3937-3943 (2012).
- (152) Niranjana, M. K., Veleev, J. P., Duan, C.-G., Jaswal, S. S. & Tsymbal, E. Y. Magnetoelectric effect at the Fe₃O₄/BaTiO₃(001) interface: A first-principles study. *Phys. Rev. B* **78**, 104405 (2008).
- (153) Chen, L. Y., Chen, C. L., Jin, K. X. & Du X. J. Potential enhancement in magnetoelectric effect at Mn-rich Co₂MnSi/BaTiO₃ (001) interface. *EPL* **99**, 57008 (2012).

- (154) Leistner, K. Electrochemical approaches to room temperature magnetoelectric materials. *Curr. Opin. Electrochem.* **25**, 100636 (2021).
- (155) Duschek, K., Uhlemann, M., Schlörb, Nielsch K. & Leistner, K. Electrochemical and in situ magnetic study of iron/iron oxide films oxidized and reduced in KOH solution for magneto-ionic switching. *Electrochem commun.* **72**, 153-156 (2016).
- (156) Duschek, K., Petr, A., Zehner, J., Nielsch, K. & Leistner, K. All-electrochemical voltage-control of magnetization in metal oxide/metal nanoislands. *J. Mater. Chem. C* **6**, 8411-8417 (2018).
- (157) de Rojas, J. *et al.* Boosting Room-Temperature Magneto-Ionics in a Non-Magnetic Oxide Semiconductor. *Adv. Funct. Mater.* **30**, 2003704 (2020).
- (158) Zhou, X. *et al.* Role of oxygen ion migration in the electrical control of magnetism in Pt/Co/Ni/HfO₂ films. *J. Phys. Chem. C* **120**, 1633-1639 (2016).
- (159) Schott, M. *et al.* The skyrmion switch: turning magnetic skyrmion bubbles on and off with an electric field. *Nano Lett* **17**, 3006-3012 (2017).
- (160) Lee, K. Y. *et al.* Fast magneto-ionic switching of interface anisotropy using yttria-stabilized zirconia gate oxide. *Nano Lett* **20**, 3435-3441 (2020).
- (161) Dasgupta, S. *et al.* Intercalation-driven reversible control of magnetism in bulk ferromagnets. *Adv. Mater.* **26**, 4639-4644 (2014).
- (162) Rongeat, C., Reddy, M. A., Raiker, W. & Fichtner, M. Solid electrolytes for fluoride ion batteries: ionic conductivity in polycrystalline tysonite-type fluorides. *ACS Appl. Mater. Interfaces* **6**, 2103-2110 (2014).
- (163) Vasala, S. *et al.* Reversible tuning of magnetization in a ferromagnetic ruddlesdenpopper-Type manganite by electrochemical fluoride-ion Intercalation. *Adv. Electron. Mater.* **6**, 1900974 (2020).
- (164) De Rojas, J. *et al.* Magneto-ionics in single-layer transition metal nitrides. *ACS Appl. Mater. Interfaces* **13**, 30826-30834 (2021).
- (165) De Rojas, J. *et al.* Critical role of electrical resistivity in magnetoionics. *Phys. Rev. Appl.* **16**, 034042 (2021).
- (166) Bi, C. *et al.* Reversible control of Co magnetism by voltage-induced oxidation. *Phys. Rev. Lett.* **113**, 267202 (2014).
- (167) Yan, Y. N. *et al.* Electrical control of Co/Ni magnetism adjacent to gate oxides with low oxygen ion mobility. *Appl. Phys. Lett.* **107**, 122407 (2015).

- (168) Duschek, K., Pohl, D., Fähler, S., Nielsch, K. & Leistner, K. Research Update: Magnetoionic control of magnetization and anisotropy in layered oxide/metal heterostructures. *APL Mater.* **4**, 032301 (2016).
- (169) Zehner, J. *et al.* Voltage-Controlled Deblocking of Magnetization Reversal in Thin Films by Tunable Domain Wall Interactions and Pinning Sites. *Adv. Electron. Mater.* **6**, 2000406 (2000).
- (170) Gilbert, D. A. *et al.* Controllable positive exchange bias via redox-driven oxygen migration. *Nat. Commun.* **7**, 11050 (2016).
- (171) Jensen, C. J. *et al.* Ion irradiation and implantation modifications of magneto-ionically induced exchange bias in Gd/NiCoO. *J. Magn. Magn. Mater.* **540**, 168479 (2021).
- (172) Herrera Diez, L. *et al.* Nonvolatile ionic modification of the Dzyaloshinskii-Moriya Interaction. *Phys. Rev. Appl.* **12**, 034005 (2019).
- (173) Mühlbauer, S. *et al.* Skyrmion lattice in a chiral magnet. *Science* **323**, 915-919 (2009).
- (174) Luo, Z. *et al.* Chirally coupled nanomagnets. *Science* **363**, 1435-1439 (2019).
- (175) Bode, M. *et al.* Chiral magnetic order at surfaces driven by inversion asymmetry. *Nature* **447**, 190-193 (2007).
- (176) Zehner, J. *et al.* Nonvolatile electric control of exchange bias by a redox transformation of the ferromagnetic Layer. *Adv. Electron. Mater.* **5**, 1900296 (2019).
- (177) Li, H. B. *et al.* Electric-field control of ferromagnetism through oxygen ion gating. *Nat. Commun.* **8**, 2156 (2017).
- (178) Martins, S. *et al.* Enhancing magneto-ionic effects in cobalt oxide films by electrolyte engineering. *Nanoscale Horiz.* **8**, 118-126 (2023).
- (179) Navarro-Senent, C. *et al.* Large magnetoelectric effects in electrodeposited nanoporous microdisks driven by effective surface charging and magneto-ionics. *ACS Appl. Mater. Interfaces* **10**, 44897-44905 (2018).
- (180) Molinari, A. *et al.* Voltage-control of magnetism in all-solid-state and solid/liquid magnetoelectric composites. *Adv. Mater.* **31**, 1806662 (2019).
- (181) Yamada, T., Morita, K., Kume, K., Yoshikawa H. & Awaga, K. The solid-state electrochemical reduction process of magnetite in Li batteries: in situ magnetic

- measurements toward electrochemical magnets. *J. Mater. Chem. C* **2**, 5183-5188 (2014).
- (182) Zhu, X. *et al.* In situ nanoscale electric field control of magnetism by nanoionics. *Adv. Mater.* **28**, 7658-7665 (2016).
- (183) Tsuchiya, T. *et al.* In situ tuning of magnetization and magnetoresistance in Fe₃O₄ thin film achieved with all-solid-state redox device. *ACS Nano* **10**, 1655-1661 (2016).
- (184) Wei, G. *et al.* Reversible control of the magnetization of Fe₃O₄ via lithium ions. *RSC Adv.* **7**, 2644-2649 (2017).
- (185) Cheng, B. *et al.* Electric-field control of magnetic properties for amorphous Fe₂O₃/LiTaO₃ thin film. *J. Mater. Chem. C* **6**, 11608-11614 (2018).
- (186) Dubraja, L. A. *et al.* Electrochemical tuning of magnetism in ordered mesoporous transition-metal ferrite films for micromagnetic actuation. *ACS Appl. Nano Mater.* **1**, 65-72 (2018).
- (187) Reitz, C., Suchomski, C., Wang, D., Hahn H.& Brezesinski, T. In situ tuning of magnetization via topotactic lithium insertion in ordered mesoporous lithium ferrite thin films. *J. Mater. Chem. C* **4**, 8889-8896 (2016).
- (188) Ameziane, M., Mansell, R., Havu, V., Rinke, P., Van Dijken, S. Lithium-ion battery technology for voltage control of perpendicular magnetization. *Adv. Func. Mater.* **32**, 2113118 (2022).
- (189) Ameziane, M., Huhtasalo, J., Flajšman, L., Mansell, R., Van Dijken, S. Solid-state lithium ion supercapacitor for voltage control of skyrmions. *Nano Lett.* **23**, 3167-3173 (2023)
- (190) Ameziane, M., Rosenkamp, R., Flajšman, L., Van Dijken, S., Mansell, R. Electric Field Control of RKKY Coupling Through Solid-state Ionics. *Appl. Phys. Lett.* **122**, 232401 (2023).
- (191) Dhanapal, P. *et al.* Reversible control of magnetic anisotropy and magnetization in amorphous Co₄₀Fe₄₀B₂₀ thin films via all-solid-state Li-ion redox capacitor. *Phys. Rev. Applied* **12**, 054065 (2019).
- (192) Leistner, K. *et al.* Electric-field control of magnetism by reversible surface reduction and oxidation reactions. *Phys. Rev. B* **87**, 224411 (2013).

- (193) Nichterwitz, M. *et al.* Voltage-controlled ON switching and manipulation of magnetization via the redox transformation of β -FeOOH nanoplatelets. *J. Phys. D: Appl. Phys.* **53**, 084001 (2019).
- (194) Clemens, O. *et al.* Electrochemical fluorination of perovskite type BaFeO_{2.5}. *Dalton Trans.* **43**, 15771-15778 (2014).
- (195) Nowroozi, M. A., Wissel, K., Rohrer, J., Munnangi, A. R. & Clemens, O. LaSrMnO₄: reversible electrochemical intercalation of fluoride ions in the context of fluoride ion batteries. *Chem. Mater.* **29**, 3441-3453 (2017).
- (196) Nowroozi, M. A. & Clemens, O. Insights on the behavior of conversion-based anode materials for fluoride ion batteries by testing against an intercalation-based reference cathode. *ACS Appl. Energy Mater.* **1**, 6626-6637 (2018).
- (197) Nowroozi, M. A., Ivlev, S., Rohrer, J. & Clemens, O. La₂CoO₄: a new intercalation based cathode material for fluoride ion batteries with improved cycling stability. *J. Mater. Chem. A*, **6**, 4658-4669 (2018).
- (198) Lin, W., Tsai, C., Wang, B., Kao, C. & Pong, W. Hydrogenation induced reversible modulation of perpendicular magnetic coercivity in Pd/Co/Pd films. *Appl. Phys. Lett.* **102**, 252404 (2013).
- (199) Kirchheim, R. Hydrogen solubility and diffusivity in defective and amorphous metals. *Prog. Mater. Sci.* **32**, 261-325 (1988).
- (200) Jani, H. *et al.* Reversible hydrogen control of antiferromagnetic anisotropy in α -Fe₂O₃. *Nat. Commun.* **12**, 1668 (2021).
- (201) Sheffels, S. *et al.* Insight on hydrogen injection and GdO_x/Co interface chemistry from in operando neutron reflectometry and secondary ion mass spectrometry. *Appl. Phys. Lett.* **122**, 022407 (2023).
- (202) Huang, M. *et al.* Voltage control of ferrimagnetic order and voltage-assisted writing of ferrimagnetic spin textures. *Nat. Nanotech.* **16**, 981-988 (2021).
- (203) Kossak, A. E., Huang, M., Reddy, P., Wolf, D. & Beach, G. S. D. Voltage control of magnetic order in RKKY coupled multilayers. *Sci. Adv.* **9**, eadd0548 (2023).
- (204) Gößler, M. *et al.* Magneto-ionic switching of superparamagnetism. *Small* **15**, 1904523 (2019).
- (205) Chen, G. *et al.* Observation of hydrogen-induced Dzyaloshinskii-Moriya interaction and reversible switching of magnetic chirality. *Phys. Rev. X* **11**, 021015 (2021).

- (206) Fillion, C. E. *et al.* Gate-controlled skyrmion and domain wall chirality. *Nat. Commun.* **13**, 5257 (2022).
- (207) Lu, N. *et al.* Electric-field control of tri-state phase transformation with a selective dual-ion switch. *Nature* **546**, 124-128 (2017).
- (208) Wang, M. *et al.* Manipulate the electronic and magnetic states in NiCo₂O₄ films through electric-field-induced protonation at elevated temperature. *Adv. Mater.* **31**, 1900458 (2019).
- (209) Gilbert, D. A. *et al.* Tunable low density palladium nanowire foams. *Chem. Mater.* **29**, 9814-9818 (2017).
- (210) Mishra, R., Kumar, D. & Yang, H. Oxygen-migration-based spintronic device emulating a biological synapse. *Phys. Rev. Appl.* **11**, 054065 (2019).
- (211) Todeschini, M., Bastos Da Silva Fanta, A., Jensen, F., Wagner, J. B., Han, A. Influence of Ti and Cr adhesion layers on ultrathin Au films. *ACS Appl. Mater. Interfaces* **9**, 37374-37385 (2017)
- (212) Elton, L. R. B. & Jackson, D. F. X-Ray diffraction and the Bragg law. *Am. J. Phys.* **34**, 1036-1038 (1966).
- (213) Barla, A. *et al.* Design and performance of BOREAS, the beamline for resonant X-ray absorption and scattering experiments at the ALBA synchrotron light source. *J. Synchrotron. Radiat.* **23**, 1507-1517 (2016).
- (214) Yano, J. & Yachandra, V. K. X-ray absorption spectroscopy. *Photosynth. Res.* **102**, 241-254 (2009).
- (215) Griffiths, P. R. Beer's Law. *Handbook of Vibrational Spectroscopy. Chichester: John Wiley & Sons*, 2225-34 (2001).
- (216) Wang, M. *et al.* In situ x-ray absorption spectroscopy studies of nanoscale electrocatalysts. *Nano-Micro Lett.* **11**, 47 (2019).
- (217) Sofia Martins *et al.* Dynamic electric-field-induced magnetic effects in cobalt oxide thin films: towards magneto-ionic synapses. *Nanoscale* **14**, 842-852 (2022).
- (218) Meersschaut, J. & Vandervorst, W. High-throughput ion beam analysis at imec. *Nucl. Instrum. Methods Phys. Res. B* **406**, 25-29 (2017).
- (219) Liedke, M. O. *et al.* Open volume defects and magnetic phase transition in Fe₆₀Al₄₀ transition metal aluminide. *J. Appl. Phys.* **117**, 163908 (2015).

- (220) Dryzek, J. & Horodek, P. GEANT4 simulation of slow positron beam implantation profiles. *Nucl. Instrum. Methods Phys. Res. B* **266**, 4000-4009 (2008).
- (221) Wagner, A., Butterling, M., Liedke, M. O., Potzger, K. & Krause-Rehberg, R. Positron annihilation lifetime and Doppler broadening spectroscopy at the ELBE facility. *AIP Conf. Proc.* **1970**, 040003 (2018).
- (222) Rietveld, G. *et al.* DC conductivity measurements in the Van Der Pauw geometry. *IEEE Trans. Instrum. Meas.* **52**, 449-453 (2003).
- (223) Blöchl, P. E. Projector augmented-wave method. *Phys. Rev. B* **50**, 17953 (1994).
- (224) Henkelman, G. & Jónsson, H. Improved tangent estimate in the nudged elastic band method for finding minimum energy paths and saddle points. *J Chem. Phys.* **113**, 9978 (2000).
- (225) Henkelman, G., Uberuaga, B. P. & Jónsson, H. A climbing image nudged elastic band method for finding saddle points and minimum energy paths. *J Chem. Phys.* **113**, 9901 (2000).

3 Results

In this chapter, the Thesis results are compiled into a collection of articles. Specifically, three peer-reviewed publications are included:

3.1) Frequency-dependent stimulated and post-stimulated voltage control of magnetism in transition metal nitrides: towards brain-inspired magneto-ionics.

3.2) From Binary to Ternary Transition-Metal Nitrides: A Boost toward Nitrogen Magneto-Ionics.

3.3) Regulating Oxygen Ion Transport at the Nanoscale to Enable Highly Cyclable Magneto-Ionic Control of Magnetism.

Each article is prefaced by a summary highlighting the main points of the study, followed by a thorough exploration of the findings in the articles themselves. These discussions provide a detailed demonstration of the results, explaining their significance and implications in depth.

3.1 Frequency-dependent stimulated and post- stimulated voltage control of magnetism in transition metal nitrides: towards brain-inspired magneto-ionics

Zhengwei Tan^a, Julius de Rojas^a, Sofia Martins^a, Aitor Lopeandia^{a,b}, Alberto Quintana^c, Matteo Cialone^d, Javier Herrero-Martín^e, Johan Meersschaut^f, André Vantomme^g, José L. Costa-Krämer^h, Jordi Sort*^{a,i} and Enric Menéndez*^a

^aDepartament de Física, Universitat Autònoma de Barcelona, E-08193 Cerdanyola del Vallès, Spain.

^bCatalan Institute of Nanoscience and Nanotechnology (ICN2), CSIC and BIST, Campus UAB, Cerdanyola del Vallès, E-08193 Barcelona, Spain.

^cInstitut de Ciència de Materials de Barcelona (ICMAB-CSIC), Campus UAB, Bellaterra, E-08193 Barcelona, Spain.

^dCNR-SPIN Genova, Corso F. M. Perrone 24, 16152 Genova, Italy.

^eALBA Synchrotron Light Source, 08290 Cerdanyola del Vallès, Spain.

^fIMEC, Kapeldreef 75, B-3001 Leuven, Belgium.

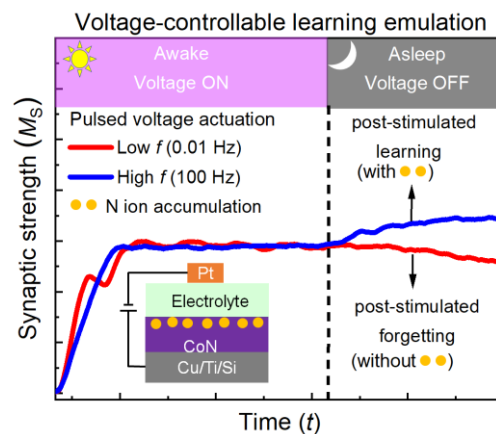
^gQuantum Solid State Physics, KU Leuven, Celestijnenlaan 200 D, B-3001 Leuven, Belgium.

^hIMN-Instituto de Micro y Nanotecnología (CNM-CSIC), Isaac Newton 8, PTM, 28760 Tres Cantos, Madrid, Spain.

ⁱInstitució Catalana de Recerca i Estudis Avançats (ICREA), Pg. Lluís Companys 23, E-08010 Barcelona, Spain.

In this study, we introduce an innovative strategy for governing the evolution of magnetization in both stimulated and post-stimulated states. This approach relies on voltage-driven ferromagnetism within CoN-based heterostructures, facilitated by the transport of N^{3-} ions, showcasing an impressive ion motion response on the order of 10^{-2} s. Through the application of consecutive voltage pulses, various functions such as information processing, memory (retention), recovering or self-evolution by maturity (i.e., steady increase of magnetization even when a voltage is no longer applied) can be emulated in a controlled manner. Such control is achieved by fine-tuning the thickness of the CoN film, which dictates ion motion rates, along with adjusting the pulse frequency. The observed outcomes stem from the interplay between magnetization generation during voltage application and partial depletion when the voltage is off.

Beyond energy-efficient attributes of this strategy, it also introduces a significant additional feature: once voltage is initially applied, the device can be programmed to learn or forget without requiring continuous energy input. This behaviour offers a new logical function that enables, for instance, the possibility to mimic neuromorphic learning under deep sleep, enabling ongoing information processing in the absence of external signals. Importantly, such functionality cannot be emulated with existing types of neuromorphic materials (e.g., resistive switching or spintronic materials). This reported effect opens opportunities, at the materials level, for advanced brain-inspired computing functionalities.





Cite this: DOI: 10.1039/d2mh01087a

Received 30th August 2022,
Accepted 12th October 2022

DOI: 10.1039/d2mh01087a

rs.c.li/materials-horizons

Frequency-dependent stimulated and post-stimulated voltage control of magnetism in transition metal nitrides: towards brain-inspired magneto-ionics†

 Zhengwei Tan,^a Julius de Rojas,^a Sofia Martins,^a Aitor Lopeandia,^{ab}
 Alberto Quintana,^c Matteo Cialone,^d Javier Herrero-Martín,^e
 Johan Meersschaut,^f André Vantomme,^g José L. Costa-Krämer,^h
 Jordi Sort^{id}*^{ai} and Enric Menéndez^{id}*^a

Magneto-ionics, which deals with the change of magnetic properties through voltage-driven ion migration, is expected to be one of the emerging technologies to develop energy-efficient spintronics. While a precise modulation of magnetism is achieved when voltage is applied, much more uncontrolled is the spontaneous evolution of magneto-ionic systems upon removing the electric stimuli (i.e., post-stimulated behavior). Here, we demonstrate a voltage-controllable N ion accumulation effect at the outer surface of CoN films adjacent to a liquid electrolyte, which allows for the control of magneto-ionic properties both during and after voltage pulse actuation (i.e., stimulated and post-stimulated behavior, respectively). This effect, which takes place when the CoN film thickness is below 50 nm and the voltage pulse frequency is at least 100 Hz, is based on the trade-off between generation (voltage ON) and partial depletion (voltage OFF) of ferromagnetism in CoN by magneto-ionics. This novel effect may open opportunities for new neuromorphic computing functions, such as post-stimulated neural learning under deep sleep.

New concepts

We propose an approach to control the magnetization evolution of electrolyte-gated CoN-based heterostructures both during (stimulated) and after (post-stimulated) voltage actuation by means of electric-field-driven transport of N ions. Specifically, upon voltage removal (i.e., once voltage stimuli are off), magnetization in our magneto-ionic systems can be either reduced or increased, without any further energy input, depending on the interplay between film thickness and the prior voltage actuation protocols. The latter offers a new logical function that enables, for instance, the possibility to mimic neuromorphic learning under deep sleep. Such functionality cannot be emulated with existing types of neuromorphic materials (e.g., resistive switching or spintronic materials). Here, post-stimulated magneto-ionic control is possible by a voltage-driven N ion accumulation effect at the outer surface of CoN films adjacent to a liquid electrolyte, which is generated for sufficiently thin CoN films and high voltage actuation frequencies, thus offering a new concept, at the materials level, for advanced brain-inspired computing functions.

Introduction

Magneto-ionics, relying on the control of magnetic properties through voltage-driven ion (O^{2-} , H^+ , Li^+ , F^{-10} or $N^{3-11-14}$) migration, holds potential for being one of the technologies to develop low-power memory applications. In recent years, significant progress has been made in improving ion motion rates and endurance, which are the two main bottlenecks to exploit the full potential of magneto-ionics at room temperature. This has been achieved by proper selection of the moving ion species, target materials, heterostructure designs, electrolytes and voltage actuation protocols. These advances have made it possible to propose magneto-ionic materials as suitable candidates for new spintronic applications,^{15,16} as well as for new computation paradigms, such as neuromorphic systems.^{17,18} The precise modulation of magnetism by magneto-ionics has been already successful to emulate the main synaptic functions: activation threshold, plasticity (potentiation and depression),

^a Departament de Física, Universitat Autònoma de Barcelona, E-08193 Cerdanyola del Vallès, Spain. E-mail: jordi.sort@uab.cat, enric.menendez@uab.cat

^b Catalan Institute of Nanoscience and Nanotechnology (ICN2), CSIC and BIST, Campus UAB, Cerdanyola del Vallès, E-08193 Barcelona, Spain

^c Institut de Ciència de Materials de Barcelona (ICMAB-CSIC), Campus UAB, Bellaterra, E-08193 Barcelona, Spain

^d CNR-SPIN Genova, Corso F. M. Perrone 24, 16152 Genova, Italy

^e ALBA Synchrotron Light Source, 08290 Cerdanyola del Vallès, Spain

^f IMEC, Kapeldreef 75, B-3001 Leuven, Belgium

^g Quantum Solid State Physics, KU Leuven, Celestijnenlaan 200 D, B-3001 Leuven, Belgium

^h IMN-Instituto de Micro y Nanotecnología (CNM-CSIC), Isaac Newton 8, PTM, 28760 Tres Cantos, Madrid, Spain

ⁱ Institució Catalana de Recerca i Estudis Avançats (ICREA), Pg. Lluís Companys 23, E-08010 Barcelona, Spain

† Electronic supplementary information (ESI) available. See DOI: <https://doi.org/10.1039/d2mh01087a>



spike-magnitude dependence, spike-timing-dependent plasticity, spike-rate-dependent plasticity and forgetting.^{17,18} Plasticity is linked to learning and memory, and, in particular, spike-rate-dependent plasticity is considered the most accurate model to describe learning and memory.^{19–24}

Among materials to mimic synapses, magneto-ionic systems stand out from phase-change compounds,²⁵ resistive-switching oxides^{20,26–28} or spintronic multilayers^{21,23} basically due to the potential improvement of energy efficiency, envisaging ultra-low power hardware with minimized Joule heating effects.^{29–31} In addition, magneto-ionics could exploit the extra degree of freedom provided by the vector nature of magnetization which may allow synapses to be directly programmed with positive and negative synaptic weights without need of additional electronics.¹⁷ However, while the weight (*e.g.*, resistance,^{20,22,26,28} magnetization^{21,23}) update in most current non-volatile technologies can be manipulated by changing the input electric signal (value and sign), the post-stimulated (without input) states are usually not controllable due to system-inherent relaxation effects.^{32,33} This post-stimulus uncontrollability greatly limits the emulation of some important brain-inspired functions, such as maintaining learning efficiency even during deep sleep.³⁴ Therefore, procedures capable of controlling post-stimulated evolution while maintaining good tunability in modulation of weight update are highly desired.

Here, we propose a new approach to control the magnetization evolution both in stimulated and post-stimulated states based on voltage-driven ferromagnetism in CoN-based heterostructures through the transport of N^{3-} ions, with a cumulative 10^{-2} s ion motion response. By application of successive voltage pulses, information processing, memory (retention), recovering or self-evolution by maturity (*i.e.*, controllable updating even when a voltage is no longer applied) can be emulated in a controlled manner. Such control is possible by tuning the CoN film thickness (which determines ion motion rates) and the pulse frequency. The observed effects result from the trade-off between generation (voltage ON) and partial depletion (voltage OFF) of magnetization. Besides boosting energy efficiency, this approach offers an important additional logical function: after voltage has been applied, the device can be either programmed to learn or forget without any further energy input, thus mimicking synaptic functions under deep sleep, when processing of information can continue without any external signal input.

Experimental

Sample preparation

CoN films with thicknesses ranging from 5 to 200 nm were grown using reactive sputtering, as described earlier.¹¹ A 20 nm Ti and 60 nm Cu buffer layers were first prepared by sputtering on B-doped, highly conducting [100]-oriented Si wafers (60 nm Cu/20 nm Ti/0.5 mm [100]-oriented Si). The CoN films were grown in a home-made triode sputtering system with a base pressure as low as 10^{-8} Torr to provide an ultra-high vacuum, oxygen-free growth condition, and exclude interferences of

oxygen magneto-ionics. Prior to CoN deposition, a portion of the Cu/Ti/Si substrate was masked to make the required electric contact on Cu for *in situ* magnetoelectric experiments. The distance between the target and the substrate was approximately 10 cm and the sputtering rate was about 1 \AA s^{-1} . CoN was grown under a total pressure of 8×10^{-3} Torr with an atmosphere of $N_2 : Ar = 1 : 1$.

Magneto-ionic characterization

In-plane magnetization was measured at room temperature using a commercial vibrating sample magnetometer (VSM) from Micro Sense (LOT-Quantum Design), with a maximum applied magnetic field of 2 T. The CoN samples were electrolyte-gated (with an external Agilent B2902A power supply). A Pt wire was used as counter electrode, whereas the working electrode was the investigated CoN/Cu/Ti/Si film. (*i.e.*, home-made electrochemical capacitor geometry). Negative voltages here mean that negative charges accumulate at the working electrode (and *vice versa* for positive voltages). Anhydrous propylene carbonate with Na^+ and OH^- solvated species (5–25 ppm) was used as electrolyte. Metallic sodium was immersed in the electrolyte to react with any traces of water. The magnetization (M) arises from normalizing the magnetic signal to the sample volume mounted in the electrolyte. Note that the linear background of the hysteresis loops (stemming from paramagnetic and diamagnetic contributions) was removed using the signal at high fields (*i.e.*, fields always far above saturation fields).

Structural and compositional measurements

θ/θ X-ray diffraction (XRD) patterns were measured on a Materials Research Diffractometer (MRD) from Malvern PANalytical company, equipped with a PIXcel^{1D} detector, using Cu $K\alpha$ radiation. High-resolution transmission electron microscopy (HRTEM), high-angle annular dark-field scanning transmission electron microscopy (HAADF-STEM), and electron energy loss spectroscopy (EELS) were performed on a TECNAI F20 HRTEM/STEM microscope operated at 200 kV. Cross sectional lamellae were prepared by focused ion beam and placed onto a Cu transmission electron microscopy grid. X-ray absorption spectroscopy (XAS) at the Co $L_{2,3}$ edges was performed using the BL29-BOREAS beamline at ALBA Synchrotron Light Source (Barcelona, Spain).³⁵ The spectra were measured in total electron yield (TEY), under ultra-high vacuum conditions (10^{-7} Torr) and at room temperature (300 K). For the elastic recoil detection (ERD) analysis, an impinging ion beam of 9.6 MeV $^{79}Br^{5+}$ particles was used. The sample was tilted to a grazing incidence angle of 20° between the ion beam and the surface of the film. The elastic collision between the impinging nuclei and target atoms can result in recoiling target species. The mass, energy and probability of the atoms emitted from the sample in forward direction were recorded by means of a multi-dispersive detector telescope.³⁶ ERD analysis yields a quantitative elemental depth profile of the sample, including that of light elements.



Results and discussion

Enhancing ion motion by film thickness reduction: enabling magneto-ionics for brain-inspired computing

To investigate magneto-ionics, CoN films with a thickness ranging from 5 to 200 nm were electrolyte-gated in an electrochemical capacitor configuration using a Pt wire as counter electrode (as sketched in Fig. 1a),^{3,11} while performing in-plane vibrating sample magnetometry (VSM). As shown in Fig. 1b, an anhydrous polar liquid electrolyte (propylene carbonate, PC, with Na⁺ and OH⁻ solvated species)^{37,38} was employed to allow the formation of an electric double layer (EDL)³⁹ and to serve as a N ion reservoir.¹¹

The as-grown CoN films are highly nanostructured (Fig. S1, ESI†) and textured along (111) (Fig. S2, ESI†). As seen in Fig. S3 (ESI†), the X-ray absorption spectra of 5 nm- and 25 nm-thick CoN films show virtually the same shape, suggesting that the CoN stoichiometry is generally preserved regardless of film thickness. As seen in Fig. S4 (ESI†), the as-grown films exhibit virtually no ferromagnetism ($M_s < 10 \text{ emu cm}^{-3}$) in agreement with the paramagnetic character of polycrystalline CoN.¹¹ Consecutive hysteresis loops (each lasting 30 min) were recorded while electrolyte-gating to track the evolution of magnetic properties with time and, thus, characterize the magneto-ionic response. Irrespectively of the film's thickness, all pristine CoN films exhibit magneto-ionic effects after being subjected to a DC voltage of -25 V , confirming voltage-driven transport of N³⁻ ions (Fig. S4 and Table S1, ESI†).¹¹ As also seen in Fig. S4 (ESI†), the timescale to achieve a steady magnetic hysteresis

loop turns out to be highly dependent on the CoN film thickness. Since the largest generation of magnetization takes place during the first 5 min (*i.e.*, during the descending branch of the first hysteresis loop), saturation magnetization measurements as a function of time were recorded while electrolyte-gating at -25 V to properly determine the ion motion rates at the beginning of the magneto-ionic effect from saturation magnetization changes (Fig. 1c and d). For this, an external magnetic field of 10 kOe, above the anisotropy field of the generated ferromagnetic Co, was applied to ensure magnetic saturation. At the initial stages of voltage actuation, the rate of magnetization generation increases as the CoN film thickness decreases. This generation of magnetization reaches saturation (*i.e.*, showing a steady M_s) faster for thin than for thick films. However, the achieved steady value of M_s increases with film thickness (Table S1, ESI†) in agreement with the results of consecutive magnetic hysteresis loops recorded under the same voltage actuation (Fig. S4, ESI†). In addition, the steady coercivities H_c and squareness M_R/M_s (%) follow a dissimilar trend with thickness reduction. While coercivity decreases with film reduction, squareness increases, suggesting that the generated ferromagnetic Co grows more uniformly, enhancing exchange interactions among Co clusters which are in detriment of coercivity.⁴⁰ Fig. 1d shows the time evolution of growth rates of generated magnetization for all CoN films obtained by differentiating M_s with respect to time t : dM_s/dt . This allows determining initial ion motion rates. An around 7.4-fold enhancement of the highest ion motion rate is achieved by reducing the thickness from 200 nm to 5 nm, showing that of

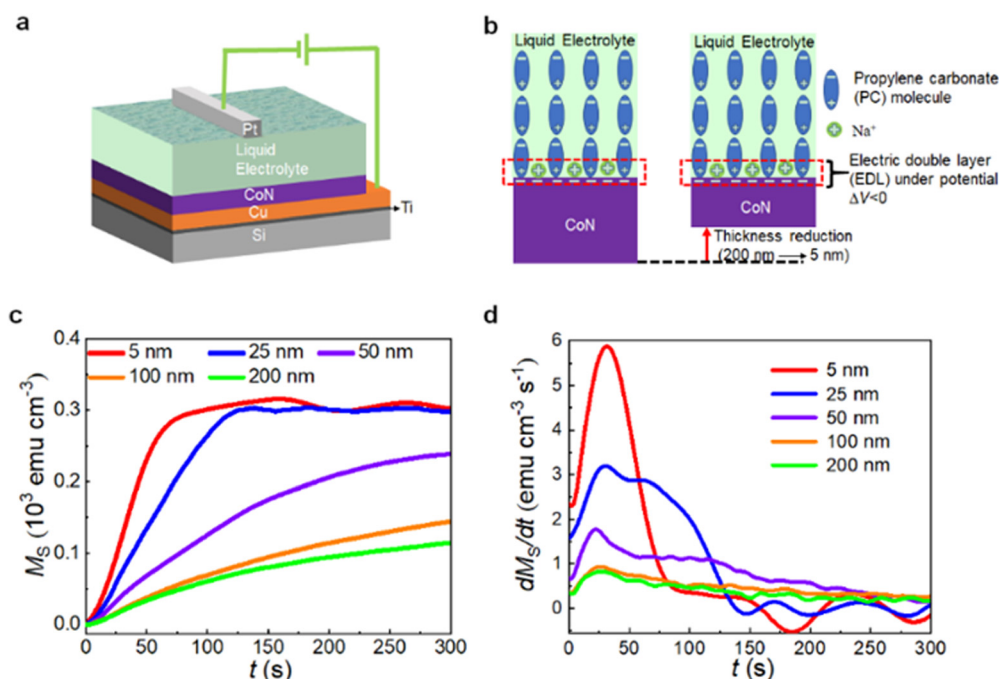


Fig. 1 Role of CoN film thickness in ion motion. (a) Schematic representation of the voltage actuation on CoN films by electrolyte-gating. (b) Sketch of the electric double layer (EDL) formed at the surface of the CoN films while electrolyte-gating at $\Delta V < 0$. (c) Saturation magnetization (M_s) as a function of time t for all the investigated CoN films under electrolyte-gating at -25 V while applying an external in-plane magnetic field of 10 kOe. (d) Derivative of the $M_s(t)$ dependences: dM_s/dt of the results in panel (c).



0.8 emu cm⁻³ s⁻¹ and 5.9 emu cm⁻³ s⁻¹, respectively. The latter represents the largest ion motion speed achieved so far in the self-contained magneto-ionic approach (see Table S2, ESI†).^{11–13} Considering that 1 s is the time resolution of the employed magnetometer, all CoN films clearly exhibit sub-1s magneto-ionic response since the generated magnetic moment at 1 s is always larger than the highest sensitivity of the VSM (125 nemu), a value which implies changes in magnetic moment above the resolution of the setup (Fig. S5 and Table S1, ESI†). In Table S1 (ESI†), the ΔM in 1 s increases greatly as the thickness decreases, indicating a considerable improvement of the trigger efficiency of the magneto-ionic motion because of thickness reduction. This suggests feasibility of our approach as a framework for synaptic-like materials since synapse functions require responses to repeated 10⁻² s stimuli.⁴¹ The leap in ion motion for thinner films is mainly associated with the enhancement of the applied electric field due to film thickness reduction. In a first approximation, the system can be considered as a condenser-like structure with parallel plates (*i.e.*, parallel plate capacitor), as shown in Fig. 1b. Given a certain potential V , the electric field E is inversely proportional to active dielectric thickness (the total thickness of the CoN film plus the EDL).⁴² Hence, the thinner the film, the thinner the active dielectric thickness and the more intense the electric field, providing a higher driving force to overcome the energy barrier for ion diffusion and to accelerate transport of nitrogen ions.

Dynamic (pulsed DC actuation) characterization of the magneto-ionic response: tuning the learning performance and emulation of ‘self-learning by maturity’ function (with no external voltage input)

Since communication among neurons is frequency-encoded, a dynamic characterization of the magneto-ionic response is crucial to determine its capability to mimic synaptic functions. Therefore, for magneto-ionic characterization, electrolyte-gating *via* electric voltage pulses was performed. Static constant voltages (DC) were used as reference. Fig. 2a shows schematically the voltage protocol used for the dynamic characterization: voltages square waves (from 0 V to -25 V) of period T (and corresponding frequency of $f=1/T$) and pulse duration of $T/2$ (resulting in a duty cycle of 50%). The period was varied from 10² s to 10⁻² s to obtain actuation frequencies from 10⁻² Hz to 10² Hz. CoN films with thicknesses of 25 nm and 200 nm were chosen as representative heterostructures to characterize the magneto-ionic response during pulsed DC voltage actuation, due to their significantly different ion motion speed. Both films were electrolyte-gated at different frequencies for gating times of around 550 s and 900 s, respectively, to ensure reaching a saturated magnetization state. While gating, time-dependent magnetization measurements under an applied magnetic field of 10 kOe were recorded by VSM.

As can be seen in Fig. 2b, which corresponds to the magneto-ionic response of the 200 nm film, M_S gradually increases up to 248 emu cm⁻³ upon treatment at -25 V DC voltage for 900 s. Then, after turning off the voltage, M_S slightly

decays, in agreement with the partial magnetization depletion (*i.e.*, recovery) that occurs in these systems, which shares resemblance with a nitriding process of metallic Co.¹¹ From a synaptic-like viewpoint and taking saturation magnetization as synaptic weight, this allows mimicking plasticity (*i.e.*, change in magnetization with time). Specifically, potentiation (*i.e.*, magnetization increase, voltage on), representing learning, and depression (*i.e.*, magnetization reduction, voltage off), reproducing forgetting¹⁷ can be mimicked. Fig. 2b also shows the evolution of M_S vs. t upon subjecting the 200 nm CoN films to voltage pulses of different frequency where the generated magnetization scales with frequency. As f increases from 1 to 100 Hz, the M_S values at 960 s increase one order of magnitude, from 17.6 to 168.2 emu cm⁻³ (see also Fig. S6, ESI†). Moreover, the steady M_S values and its recovery are also frequency dependent, emulating spike-rate-dependent plasticity. Resembling human brain, repeated spiking (*i.e.*, high frequency voltage pulsing) reinforces retention of information and thus learning.^{43,44} Human learning also takes place by transforming ‘short-term memory’ (STM) into ‘long-term memory’ (LTM) through the increase in frequency of the voltage stimuli.²⁸ STM refers to the temporal storage of input information in the hippocampus, which lasts only a few seconds. By increasing the frequency of training and stimulation, information obtained from outside can be continuously transferred to and stored in the cerebral cortex for hours or even years (LTM). As depicted in Fig. 2b, this transition can be mimicked by voltage-driven generation of ferromagnetism in CoN through voltage pulse waves of different frequency. This learning emulation capacity raises from the pulsed DC actuation which results in a trade-off between generation (voltage ON) and partial depletion/recovery (voltage OFF) of magnetization. With increased frequency, generation of magnetization prevails over dynamic recovery, resulting in larger M_S values. As seen in Fig. S1b (ESI†), nitrogen migration when applying pulsed DC voltage actuation takes place *via* planar-migration fronts, similarly to CoN films subjected to DC voltage actuation,¹¹ suggesting that the ion motion mechanisms are independent from voltage actuation characteristics.

Conversely, the 25 nm-thick CoN films offer a completely different scenario, where trade-off between generation (voltage ON) and partial depletion (voltage OFF) of magnetization is strongly altered. Specifically, for DC and pulsed actuation at high frequencies (*i.e.*, 1, 10 and 100 Hz), once the voltage actuation is switched off (*i.e.*, after $t = 620$ s in Fig. 2c), the saturation magnetization increases (Fig. 2c), rather than decreasing (as for the 200 nm-thick film), hence emulating a self-learning process with no external stimulus. This suggests that, once voltage is switched off, an additional driving force is set in place in the thinner films to pump ions towards the electrolyte, which screens and, in fact, overcomes recovery. This self-learning effect is particularly obvious after non-pulsed DC voltage actuation (blue curve in Fig. 2c). Given the high motion rates of N³⁻ ions across the 25 nm-thick CoN films (much larger than for thicker films –see Table S1, ESI†) and the limited N³⁻ solubility in the liquid electrolyte,^{45,46} a N³⁻ ion accumulation



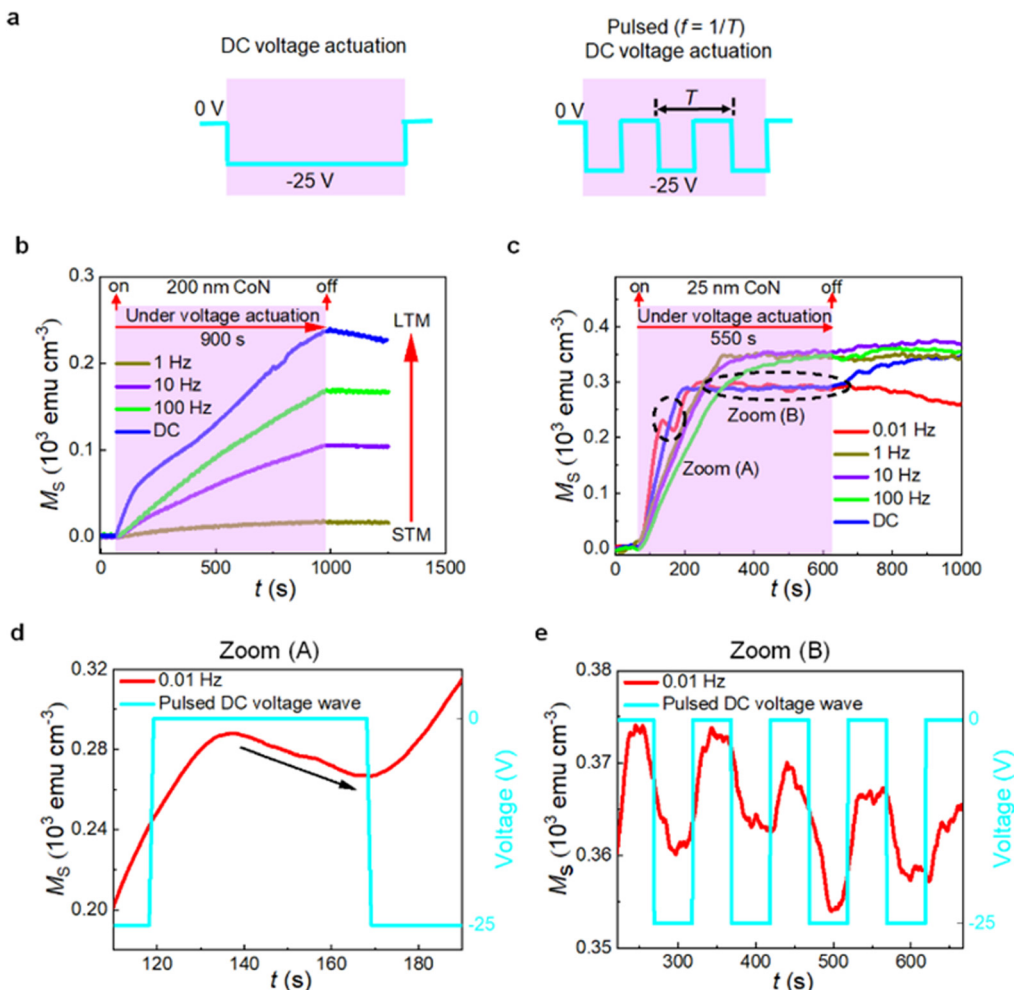


Fig. 2 Pulsed DC (dynamic) voltage actuation. (a) Schematic representation of the DC and pulsed DC voltage actuations. (b) Time evolution of the saturation magnetization (M_s vs. t) while electrolyte-gating at -25 V with DC and pulsed DC (at f from 1 to 100 Hz) voltages for the 200 nm CoN film. STM and LTM represent the short-term memory and the long-term memory, respectively. (c) Time evolution of the saturation magnetization (M_s vs. t) while electrolyte-gating at -25 V with DC and pulsed DC voltages (at f from 0.01 Hz to 100 Hz) for the 25 nm CoN film. (d) Zoom (A) of panel (c). (e) Zoom (B) of panel (c).

effect at the interface between the magneto-ionic film and the liquid reservoir is envisaged. Due to the N^{3-} concentration gradient, these ions will be presumably released to the electrolyte once voltage is switched off (following Fick's laws⁴⁷), leading to the increase of M_s . Note that whereas the frequency influence on M is clear, the larger M at higher frequency may also be due to the larger number of applied pulses, which results in more nitrogen ion movement and, thus, higher amounts of Co formed behind.

Remarkably, compared with 25 nm-thick CoN films, the 50 nm-thick ones display a weaker increase of M_s when the voltage actuation is turned off (Fig. S7, ESI[†]) whereas the 200 nm-thick films do not show this effect at all (Fig. 2b), indicating that the voltage-driven ion motion rate across the film is sufficiently slow in that case. Thus, the ion motion rate is a critical parameter to observe ion accumulation. As seen in Fig. S7 (ESI[†]), this voltage-free magnetization generation is limited in time since, after a while, magnetization recovery

starts (after 170 s for 50 nm and after 695 s for 25 nm thick films). This effect becomes less pronounced when the actuation frequency is decreased. In such a case, dynamic recovery occurs already during the $\Delta V = 0$ V intervals of the pulse voltage actuation, precluding the ion accumulation effect at the interface between the CoN films and the electrolyte (Fig. 2c). Indeed, when using a frequency of 0.01 Hz, recovery can be clearly observed upon voltage actuation (Fig. 2c and d), during the sub-segments with $\Delta V = 0$ V. Fig. 2d and e show two zooms of the M_s vs. t dependencies for voltage actuations at a frequency of 0.01 Hz. In zoom (A), a rise followed by a continuous depletion of M_s can be clearly seen (Fig. 2d). Zoom (B) indicates that the system exhibits an effective cyclability due to the trade-off between generation and magnetization recovery (Fig. 2e). Partial cyclability can be reproduced without the need of biases of opposite polarity, providing an energy-efficient and enduring way to cycle the system, since repeatedly switching voltage polarities is often linked to degradation. Remarkably, this ion



accumulation effect can be tuned by controlling just two external parameters: the CoN film thickness, which largely determines the ion motion speed, and the frequency of the pulsed voltage actuation. This demonstrates that it is possible to tune learning and forgetting at will by solely modifying the voltage actuation frequency since this parameter allows tuning the interplay between magnetization generation, recovery and, thus, ion accumulation at the CoN film/reservoir interface. Existing emulation of learning in artificial intelligence heavily relies on external inputs, which makes it difficult to simulate some synaptic functions under deep sleep, when information retention can continue even after stopping the input signal. In fact, the possibility of learning even without stimulus is analogous to a 'learning by maturity' process, *i.e.*, the possibility to remember fine details after resting. During sleep, biological synapses relax but maintain the brain's neuroplasticity and the ability to learn.³⁴ Recently, incorporation of slow-wave sleep periods has been shown advantageous also for artificial neuromorphic computing algorithms, to enhance the dynamical computation stability.⁴⁸ Remarkably, the reported effect could also be understood as a useful method to simulate overstimulation and neuronal malfunction.⁴⁹

Microscopic mechanism behind the magneto-ionic emulation of the self-learning neuromorphic function Fig. 3a schematically shows the M_S vs. t evolution for systems displaying and lacking the ion accumulation effect, respectively. If we define M_{S0} as the steady saturation magnetization achieved while actuating with voltage and M_{S1} the saturation magnetization reached within a short period of time after removing the voltage, the sign of the difference between M_{S0} and M_{S1} will represent the existence or absence of the ion accumulation effect: $M_{S0} - M_{S1} > 0$ (no accumulation) and $M_{S0} - M_{S1} < 0$ (accumulation). The ion accumulation effect at the surface of the CoN layer can be understood as the interplay between several dynamic processes at the atomic level. Highlighted among them are: (1) conventional electric-field-induced N^{3-} ion migration across CoN towards the electrolyte¹¹ (represented by a velocity v_E), (2) redistribution (*i.e.*, intermixing) between solvated N^{3-} ions (identified as N-PC) and N-free PC molecules driven by the gradient^{50–52} in number of PC molecules carrying N^{3-} along the direction perpendicular to the interface (the velocity of this redistribution process is represented by v_{Red}), (3) diffusion of N^{3-} ions accumulated at the interface (v_A), and (4) N^{3-} ion recovery from the electrolyte to the CoN film (v_{Rec}).¹¹ Fig. 3b schematically depicts the generation of magnetization in a thin CoN from an atomistic viewpoint that shows ion accumulation effects. When a negative voltage is applied, N^{3-} ions continuously migrate towards the electrolyte, leaving behind Co-rich areas in the CoN film responsible for the increase in saturation magnetization (stage (i) in Fig. 3b). Concomitantly, N^{3-} dissolution takes above. However, after a while, the generation of saturation magnetization slows down, tending to saturate (stage (ii) in Fig. 3b). This is ascribed to the fact that the N^{3-} ion migration occurs faster than the redistribution of PC molecules, thus limiting further dissolution of N^{3-} ions into the electrolyte (due to the limited N solubility in

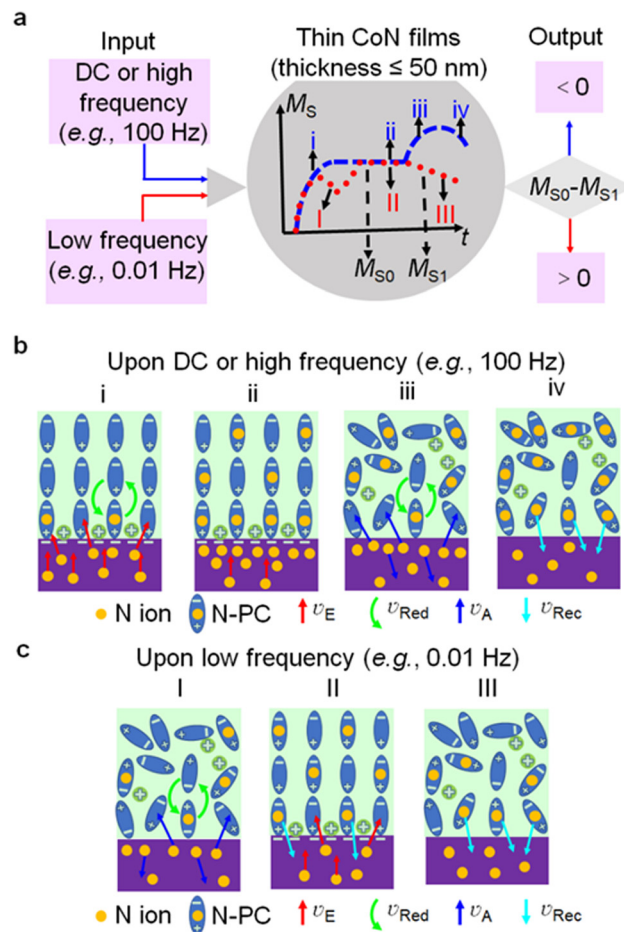


Fig. 3 Frequency dependence of the ion accumulation effect. (a) Schematic representation of the typical M_S vs. t dependences of heterostructures with thin CoN films (thicknesses ≤ 50 nm) showing (DC and pulsed DC at a frequency ≥ 1 Hz: blue dashed line) or not showing (pulsed DC at a frequency < 1 Hz: red dots) an ion accumulation interfacial effect. (b) (c) Microscopic mechanisms for the existence and absence of ion accumulation, respectively. v_E , v_{Red} , v_A , v_{Rec} represent the speed of N ion migration in CoN, redistribution of PC molecules, migration of accumulated N ions, and N ion recovery, respectively. For simplicity, N denotes N^{3-} in the picture.

PC, *i.e.*, absence of N-free PC molecules) and forcing N^{3-} ions to accumulate at the surface of the CoN film. After switching the voltage off, the concentration gradient between PC molecules tends to balance, further redistributing regular PC molecules and PC molecules saturated with N^{3-} . In this way, some regular PC molecules are able to reach the interface, providing more sites to incorporate N and, thus, to dissolve it. At the same time, the accumulated N^{3-} ions at the upper part of the CoN films can diffuse into the electrolyte and inside the CoN films (*i.e.*, towards the inner parts of the film, which normally occurs quite slowly). The former process, *i.e.*, N dissolving in the electrolyte, is the mechanism behind the increase in M_S even without voltage (stage (iii) in Fig. 3b). After some time, the N^{3-} diffusion process in the film weakens due to the decreasing concentration gradient and becomes surpassed by the conventional ion recovery process, which accounts for the decrease in M_S (stage (iv) in Fig. 3b). Remarkably, ion accumulation takes



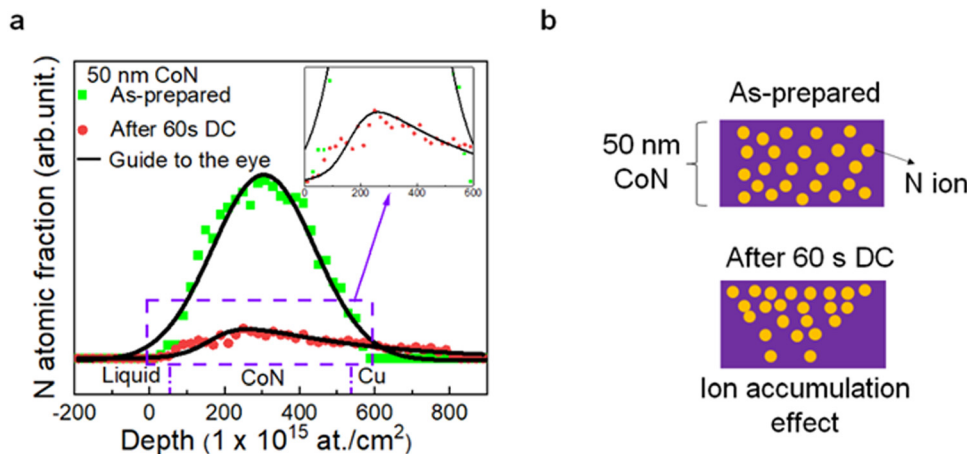


Fig. 4 Direct proof of the ion accumulation effect. (a) Elastic recoil detection measurements revealing the N depth distribution of an as-prepared and an actuated (-25 V DC voltage for 60 s) 50 nm-thick film, with a zoomed-in view of the area surrounded by the purple dashed box. (b) Cartoon representing the N ion distribution in an as-prepared sample and an actuated sample showing the ion accumulation effect.

place only in thin films (thickness ≤ 50 nm), since they exhibit sufficiently high voltage-driven ion motion (*i.e.*, v_E) values when actuated with either DC or pulsed DC voltage at high frequencies ($f \geq 1, 10$ and 100 Hz). Fig. 3c shows the atomistic mechanism when the heterostructure does not show ion accumulation effects, which corresponds to the situation in which the frequency of the pulsed DC actuation is low (*e.g.*, $f = 0.01$ Hz). Even though weak ion accumulation effects are feasible (stage (I)), they tend to rapidly vanish due to the long voltage interruption between the consecutive pulses, facilitating recovery processes and thus causing a partial magnetization depletion (stages (II) and (III)) during pulsing, as experimentally seen in Fig. 2c and e and depicted in the red dotted curve of Fig. 3a.

With the goal of obtaining direct evidence of this ion accumulation effect at the interface between the film and the electrolyte, the N^{3-} depth distribution of a 50 nm-thick sample upon DC voltage actuation has been assessed by elastic recoil detection analysis. As clearly seen in Fig. 4a, the depth distribution of N^{3-} for as-prepared CoN films is symmetric but becomes asymmetric during the DC voltage treatment. After applying a short 60 s DC voltage, this distribution is positively skewed, confirming that the N^{3-} content at the upper part of the film is larger than that at the bottom (*i.e.*, deeper) region and, thus, validating the ion accumulation effect (Fig. 4b).

Conclusion

Our work demonstrates a controllable ion accumulation effect at the interface between the CoN films and the adjacent electrolyte, which is set by a proper selection of the CoN film thickness and the pulse frequency of the voltage actuation. This effect, which takes place when the CoN film thickness is below 50 nm and the voltage pulse frequency is at least 100 Hz, is based on the trade-off between generation (voltage ON) and partial depletion (voltage OFF) of ferromagnetism in CoN by magneto-ionics. This effect allows for both the control of

magneto-ionic properties both while and upon removing voltage pulse actuation (effect off and on, resulting in stimulated and post-stimulated behaviour, respectively), expanding the potential of magneto-ionics in the emulation of post-stimulated neuromorphic functions, such as neural learning under deep sleep.

Author contributions

Z. T., J. S. and E. M. designed the experiment and the study. J. L. C.-K. synthesized the material. Z. T., S. M., A. Q., J. S. and E. M. carried out the VSM measurements and analysed the data. Z. T. and J. L. C.-K. performed the XRD characterization. Z. T. and A. L. prepared the cross-section lamellae for TEM. Z. T., A. L., J. S. and E. M. performed the HRTEM, STEM-HAADF and EELS and the corresponding data analysis. Z. T., J. deR., M. C. and J. H.-M. conducted the XAS experiments. J. M. and A. V. carried out the elastic recoil detection (ERD) analysis. All authors discussed the results and commented on the article. The article was written by Z. T., J. S. and E. M.

Conflicts of interest

There are no conflicts to declare.

Acknowledgements

Financial support by the European Research Council (MAGIC-SWITCH 2019-Proof of Concept Grant, Agreement No. 875018), the European Union's Horizon 2020 research and innovation programme (European Training Network, BeMAGIC ETN/ITN Marie Skłodowska-Curie grant No. 861145; and Integrated Infrastructure, RADIATE, grant No. 824096), the Spanish Government (MAT2017-86357-C3-1-R, PID2020-116844RB-C21 and PDC2021-121276-C3), the Generalitat de Catalunya (2017-SGR-292 and 2018-LLAV-00032), the European Regional Development Fund (MAT2017-86357-C3-1-R and 2018-LLAV-00032) and



the KU Leuven (BOF program) is acknowledged. A. Q. acknowledges financial support from the Spanish Ministry of Science, Innovation and Universities through the “Severo Ochoa” Programme for Centers of Excellence in R&D (FUNFUTURE CEX2019-000917-S) and the Juan de la Cierva formación contract (FJC2019-039780-I). J. S. thanks the Spanish Fábrica Nacional de Moneda y Timbre (FNMT) for fruitful discussions. The XAS measurements were performed at BL29-BOREAS beamline at ALBA Synchrotron with the collaboration of ALBA staff. We acknowledge service from MiNa Laboratory at IMN, and funding from CM (project S2018/NMT-4291 TEC2SPACE), MINECO (project CSIC13-4E-1794) and EU (FEDER, FSE). E. M. is a Serra Hünter Fellow.

References

- U. Bauer, L. Yao, A. J. Tan, P. Agrawal, S. Emori, H. L. Tuller, S. van Dijken and G. S. D. Beach, *Nat. Mater.*, 2015, **14**, 174.
- D. A. Gilbert, A. J. Grutter, E. Arenholz, K. Liu, B. J. Kirby, J. A. Borchers and B. B. Maranville, *Nat. Commun.*, 2016, **7**, 12264.
- J. de Rojas, A. Quintana, A. Lopeandía, J. Salguero, J. L. Costa-Krämer, L. Abad, M. O. Liedke, M. Butterling, A. Wagner, L. Henderick, J. Dendooven, C. Detavernier, J. Sort and E. Menéndez, *Adv. Funct. Mater.*, 2020, **30**, 2003704.
- A. Quintana, E. Menéndez, M. O. Liedke, M. Butterling, A. Wagner, V. Sireus, P. Torruella, S. Estradé, F. Peiró, J. Dendooven, C. Detavernier, P. D. Murray, D. A. Gilbert, K. Liu, E. Pellicer, J. Nogues and J. Sort, *ACS Nano*, 2018, **12**, 10291.
- M. Cialone, A. Nicolenco, S. Robbenolt, E. Menéndez, G. Rius and J. Sort, *Adv. Mater. Interfaces*, 2021, **8**, 2001143.
- A. J. Tan, M. Huang, C. O. Avci, F. Büttner, M. Mann, W. Hu, C. Mazzoli, S. Wilkins, H. L. Tuller and G. S. D. Beach, *Nat. Mater.*, 2019, **18**, 35.
- M. Gößler, M. Albu, G. Klinser, E. M. Steyskal, H. Krenn and R. Würschum, *Small*, 2019, **15**, 1904523.
- X. Ye, H. K. Singh, H. Zhang, H. Geßwein, M. R. Chellali, R. Witte, A. Molinari, K. Skokov, O. Gutfleisch, H. Hahn and R. Kruk, *Nat. Commun.*, 2020, **11**, 4849.
- S. Dasgupta, B. Das, M. Knapp, R. A. Brand, H. Ehrenberg, R. Kruk and H. Hahn, *Adv. Mater.*, 2014, **26**, 4639.
- S. Vasala, A. Jakob, K. Wissel, A. I. Waidha, L. Alff and O. Clemens, *Adv. Electron. Mater.*, 2020, **6**, 1900974.
- J. de Rojas, A. Quintana, A. Lopeandía, J. Salguero, B. Muñiz, F. Ibrahim, M. Chshiev, A. Nicolenco, M. O. Liedke, M. Butterling, A. Wagner, V. Sireus, L. Abad, C. J. Jensen, K. Liu, J. Nogués, J. L. Costa-Krämer, E. Menéndez and J. Sort, *Nat. Commun.*, 2020, **11**, 5871.
- J. de Rojas, J. Salguero, F. Ibrahim, M. Chshiev, A. Quintana, A. Lopeandía, M. O. Liedke, M. Butterling, E. Hirschmann, A. Wagner, L. Abad, J. L. Costa-Krämer, E. Menéndez and J. Sort, *ACS Appl. Mater. Interfaces*, 2021, **13**, 30826.
- J. de Rojas, J. Salguero, A. Quintana, A. Lopeandía, M. O. Liedke, M. Butterling, A. G. Attallah, E. Hirschman, A. Wagner, L. Abad, J. L. Costa-Krämer, J. Sort and E. Menéndez, *Phys. Rev. Appl.*, 2021, **16**, 034042.
- Z. Tan, S. Martins, M. Escobar, J. De Rojas, F. Ibrahim, M. Chshiev, A. Quintana, A. Lopeandía, J. L. Costa-Krämer, E. Menéndez and J. Sort, *ACS Appl. Mater. Interfaces*, 2022, **14**, 44581.
- L. Herrera Diez, R. Kruk, K. Leistner and J. Sort, *APL Mater.*, 2021, **9**, 050401.
- Y. Gu, C. Song, Q. Wang, W. Hu, W. Liu, F. Pan and Z. Zhang, *APL Mater.*, 2021, **9**, 040904.
- R. Mishra, D. Kumar and H. Yang, *Phys. Rev. Appl.*, 2019, **11**, 054065.
- S. Martins, J. De Rojas, Z. Tan, M. Cialone, A. Lopeandía, J. Herrero-Martín, J. L. Costa-Krämer, E. Menéndez and J. Sort, *Nanoscale*, 2022, **14**, 842.
- J. Xiong, R. Yang, J. Shaibo, H.-M. Huang, H.-K. He, W. Zhou, X. Guo, J. Xiong, R. Yang, J. Shaibo, H. Huang, H. He, W. Zhou and X. Guo, *Adv. Funct. Mater.*, 2019, **29**, 1807316.
- Z. Wang, S. Joshi, S. E. Savel'ev, H. Jiang, R. Midya, P. Lin, M. Hu, N. Ge, J. P. Strachan, Z. Li, Q. Wu, M. Barnell, G. L. Li, H. L. Xin, R. S. Williams, Q. Xia and J. J. Yang, *Nat. Mater.*, 2017, **16**, 101.
- J. Torrejon, M. Riou, F. A. Araujo, S. Tsunegi, G. Khalsa, D. Querlioz, P. Bortolotti, V. Cros, K. Yakushiji, A. Fukushima, H. Kubota, S. Yuasa, M. D. Stiles and J. Grollier, *Nature*, 2017, **547**, 428.
- H. Yeon, P. Lin, C. Choi, S. H. Tan, Y. Park, D. Lee, J. Lee, F. Xu, B. Gao, H. Wu, H. Qian, Y. Nie, S. Kim and J. Kim, *Nat. Nanotechnol.*, 2020, **15**, 574.
- J. Grollier, D. Querlioz, K. Y. Camsari, K. Everschor-Sitte, S. Fukami and M. D. Stiles, *Nat. Electron.*, 2020, **3**, 360.
- T. Ohno, T. Hasegawa, T. Tsuruoka, K. Terabe, J. K. Gimzewski and M. Aono, *Nat. Mater.*, 2011, **10**, 591.
- W. Zhang, R. Mazzarello, M. Wuttig and E. Ma, *Nat. Rev. Mater.*, 2019, **4**, 150.
- F. Zhou, Z. Zhou, J. Chen, T. H. Choy, J. Wang, N. Zhang, Z. Lin, S. Yu, J. Kang, H.-S. P. Wong and Y. Chai, *Nat. Nanotechnol.*, 2019, **14**, 776.
- M. Prezioso, F. Merrikh-Bayat, B. D. Hoskins, G. C. Adam, K. K. Likharev and D. B. Strukov, *Nature*, 2015, **521**, 61.
- J. Rao, Z. Fan, L. Hong, S. Cheng, Q. Huang, J. Zhao, X. Xiang, E.-J. Guo, H. Guo, Z. Hou, Y. Chen, X. Lu, G. Zhou, X. Gao and J.-M. Liu, *Mater. Today Phys.*, 2021, **18**, 100392.
- M. Bibes and A. Barthélémy, *Nat. Mater.*, 2008, **7**, 425.
- A. Molinari, H. Hahn and R. Kruk, *Adv. Mater.*, 2019, **31**, 1806662.
- M. Nichterwitz, S. Honnali, M. Kutuzau, S. Guo, J. Zehner, K. Nielsch and K. Leistner, *APL Mater.*, 2021, **9**, 30903.
- J. J. Yang and Q. Xia, *Nat. Mater.*, 2017, **16**, 396.
- J. Tian, Z. Tan, Z. Fan, D. Zheng, Y. Wang, Z. Chen, F. Sun, D. Chen, M. Qin, M. Zeng, X. Lu, X. Gao and J.-M. Liu, *Phys. Rev. Appl.*, 2019, **11**, 024058.
- S. Fattinger, T. T. de Beukelaar, K. L. Ruddy, C. Volk, N. C. Heyse, J. A. Herbst, R. H. R. Hahnloser, N. Wenderoth and R. Huber, *Nat. Commun.*, 2017, **8**, 15405.
- A. Barla, J. Nicolás, D. Cocco, S. M. Valvidares, J. Herrero-Martín, P. Gargiani, J. Moldes, C. Ruget, E. Pellegrin and S. Ferrer, *J. Synchrotron Radiat.*, 2016, **23**, 1507.



- 36 J. Meersschaut and W. Vandervorst, *Nucl. Instrum. Methods Phys. Res., Sect. B*, 2017, **406**, 25.
- 37 C. Navarro-Senent, A. Quintana, E. Menéndez, E. Pellicer and J. Sort, *APL Mater.*, 2019, **7**, 030701.
- 38 G. G. Eshetu, G. A. Elia, M. Armand, M. Forsyth, S. Komaba, T. Rojo and S. Passerini, *Adv. Energy Mater.*, 2020, **10**, 2000093.
- 39 M. Weisheit, S. Fähler, A. Marty, Y. Souche, C. Poinignon and D. Givord, *Science*, 2007, **315**, 349.
- 40 E. Menéndez, J. Demeter, J. van Eyken, P. Nawrocki, E. Jedryka, M. Wójcik, J. F. Lopez-Barbera, J. Nogués, A. Vantomme and K. Temst, *ACS Appl. Mater. Interfaces*, 2013, **5**, 4320.
- 41 C. C. McIntyre and R. W. Anderson, *J. Neurochem.*, 2016, **139**, 338.
- 42 D. Halley, N. Najjari, H. Majjad, L. Joly, P. Ohresser, F. Scheurer, C. Ulhaq-Bouillet, S. Berciaud, B. Doudin and Y. Henry, *Nat. Commun.*, 2014, **5**, 3167.
- 43 D. Hassabis, D. Kumaran, C. Summerfield and M. Botvinick, *Neuron*, 2017, **95**, 245.
- 44 D. Marković, A. Mizrahi, D. Querlioz and J. Grollier, *Nat. Rev. Phys.*, 2020, **2**, 499.
- 45 J. Read, K. Mutolo, M. Ervin, W. Behl, J. Wolfenstine, A. Driedger and D. Foster, *J. Electrochem. Soc.*, 2003, **150**, A1351.
- 46 W. Chen, M. Chen, M. Yang, E. Zou, H. Li, C. Jia, C. Sun, Q. Ma, G. Chen and H. Qin, *Appl. Energy*, 2019, **240**, 265.
- 47 I. M. Sokolov, J. Klafter and A. Blumen, *Phys. Today*, 2002, **55**, 48.
- 48 Y. Watkins, E. Kim, A. Sornborger and G. T. Kenyon. In Proceedings of the IEEE/CVF Conference on Computer Vision and Pattern Recognition Workshops, TN, USA, July, 2020.
- 49 H. Huang, C. Ge, Z. Liu, H. Zhong, E. Guo, M. He, C. Wang, G. Yang and K. Jin, *J. Semicond.*, 2021, **42**, 103103.
- 50 W. Guo, L. Cao, J. Xia, F.-Q. Nie, W. Ma, J. Xue, Y. Song, D. Zhu, Y. Wang and L. Jiang, *Adv. Funct. Mater.*, 2010, **20**, 1339.
- 51 A. Ozcan, C. Perego, M. Salvalaglio, M. Parrinello and O. Yazaydin, *Chem. Sci.*, 2017, **8**, 3858.
- 52 A. P. Thompson, D. M. Ford and G. S. Heffelfinger, *J. Chem. Phys.*, 1998, **109**, 6406.



Electronic Supplementary Information (ESI) for:

Frequency-dependent stimulated and post-stimulated voltage control of magnetism in transition metal nitrides: towards brain-inspired magneto-ionics

Zhengwei Tan^a, Julius de Rojas^a, Sofia Martins^a, Aitor Lopeandia^{a,b}, Alberto Quintana^c, Matteo Cialone^d, Javier Herrero-Martín^e, Johan Meersschaut^f, André Vantomme^g, José L. Costa-Krämer^h, Jordi Sort^{a,i,*} and Enric Menéndez^{a,*}

^aDepartament de Física, Universitat Autònoma de Barcelona, E-08193 Cerdanyola del Vallès, Spain.

^bCatalan Institute of Nanoscience and Nanotechnology (ICN2), CSIC and BIST, Campus UAB, Cerdanyola del Vallès, E-08193 Barcelona, Spain.

^cInstitut de Ciència de Materials de Barcelona (ICMAB-CSIC), Campus UAB, Bellaterra, E-08193 Barcelona, Spain.

^dCNR-SPIN Genova, Corso F. M. Perrone 24, 16152 Genova, Italy.

^eALBA Synchrotron Light Source, 08290 Cerdanyola del Vallès, Spain.

^fIMEC, Kapeldreef 75, B-3001 Leuven, Belgium.

^gQuantum Solid State Physics, KU Leuven, Celestijnenlaan 200 D, B-3001 Leuven, Belgium.

^hIMN-Instituto de Micro y Nanotecnología (CNM-CSIC), Isaac Newton 8, PTM, 28760 Tres Cantos, Madrid, Spain.

ⁱInstitució Catalana de Recerca i Estudis Avançats (ICREA), Pg. Lluís Companys 23, E-08010 Barcelona, Spain.

*Correspondence to: jordi.sort@uab.cat (J. Sort), enric.menendez@uab.cat (E. Menéndez)

Compositional and structural characterization

High-angle annular dark-field scanning transmission electron microscopy (HAADF-STEM) and electron energy loss spectroscopy (EELS) were performed along the cross-sections of as-prepared 200 nm-thick CoN films and a 200 nm-thick CoN film electrolyte-gated at -25 V for 10 min. As shown in Fig. S1a and b, the as-prepared 200 nm-thick CoN films show a highly nanostructured morphology with homogeneous composition. As shown in Fig. S1b, upon gating at -25 V for 10 min, a well-defined interface between a N-free and highly porous Co top layer and the rest of unaltered CoN film can be observed both in the HAADF-STEM image and the EELS mappings, evidencing the existence of a planar N migration front in agreement with previous results¹¹.

As seen in Fig. S2, the $\theta/2\theta$ X-ray diffraction (XRD) pattern of an as-prepared 200 nm-thick CoN film reveals the presence of the (111) peak of CoN, indicating the growth of a textured phase. Upon subjecting a 200 nm-thick CoN film at -25 V for 15 min, the intensity of the (111) peak of CoN significantly decreases, in agreement with the denitriding caused but the transport of N ions towards the electrolyte.

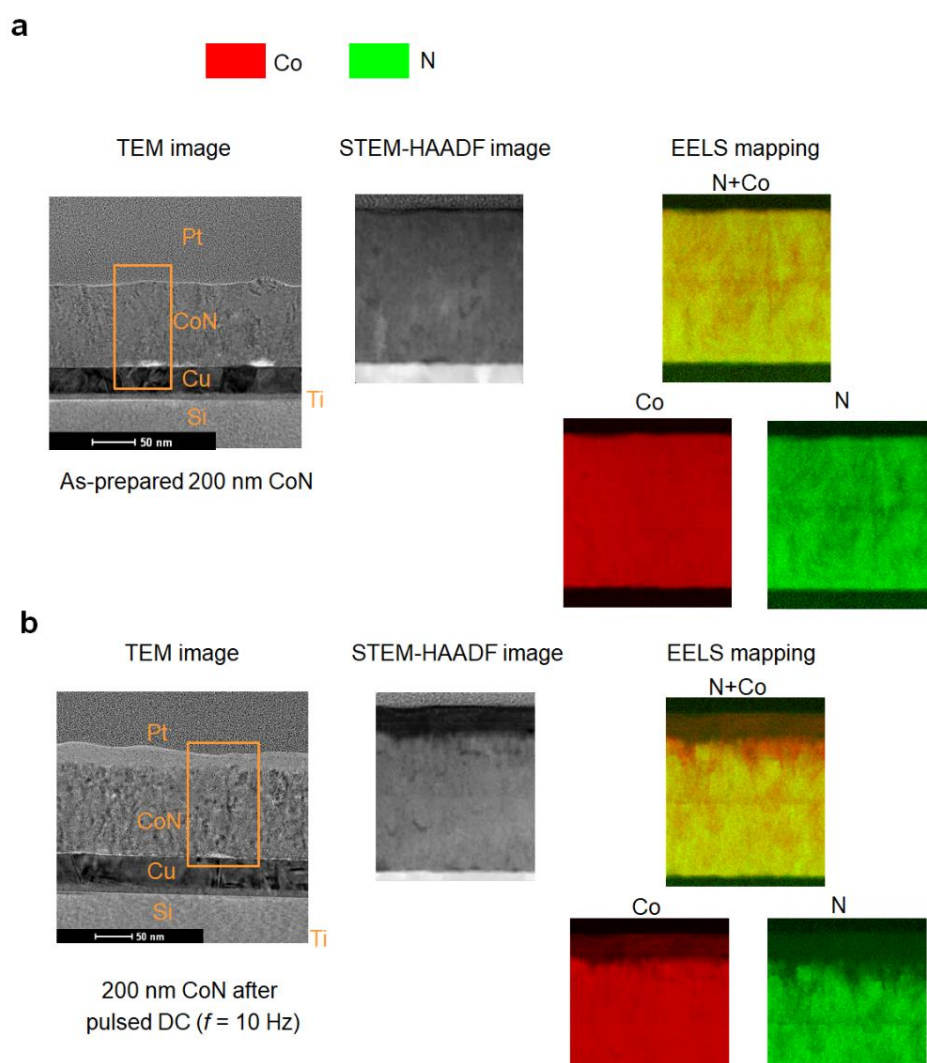


Fig. S1. Compositional characterization by high-angle annular dark-field scanning transmission electron microscopy (HAADF-STEM) and electron energy loss spectroscopy (EELS), and structural characterization by transmission electron microscopy (TEM). (a) TEM image of an as-prepared 200 nm-thick CoN film together with the HAADF-STEM image and corresponding Co and N EELS mappings of the area marked with a rectangle. (b) TEM image of a 200 nm-thick CoN film subjected to a -25 V for 600 s together with the HAADF-STEM image and corresponding Co and N EELS mappings of the area marked with a rectangle.

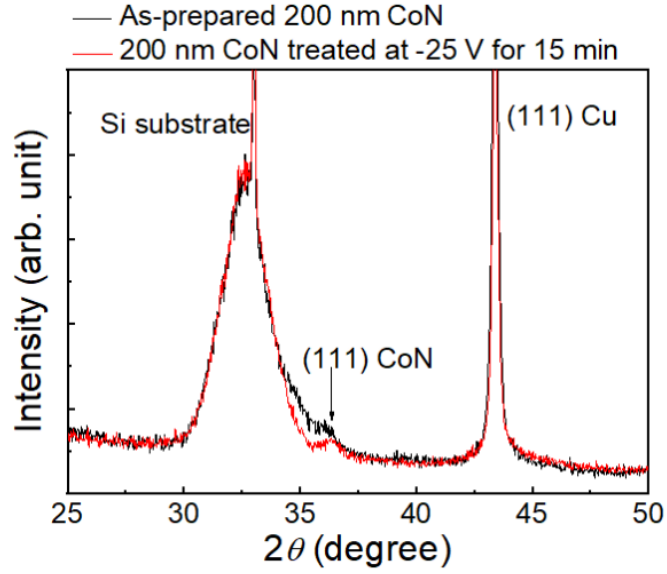


Fig. S2. Structural characterization by X-ray diffraction (XRD). $\theta/2\theta$ XRD diffraction patterns of an as-prepared 200 nm-thick CoN film and a 200 nm-thick CoN film after being treated at -25V for 15 min. For phase identification, the cards no. ICDD JCPDF 00-001-1241 and ICDD JCPDF 00-016-0116, were used for Cu and CoN, respectively.

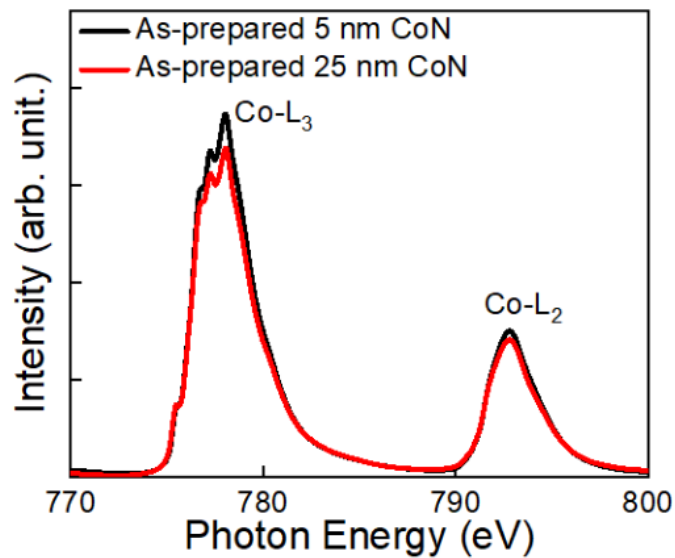


Fig. S3. Compositional characterization by X-ray absorption spectroscopy. Co L_{2,3}-edge X-ray absorption spectroscopy measurements of the 5 nm- and 25 nm-thick CoN films.

Magneto-ionic characterization

Fig. S4 shows the hysteresis loops of CoN films with thickness ranging from 5 to 200 nm, sequentially recorded while electrolyte-gated at -25 V until reaching a stable state. The as-prepared CoN-based heterostructures exhibit some traces of ferromagnetic signal (< 10 emu cm^{-3}), which could be ascribed to local deviations of CoN stoichiometry at the Cu-CoN interface.

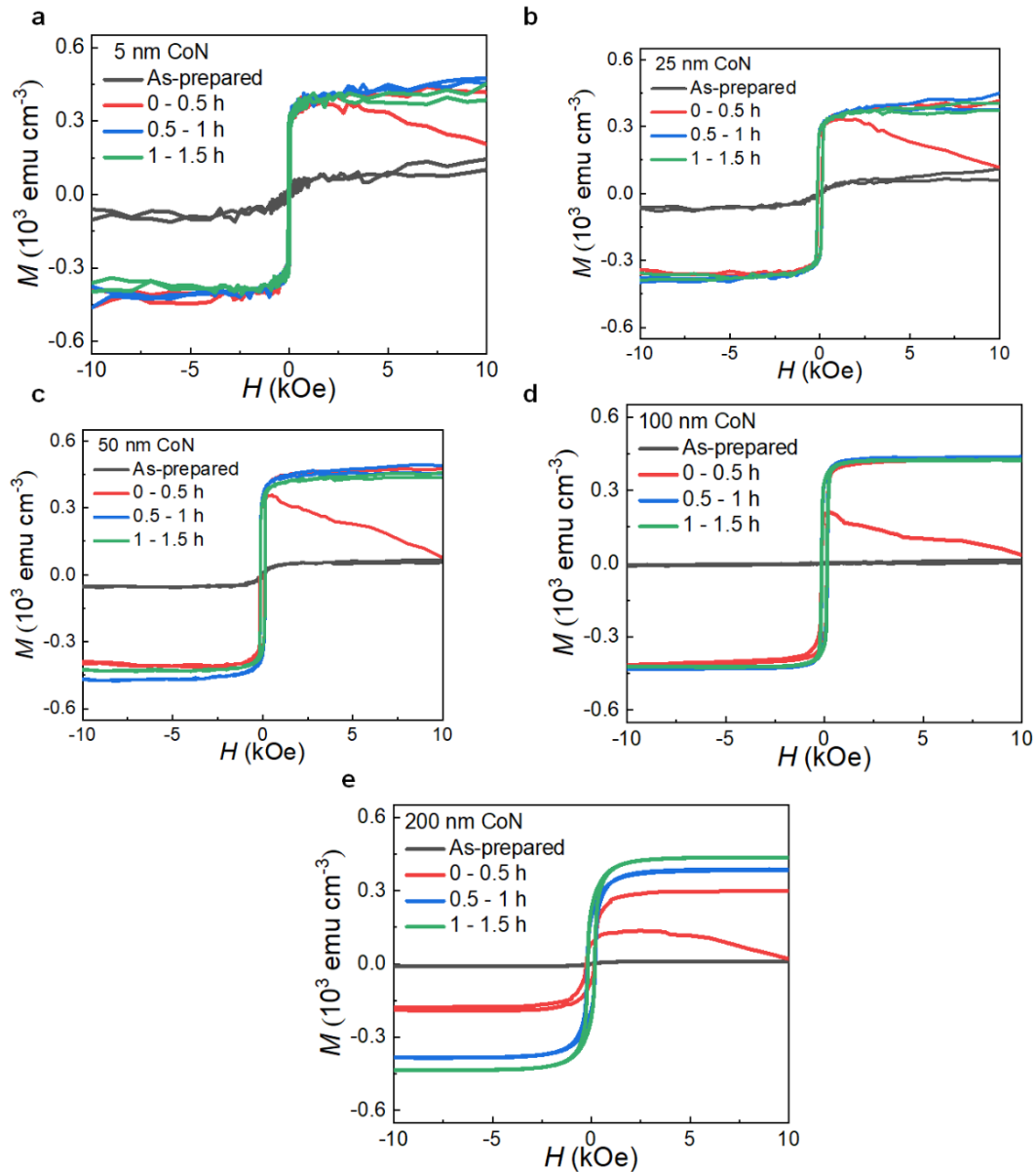


Fig. S4. Consecutive in-plane VSM hysteresis loops (each lasting 30 min) of the as-prepared film (black) and the films biased under -25 V: **a**, 5 nm, **b**, 25 nm, **c**, 50 nm, **d**, 100 nm, and **e**, 200 nm CoN films.

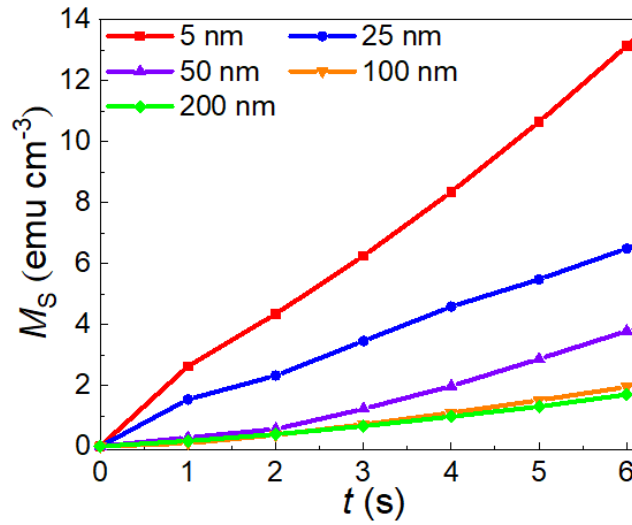


Fig. S5. Zoom of Fig. 1c in initial stages to highlight the generation of magnetization. Saturation magnetization (M_S) as a function of time t from 0 to 6 s for a CoN films with thickness ranging from 5 to 200 nm under electrolyte-gating at -25 V while applying an external in-plane magnetic field of 10 kOe.

Table S1. Thickness-dependent magnetic and magnetoelectric parameters obtained from the consecutive hysteresis loops presented in Fig. S4 and M_S vs. t plots of Fig. S5.

Thickness (nm)	ΔM ($H = 10$ kOe) (emu cm^{-3}) upon -25 V for 1 s	ΔM ($H = 10$ kOe) (10^3 emu cm^{-3}) upon -25 V for 50 s	ΔM ($H = 10$ kOe) (10^3 emu cm^{-3}) upon saturation [minimum time required to reach a stable M_S]	H_C (Oe)
5	2.6	0.235	0.297 [60 s]	35
25	1.5	0.132	0.305 [130 s]	132
50	0.3	0.068	0.379 [< 1 h]	132
100	0.1	0.040	0.423 [< 1 h]	143
200	0.1	0.037	0.507 [12 h]	179

Table S2. M_S attained once magneto-ionic process saturates (*i.e.*, maximum value), normalized by the time required to reach it (Δt) and by the absolute value of the applied voltage ($|\Delta V|$), from the current results and previous related works from the literature^{3,11-14,17}

Film	85 nm-thick Co ₃ O ₄ film	85 nm-thick CoN film	85 nm-thick FeN film	5 nm-thick Co ₃ O ₄ film	30 nm-thick CoMnN film	5 nm-thick CoN film (current work)
$M_S/(\Delta t \Delta V)$ (emu cm ⁻³ h ⁻¹ V ⁻¹)	7.8	52.0	7.2	32.0	64.5	432.0

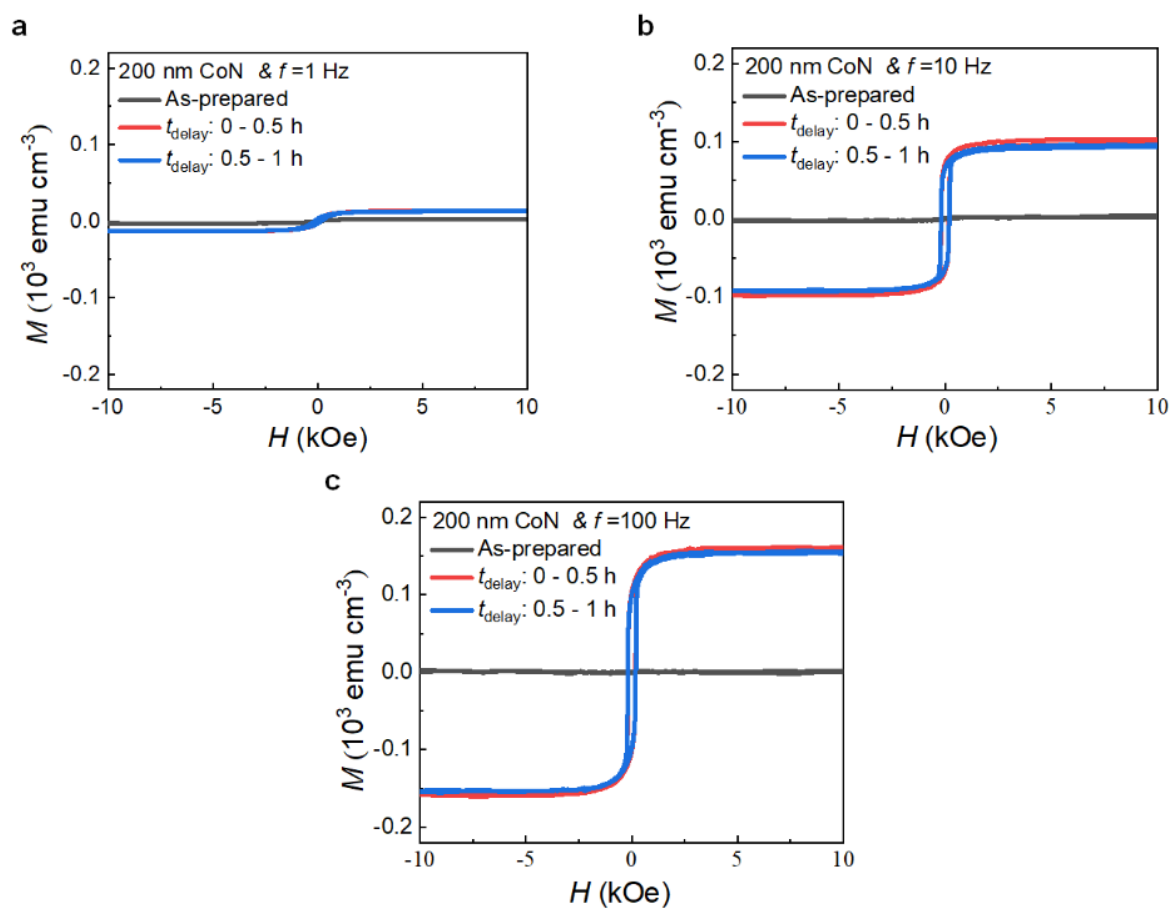


Fig. S6. In-plane vibrating sample magnetometry hysteresis loops (each lasting 30 min) of an as-prepared 200 nm CoN thin film and a 200 nm CoN film subjected to pulsed DC voltage

actuation for 0.5 and 1h at a frequency of (a) 1 Hz, (b) 10 Hz and (c) 100 Hz. Note that t_{delay} refers to the time after the voltage has been switched off.

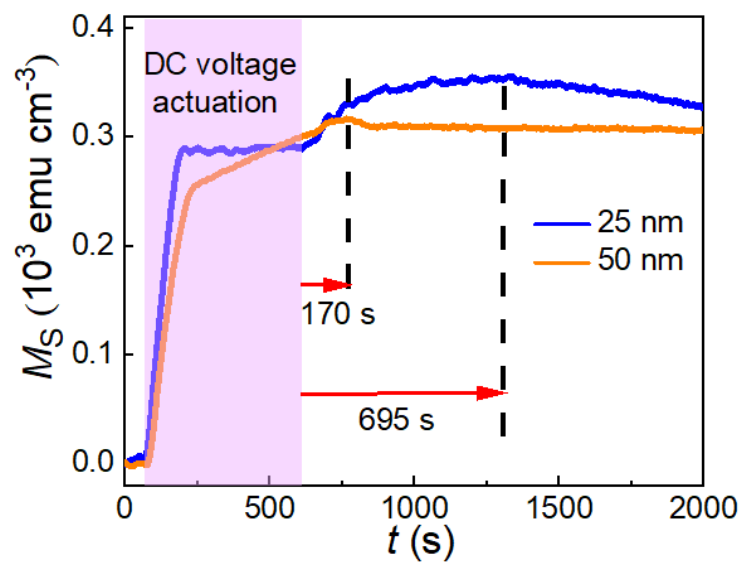


Fig. S7. Time evolution of the saturation magnetization (M_S vs. t) during and after DC voltage actuation at -25V for 20 nm and 50 nm thick CoN films. Dashed lines mark the start of magnetization turning point.

3.2 From binary to ternary transition-metal nitrides: a boost toward nitrogen magneto-ionics

Zhengwei Tan^a, Sofia Martins^a, Michael Escobar^a, Julius de Rojas^{a,b}, Fatima Ibrahim^c, Mairbek Chshiev^{c,d}, Alberto Quintana^e, Aitor Lopeandia^{a,f}, José L. Costa-Krämer^g, Enric Menéndez*^a and Jordi Sort*^{a,h}

^aDepartament de Física, Universitat Autònoma de Barcelona, E-08193 Cerdanyola del Vallès, Spain.

^bDepartment of Physics, Durham University, South Rd., Durham DH1 3LE, United Kingdom

^cUniversity of Grenoble Alpes, CEA, CNRS, Grenoble 38000, France

^dInstitut Universitaire de France, 75231 Paris, France

^eInstitut de Ciència de Materials de Barcelona (ICMAB-CSIC), Campus UAB, Bellaterra, E-08193 Barcelona, Spain.

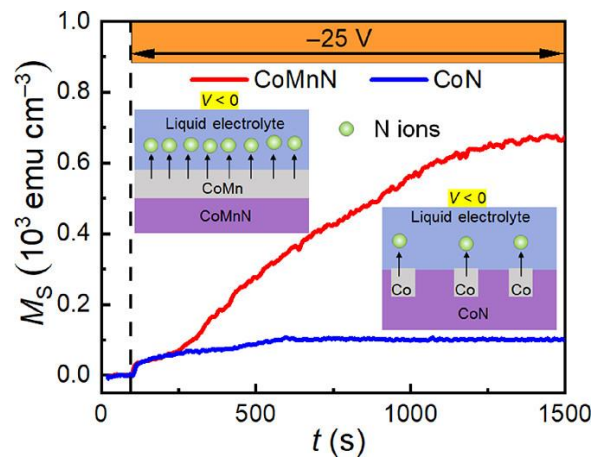
^fCatalan Institute of Nanoscience and Nanotechnology (ICN2), CSIC and BIST, Campus UAB, Cerdanyola del Vallès, E-08193 Barcelona, Spain.

^gIMN-Instituto de Micro y Nanotecnología (CNM-CSIC), Isaac Newton 8, PTM, 28760 Tres Cantos, Madrid, Spain.

^hInstitució Catalana de Recerca i Estudis Avançats (ICREA), Pg. Lluís Companys 23, E-08010 Barcelona, Spain.

The previous study proposed an approach for post-stimulated magneto-ionic control, promising new neuromorphic computing functions, such as post-stimulated neural learning under deep sleep. This magneto-ionic effect largely relies on the strength and penetration of the induced electric field into the target material, the amount of generated ion transport pathways, and the ionic mobility inside the magnetic media. Yet, optimizing all these factors in a simple manner presents a formidable challenge, despite its strong desirability for practical applications.

In this work, we demonstrate that strategically introducing transition-metal elements into binary nitride compounds can unveil a significant advancement in magneto-ionics. More specifically, we showcase the remarkable enhancement of magneto-ionic effects within CoN films, including saturation magnetization, toggling speeds, and cyclability, achieved through a mere 10 at. % substitution of Co with Mn during the thin-film deposition. This introduction of Mn triggers a transformation from nanocrystalline to amorphous-like structures, as well as from metallic to semiconducting behaviors, resulting in an increase in N-ion transport channels. Ab initio calculations further reveal a lowered energy barrier for CoMn-N compared to Co-N that provides a fundamental understanding of the crucial role of Mn addition in the voltage-driven magnetic effects. These results constitute an important step forward toward enhanced voltage control of magnetism via electric field-driven ion motion.



From Binary to Ternary Transition-Metal Nitrides: A Boost toward Nitrogen Magneto-Ionics

Zhengwei Tan, Sofia Martins, Michael Escobar, Julius de Rojas, Fatima Ibrahim, Mairbek Chshiev, Alberto Quintana, Aitor Lopeandia, José L. Costa-Krämer, Enric Menéndez,* and Jordi Sort*

Cite This: *ACS Appl. Mater. Interfaces* 2022, 14, 44581–44590

Read Online

ACCESS |

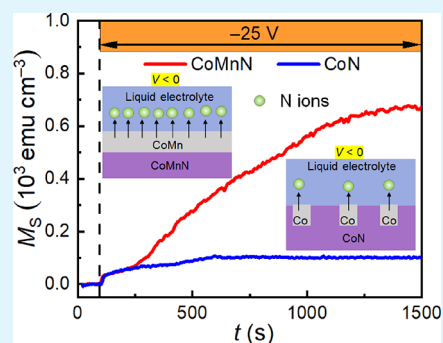
Metrics & More

Article Recommendations

Supporting Information

ABSTRACT: Magneto-ionics is an emerging actuation mechanism to control the magnetic properties of materials *via* voltage-driven ion motion. This effect largely relies on the strength and penetration of the induced electric field into the target material, the amount of generated ion transport pathways, and the ionic mobility inside the magnetic media. Optimizing all these factors in a simple way is a huge challenge, although highly desirable for technological applications. Here, we demonstrate that the introduction of suitable transition-metal elements to binary nitride compounds can drastically boost magneto-ionics. More specifically, we show that the attained magneto-ionic effects in CoN films (*i.e.*, saturation magnetization, toggling speeds, and cyclability) can be drastically enhanced through 10% substitution of Co by Mn in the thin-film composition. Incorporation of Mn leads to transformation from nanocrystalline into amorphous-like structures, as well as from metallic to semiconducting behaviors, resulting in an increase of N-ion transport channels. *Ab initio* calculations reveal a lower energy barrier for CoMn–N compared to Co–N that provides a fundamental understanding of the crucial role of Mn addition in the voltage-driven magnetic effects. These results constitute an important step forward toward enhanced voltage control of magnetism *via* electric field-driven ion motion.

KEYWORDS: *magnetolectricity, voltage control of magnetism (VCM), magneto-ionics, transition metal nitride, ion diffusion*



INTRODUCTION

The intentional incorporation of impurities into a host material, a process known as element substitution,¹ is of fundamental significance in reconstructing nanocrystals,² modifying electronic characteristics,³ or modulating magnetism,^{4,5} among others. Controlled element introduction has been proved effective in yielding semiconductor-based hybrid materials with desirable properties for target applications, such as solar cells,⁶ batteries,⁷ novel transistors,^{8,9} superconductors,¹⁰ or spintronics devices.^{4,5,11,12} Recently, unprecedented control of magnetic properties (including “ON–OFF” switching of ferromagnetic states¹³) has been realized using magneto-ionic actuation.¹⁴ This is an emerging energy-efficient approach to tune magnetism based on electric field-induced ions (*e.g.*, O²⁻,^{13–17} Li⁺,¹⁸ F⁻,¹⁹ H⁺,^{20–22} or N^{3–23–25}) motion. However, element introduction in magneto-ionic systems, that may allow for further engineering of magnetic properties with voltage, is still unexplored.

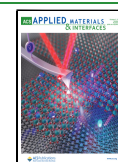
A typical magneto-ionic system comprises the target material, usually a ferromagnetic (FM) metal or an oxide,²⁶ and a solid or liquid electrolyte (adjacent to the target material), working as dielectric and ion reservoir layers. One of the most studied systems is Co/GdOx, in which control of the perpendicular magnetic anisotropy through voltage-driven oxygen migration has been demonstrated.¹⁴ One problem

with O²⁻ transport-based magneto-ionics at room temperature is its poor endurance, owing to slow and irreversible chemical/structural changes that occur when voltage polarity is reversed.¹⁵ Smaller ions, such as H⁺, F⁻, or Li⁺, have been utilized to achieve faster and more cyclable voltage-induced changes of the magnetic properties. However, these systems pose some limitations in terms of compatibility with traditional complementary metal-oxide semiconductor (CMOS)-based devices.²⁷ Alternatively, nitrogen magneto-ionics have been demonstrated by using a cobalt nitride target material (*i.e.*, CoN²³), which provides “ready-prepared” lattice sites for ionic diffusion, leading to improved endurance at room temperature, without sacrificing operating speed and compatibility. In addition, the microstructure of the magneto-ionic target materials play an important role in the attained values of resistivity and ion transport mechanisms, resulting in a planar-like migration front for ions,^{24,25} that is highly appealing for devices when compared to traditional inhomogeneous or

Received: July 18, 2022

Accepted: September 13, 2022

Published: September 21, 2022



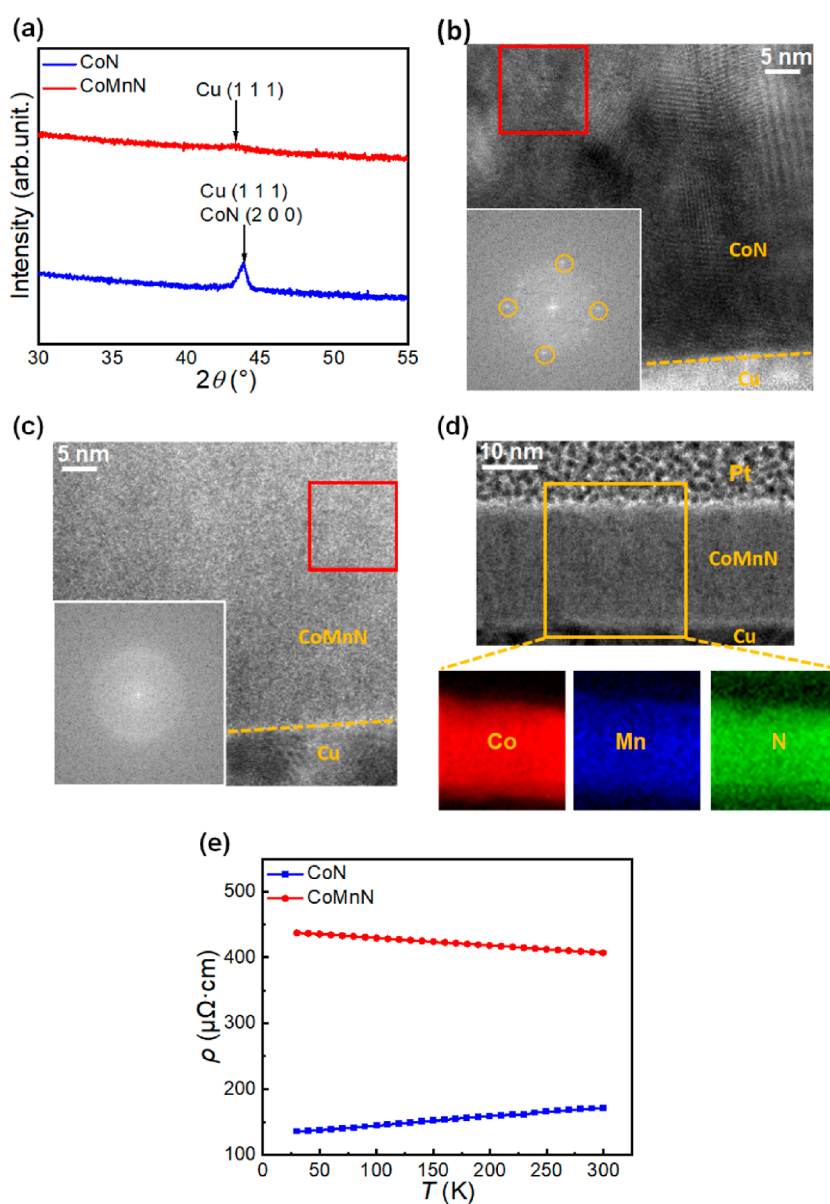


Figure 1. Structural, compositional, and electric transport characterization of as-deposited films. (a) $\theta/2\theta$ XRD patterns of the as-prepared 100 nm thick CoN and CoMnN films. (b,c) High-resolution TEM images of the cross section of 30 nm thick CoN and CoMnN films. The inset shows the fast Fourier transform of the area marked with a red square. (d) HAADF-STEM micrograph and EELS Co, Mn, and N elemental mappings for as-prepared 30 nm thick CoMnN films. (e) Electrical resistivity (ρ) measured as a function of temperature from 30 to 300 K, for as-deposited 30 nm thick CoN and CoMnN films.

cross-sectional ion diffusion channels typically occurring upon O^{2-} -ion migration.^{13,16} Magneto-ionics is essentially a dynamic process,¹⁷ which involves breaking and recombining metal-O or metal-N bonds. This approach requires an effective electric field to drive the process, as well as properly tuned magnetic materials to be modulated.²⁸ Although ferromagnetic metals show large and stable magnetization, high T_C , and, eventually, a well-defined perpendicular magnetic anisotropy,²⁹ their direct utilization for magneto-ionics also poses some drawbacks. Among those is the limited electric-field screening length stemming from their high electric conductivity, which means that the effects of voltage are strongly limited to the outer surface of the metal.³⁰ This limitation can be overcome, to some extent, using semiconductors instead of metals.²⁹ Thus, if semiconducting properties could be imparted to target materials without sacrificing their magnetic properties,

magneto-ionics performance may be potentially boosted. To achieve this goal, introduction of certain elements leading to precise structural and compositional engineering at the nanoscale, together with highly tunable magnetic and electrical properties, may turn out to be a suitable strategy. Finding a suitable element and introducing it in a controlled manner into a host FM target material is thus critical. In metallic alloys, efforts have been made to substitute Co, Ni, or Fe by Mn as an effective means to alter their magnetic and electrical behavior.^{31–34} In magneto-ionics, Mn introduction may also give specific advantages. First, Mn, as an “amorphizing” agent,³⁵ could favor the formation of an amorphous phase, which would promote planar-like diffusion fronts for ion motion (because, otherwise, ion motion preferentially occurs along grain boundaries). Also, Mn-substitution could introduce more defects in the crystal lattice and increase electrical

resistivity, possibly leading to the modification of electrical properties, from metallic-like to semi-metallic or semiconducting behavior.³³ Incorporation of Mn may trigger hopping mechanisms and hence change the transport properties, as studied in earlier cobalt ferrite systems.^{33,34} Most importantly, the enhancement of saturation magnetization and perpendicular magnetic anisotropy of host FM target materials with moderate Mn introduction has also been confirmed both from experimental and theoretical studies.^{36–38} Therefore, introducing Mn into FM nitrides (e.g., CoN) might result in synergetic effects and could make magneto-ionics more attractive for spin-based and other magnetoelectric devices.

In this work, we show multiple benefits that moderate substitution of Co by Mn brings to the magneto-ionic performance of CoN-based heterostructures. With the addition of Mn, a change from nanocrystalline to amorphous structures is observed, accompanied by a transition from metallic-like to semiconducting properties. The former increases N-ion transport channels, as verified by high-angle annular dark-field scanning transmission electron microscopy (HAADF-STEM) and electron energy loss spectroscopy (EELS). The latter significantly extends the electric field effect that is normally limited to a few Å in metals.³⁰ Mn incorporation leads to a 6.7-fold voltage-driven enhancement of the saturation magnetization (M_S) and improved high-frequency cyclability. In addition, *ab initio* calculations have been performed to estimate the Co–N and CoMn–N energy barriers using different crystal orientations and N atom insertion paths. In all cases, a reduced energy barrier for CoMnN is obtained, compared to CoN. These experimental and theoretical findings prove the highly beneficial effect of Mn-substitution in enhancing magneto-ionics. These results could have implications in diverse technological areas, like neuromorphics^{39,40} or iontronics in general.

RESULTS AND DISCUSSION

Cobalt nitride (CoN) and cobalt manganese nitride ($\text{Co}_{0.9}\text{Mn}_{0.1}\text{N}$, identified as CoMnN throughout the text), both 30 or 100 nm thick, were grown on Cu (10 nm)/Ti (10 nm)/[100]-oriented Si substrates by reactive magnetron sputtering (see the [Methods](#) section).

[Figure 1a](#) shows the X-ray diffraction (XRD) patterns of 100 nm thick CoN and CoMnN films. A single diffraction peak is observed for the CoN film at a $2\theta \approx 43.84^\circ$, which is consistent with both (111) Cu (JCPDF card no. 00-001-1241) or expanded (200) CoN (JCPDF card no. 00-016-0116) phases. In contrast to CoN, the CoMnN film does not show such well-defined peaks but only a broad and weak peak centered at $2\theta \approx 43.28^\circ$, which is also consistent with (111) Cu or expanded (200) CoMnN. However, CoMnN clearly exhibits a much lower crystallite size value, evidencing the nanostructuring effect caused by Mn. Because the nitride films are 10 times thicker than the Cu buffer layer, the signal arising from both patterns is mainly attributed to the CoN and CoMnN phases. Both films are textured along (200) planes and nanocrystalline. In the case of the CoMnN, the degree of nanostructuring is more pronounced, approaching a highly disordered (eventually amorphous-like) structure.

This result is confirmed by high-resolution transmission electron microscopy (HRTEM) images of the cross-sections of as-prepared CoN and CoMnN films, as demonstrated in [Figure 1b,c](#), respectively. The areas marked with red squares were chosen for fast Fourier transform (FFT) analyses, as

shown in the insets, in which clear diffraction spots can be found for CoN films [points inside yellow circles, corresponding to an interplanar distance $d = 2.13 \text{ \AA}$, consistent with a cubic CoN (200) orientation], whereas no spot is observed for CoMnN films, in agreement with XRD results and evidencing the role of Mn as a “amorphizing” agent.³⁵ To further understand the compositional distribution of CoMnN films, HAADF-STEM and EELS were performed on as-deposited CoMnN films, with corresponding mappings shown in [Figure 1d](#). The Co (red), Mn (blue), and N (green) elements are all uniformly distributed in the films, evidencing the homogeneous growth process of CoMnN. An amorphous or very nanocrystalline structure should promote the formation of a larger density of ion diffusion channels under the application of an applied voltage, compared to a well-crystallized structure with limited amounts of grain boundaries, eventually allowing for a greater modulation of magnetic properties with an electric field.^{23,24}

To investigate the role of Mn on electric transport, resistivity (ρ) as a function of temperature (T , in the range 30–300 K) was measured on both as-prepared CoN and CoMnN films. As seen in [Figure 1e](#), the resistivity at room temperature (300 K) is approximately $172 \mu\Omega \text{ cm}$ for CoN films (the value is close to that of metallic Co⁴¹ and previously reported less-stoichiometric Co-rich CoN films prepared by a triode system²⁵) and about $406 \mu\Omega \text{ cm}$ for CoMnN films. Moreover, the resistivity of CoN is observed to monotonically increase ($d\rho/dT > 0$) throughout the whole measured temperature range, which is consistent with metallic behavior.⁴² This metallic behavior has also been reported in other transition-metal nitrides,⁴³ and it is attributed to some degree of wavefunction overlap. In CoN, electrons are localized and there is a little overlap between the wavefunction of ions situated on adjacent sites.⁴⁴ In contrast, the CoMnN films show a monotonic decrease ($d\rho/dT < 0$), corresponding to semiconducting behavior,⁴⁵ due to the increase in drift mobility of charge carriers at higher temperatures. This result demonstrates that partial substitution of Co by Mn not only increases the resistivity but also turns the film semiconductor. In addition, the variation of carrier densities (n/p) as a function of temperature for CoMnN ([Figure S1](#)) reveals an overall negative value (by convention meaning predominant electron transport, as opposed to positive when holes would dominate), hence showing that introducing Mn makes electrons the dominant charge carriers while changing the behavior from metallic-like to semiconductor ([Figure 1d](#)). Additionally, the resistivities of N-free Co and CoMn films ($\text{Co}_{0.9}\text{Mn}_{0.1}$) were measured to be 100 and $470 \mu\Omega \text{ cm}$, respectively. Thus, Mn incorporation increases ρ both for N-free and the nitride films. While the introduction of Mn plays a role like increasing the nitrogen concentration in the films in terms of electrical properties, the interplay between nitrogen content and defects on resistivity still remains to be fully elucidated. Namely, the degree of bonding with nitrogen, effects of variable amounts of introduced Mn, possible charge compensation effects and impurity scattering in these polycrystalline films need to be further studied. Anyhow, the increased resistivity and thus the change of electric behavior from metallic to semiconducting achieved by the addition of Mn enables a deeper penetration of the electric field ([Figure S2](#)), up to few tens of nm,²⁵ enhancing magneto-ionic effects, as will be shown below.

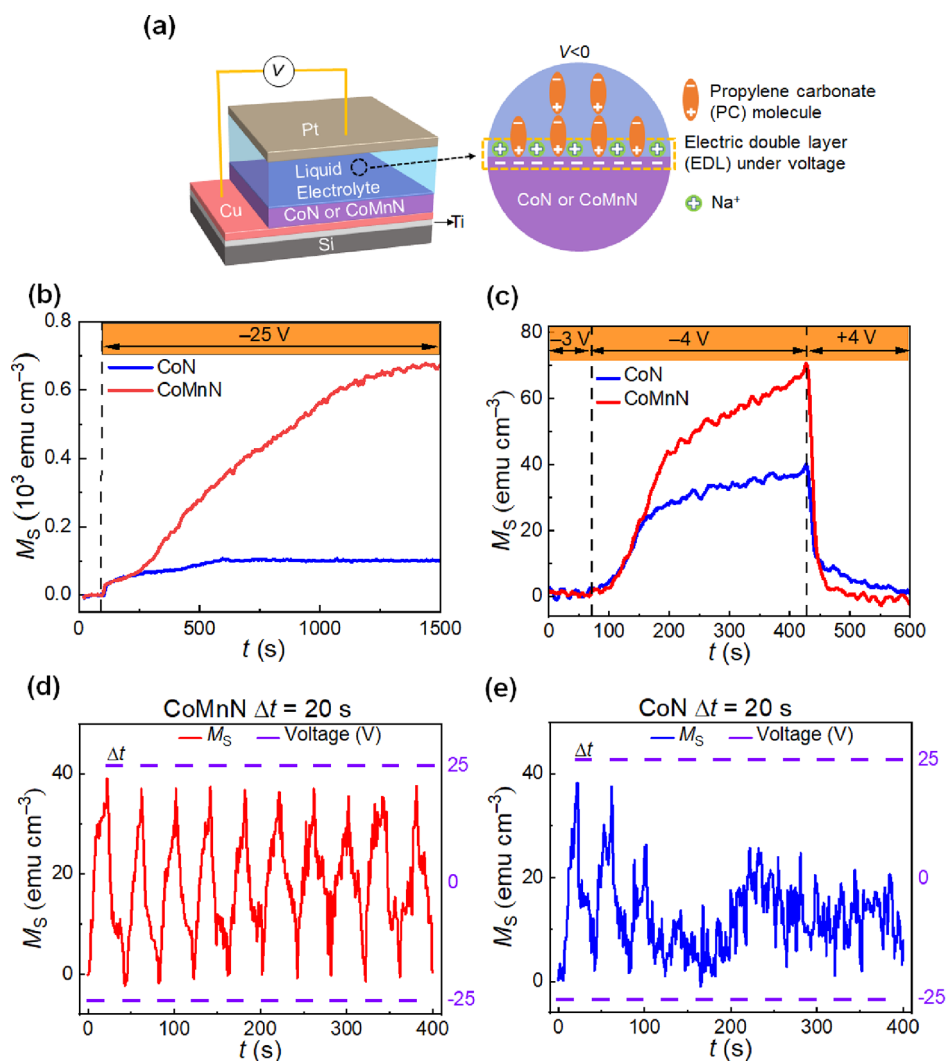


Figure 2. Magneto-ionic characterization of 30 nm thick CoN and CoMnN films under electrolyte gating. (a) Schematic of the designed structure for electrolyte actuation (left) and sketch of the formation of electric double layer during voltage actuation (right). (b) Time (t) evolution of the saturation magnetization M_S for CoN and CoMnN films under -25 V . (c) t evolution of M_S when the voltage is monotonically increased in steps of -1 V to determine the onset voltage required to trigger magneto-ionics in CoN and CoMnN films. (d,e) Magneto-ionic cyclability of the CoMnN and CoN films subjected to $-25 \text{ V}/+25 \text{ V}$ voltage pulses applied with a periodicity of 20 s.

To investigate the effect of Mn introduction on the magneto-ionic performance, both 30 nm thick CoN and CoMnN thin films were electrolyte-gated in a capacitor-like configuration using a Pt wire as the counter electrode, while performing in-plane magnetic measurements by vibrating sample magnetometry (VSM) at room temperature. Propylene carbonate with Na^+ - and OH^- -solvated species was employed as an aprotic, anhydrous polar liquid electrolyte to serve as a nitrogen-ion reservoir^{25–25} and to apply a uniformly distributed, out-of-plane electric field through the formation of an electric double layer (EDL)^{30,46} at the films' upper surface (as shown in Figure 2a).

As seen in Figure S3a, the as-prepared CoN sample exhibits some traces of ferromagnetic signal ($<21 \text{ emu cm}^{-3}$, which is equivalent to $\approx 1.5\%$ the magnetization of pure Co⁴⁷), whereas the as-prepared CoMnN sample shows a virtually paramagnetic behavior ($<3 \text{ emu cm}^{-3}$). This reduction of residual ferromagnetism in the as-prepared sample by addition of Mn is possibly the result of the reported difference of cohesive energy between Mn–N and Cu–N ($\approx 1.17 \text{ eV/atom}$) being smaller than that between Co–N and Cu–N ($\approx 2.01 \text{ eV/atom}$).⁴⁸

This means that the tendency to form off-stoichiometric regions (*i.e.*, Co-rich CoN clusters) near the CoN/Cu(N) interface is slightly larger than for CoMnN/Cu(N).

Figure 2b shows the variation of M_S of CoN and CoMnN films as a function of time (t) during electrolyte gating at -25 V , while an external magnetic field of 10 kOe (above the anisotropy field of the generated ferromagnetic counterpart) was applied to ensure magnetic saturation. In response to the applied voltage, an immediate increase of M_S is observed in both CoN and CoMnN films, indicating a quick onset for nitrogen motion, resulting in the appearance of metallic Co(Mn) ferromagnetic phase.²³ Interestingly, while CoN and CoMnN show similar increasing trends of M_S during the initial stages of voltage actuation (*i.e.*, the first 150 s), M_S subsequently levels off for CoN films but continues to increase in CoMnN films before reaching a stable value for times close to 1500 s. As a result, a 6.7-fold enhancement in the obtained steady-state value of M_S is achieved in voltage-actuated CoMnN compared to CoN, from 102 to 672 emu cm^{-3} , respectively (in agreement with the magnetic hysteresis loops shown in Figure S3b,c). Note that, as reported earlier,^{37,38} M_S

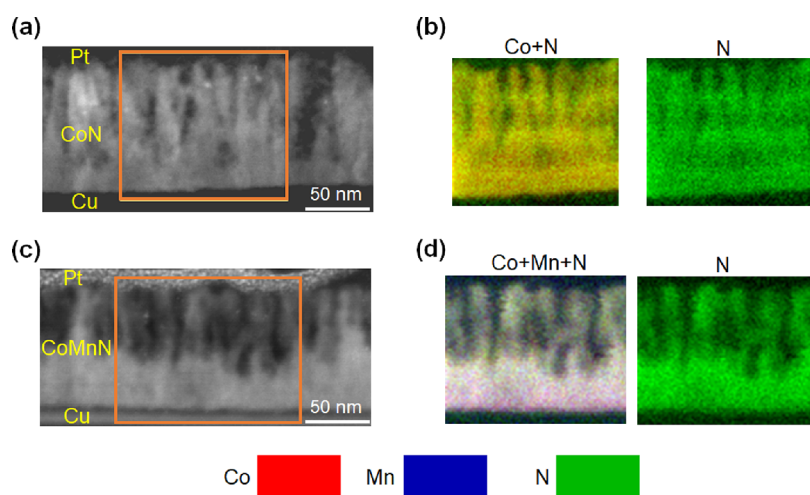


Figure 3. Compositional characterization by HAADF-STEM and EELS of the magnetoelectrically actuated films. HAADF-STEM and elemental EELS mappings corresponding to areas marked in orange for 100 nm thick (a,b) CoN and (c,d) CoMnN films gated at -25 V for 40 min, respectively. Cu and Pt layers serve as working electrodes and protective capping layer for lamellae preparation, respectively. Colors corresponding to each element are noted at the bottom of the figure, that is, Co, Mn, and N are represented by red, blue, and green colors in the EELS elemental mappings, respectively.

for CoMn is slightly larger than for pure Co (Figure S3d), but this fact by itself alone cannot explain the obvious magneto-ionic enhancement of M_S observed in their nitrides and demonstrates that Mn-substitution boosts magneto-ionics by some other mechanisms, for example, the dissimilar resistivity variations during the denitriding processes in CoN and CoMnN films. With the goal to investigate the eventual influence of the growing method and to be able to compare with previously reported results, 85 nm thick CoN and CoMnN films were also grown by triode sputtering. This is the thickness of the CoN films investigated in our previous works.^{23–25} As shown in Figure S4, the incorporation of Mn also results in a larger generation of magnetization analogously to what happens when comparing the magneto-ionic response of CoN and CoMnN films grown by magnetron sputtering (Figure 2b). It is remarkable that, even though the films grown by triode sputtering are thicker than those prepared by magnetron sputtering (85 nm vs 30 nm, respectively), larger magnetization values are attained upon voltage applications in films grown by triode sputtering, both in the CoN and CoMnN systems. This suggests the importance of a more nanocrystalline microstructure obtained by triode sputtering in the enhanced nitrogen-ion motion due typically to a larger defect size and density. In any case, our results confirm the role of Mn as an “amorphizing” agent in improving magneto-ionics, regardless of the growing method.

The minimum threshold voltage required to trigger magneto-ionic effects is of large importance for device implementation.²⁴ Thus, the onset voltages were also evaluated in both systems by monotonically increasing the external voltage in steps of -1 V until M_S started to increase, as shown in Figure 2c. The obtained results reveal that the onset voltage is approximately -4 V for both CoN and CoMnN films. Figure 2c also shows that, in spite of a larger M_S , the recovery time for CoMnN films is significantly shorter than for CoN films, thereby a better endurance in the case of CoMnN films is envisaged. Taking this into account, the cyclability was investigated by subjecting the CoN and CoMnN films to -25 V/ $+25$ V pulses with a periodicity of 20 s. As shown in Figure 2d, a very stable and reversible cycling behavior for

CoMnN is obtained, whereas no signs of magneto-ionic effects are continued after two cycles for CoN films (Figure 2e). Nonetheless, for longer pulse duration (with voltage switched every 2 min), CoN films show a relatively stable cyclability as well (Figure S3e). This demonstrates that Mn-substitution is not only favorable to enhance the magneto-ionic rates or the attained M_S values but also the cyclability (or endurance) through improvement of the recovery process.

To further understand the effect of Mn substitution from the perspective of voltage-driven ion transport, cross-sectional lamellae of 100 nm thick CoN and CoMnN films electrolyte-gated at -25 V for 40 min were studied by HAADF-STEM and EELS. As shown in Figure 3a, a moderate denitriding process occurs in CoN, which results in sparse, cross-sectional (*i.e.*, perpendicular-to-film) channels after nitrogen-ion diffusion has taken place, similar to what was reported in other magneto-ionic systems like Co_3O_4 also grown by magnetron sputtering.^{13,16} This columnar morphology suggests that N-ion motion takes place, at least to some extent, along these channels generated perpendicular to the film plane during voltage applications. As shown in Figure 3b, EELS mappings reveal a lack of N and depletion of Co in the channels, in accordance with the formation nanoporosity in the films (in the form of elongated vertical pore channels of 5–10 nm in width). The formation of these channels in the upper part of the films is even more evident for the magneto-ionically treated CoMnN films (see Figure 3c,d). The formation of such channels can have an influence on both the electric properties (electronic hopping) as well as the time-dependence evolution of magneto-ionic effects, although it is quite difficult to establish the exact current flow paths in this kind of nanocrystalline materials. Remarkably, in this case, a planar horizontal front, separating porous and denser areas, is observed. The occurrence of such planar diffusion fronts was previously reported in CoN films grown by triode sputtering (not by magnetron sputtering as in the current work) exhibiting a highly nanocrystalline microstructure and larger generated magnetization.^{23,24} Remarkably, the presence of metallic Co was confirmed by the fast Fourier transform (FFT) spots obtained from high-resolution TEM, as shown in Figure

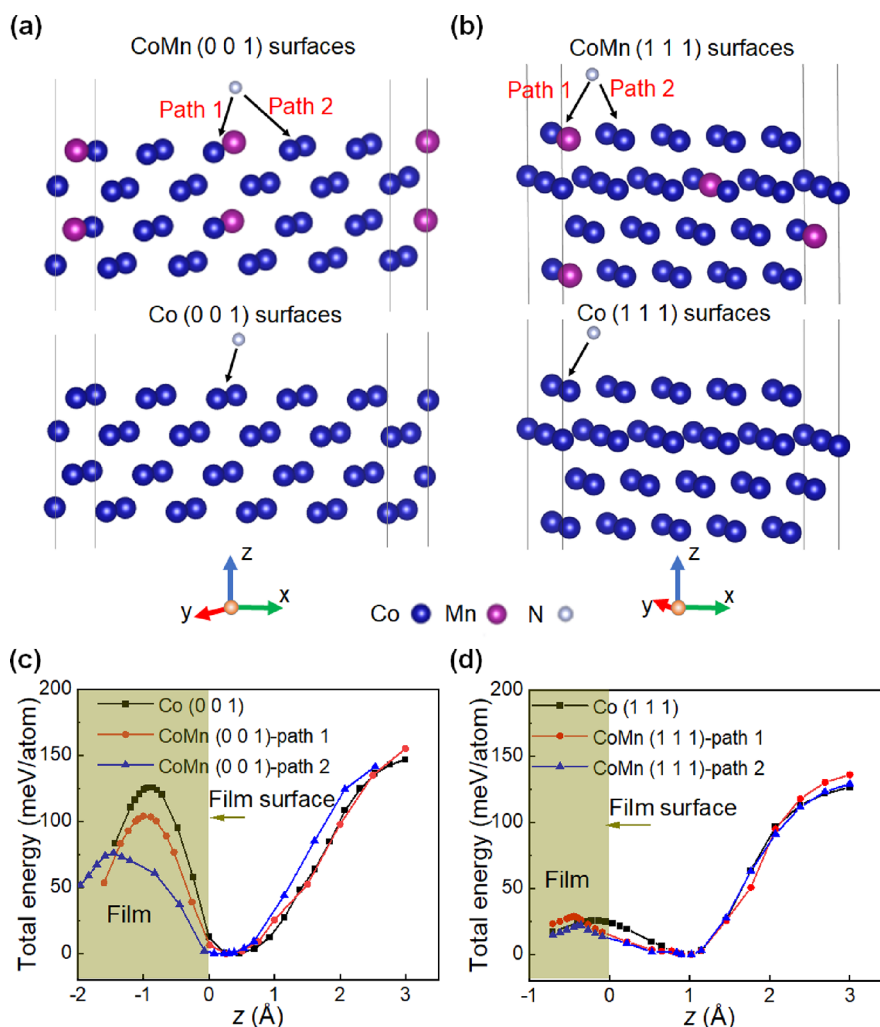


Figure 4. *Ab initio* calculations of Co–N and CoMn–N energy barriers. Schematic of (a) CoMn and Co (001) surfaces and (b) CoMnN and CoN (111) surfaces, respectively, designed for N-atom insertion. For CoMnN surfaces, both Co–Mn path (path 1) and Co–Co path (path 2) have been considered. (c,d) Total energy per atom as a function of distance for the aforementioned surfaces. The total energy is plotted relative to the minimum energy values, as a function of the displacement between the reference CoMn or Co outermost surface atom and the inserted N atom.

S5, which is responsible for the M_S increase after voltage treatment (Figure 2b). These observations are consistent with vertical and horizontal line profiles of the N element, as shown in Figure S6, which reveal an obvious difference in N content between the upper and bottom parts of the CoMnN films (in contrast to CoN, where the N concentration is more homogeneous). Additionally, the nanoporosity causes sudden jumps of the N content along the horizontal profiles for both CoN and CoMnN films. These results reveal that, under the same magnetoelectric actuation conditions, a larger amount of nitrogen is released to the electrolyte in CoMnN compared to CoN films. This agrees with Figure 2b,c, which show a larger increase of M_S in CoMnN. Overall, the HAADF-STEM and EELS observations on CoN and CoMnN films illustrate that Mn substitution significantly increases nitrogen transport channels, leading to an enhanced magneto-ionic behavior (thus explaining the shorter recovery time and the improved cyclability).

The efficiency of magneto-ionics initially depends on the minimum energy required for breaking and re-forming magnetic metal-ion bonds. Using the nudged elastic band method (NEB)^{49,50} (see the Methods section), the Co–N and CoMn–N energy barriers were calculated in a case where a

nitrogen ion is inserted into a cobalt or cobalt manganese surface with 10 atoms per layer (Figure 4a,b). Two orientations, (001) and (111), were considered and the total energies per atom were calculated as a function of the distance z between the inserted N atom and a Co or CoMn upper surface (see Figure 4c,d, respectively). Furthermore, for the case of CoMnN films, the formation energy of the N insertion into either Co–Mn (path 1) or Co–Co (path 2) were also calculated. The position $z = 0 \text{ \AA}$ refers to the outermost layer of Co or CoMn, while its negative sign represents the displacement inside of the film (and vice versa for the positive sign). For the Co (001) surface, CoMn (001) surface-path 1 and CoMn (001) surface-path 2, the local minimum (maximum) energies are located at around $z = 0.4$ (-1 \AA), 0.4 (-1 \AA), and 0.3 (-1.4 \AA), respectively, with corresponding energy barriers between the two extrema are calculated to be 126, 104, and 76 meV/atom. Further calculation shows that the energy barrier needed to be overcome by N is lower for the CoMn (001) surface (by 22 meV/atom for path 1 and 50 meV/atom for path 2) compared with the Co (001) surface. This reduction of energy barrier by Mn addition is consistent with the larger quantity of channels and nanoporosity due to N-ion movement observed in CoMnN compared to CoN

films, which brings about a larger M_S and faster recovery process (thus improved cyclability) for CoMnN films.

The results for the (111) surfaces, however, are more complex. When a N atom is introduced into the Co surface, the positions of local minimum and maximum energies are $z = 1.1$ and -0.1 Å, respectively, while the corresponding positions for the CoMn-path 1 case are $z = 1.1$ and -0.4 Å. In turn, the calculated energy barriers between the two extrema are 25.4 and 28.9 meV/atom for nitrogen displacement in Co and CoMn-path 1 structures, respectively. Note that we find a reduced barrier height for Co–N in the present study compared to ref 23. This is explained by the dependence of the energy barrier on the concentration of the inserted atoms into a surface. In ref 23, the ratio of N to Co atoms per surface layer was 1:1 and this implies the 100% concentration of N insertion into the surface, whereas here we have a supercell, which is laterally larger to simulate a 10% N insertion into the surface. When comparing Co and CoMn-path 1 structures, the minimum energy required by N to enter the CoMn (111) orientation is slightly larger than for Co (111). However, further energy barrier calculation for CoMnN-path 2 structure gives a value of 21.8 meV for (111) interfaces, which is lower than that obtained in case of path 1. Therefore, overall, the differences in energy barriers between Co and CoMn along this lattice orientation are less evident than along the (001) orientation, and they are path dependent. In fact, the considered N paths in the calculations are particular, while in the experiment not all N atoms have essentially the same path into the surface and thus a collective effect of perhaps several paths is observed. Also, it is instructive to comment on the difference in the positions of the minima/maxima in Figure 4c,d. We believe that it is caused by the different crystallographic orientations. For the (111)-oriented surface, the maximum energy is reached when the N atom is almost located in the first atomic surface layer. However, in the (001) surface, the maximum energy is found when the N atom is integrated more into the surface. In this case, it feels less comfortable due to smaller interlayer spacing to accommodate it, and thus the barrier is larger. Remarkably, these calculations show that the lattice orientation plays a key role in the observed variations in energy barriers upon Mn-substitution, which provides a valuable guide for precisely engineering magneto-ionics from a structural perspective.

CONCLUSIONS

In summary, here we demonstrate that magneto-ionic effects in CoN films are drastically enhanced by the introduction of Mn (in low percentages) to the binary composition of the transition metal nitride. Such enhancement is ascribed to the key role of Mn in modifying the microstructure and electric transport properties of the CoN films, as well as the change in the formation energy of the metal-ion bonds. The incorporation of Mn was proven effective to bring a more amorphous microstructure and semiconducting properties to CoN. As a result, a 6.7-fold enhancement of the saturation magnetization and higher magneto-ionic cyclability are achieved. From *ab initio* calculations, the energy barrier in CoMn–N is overall smaller than for Co–N, providing hints to understand the more efficient N-ion motion. The reported enhanced ion motion effects in CoMnN films by moderate Mn introduction (and the extension to other transition-metal systems) are appealing for diverse technological areas (beyond magneto-

ionics), such as electrochemical catalysis, batteries, solar cells, or spintronics.

METHODS

Sample Fabrication. CoN and $\text{Co}_{0.9}\text{Mn}_{0.1}\text{N}$ thin films with thicknesses of 30 nm or 100 nm were grown at room temperature by magnetron sputtering in a high-vacuum chamber (with a base pressure $<8 \times 10^{-8}$ Torr) on non-doped (100)-oriented Si wafers (0.5 mm thick) previously coated with a 10 nm thick titanium adhesion layer and 10 nm thick copper seed layer. The copper was partly masked to avoid the nitride film deposition and later serve as working electrodes. Pure Co and Mn targets were co-sputtered for the deposition of CoMnN and rates were calibrated to obtain a Co/Mn ratio of 9:1. The growth of CoN and CoMnN was carried out in a mixed Ar and N_2 atmospheres always using a nitrogen partial pressure of 50% and a total working pressure of 3×10^{-3} Torr. The distance between the substrate and targets was around 10 cm, and the sputtering rate was approximately 0.8 \AA s^{-1} .

Magneto-Ionic Characterization. *In situ* magnetoelectric measurements were carried out at room temperature using a commercial vibrating sample magnetometer (VSM) from Micro Sense (LOT, Quantum Design), with a maximum applied magnetic field of 2 T. Electrolyte gating was conducted between the counter electrode (a Pt wire) and the working electrode (the investigated CoN/Cu/Ti/Si or CoMnN/Cu/Ti/Si thin films) in a home-made electrolytic cell using an external Agilent B2902A power supply, as indicated in earlier works. The electrolyte consisted of anhydrous propylene carbonate with Na^+ - and OH^- -solvated species (10–25 ppm), in which metallic sodium was immersed to react with any possible trace of water. Negative voltages in this work signify the accumulation of negative charges at the working electrode (and vice versa for positive voltages). The magnetization (M) is obtained by normalizing the magnetic moment to the sample volume exposed to the electrolyte. Note that the linear slopes in the hysteresis loops at high fields (arising from diamagnetic or paramagnetic contributions) were eliminated by correcting the background signal (*i.e.*, at fields always significantly larger than the saturation fields).

Structural and Compositional Measurements. The $\theta/2\theta$ X-ray diffraction (XRD) patterns were collected on a materials research diffractometer (MRD) from Malvern PANalytical company, equipped with a PIXcel^{1D} detector, using Cu $K\alpha$ radiation. High-resolution transmission electron microscopy (HRTEM), high-angle annular dark-field scanning transmission electron microscopy (HAADF-STEM), and electron energy loss spectroscopy (EELS) were carried out on a TECNAI F20 HRTEM/STEM microscope operated at 200 kV. Cross-sectional lamellae were prepared by a focused ion beam, placed onto a copper transmission electron microscopy grid, and topped with a protective platinum layer.

Transport Measurements. To determine the electrical properties of CoN and CoMnN thin films, both films were deposited directly onto high-resistivity Si substrates. Resistivity values were recorded from 30 to 300 K by utilizing the 4-contact van der Pauw configuration in a closed He refrigeration system.

Ab initio Calculations. First-principles calculations were based on the projector-augmented wave (PAW)⁵¹ method as implemented in the VASP package⁵² using the generalized gradient approximation.⁵³ To model a Mn-doped Co and compare it to bare Co, we used (4×2) supercells with a four-monolayer thickness for both Co(90%)-Mn(10%) and Co. To evaluate the energy barrier a N atom needs to overcome in order to be inserted in the surface, the nudged elastic band method (NEB)^{49,50} was used on the nitrogen pathway. At each step, the atomic coordinates were relaxed until the forces became as small as 1 meV \AA^{-1} . A kinetic energy cutoff of 500 eV was applied for the plane-wave basis set and $25 \times 25 \times 1$ k -point meshes were used.

ASSOCIATED CONTENT

Supporting Information

The Supporting Information is available free of charge at <https://pubs.acs.org/doi/10.1021/acsami.2c12847>.

Dependence of the carrier densities (donor/acceptor) of as-prepared CoMnN films as a function of temperature; magnetoelectric characterizations for CoN and CoMnN films; structural characterization by HRTEM; and compositional characterization by TEM and energy-dispersive X-ray analysis (EDX) line scans (PDF)

AUTHOR INFORMATION

Corresponding Authors

Enric Menéndez – *Departament de Física, Universitat Autònoma de Barcelona, E-08193 Cerdanyola del Vallès, Spain*; orcid.org/0000-0003-3809-2863;
Email: Enric.Menendez@uab.cat

Jordi Sort – *Departament de Física, Universitat Autònoma de Barcelona, E-08193 Cerdanyola del Vallès, Spain; Institució Catalana de Recerca i Estudis Avançats (ICREA), E-08010 Barcelona, Spain*; orcid.org/0000-0003-1213-3639;
Email: Jordi.Sort@uab.cat

Authors

Zhengwei Tan – *Departament de Física, Universitat Autònoma de Barcelona, E-08193 Cerdanyola del Vallès, Spain*

Sofia Martins – *Departament de Física, Universitat Autònoma de Barcelona, E-08193 Cerdanyola del Vallès, Spain*

Michael Escobar – *Departament de Física, Universitat Autònoma de Barcelona, E-08193 Cerdanyola del Vallès, Spain*

Julius de Rojas – *Departament de Física, Universitat Autònoma de Barcelona, E-08193 Cerdanyola del Vallès, Spain; Department of Physics, Durham University, DH1 3LE Durham, U.K.*; orcid.org/0000-0002-1206-4744

Fatima Ibrahim – *University of Grenoble Alpes, CEA, CNRS, SPINTEC, 38000 Grenoble, France*

Mairbek Chshiev – *University of Grenoble Alpes, CEA, CNRS, SPINTEC, 38000 Grenoble, France; Institut Universitaire de France, 75231 Paris, France*; orcid.org/0000-0001-9232-7622

Alberto Quintana – *Institut de Ciència de Materials de Barcelona (ICMAB-CSIC), Bellaterra E-08193 Barcelona, Spain*; orcid.org/0000-0002-9813-735X

Aitor Lopeandia – *Departament de Física, Universitat Autònoma de Barcelona, E-08193 Cerdanyola del Vallès, Spain; Catalan Institute of Nanoscience and Nanotechnology (ICN2), CSIC and BIST, Cerdanyola del Vallès E-08193 Barcelona, Spain*

José L. Costa-Krämer – *IMN-Instituto de Micro y Nanotecnología (CNM-CSIC), 28760 Tres Cantos, Madrid, Spain*

Complete contact information is available at:
<https://pubs.acs.org/10.1021/acsami.2c12847>

Author Contributions

The manuscript was written through contributions of all authors. All authors have given approval to the final version of the manuscript.

Notes

The authors declare no competing financial interest.

ACKNOWLEDGMENTS

Financial support by the European Research Council (MAGIC-SWITCH 2019-Proof of Concept Grant, agreement

no 875018; REMINDS 2021-ERC-Advanced Grant, agreement no 101054687), the European Union's Horizon 2020 research and innovation program (European Training Network, ETN/ITN Marie Skłodowska-Curie grant no 861145; and Integrated Infrastructure, RADIATE, grant no 824096), the Spanish Government (PID2020-116844RB-C21 and PDC2021-121276-C31), the Generalitat de Catalunya (2017-SGR-292), and the KU Leuven (BOF program) is acknowledged. We acknowledge the technical support from the MiNa Laboratory at IMN in Madrid, who received funding from the CM (project S2018/NMT-4291 TEC2SPACE), MINECO (project CSIC13-4E-1794), and EU (FEDER, FSE). A.Q. acknowledges financial support from the Spanish Ministry of Science, Innovation and Universities through the "Severo Ochoa" Programme for Centers of Excellence in R&D (FUNFUTURE CEX2019-000917-S) and the "Juan de la Cierva—Formación" contract (FJC2019-039780-I). J.S. thanks the Spanish "Fábrica Nacional de Moneda y Timbre" (FNMT) for fruitful discussions. E.M. is a Serra Hunter Fellow.

REFERENCES

- (1) Park, B. H.; Kang, B. S.; Bu, S. D.; Noh, T. W.; Lee, J.; Jo, W. Lanthanum-substituted Bismuth Titanate for Use in Non-volatile Memories. *Nature* **1999**, *401*, 682–684.
- (2) Choi, W. S.; Chisholm, M. F.; Singh, D. J.; Choi, T.; Jellison, G. E.; Lee, H. N. Wide Bandgap Tunability in Complex Transition Metal Oxides by Site-specific Substitution. *Nat. Commun.* **2012**, *3*, 689.
- (3) Manyala, N.; DiTusa, J. F.; Aeppli, G.; Ramirez, A. P. Doping a Semiconductor to Create an Unconventional Metal. *Nature* **2008**, *454*, 976–980.
- (4) Dietl, T. Functional Ferromagnets. *Nat. Mater.* **2003**, *2*, 646–648.
- (5) Ederer, C.; Spaldin, N. A. A New Route to Magnetic Ferroelectrics. *Nat. Mater.* **2004**, *3*, 849–851.
- (6) Huynh, W. U.; Dittmer, J. J.; Alivisatos, A. P. Hybrid nanorod-polymer solar cells. *Science* **2002**, *295*, 2425–2427.
- (7) Zhao, F.; Liang, J.; Yu, C.; Sun, Q.; Li, X.; Adair, K.; Wang, C.; Zhao, Y.; Zhang, S.; Li, W.; Deng, S.; Li, R.; Huang, Y.; Huang, H.; Zhang, L.; Zhao, S.; Lu, S.; Sun, X. A Versatile Sn-Substituted Argyrodite Sulfide Electrolyte for All-Solid-State Li Metal Batteries. *Adv. Energy Mater.* **2020**, *10*, 1903422.
- (8) Choi, J.; Han, J. S.; Hong, K.; Kim, S. Y.; Jang, H. W. Organic-Inorganic Hybrid Halide Perovskites for Memories, Transistors, and Artificial Synapses. *Adv. Mater.* **2018**, *30*, 1704002.
- (9) Murphy, A. R.; Fréchet, J. M. J. Organic Semiconducting Oligomers for Use in Thin Film Transistors. *Chem. Rev.* **2007**, *107*, 1066–1096.
- (10) Mizuguchi, Y.; Tomioka, F.; Tsuda, S.; Yamaguchi, T.; Takano, Y. Superconductivity in S-substituted Fete. *Appl. Phys. Lett.* **2009**, *94*, 012503.
- (11) Žutić, I.; Fabian, J.; Das Sarma, S. Spintronics: Fundamentals and Applications. *Rev. Mod. Phys.* **2004**, *76*, 323–410.
- (12) Dietl, T.; Ohno, H. Dilute Ferromagnetic Semiconductors: Physics and Spintronic Structures. *Rev. Mod. Phys.* **2014**, *86*, 187–251.
- (13) Quintana, A.; Menéndez, E.; Liedke, M. O.; Butterling, M.; Wagner, A.; Sireus, V.; Torruella, P.; Estradé, S.; Peiró, F.; Dendooven, J.; Detavernier, C.; Murray, P. D.; Gilbert, D. A.; Liu, K.; Pellicer, E.; Nogues, J.; Sort, J. Voltage-Controlled ON-OFF Ferromagnetism at Room Temperature in a Single Metal Oxide Film. *ACS Nano* **2018**, *12*, 10291–10300.
- (14) Bauer, U.; Yao, L.; Tan, A. J.; Agrawal, P.; Emori, S.; Tuller, H. L.; van Dijken, S.; Beach, G. S. D. Magneto-ionic Control of Interfacial Magnetism. *Nat. Mater.* **2015**, *14*, 174–181.
- (15) Gilbert, D. A.; Grutter, A. J.; Arenholz, E.; Liu, K.; Kirby, B. J.; Borchers, J. A.; Maranville, B. B. Structural and Magnetic Depth

Profiles of Magneto-ionic Heterostructures Beyond the Interface Limit. *Nat. Commun.* **2016**, *7*, 12264.

(16) de Rojas, J.; Quintana, A.; Lopeandia, A.; Salguero, J.; Costa-Krämer, J. L.; Abad, L.; Liedke, M. O.; Butterling, M.; Wagner, A.; Henderick, L.; Dendooven, J.; Detavernier, C.; Sort, J.; Menéndez, E. Boosting Room-Temperature Magneto-Ionics in a Non-Magnetic Oxide Semiconductor. *Adv. Funct. Mater.* **2020**, *30*, 2003704.

(17) Martins, S.; de Rojas, J.; Tan, Z.; Cialone, M.; Lopeandia, A.; Herrero-Martín, J.; Costa-Krämer, J. L.; Menéndez, E.; Sort, J. Dynamic Electric-field-induced Magnetic Effects in Cobalt Oxide Thin Films: Towards Magneto-ionic Synapses. *Nanoscale* **2022**, *14*, 842–852.

(18) Dasgupta, S.; Das, B.; Knapp, M.; Brand, R. A.; Ehrenberg, H.; Kruk, R.; Hahn, H. Intercalation-driven Reversible Control of Magnetism in Bulk Ferromagnets. *Adv. Mater.* **2014**, *26*, 4639–4644.

(19) Vasala, S.; Jakob, A.; Wissel, K.; Waidha, A. I.; Alff, L.; Clemens, O. Reversible Tuning of Magnetization in a Ferromagnetic Ruddlesden-Popper-Type Manganite by Electrochemical Fluoride-Ion Intercalation. *Adv. Electron. Mater.* **2020**, *6*, 1900974.

(20) Tan, A. J.; Huang, M.; Avci, C. O.; Büttner, F.; Mann, M.; Hu, W.; Mazzoli, C.; Wilkins, S.; Tuller, H. L.; Beach, G. S. D. Magneto-ionic Control of Magnetism Using a Solid-state Proton Pump. *Nat. Mater.* **2019**, *18*, 35–41.

(21) Ye, X.; Singh, H. K.; Zhang, H.; Gefwein, H.; Chellali, M. R.; Witte, R.; Molinari, A.; Skokov, K.; Gutfleisch, O.; Hahn, H.; Kruk, R. Giant Voltage-induced Modification of Magnetism in Micron-scale Ferromagnetic Metals by Hydrogen Charging. *Nat. Commun.* **2020**, *11*, 4849.

(22) Chen, G.; Ophus, C.; Quintana, A.; Kwon, H.; Won, C.; Ding, H.; Wu, Y.; Schmid, A. K.; Liu, K. Reversible Writing/deleting of Magnetic Skyrmions Through Hydrogen Adsorption/desorption. *Nat. Commun.* **2022**, *13*, 1350.

(23) de Rojas, J.; Quintana, A.; Lopeandia, A.; Salguero, J.; Muñoz, B.; Ibrahim, F.; Chshiev, M.; Nicolenco, A.; Liedke, M. O.; Butterling, M.; Wagner, A.; Sireus, V.; Abad, L.; Jensen, C. J.; Liu, K.; Nogués, J.; Costa-Krämer, J. L.; Menéndez, E.; Sort, J. Voltage-driven Motion of Nitrogen Ions: A New Paradigm for Magneto-ionics. *Nat. Commun.* **2020**, *11*, 5871.

(24) de Rojas, J.; Salguero, J.; Ibrahim, F.; Chshiev, M.; Quintana, A.; Lopeandia, A.; Liedke, M. O.; Butterling, M.; Hirschmann, E.; Wagner, A.; Abad, L.; Costa-Krämer, J. L.; Menéndez, E.; Sort, J. Magneto-ionics in Single-layer Transition Metal Nitrides. *ACS Appl. Mater. Interfaces* **2021**, *13*, 30826–30834.

(25) de Rojas, J.; Salguero, J.; Quintana, A.; Lopeandia, A.; Liedke, M. O.; Butterling, M.; Attallah, A. G.; Hirschman, E.; Wagner, A.; Abad, L.; Costa-Krämer, J. L.; Sort, J.; Menéndez, E. Critical Role of Electrical Resistivity in Magnetoionics. *Phys. Rev. Appl.* **2021**, *16*, 034042.

(26) de Rojas, J.; Quintana, A.; Rius, G.; Stefani, C.; Domingo, N.; Costa-Krämer, J. L.; Menéndez, E.; Sort, J. Voltage Control of Magnetism with Magneto-ionic Approaches: Beyond Voltage-driven Oxygen Ion Migration. *Appl. Phys. Lett.* **2022**, *120*, 070501.

(27) Leighton, C. Electrolyte-based Ionic Control of Functional Oxides. *Nat. Mater.* **2019**, *18*, 13–18.

(28) Gu, Y.; Song, C.; Wang, Q.; Hu, W.; Liu, W.; Pan, F.; Zhang, Z. Emerging Opportunities for Voltage-driven Magneto-ionic Control in Ferrioc Heterostructures. *APL Mater.* **2021**, *9*, 040904.

(29) Song, C.; Cui, B.; Li, F.; Zhou, X.; Pan, F. Recent Progress in Voltage Control of Magnetism: Materials, Mechanisms, and Performance. *Prog. Mater. Sci.* **2017**, *87*, 33–82.

(30) Weisheit, M.; Fähler, S.; Marty, A.; Souche, Y.; Poinignon, C.; Givord, D. Electric field-induced Modification of Magnetism in Thin-film Ferromagnets. *Science* **2007**, *315*, 349–351.

(31) Ghodake, U. R.; Chaudhari, N. D.; Kambale, R. C.; Patil, J. Y.; Suryavanshi, S. S. Effect of Mn²⁺ substitution on structural, magnetic, electric and dielectric properties of Mg-Zn ferrites. *J. Magn. Magn. Mater.* **2016**, *407*, 60–68.

(32) Chang, S. K.; Lee, K. T.; Zainal, Z.; Tan, K. B.; Yusof, N. A.; Yusoff, W. M. D. W.; Lee, J. F.; Wu, N. L. Structural and

Electrochemical Properties of Manganese Substituted Nickel Cobaltite for Supercapacitor Application. *Electrochim. Acta* **2012**, *67*, 67–72.

(33) Ahsan, M. Z.; Khan, F. A. Structural and Electrical Properties of Manganese Doped Cobalt Ferrite Nanoparticles. *Mater. Sci. Nanotechnol.* **2018**, *2*, 1–9.

(34) Ahsan, M. Z.; Khan, F. A.; Islam, M. A. Frequency and Temperature Dependent Intrinsic Electric Properties of Manganese Doped Cobalt Ferrite Nanoparticles. *Results Phys.* **2019**, *14*, 102484.

(35) Yurovskikh, A. S.; Nikul'chenkov, N. N.; Redikultsev, A. A.; Lutfiyeva, Z. Z.; Lobanov, M. L. The Effect of Copper and Manganese on the Amorphization Process in a Thin Fe-Si-Mg-O Film. *KnE Engineering* **2019**, *1*, 164–169.

(36) Yin, S.; Moro, R.; Xu, X.; de Heer, W. A. Magnetic Enhancement in Cobalt-manganese Alloy Clusters. *Phys. Rev. Lett.* **2007**, *98*, 113401.

(37) Ito, K.; Yasutomi, Y.; Zhu, S.; Nurmamat, M.; Tahara, M.; Toko, K.; Akiyama, R.; Takeda, Y.; Saitoh, Y.; Oguchi, T.; Kimura, A.; Suemasu, T. Manipulation of saturation magnetization and perpendicular magnetic anisotropy in epitaxial Co₂Mn₄-xN films with ferrimagnetic compensation. *Phys. Rev. B* **2020**, *101*, 104401.

(38) Kunimatsu, K.; Roy, T.; Okabayashi, J.; Tsuchiya, T.; Ichinose, T.; Tsujikawa, M.; Shirai, M.; Mizukami, S. Structure and magnetism in metastable bcc Co_{1-x}Mnx epitaxial films. *J. Magn. Magn. Mater.* **2022**, *548*, 168841.

(39) Grollier, J.; Querlioz, D.; Camsari, K. Y.; Everschor-Sitte, K.; Fukami, S.; Stiles, M. D. *Nat. Electron.* **2020**, *3*, 360–370.

(40) Manipatruni, S.; Nikonov, D. E.; Young, I. A. Beyond CMOS Computing with Spin and Polarization. *Nat. Phys.* **2018**, *14*, 338–343.

(41) Fischer, J. E.; Dai, H.; Thess, A.; Lee, R.; Hanjani, N. M.; Dehaas, D. L.; Smalley, R. E. Metallic Resistivity in Crystalline Ropes of Single-wall Carbon Nanotubes. *Phys. Rev. B: Condens. Matter Mater. Phys.* **1997**, *55*, R4921–R4924.

(42) Abrahams, E.; Kravchenko, S. V.; Sarachik, M. P. Metallic Behavior and Related Phenomena in Two Dimensions. *Rev. Mod. Phys.* **2001**, *73*, 251–266.

(43) Ningthoujam, R. S.; Gajbhiye, N. S. Synthesis, Electron Transport Properties of Transition Metal Nitrides and Applications. *Prog. Mater. Sci.* **2015**, *70*, 50–154.

(44) Wolowiec, C. T.; Yazici, D.; White, B. D.; Huang, K.; Maple, M. B. Pressure-induced Enhancement of Superconductivity and Suppression of Semiconducting Behavior in LnO_{0.5}Fe_{0.5}BiS₂ (Ln = La, Ce) compounds. *Phys. Rev. B: Condens. Matter Mater. Phys.* **2013**, *88*, 064503.

(45) Mott, N. F.; Twose, W. D. The Theory of Impurity Conduction. *Adv. Phys.* **1961**, *10*, 107–163.

(46) Shin, S.-J.; Kim, D. H.; Bae, G.; Ringe, S.; Choi, H.; Lim, H.-K.; Choi, C. H.; Kim, H. On the Importance of the Electric Double Layer Structure in Aqueous Electrocatalysis. *Nat. Commun.* **2022**, *13*, 174.

(47) Silva, C.; Vovk, A.; da Silva, R. C.; Strichovanec, P.; Algarabel, P. A.; Gonçalves, A. P.; Borges, R. P.; Godinho, M.; Cruz, M. M. Magnetic properties of Co-N thin films deposited by reactive sputtering. *Thin Solid Films* **2014**, *556*, 125–127.

(48) Liu, Z. T. Y.; Zhou, X.; Khare, S. V.; Gall, D. Structural, Mechanical and Electronic Properties of 3d Transition Metal Nitrides in Cubic Zincblende, Rocksalt and Cesium Chloride Structures: A First-Principles Investigation. *J. Phys.: Condens. Matter* **2013**, *26*, 025404.

(49) Henkelman, G.; Jónsson, H. Improved Tangent Estimate in the Nudged Elastic Band Method for Finding Minimum Energy Paths and Saddle Points. *J. Chem. Phys.* **2000**, *113*, 9978–9985.

(50) Henkelman, G.; Uberuaga, B. P.; Jónsson, H. A Climbing Image Nudged Elastic Band Method for Finding Saddle Points and Minimum Energy Paths. *J. Chem. Phys.* **2000**, *113*, 9901–9904.

(51) Blöchl, P. E. Projector Augmented-wave Method. *Phys. Rev. B: Condens. Matter Mater. Phys.* **1994**, *50*, 17953–17979.

(52) Kresse, G.; Furthmüller, J. Efficient Iterative Schemes For a Brillouin Zone Sampling Using a Plane-wave Basis Set. *Phys. Rev. B: Condens. Matter Mater. Phys.* **1996**, *54*, 11169–11186.

(53) Perdew, J. P.; Burke, K.; Ernzerhof, M. Generalized Gradient Approximation Made Simple. *Phys. Rev. Lett.* **1996**, *77*, 3865–3868.

Supporting Information

From Binary to Ternary Transition Metal Nitrides: A Boost toward Nitrogen Magneto-Ionics

Zhengwei Tan¹, Sofia Martins¹, Michael Escobar¹, Julius de Rojas^{1,2}, Fatima Ibrahim³, Mairbek Chshiev^{3,4}, Alberto Quintana⁵, Aitor Lopeandia^{1,6}, José L. Costa-Krämer⁷, Enric Menéndez^{1,} and Jordi Sort^{1,8,*}*

¹Departament de Física, Universitat Autònoma de Barcelona, E-08193 Cerdanyola del Vallès, Spain

²Department of Physics, Durham University, South Rd., Durham DH1 3LE, United Kingdom

³Univ. Grenoble Alpes, CEA, CNRS, SPINTEC, 38000 Grenoble, France

⁴Institut Universitaire de France, 75231 Paris, France

⁵Institut de Ciència de Materials de Barcelona (ICMAB-CSIC), Campus UAB, Bellaterra, E-08193 Barcelona, Spain

⁶Catalan Institute of Nanoscience and Nanotechnology (ICN2), CSIC and BIST, Campus UAB, Cerdanyola del Vallès, E-08193 Barcelona, Spain

⁷IMN-Instituto de Micro y Nanotecnología (CNM-CSIC), Isaac Newton 8, PTM, 28760 Tres Cantos, Madrid, Spain

⁸Institució Catalana de Recerca i Estudis Avançats (ICREA), Pg. Lluís Companys 23, E-08010 Barcelona, Spain

*Corresponding authors: E. Menéndez (Email: enric.menendez@uab.cat) and J. Sort (jordi.sort@uab.cat)

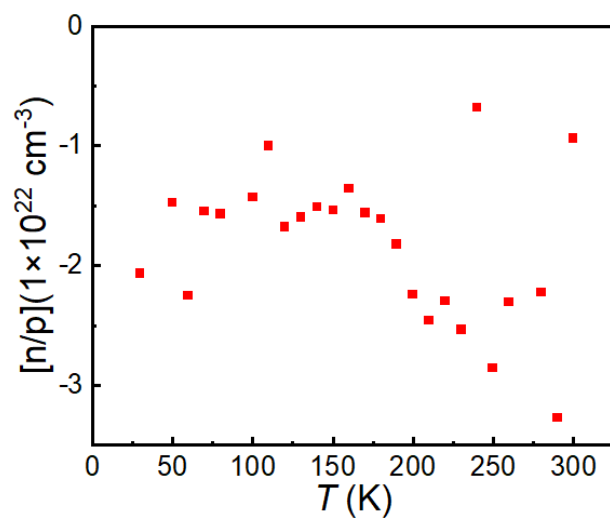


Figure S1. Dependence of the carrier densities (donor/acceptor) of as-prepared CoMnN films as a function of temperature.

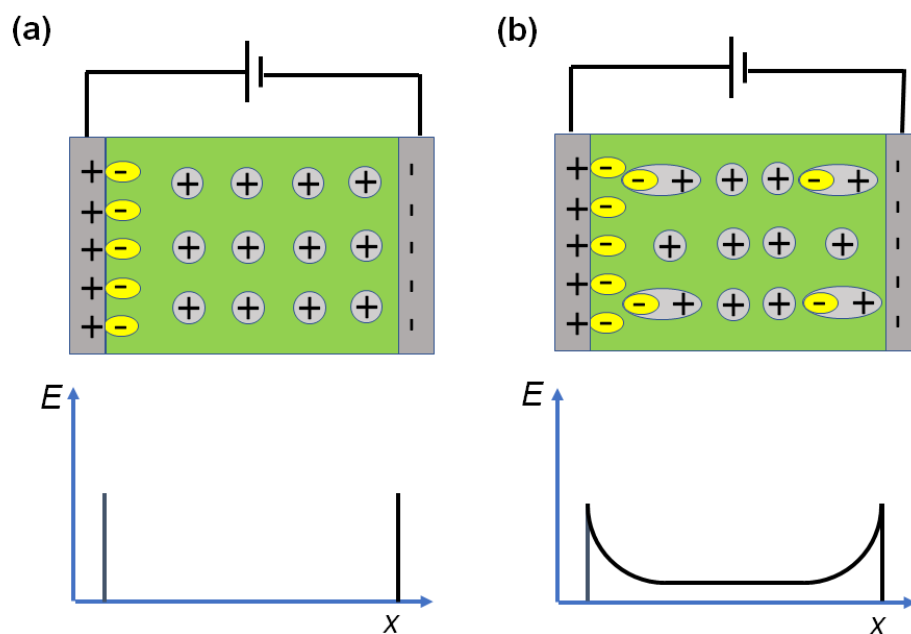


Figure S2. Cartoon representing electric penetration in a metallic (a) and a semiconducting (b) film based on the results of CoN films with dissimilar microstructure and electric properties as reported in reference 25. x represents the length across the film.

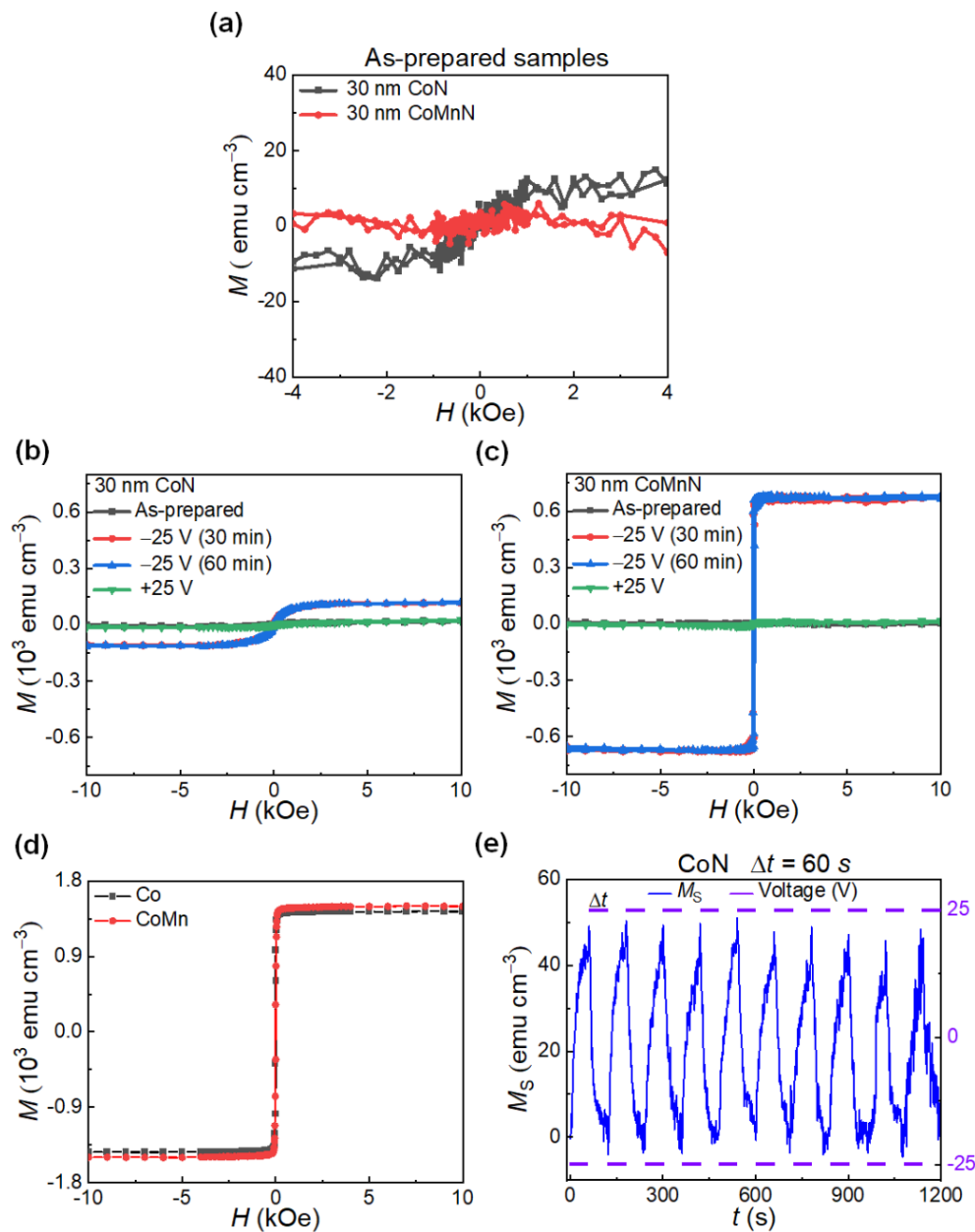


Figure S3. Magneto-electric characterization of CoN and CoMnN films by in-plane vibrating sample magnetometry (each hysteresis loops of 30 min of duration) while electrolyte-gating. (a) Hysteresis loops of the as-prepared CoN and CoMnN films. (b) and (c) Hysteresis loops of the as-prepared film (black), while gating at -25 V for 60 min (red, 1st loop, and blue, 2nd loop) and after subsequent $+25$ V gating (green) for the CoN and CoMnN films, respectively. (d) Hysteresis loops corresponding to Co and CoMn (10 at. % Mn) films prepared in the same fashion as the nitrides but in vacuum and, thus, without nitrogen. (e) Magneto-ionic cyclability of the CoN films subjected to -25 V/ $+25$ V for 1 min at each voltage.

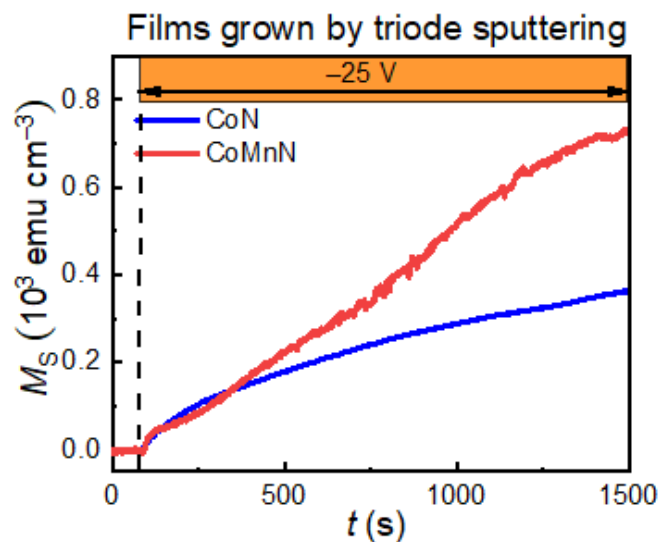


Figure S4. Time evolution of the saturation magnetization (M_S vs. t) of 85 nm-thick CoN and CoMnN films grown by homemade triode sputtering under electrolyte-gating at -25 V.

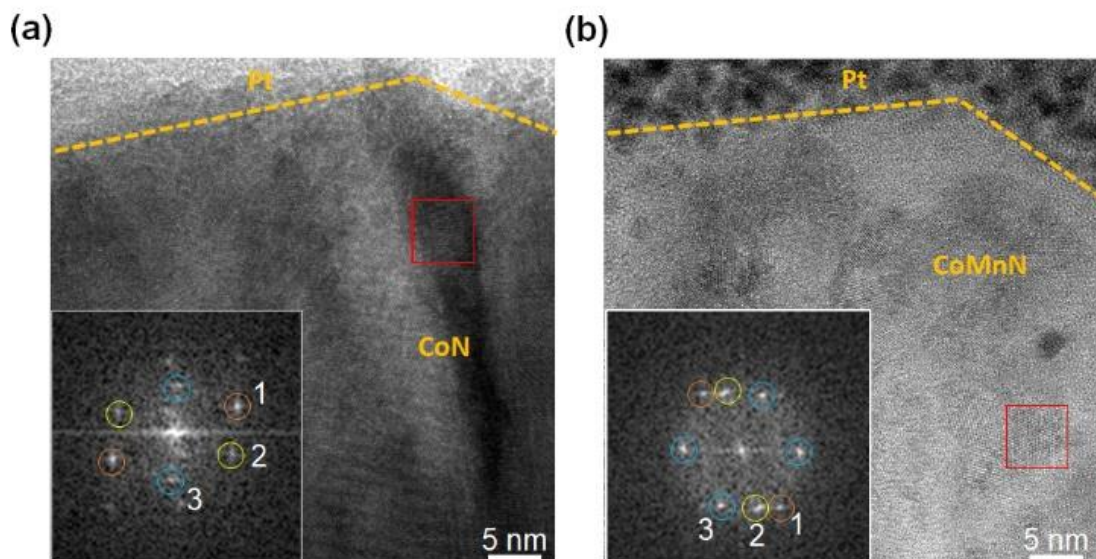


Figure S5. Structural characterization by High resolution transmission electron microscopy (HRTEM). (a), (b) HRTEM images of the cross section of CoN and CoMnN films after voltage treated upon -25 V for 40 minutes. The inset shows the fast Fourier transform (FFT) of the area marked with a red rectangle. For phase identification, the cards no. ICDD JCPDF 00-001-1277, ICDD JCPDF 00-009-0418 and ICDD JCPDF 01-078-1991 were taken for Co, Co_3O_4 and $\text{Co}_{0.9}\text{Mn}_{0.1}\text{O}$, respectively. Pt layers serve as protective capping layer for lamellae preparation.

<i>Spot label</i>	<i>Interplanar distance d (Å)</i>	<i>(h k l) planes</i>
Figure S5 (a)-CoN		
1	2.06	(0 0 2) Co
2	2.19	(1 0 0) Co
3	2.41	(3 1 1) Co ₃ O ₄
Figure S5 (b)-CoMnN		
1	2.18	(1 0 0) Co
2	2.43	(3 1 1) Co ₃ O ₄
3	2.47	(1 0 0) Co _{0.9} Mn _{0.1} O

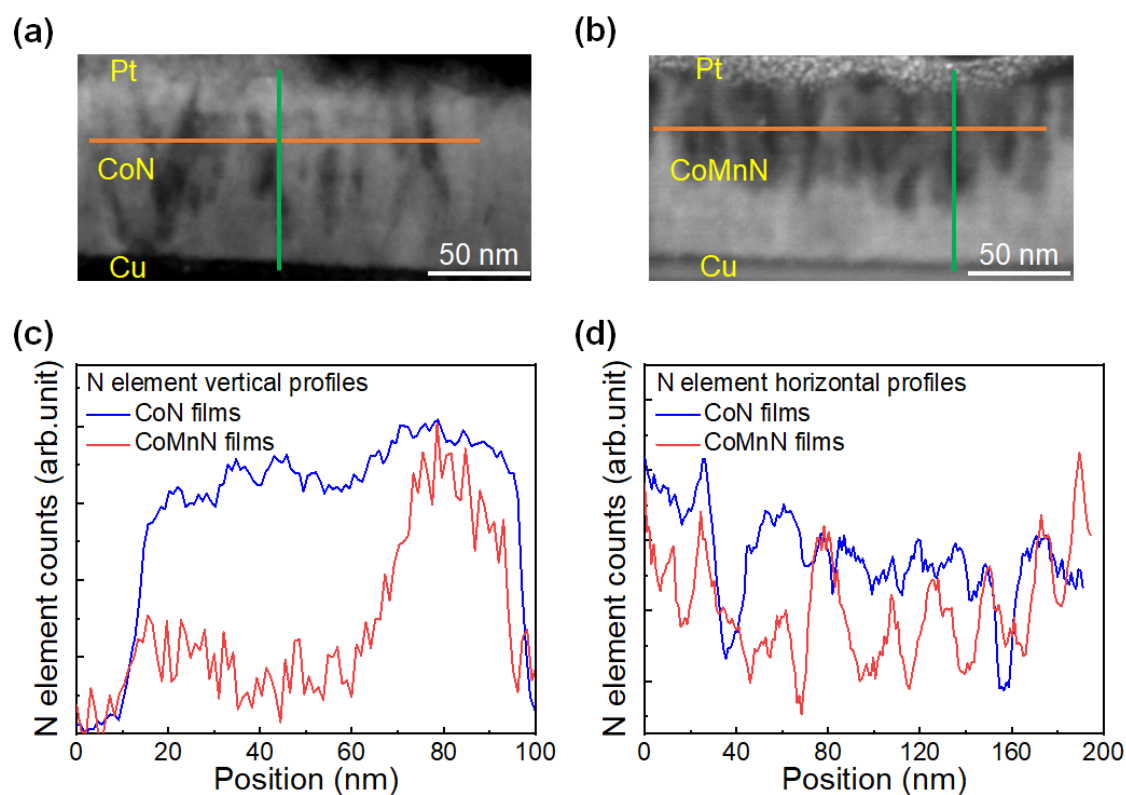


Figure S6. Compositional characterization by TEM and EDX line scans. (a) (b) TEM areas chosen for N element detection along depth (green line) and along horizontal (orange line) profiles for CoN and CoMnN films, respectively. (c) (d) are the N element line scans as a function of displacement along the vertical (depth) and horizontal directions.

3.3 Regulating oxygen ion transport at the nanoscale to enable highly cyclable magneto-ionic control of magnetism

Zhengwei Tan^a, Zheng Ma^a, Laura Fuente^{b,c}, Maciej Oskar Liedke^d, Maik Butterling^d, Ahmed G. Attallah^d, Eric Hirschmann^d, Andreas Wagner^d, Llibertat Abad^c, Nieves Casañ-Pastor^b, Aitor F. Lopeandia^{a,e}, Enric Menéndez^{*a} and Jordi Sort^{* a,f}

^aDepartament de Física, Universitat Autònoma de Barcelona, E-08193 Cerdanyola del Vallès, Spain.

^bInstitut de Ciència de Materials de Barcelona, CSIC, 08193 Bellaterra, Barcelona, Spain.

^cCentre Nacional de Microelectrònica, Institut de Microelectrònica de Barcelona-CSIC, 08193 Bellaterra, Barcelona, Spain.

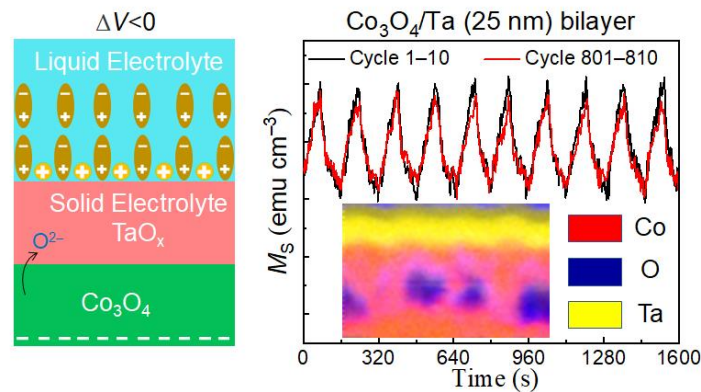
^dInstitute of Radiation Physics, Helmholtz-Zentrum Dresden - Rossendorf, Dresden 01328, Germany.

^eCatalan Institute of Nanoscience and Nanotechnology (ICN2), CSIC and BIST, Campus UAB, Cerdanyola del Vallès, E-08193 Barcelona, Spain.

^fInstitució Catalana de Recerca i Estudis Avançats (ICREA), Pg. Lluís Companys 23, E-08010 Barcelona, Spain.

In magneto-ionic systems, effective electric fields are generated using either solid or liquid electrolytes, which also function as reservoirs for ions. However, challenges arise with thin solid electrolytes due to their susceptibility to electric pinholes under high fields and the difficulty in maintaining stable ion transport over extended periods. Liquid electrolytes, on the other hand, can suffer from poor cyclability, limiting their usability.

In this work, to address these issues, we propose a nanostructured magneto-ionic architecture, involving a thin solid electrolyte coupled with a liquid electrolyte, which enhances cyclability while maintaining sufficiently strong electric fields to trigger ion movement. Specifically, by inserting an amorphous-like Ta layer with appropriate thickness and electric resistivity between the magneto-ionic target material (Co_3O_4) and the liquid electrolyte, we substantially enhance magneto-ionic cyclability from less than 30 cycles (without the Ta layer) to over 800 cycles. Transmission electron microscopy together with variable energy positron annihilation spectroscopy reveal that the generated TaO_x interlayer acts as a solid electrolyte (ionic conductor), enhancing magneto-ionic endurance by regulating voltage-driven structural defects. The Ta layer effectively traps oxygen, restraining the movement of O^{2-} ions into the liquid electrolyte, and primarily directing O^{2-} motion between Co_3O_4 and Ta when alternating-polarity voltage is applied. This strategy successfully combines the benefits of solid and liquid electrolytes, yielding a promising avenue to enhance magneto-ionics.



Regulating Oxygen Ion Transport at the Nanoscale to Enable Highly Cyclable Magneto-Ionic Control of Magnetism

Zhengwei Tan, Zheng Ma, Laura Fuentes, Maciej Oskar Liedke, Maik Butterling, Ahmed G. Attallah, Eric Hirschmann, Andreas Wagner, Llibertat Abad, Nieves Casañ-Pastor, Aitor F. Lopeandia, Enric Menéndez,* and Jordi Sort*



Cite This: *ACS Nano* 2023, 17, 6973–6984



Read Online

ACCESS |

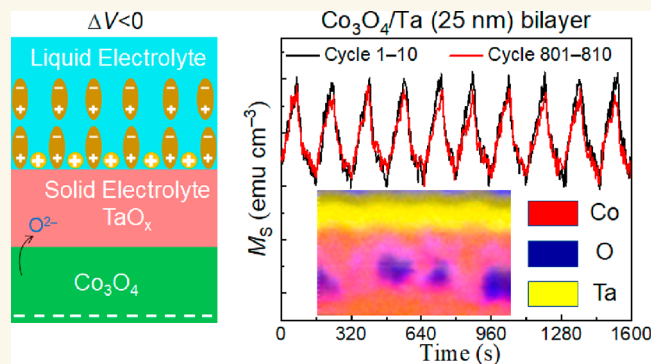
Metrics & More

Article Recommendations

Supporting Information

ABSTRACT: Magneto-ionics refers to the control of magnetic properties of materials through voltage-driven ion motion. To generate effective electric fields, either solid or liquid electrolytes are utilized, which also serve as ion reservoirs. Thin solid electrolytes have difficulties in (i) withstanding high electric fields without electric pinholes and (ii) maintaining stable ion transport during long-term actuation. In turn, the use of liquid electrolytes can result in poor cyclability, thus limiting their applicability. Here we propose a nanoscale-engineered magneto-ionic architecture (comprising a thin solid electrolyte in contact with a liquid electrolyte) that drastically enhances cyclability while preserving sufficiently high electric fields to trigger ion motion. Specifically, we show that the insertion of a highly nanostructured (amorphous-like) Ta layer (with suitable thickness and electric resistivity) between a magneto-ionic target material (*i.e.*, Co_3O_4) and the liquid electrolyte increases magneto-ionic cyclability from <30 cycles (when no Ta is inserted) to more than 800 cycles. Transmission electron microscopy together with variable energy positron annihilation spectroscopy reveals the crucial role of the generated TaO_x interlayer as a solid electrolyte (*i.e.*, ionic conductor) that improves magneto-ionic endurance by proper tuning of the types of voltage-driven structural defects. The Ta layer is very effective in trapping oxygen and hindering O^{2-} ions from moving into the liquid electrolyte, thus keeping O^{2-} motion mainly restricted between Co_3O_4 and Ta when voltage of alternating polarity is applied. We demonstrate that this approach provides a suitable strategy to boost magneto-ionics by combining the benefits of solid and liquid electrolytes in a synergetic manner.

KEYWORDS: magneto-electricity, voltage control of magnetism, magneto-ionics, transition metal oxide, ion diffusion



With the advent of global phenomena such as the Internet of Things, artificial intelligence, machine learning, or Big Data, the demand for highly functional and energy-efficient miniaturized microelectronic components is growing exponentially.^{1,2} Spintronic systems^{3,4} operated using electric currents through spin-transfer torque^{5,6} or spin-orbit torque^{7,8} effects are becoming key elements for next-generation nanoelectronics with enhanced memory and information processing capabilities. However, magnetization switching using electric current involves an undesirable Joule heating effect, which is detrimental to energy efficiency.^{9,10} An interesting alternative is to modulate magnetic properties by applying electric fields instead of electric current, thus minimizing power dissipation. This has rapidly evolved into

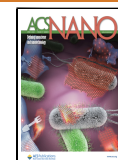
a whole area of research referred to as voltage control of magnetism (VCM).

Magneto-ionics refers to a particular mechanism for VCM in which voltage-driven ion transport (of, *e.g.*, O^{2-} ,^{11–15} Li^+ ,¹⁶ F^- ,¹⁷ H^+ ,^{18–21} or N^{3-} ^{22–26} species) leads to a large and controllable modulation of magnetism without the need of strain transfer. This is different from voltage-controlled strain-mediated multiferroic heterostructures, which are less con-

Received: February 6, 2023

Accepted: March 21, 2023

Published: March 27, 2023



venient for spintronics because repeated voltage actuation can lead to mechanical fatigue and eventual device failure. Archetypical magneto-ionic structures comprise a gate electrolyte (either solid or liquid)^{27,28} in contact with a ferromagnetic (FM) target material. Voltage is applied across the electrolyte, using the FM film as a working electrode and causing a voltage polarity-dependent insertion/removal of ions into/from the target material. In this way, magnetic properties, such as saturation magnetization,^{11,22} magnetic anisotropy and coercivity,^{12,18} exchange bias field,^{13,29} or skyrmion generation/suppression,²⁰ among others, can be reversibly controlled, making magneto-ionic materials highly promising for ultra-low-power magnetic devices. An extreme case is when voltage induces a complete reversible transition between FM and nonmagnetic states, leading to voltage-driven ON–OFF switching of ferromagnetism. This has been reported in a number of magneto-ionic systems, such as Co_3O_4 ,^{11,14,30} Li^+ -intercalated $\alpha\text{-Fe}_2\text{O}_3$,³¹ F^- -intercalated $\text{La}_{2-2x}\text{Sr}_{1+2x}\text{Mn}_2\text{O}_7$,¹⁷ CoN ,^{26,28} CoMnN ,²³ or $\alpha\text{-Co(OH)}_2$.³² ON–OFF switching of the ferromagnetic state has been also induced by electrostatic surface charging in FeS_2 .³³

In most magneto-ionic systems, the source of the moving ions is electrolytes (e.g., GdO_x , HfO_x , propylene carbonate with dissolved LiPF_6 or KI) that are in direct contact with pristine FM or ferrimagnetic layers (e.g., Co , Fe , Fe_2O_3), whose properties are manipulated with voltage.^{27,34–36} Magneto-ionic systems based on O^{2-} insertion from an external electrolyte to a target FM material often suffer from slow dynamics at room temperature and irreversible compositional/structural changes in the FM phase, eventually leading to degradation and limited cyclability.¹² In addition, for relatively thick films, it is challenging to achieve a fully OFF magnetic state with voltage due to the limited penetration of the external ions toward the interior of the FM target layers.³⁷ Recently, smaller ions (e.g., H^+ , F^- , or Li^+) have been introduced to achieve faster and more cyclable voltage-induced manipulation of magnetic properties. Fast, reversible, and cyclable tuning of perpendicular magnetic anisotropy,¹⁸ Dzyaloshinskii–Moriya interaction,^{38,39} or ferrimagnetic spin textures⁴⁰ has been achieved through chemisorbed O^{2-} or H^+ ion species. However, systems relying on H^+ are either sensitive to environmental conditions (e.g., humidity) or restricted by their incompatibility with traditional complementary metal-oxide semiconductor (CMOS)-based devices (i.e., standard fabrication processes for semiconductor devices, such as metal oxide field-effect transistors).²⁸ An alternative approach is to use structural oxygen or nitrogen, self-contained in the target materials, as the source of the moving ions. Examples of such materials are Co_3O_4 ,¹¹ CoN ,^{22,26} or CoMnN ²⁵ films. These target materials, which are CMOS compatible, exhibit an initially fully OFF (i.e., paramagnetic) state and provide “ready-prepared” lattice sites for ion diffusion, allowing for net magneto-ionic generation of ferromagnetism by voltage-triggered O^{2-} or N^{3-} ion motion from the films toward a neighboring electrolyte. Unfortunately, achieving a high magneto-ionic cyclability in these materials (i.e., removing and reinserting the $\text{O}^{2-}/\text{N}^{3-}$ ions many times by switching voltage polarity) remains a challenge.

To induce magneto-ionics, either solid or liquid electrolytes can be utilized. Solid electrolytes (with ultrathin dielectric layers) are preferred for solid-state spintronics. Ultrathin solid dielectric layers are needed to induce sufficiently large electric fields under moderate applied voltages. However, at such small

thicknesses, difficulties arise to withstand high electric fields without electric pinholes. Moreover, thin solid electrolytes offer a limited ion buffering capability (i.e., they easily become saturated with ions and cannot sustain stable ion transport during long-term operation, especially when the magneto-ionic layer is thicker than the solid electrolyte layer). Liquid electrolytes are convenient for other magnetoelectric applications, such as magnetophoresis/microfluidics⁴¹ or to emulate neuromorphic functionalities (the brain operates in a liquid environment).^{15,26} Owing to the formation of the “electric double layer”, whose thickness is <1 nm, liquid electrolytes are able to generate ultralarge electric fields (hundreds of MV cm^{-1}) at the interface between the liquid and the target magneto-ionic layer, without electric pinholes.²⁷ Liquid electrolytes may also be good ion reservoirs.^{11,14,22} However, when voltage is applied, the mobile ions released from the target layer into the liquid can travel long distances toward the counter electrode, making their reintroduction into the magneto-ionic layer (with voltage of opposite polarity) difficult. In addition, at the counter electrode, if sufficiently high voltage is applied, the dissolved ions (e.g., O^{2-} , H^+ , or N^{3-}) can transform into the corresponding oxygen, hydrogen, or nitrogen gases and be released to the atmosphere in the form of bubbles. These effects are difficult to control and are highly detrimental for magneto-ionic reversibility and endurance. Restricting ion transport within the magneto-ionic layers could avoid these problems and is expected to improve the magneto-ionic cyclability.

Here, we propose an improved nanoscale-engineered magneto-ionic structure that results from inserting an amorphous Ta layer (which gets spontaneously passivated in air) between the Co_3O_4 film (magneto-ionic target material) and propylene carbonate, PC (liquid electrolyte). Upon application of negative voltage, O^{2-} ions migrate from Co_3O_4 to Ta, promoting the formation of TaO_x (Ta is a good oxygen getter), which acts as a thin solid electrolyte with good ionic conductivity. This architecture preserves sufficiently high electric fields to trigger ion motion while allowing to repeatedly induce ON–OFF switching of ferromagnetism at room temperature. By optimizing the thickness of the Ta layer, a drastic increase of cyclability is achieved in $\text{Co}_3\text{O}_4/\text{Ta}$ (25 nm)/PC (>800 cycles) compared to $\text{Co}_3\text{O}_4/\text{PC}$ with no Ta insertion (<30 cycles). The Ta layer hinders oxygen ions from entering the liquid electrolyte and allows for O^{2-} redistribution inside the Co_3O_4 and Ta layers, as assessed by high-angle annular dark-field scanning transmission electron microscopy (HAADF-STEM) and electron energy loss spectroscopy (EELS). Positron annihilation spectroscopy is used to precisely characterize the defect structure in Ta, which strongly contributes to the O^{2-} ion transport. An increase of the defect size during biasing is observed. The reduced electric conductivity of the passivated amorphous Ta layer is important to allow the penetration of the electric field inside the Co_3O_4 layer and the concomitant O^{2-} ion transport. Since O^{2-} diffusion becomes mainly restricted within the $\text{Co}_3\text{O}_4/\text{TaO}_x$ structure (instead of O^{2-} being released to PC), this greatly improves the efficiency of ion transport in the material, resulting in largely enhanced magneto-ionic cyclability.

RESULTS AND DISCUSSION

The basic building block of the investigated magneto-ionic system is a 40 nm thick Co_3O_4 film grown by DC reactive sputtering at room temperature onto Cu (60 nm)/Ti (20

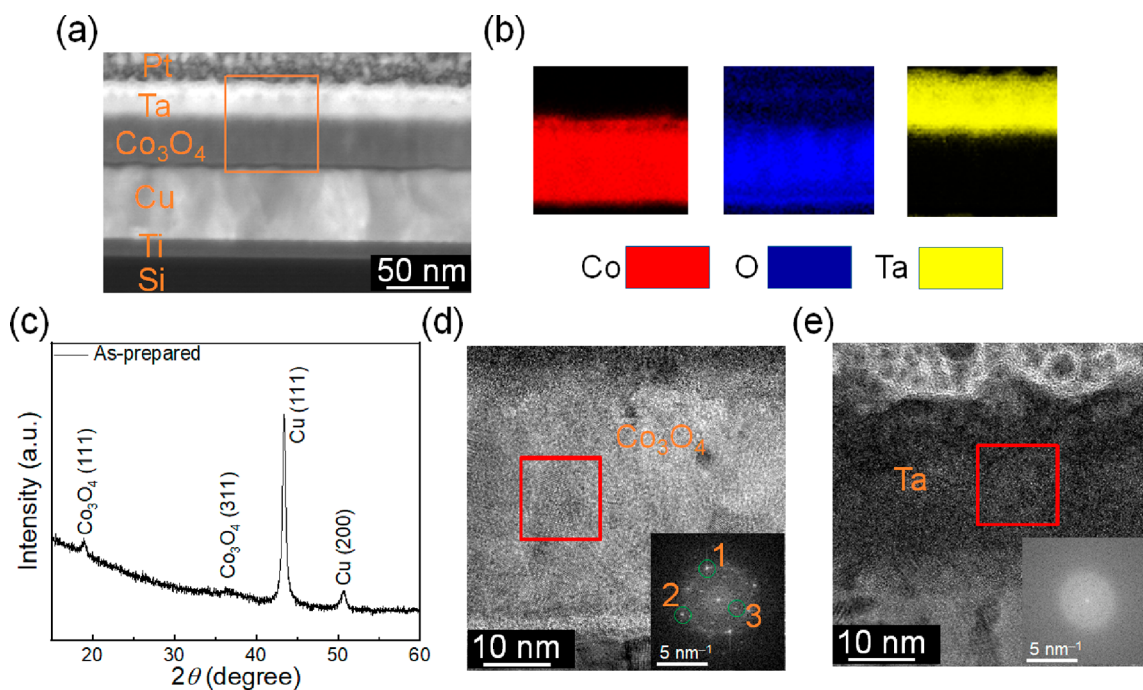


Figure 1. Structural and compositional characterization of as-deposited films. (a) HAADF-STEM micrograph of an as-grown sample. (b) EELS Co (in red), O (in blue), and Ta (in yellow) elemental mappings of the area marked with an orange rectangle in (a). (c) $\theta/2\theta$ XRD patterns of the as-prepared samples. (d, e) High-resolution TEM images of the cross section of the as-deposited Co_3O_4 and Ta films, respectively. The inset shows the fast Fourier transform of the areas marked with red squares. In panel (e), the “1” spot corresponds to an interplanar distance of 0.248 nm and is consistent with (311) Co_3O_4 (PDF 00-009-0418) or (111) CoO (PDF 00-001-1227) interplanar distances (0.244 and 0.245 nm, respectively), while spot “2” corresponds to an interplanar distance of 0.225 nm and is unambiguously ascribed to the (200) CoO (PDF 00-001-1227) interplanar distance (0.212 nm). The “3” spot corresponds to an interplanar distance of 0.448 nm, which is consistent with (311) Co_3O_4 (0.467 nm, PDF 00-009-0418).

nm)/[100]Si (725 μm) substrates. The Co_3O_4 films were coated with sputtered amorphous Ta protective layers of variable thickness (from 5 to 50 nm), which were left to passivate in air (see [Experimental Section](#)). Uncoated Co_3O_4 films were also grown as a reference. [Figure 1\(a\)](#) shows a low-magnification HAADF-STEM image of the as-prepared sample with a 25-nm-thick Ta protective capping layer. Clear interfaces between the various layers can be seen, and their thicknesses are in good agreement with the nominal ones. Note that the topmost Pt capping layer was grown only during the TEM lamella preparation (*i.e.*, it was not present during magneto-ionic experiments). To investigate the Co, O, and Ta distribution, Co, O, and Ta EELS mappings from the area marked with an orange rectangle in [Figure 1\(a\)](#) were acquired. As shown in [Figure 1\(b\)](#), Co and O elements are homogeneously distributed within the Co_3O_4 films. Additionally, some O signal is also detected inside the Ta layer, particularly on its upper part. This is ascribed to surface self-passivation of Ta in air, which is known to result in the formation of a stable TaO_x top layer.^{42,43} [Figure 1\(c\)](#) shows the $\theta/2\theta$ X-ray diffraction (XRD) pattern of an as-grown film. The XRD peak observed at $2\theta \approx 19.1^\circ$ is consistent with (111) Co_3O_4 (PDF 00-009-0418), whereas that at $2\theta \approx 36.7^\circ$ could be ascribed to either (111) Co_3O_4 or (111) CoO (PDF 00-001-1227). Peaks corresponding to the Cu buffer layer are also detected. Conversely, no traces of Ta are evidenced, suggesting that Ta is highly nanostructured or even amorphous-like. Growth of amorphous Ta by physical deposition methods has been previously reported,^{44,45} and it is promoted by the existence of ions and particles with high kinetic energy when sputtering at sufficiently high gun powers. Amorphous Ta

exhibits higher electric resistivity than its crystalline counterparts.⁴⁴ This is beneficial to keep sufficient electric field strength inside the actuated films while voltage is applied, thereby enabling magneto-ionics.

To further investigate the structure of the samples, high-resolution transmission electron microscopy (HRTEM) images of the cross sections of as-prepared Co_3O_4 and Ta layers were taken, as shown in [Figure 1\(d\)](#) and (e), respectively. The areas marked with red squares were chosen for fast Fourier transform (FFT) analyses, as shown in the insets. In [Figure 1\(d\)](#), the “1” spot corresponds to an interplanar distance of 0.248 nm and is consistent with (311) Co_3O_4 (PDF 00-009-0418) or (111) CoO (PDF 00-001-1227) interplanar distances (0.244 and 0.245 nm, respectively), while spot “2” corresponds to an interplanar distance of 0.225 nm and is unambiguously ascribed to the (200) CoO (PDF 00-001-1227) interplanar distance (0.212 nm). The “3” spot corresponds to an interplanar distance of 0.448 nm, which is consistent with (311) Co_3O_4 (0.467 nm, PDF 00-009-0418). This indicates that a mixture of CoO and Co_3O_4 phases is plausible in the Co oxide film, in agreement with previously reported results.¹⁵ For simplicity, in spite of the presence of CoO in particular close to the interface, the Co oxide film is labeled Co_3O_4 throughout the article. Remarkably, no spots are observed for Ta, in agreement with its amorphous nature, as also evidenced by XRD ([Figure 1\(c\)](#)).

To induce magneto-ionics, electrolyte gating was performed in a capacitor-like configuration ([Figure 2\(a\)](#))¹⁴ using a platinum wire as counter electrode and an aprotic, anhydrous polar liquid electrolyte composed of propylene carbonate with Na^+ and OH^- solvated species.^{27,46,47} When voltage is applied,

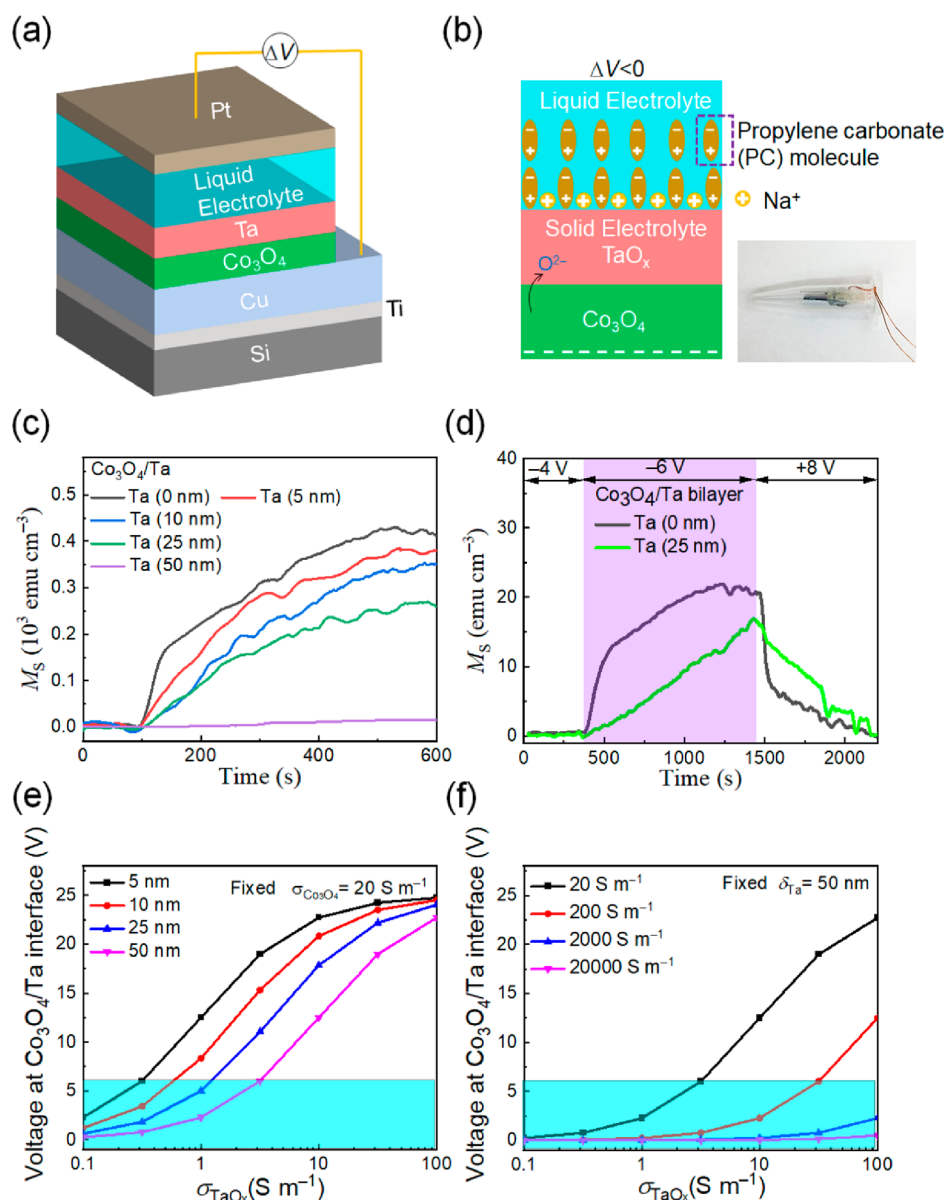


Figure 2. Magneto-ionic characterization of Co_3O_4 thin films and $\text{Co}_3\text{O}_4/\text{Ta}$ bilayer films under electrolyte gating. (a) Schematic of the designed structure for electrolyte actuation. (b) Left: Sketch of the formation of electric double layer during voltage actuation; right: photograph of the homemade electrolytic cell used to apply voltage to our system, which consists of an Eppendorf filled with propylene carbonate, our sample as working electrode, and a Pt wire counter electrode. (c) Time evolution of the saturation magnetization, M_S , for Co_3O_4 thin films and $\text{Co}_3\text{O}_4/\text{Ta}$ bilayer films (with a Ta thickness of 5, 10, 25, and 50 nm) under an applied voltage of -25 V. (d) Estimation of the onset voltage required to trigger magneto-ionics in Co_3O_4 thin films and $\text{Co}_3\text{O}_4/\text{Ta}$ (25 nm) bilayer films, as well as the recovery process. (e) Calculated absolute value of the voltage at the $\text{Co}_3\text{O}_4/\text{Ta}$ interface, $|\Delta V_{\text{int}}|$, as a function of the TaO_x conductivity, σ_{TaO_x} , when externally applying $|\Delta V| = 25$ V for different thicknesses of the Ta layer, δ_{Ta} , and a fixed Co_3O_4 conductivity, $\sigma_{\text{Co}_3\text{O}_4} = 20 \text{ S m}^{-1}$. (f) Calculated interface voltage as a function of σ_{TaO_x} for different values of conductivity of $\sigma_{\text{Co}_3\text{O}_4}$ and a fixed Ta thickness ($\delta_{\text{Ta}} = 50 \text{ nm}$). The regions highlighted with a cyan rectangle in (e) and (f) are those where $|\Delta V_{\text{int}}|$ would be below the magneto-ionic threshold voltage of the system.

a sub-nm-thick electric double layer forms at the electrolyte side of the electrolyte/Ta interface, allowing for the generation of a high electric field.⁴⁷ This electric field is ultimately responsible for driving oxygen ions from the Co_3O_4 to the Ta/ TaO_x layers (as illustrated in Figure 2(b)). Voltage treatments were performed *in situ*, while hysteresis loops were recorded at room temperature by vibrating sample magnetometry (VSM), with an in-plane applied magnetic field. The total measured magnetic moment of the samples (in emu) was normalized to the area of the sample and the nominal thickness of Co_3O_4 (to

obtain emu cm^{-3}). As seen in Figure 3, irrespective of the thickness of the Ta layer (*i.e.*, 0, 5, 10, 25, or 50 nm), all films in the as-grown state show very little ferromagnetic response ($<33 \text{ emu cm}^{-3}$, which is equivalent to $\approx 2.3\%$ the magnetization of pure FCC-Co⁴⁸). This small ferromagnetic signal is common in sputtered Co_3O_4 ¹⁵ and is likely due to either a small fraction of residual Co clusters that do not become fully oxidized during the sputtering process or substrate contamination. The deposition of Ta onto Co_3O_4 has a negligible effect on the initial ferromagnetic signal of the Co_3O_4 films.

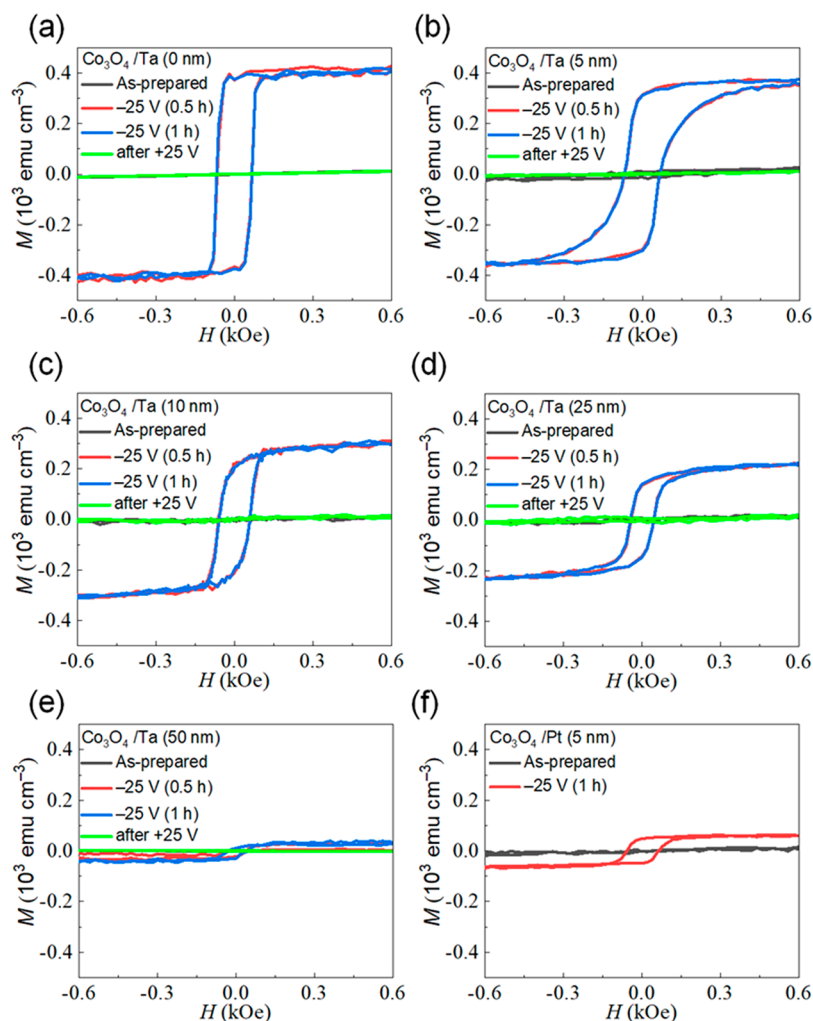


Figure 3. In-plane VSM hysteresis loops (each lasting 30 min) of the as-prepared $\text{Co}_3\text{O}_4/\text{Ta}$ films (black), the films biased under -25 V (for 30 min in red and for 1 h in blue), and subsequently recovered after applying $+25$ V for 30 min. The different panels correspond to different Ta thicknesses: (a) 0 nm, (b) 5 nm, (c) 10 nm, (d) 25 nm, (e) 50 nm. Panel (f) corresponds to $\text{Co}_3\text{O}_4/\text{Pt}$ without a Ta interlayer (with a Pt thickness of 5 nm).

Upon negative biasing at -25 V for 30 min or 1 h, clear hysteresis loops are observed. The generated saturation magnetization (M_S) is maximum for the sample without Ta (around 400 emu cm^{-3} , suggesting that 27% of the volume of Co_3O_4 gets reduced to Co), and it slightly decreases when a thin Ta interlayer (5–10 nm) is inserted between the Co_3O_4 film and the liquid electrolyte. M_S further decreases for sufficiently thick Ta. Remarkably, magneto-ionic effects when Pt (instead of Ta) is grown onto Co_3O_4 are strongly reduced: a small hysteresis loop is observed only for 5 nm Pt (compare Figure 3(f) with (b)), and no ferromagnetic response is obtained for thicker Pt. In all cases, the initial virtually nonmagnetic state can be recovered by applying $+25$ V for 30 min.

Figure 3 shows that, for all samples, most of the ferromagnetic response is induced in less than 30 min, since M_S does not further increase when applying voltage for 1 h. The time evolution of M_S for all samples under -25 V is shown in Figure 2(c). An external magnetic field of 10 kOe (*i.e.*, above the anisotropy field of the generated ferromagnetic counterpart) was applied during these measurements to ensure magnetic saturation. In all films, an immediate increase of M_S is observed in response to the applied ΔV , evidencing a quick

onset of the oxygen ionic motion, which leaves metallic ferromagnetic Co behind.^{14,15} The obtained steady-state value of M_S decreases with the Ta thickness, from 401 emu cm^{-3} to 19 emu cm^{-3} (in agreement with the magnetic hysteresis loops shown in Figure 3(a)–(e)). One important parameter of large significance for device applications is the minimum threshold voltage required to trigger magneto-ionic effects.^{22,25} The onset voltage for Co_3O_4 films without and with a 25-nm-thick Ta capping layer was evaluated by subjecting the films to increasing negative voltage steps of -2 V, until M_S started to increase, as shown in Figure 2(d). The results reveal that the onset voltage is approximately -6 V for both samples, whereas a voltage of $+8$ V leads to complete recovery in both cases, which agrees with previous works on similar systems.¹¹

Figure 2(c) and (d) also show that the rate at which M_S increases under voltage application is larger for a smaller Ta layer thickness. This, together with the reduction of the steady-state M_S for thicker Ta, indicates that the effective electric field acting on the Co_3O_4 layer becomes lower for larger Ta thickness. This suggests that, for thicker Ta, there is a more severe dissipation of space charge density, while O^{2-} is migrating from Co_3O_4 to form TaO_x .⁴⁹

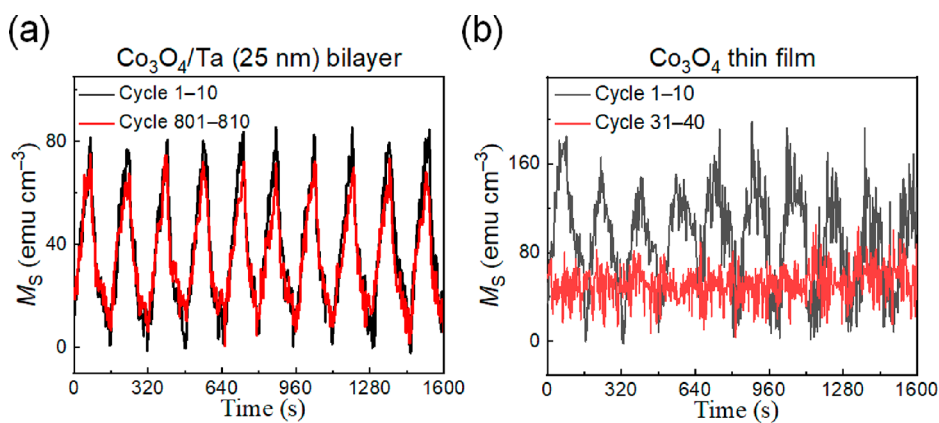


Figure 4. Magneto-ionic cyclability of (a) $\text{Co}_3\text{O}_4/\text{Ta}$ (25 nm) bilayer films and (b) the Co_3O_4 thin films subjected to -25 V/ $+25$ V voltage pulses applied with a periodicity of 80 s.

In a first approximation, this effect can be modeled considering the system as a simple voltage divider. The voltage drop at the $\text{Co}_3\text{O}_4/\text{Ta}$ interface can be estimated assuming that, during the magneto-ionic process, the Co_3O_4 and the newly formed TaO_x layers act as two resistances connected in series. In this case, the voltage at the $\text{Co}_3\text{O}_4/\text{TaO}_x$ interface is $\Delta V_{\text{int}} = \frac{R_{\text{Co}_3\text{O}_4}}{R_{\text{Co}_3\text{O}_4} + R_{\text{TaO}_x}} \Delta V$. Considering that $R = \rho \delta / A$ (where ρ is the resistivity of each material, δ is the film thickness, and A is the lateral area of the films), it is straightforward to estimate ΔV_{int} as a function of the layers' thicknesses and the electric conductivities of Co_3O_4 and TaO_x . The electrical conductivity of Co_3O_4 , measured by the Van der Pauw method, is approximately $\sigma_{\text{Co}_3\text{O}_4} = 20 \text{ S m}^{-1}$.¹⁴ The conductivity of TaO_x strongly depends on the oxygen content, and it varies by several orders of magnitude, from 10^5 S m^{-1} in amorphous metallic Ta⁴⁴ to 10^{-6} S m^{-1} for highly oxidized Ta.⁵⁰ The presence of oxygen in the naturally passivated Ta (Figure 1(b)) can easily bring ρ to values in the range 10^{-1} – 10^2 S m^{-1} before any voltage is applied.⁵¹ Figure 2(e) shows the evolution of the calculated interface voltage as a function of σ_{TaO_x} for the different Ta film thicknesses. For highly conductive Ta (or TaO_x) spacer layers, ΔV_{int} becomes independent of the Ta thickness, which means that any eventual magneto-ionic effect would be independent of the Ta thickness (and ΔV_{int} would be always equal to -25 V). However, in this case, the electric field would be highly screened at the interface and would not penetrate inside Ta (since, in metals, the electric field is confined within the Thomas–Fermi screening length, which is typically <0.5 nm).²⁷ Thus, for highly metallic interlayers (e.g., noble metals like Pt, as in Figure 3(f)), little magneto-ionic effects are expected since there is no driving force (no electric field) to induce ion motion inside the metal.²⁴ This is opposite to what happens in semiconductors (e.g., TaO_x), where the electric field will penetrate deeper into the layer. Interestingly, for low electrically conductive TaO_x (i.e., $\sigma_{\text{TaO}_x} < 100 \text{ S m}^{-1}$), ΔV_{int} becomes clearly lower as the Ta layer thickness increases (Figure 2(e)). For $\delta_{\text{Ta}} = 50$ nm, if σ_{TaO_x} is lower than 5 S m^{-1} , ΔV_{int} eventually drops below the threshold voltage (region highlighted in cyan), meaning that no magneto-ionic effects will be induced in this case (while, for thinner Ta layers, for the same σ_{TaO_x} value, ΔV_i will still be above the threshold). Note that during magneto-ionic motion of O^{2-} from Co_3O_4 to TaO_x , the values of σ_{TaO_x} will rapidly decrease, thus reducing

the interface voltage and slowing down the magneto-ionic process. Another interesting effect is that when Co_3O_4 transforms to metallic Co, the conductivity of the magneto-ionic layer ($\sigma_{\text{Co}_3\text{O}_4}$) increases. This, in turn, has an effect on ΔV_{int} which is shown in Figure 2(f). In bulk metallic Co, σ_{Co} can reach values $>10^7 \text{ S m}^{-1}$.⁵² As plotted in Figure 2(f), when $\sigma_{\text{Co}_3\text{O}_4}$ transforms to Co and $\sigma_{\text{Co}_3\text{O}_4}$ increases, the interface voltage drastically drops, and ΔV_{int} easily falls below the threshold voltage. Then any magneto-ionic response will tend to stop. As an example, for the particular case of $\delta_{\text{Ta}} = 50$ nm, any eventual O^{2-} ion motion triggered while σ_{TaO_x} is sufficiently large will tend to stop as soon as $\sigma_{\text{Co}_3\text{O}_4}$ increases above 10^3 S m^{-1} (see Figure 2(f)) or σ_{TaO_x} decreases below 5 S m^{-1} (Figure 2(e)). It is noteworthy that, although this intuitive picture is a simplified representation of the reality, it already provides some basic understanding of the role of the TaO_x layer thickness and resistivity on the induced magneto-ionic effects.

Notwithstanding the decrease of the steady-state M_S with the deposition of a Ta capping layer (by approximately 25% for $\delta_{\text{Ta}} = 25$ nm), the formation of TaO_x (which acts as a solid electrolyte) has one very beneficial effect: it drastically enhances magneto-ionic cyclability. This is evidenced in Figure 4, which shows the cyclability results (i.e., repeated increase/decrease of M) in a Co_3O_4 thin film and $\text{Co}_3\text{O}_4/\text{Ta}$ (25 nm) bilayer films upon application of -25 V/ $+25$ V voltage pulses with a duration of 80 s. As shown in Figure 4(a) and (b), a very stable and reversible behavior is observed during the first 10 cycles for both samples. However, the $\text{Co}_3\text{O}_4/\text{Ta}$ (25 nm) bilayer sample maintains a very stable cyclability even after 800 cycles (Figure 4(a)), whereas no sign of magneto-ionic effect is detected for Co_3O_4 films after 30 cycles (Figure 4(b)). This demonstrates a significant enhancement of the endurance of the system by the deposition of a Ta overlayer with appropriate thickness.

The improved cyclability in the $\text{Co}_3\text{O}_4/\text{Ta}$ (25 nm) bilayer is ascribed to the role of Ta in allowing diffusion of oxygen ions. In this sample, when negative voltage is applied, the O^{2-} ions exiting Co_3O_4 are captured by Ta, forming a TaO_x solid electrolyte, instead of being directly released to the liquid electrolyte. Ta is a well-known oxygen getter,⁵³ and TaO_x is a good ionic conductor.⁵⁴ In unprotected Co_3O_4 films, O^{2-} ions are directly dissolved in the propylene carbonate, and once solvated with the PC chains, they can travel long distances toward the positively charged counter electrode (i.e., the Pt

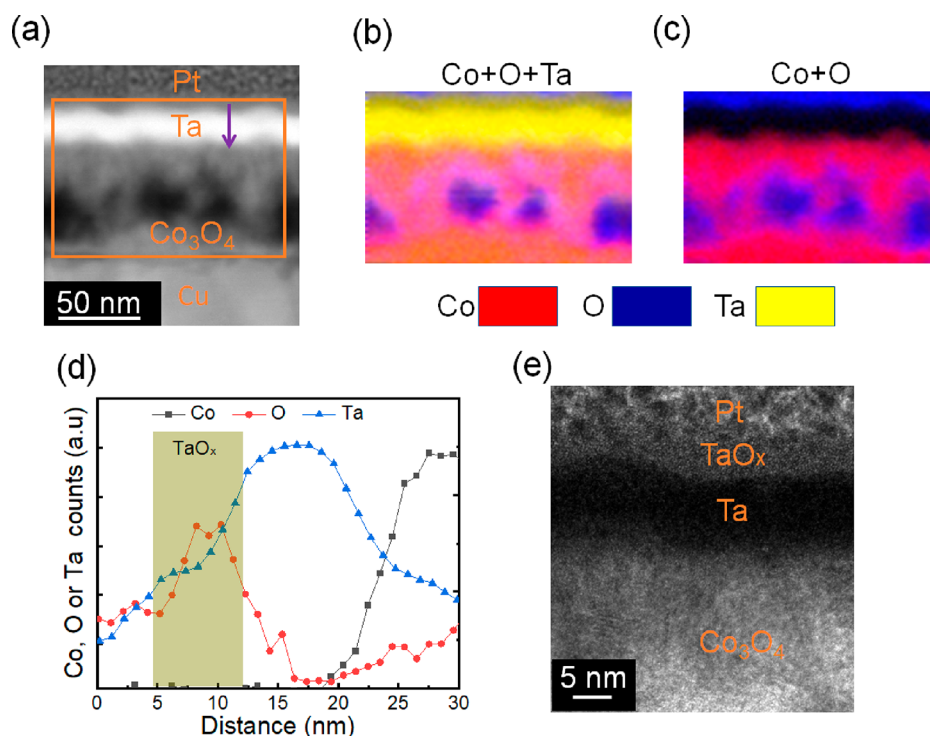


Figure 5. Compositional characterization of the $\text{Co}_3\text{O}_4/\text{Ta}$ (25 nm) films gated at -25 V for 1 h. (a) HAADF-STEM and (b, c) elemental EELS mappings corresponding to the area marked with an orange rectangle in the HAADF-STEM image. Cu and Pt layers serve as working electrode and protective capping layer during TEM lamellae preparation, respectively. Co, O, and Ta are represented by red, blue, and yellow colors in the EELS elemental mappings. (d) Depth profile of Co, O, and Ta elements along the dark pink arrow drawn in (a). (e) High-resolution TEM image of the sample treated at -25 V for 1 h.

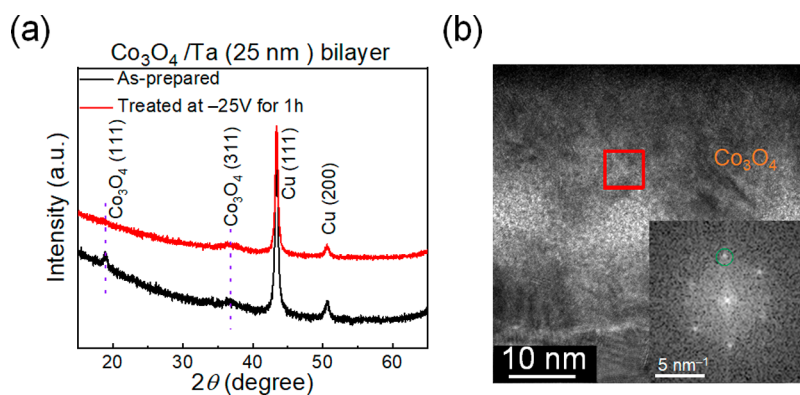


Figure 6. Structural characterization by X-ray diffraction (XRD) and high-resolution transmission electron microscopy (HRTEM). (a) $\theta/2\theta$ XRD diffraction patterns of $\text{Co}_3\text{O}_4/\text{Ta}$ (25 nm) films in the as-prepared state and after being treated at -25 V for 1 h. (b) HRTEM images of the cross section of the $\text{Co}_3\text{O}_4/\text{Ta}$ (25 nm) film after applying -25 V for 1 h. The inset shows the fast Fourier transform (FFT) of the area marked with a red rectangle, and it shows spots with an average interplanar distance of 0.19 nm, which corresponds to (101) hexagonal-closed-packed (HCP) metallic Co. For phase identification, the cards no. PDF 00-005-0727 and PDF 00-009-0418 were taken for Co and Co_3O_4 , respectively.

wire), where they eventually form O_2 gas bubbles and are released to the atmosphere at sufficiently high voltages. This long-distance transport of ions in the liquid is the main reason for the poor cyclability of uncapped Co_3O_4 films. However, when a Ta interlayer is grown adjacent to Co_3O_4 , O^{2-} ions move back and forth along relatively short distances (for alternating applied voltages of opposite polarities), and the process is confined between Co_3O_4 and the TaO_x solid electrolyte, thus drastically improving cyclability.

To further understand the effect of the top Ta layer on the induced magnetic properties from the perspective of the ion

transport mechanism, cross-sectional lamellae of a bilayer sample (40-nm-thick Co_3O_4 plus 25-nm-thick Ta overlayer) electrolyte-gated at -25 V for 1 h were studied by HAADF-STEM and EELS. As shown in Figure 5(a)–(c), an inhomogeneous microstructure inside the Co_3O_4 layer is generated upon voltage application, with Co-rich and O-rich regions, leading to void-like morphologies, in agreement with previous studies on this kind of magneto-ionic material.¹¹ In turn, an enrichment in O is observed in the upper part of the Ta layer. This is clearly evidenced by quantitative EELS analysis (Figure 5(d)) and high-resolution TEM (Figure 5(e)).

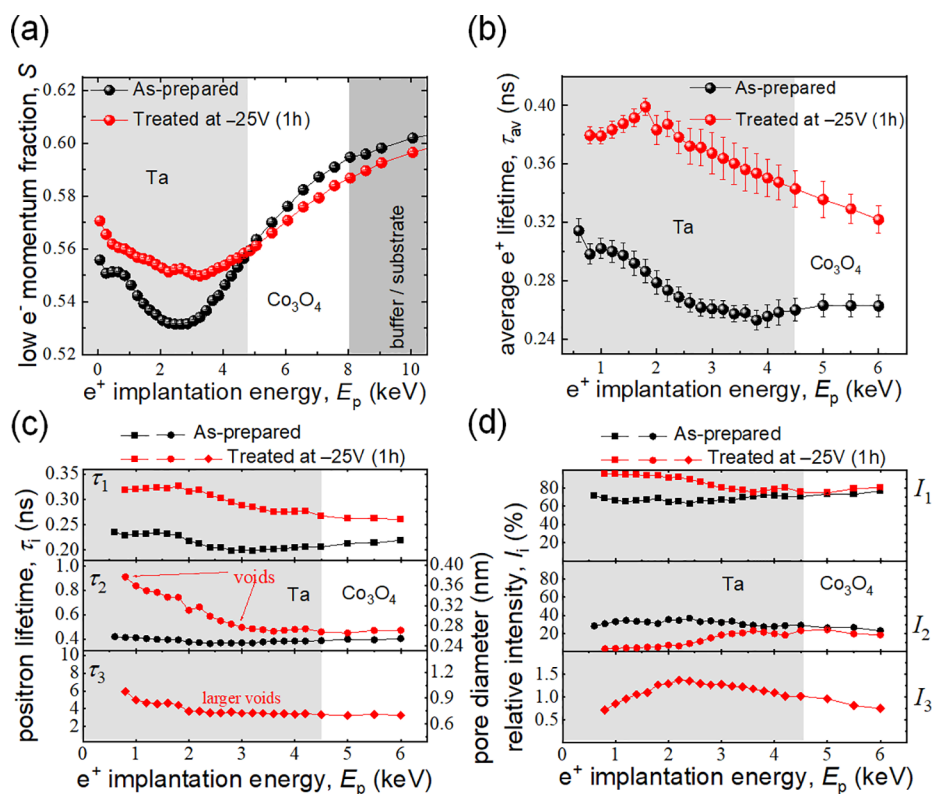


Figure 7. Positron annihilation spectroscopy characterization of the as-grown and voltage-treated (-25 V for 1 h) Co_3O_4/Ta (25 nm) sample. (a) Dependence of the low electron momentum fraction (S) on the positron implantation energy (E_p). (b) Dependence of the average positron lifetime, τ_{av} , on E_p . (c) Dependence of the positron lifetime components (τ_i) on E_p . (d) Dependence of the relative defect type intensity (I_i) on E_p .

This indicates that, besides the O^{2-} ion transport from Co_3O_4 toward and across the Ta layer, O^{2-} ions also locally migrate and redistribute inside the Co_3O_4 layer, eventually forming metallic Co.¹¹ Interestingly, the mixing of O and Ta elements on the top part of the Ta layer demonstrates the oxidation of Ta. Considering that the liquid electrolyte used in this work provides a nonaqueous environment, the observed O signal can only originate from oxygen transport from Co_3O_4 . The accumulation of O^{2-} on the top of the TaO_x layer suggests that ion transport remains rather restricted within the Co_3O_4/TaO_x bilayers (*i.e.*, short-distance ion diffusion). In other words, the presence of the thin TaO_x solid electrolyte limits the amount of O^{2-} released to the liquid, thereby enhancing cyclability. Furthermore, during this magneto-ionic experiment, Co_3O_4 tends to become more amorphous. This is corroborated by $\theta/2\theta$ X-ray diffraction (see Figure 6(a)), where the peak from Co_3O_4 (111) planes disappears upon voltage treatment. In addition, the FFT spots obtained from high-resolution TEM prove the existence of metallic Co in the treated sample, as can be seen in Figure 6(b). The formation of metallic Co is responsible for the M_S increase after voltage treatment (Figure 2(c) and Figure 3).

To assess the electrochemical behavior of the system, cyclic voltammetry (CV) curves were recorded for all the surfaces involved in the main magneto-ionic setup (see Figure S1 in the Supporting Information). When the Cu grown on Ti is exposed to the electrolyte, a cathodic wide peak is observed, centered at -0.9 V vs Pt reference electrode, while further anodic runs evidence a flat peak. This is consistent, in principle, with the reduction of Cu_2O (native oxide layer formed on Cu when exposed to air) to Cu (first wave) and

consequent oxidation of Cu to Cu_2O . The CV curve of Co_3O_4 grown onto the Ti/Cu does not show the Cu waves, confirming that the cobalt oxide layer does cover completely the Cu phase and prevents its oxidation/reduction. Once Ta is grown on Co_3O_4 , a tiny wide oxidation wave is observed, centered at 0.6 V vs Pt, in agreement with the expected oxidation of Ta. Since both coatings (Co_3O_4 and TaO_x) are less conductive than Cu, the redox processes are hindered compared to the case of Cu.

To shed further light on the microstructure of the films upon magneto-ionic actuation, Doppler broadening variable energy positron annihilation spectroscopy (DB-VEPAS)⁵⁵ and variable energy positron annihilation lifetime spectroscopy (VEPALS)⁵⁶ experiments were performed (see Experimental Section). PAS is a sensitive probe to open volume defects on atomic scales and across depth due to positrons' preferential localization and subsequent annihilation with electrons in crystal empty spaces, *i.e.*, vacancies and their agglomerates. The energy distribution and time necessary for annihilation depends on the local electron density.⁵⁷ As shown in Figure 7, after negative biasing at -25 V, the low electron momentum fraction, S (directly proportional to the size and concentration of defects),⁵⁸ increases in the Ta region but slightly drops in the Co_3O_4 layer, suggesting a substantial raise of defect density in Ta and a slight drop of defect concentration in Co_3O_4 . The increase of defect density in Ta is probably a consequence of the O^{2-} interdiffusion and the formation of TaO_x . Additionally, the average defect size (which is proportional to the average positron lifetime, τ_{av}), strongly increases in both TaO_x and Co_3O_4 layers after voltage actuation (Figure 7(b)). The expected average size is in the

range of large vacancy agglomerates (8–10 vacancies).⁵⁹ Figure 7(b) and (c) show the existence of three discrete lifetime components (τ_1 , τ_2 , and τ_3),⁵⁹ which correspond to three different average defect sizes.¹¹ They were obtained by deconvolution of PALS spectra using a nonlinear least-squared fitting method (package PALSfit software).⁶⁰ The corresponding relative intensities (I_1 , I_2 , and I_3) relate to the concentration of each defect type (size). The larger τ_i is, the larger the defect size is since it takes longer for positrons to be annihilated with electrons.⁵⁷ In the as-grown sample, only τ_1 and τ_2 lifetime components are detected, meaning an absence of large void-like structures (no τ_3) in the prebiasing state. The most abundant defect size (τ_1) contributes as $I_1 = 62$ –77% of the overall signal and is in the range of bivacancy clusters in the upper subsurface Ta region (*i.e.*, passivation layer) and single vacancy in the underneath Ta sublayer.⁵⁹ $\tau_1 \approx 213$ ps for Co_3O_4 represents a defect size involving 3–4 mixed (Co and O) vacancies within a complex, based on our previous works/publications.¹¹ After biasing at -25 V, τ_1 strongly increases both in Ta and Co_3O_4 layers. Open volume is generated in the size range of 4–6 vacancy agglomerations for Ta and >7 –8 for Co_3O_4 , which results in an increase of intensity to $I_1 = 75$ –95%. The second lifetime component, τ_2 , for the as-grown sample is in the range of large vacancy agglomerations (>10 vacancies), typical for grain boundaries, with corresponding $I_2 = 28$ –37% of positrons being annihilated at these defect states. Negative biasing increases τ_2 to the range of voids (the threshold is usually about 500 ps) with an average diameter in the range of 0.28–0.37 nm,⁶¹ while their density is quite small, up to $I_2 \approx 10\%$, and they do not reach deeper than the upper 10 nm of Ta. Clearly, these defects are associated with the formation of the upper TaO_x (Figure 5). Finally, a larger pore population (0.7–0.8 nm in diameter) was found after biasing (τ_3), with low but not negligible intensity ($I_3 \approx 1.4\%$), which extends into the Co_3O_4 layer. The existence of pore-related components (especially τ_3) is a fingerprint of increasing amorphization of the TaO_x layer, whereas the Co_3O_4 layer remains less affected and nanocrystalline. The largest free volume is found in the direct vicinity of the surface, *i.e.*, the most amorphized region. The increase of positron lifetimes in the Ta layer after biasing evidences the O^{2-} transport-generated expansion of available open volume channels, which enables large cyclability of the system.

CONCLUSIONS

In summary, this work demonstrates the beneficial effect of adding a thin solid ionic conductor (in this case, a naturally passivated amorphous Ta interlayer) on the magneto-ionic response of Co_3O_4 films under the action of an electric field when immersed in liquid electrolytes. *A priori*, adding a capping layer between the Co_3O_4 film and the liquid electrolyte could be thought of as simply hindering magneto-ionics and reducing (or eventually suppressing) any oxygen ion migration triggered by the externally applied electrical voltage. This is indeed observed for thin metallic capping layers (*e.g.*, 5 nm Pt) or thick highly resistive Ta layers (with a thickness larger than 50 nm). However, for thinner Ta interlayers, in spite of a moderate reduction of the steady-state M_s (by a factor of 25% for 25-nm-thick Ta), a drastic enhancement of magneto-ionic cyclability is observed, from less than 30 cycles in uncoated Co_3O_4 to more than 800 cycles for a Ta thickness of 25 nm. Such enhancement of endurance is ascribed to the key role of the generated TaO_x layer in preventing O^{2-} from

being released to the liquid electrolyte, *i.e.*, limiting oxygen ion transport within the $\text{Co}_3\text{O}_4/\text{TaO}_x$ layers. This is confirmed by compositional/structural characterization using HAADF-STEM and EELS as well as positron spectroscopy experiments. Beyond magneto-ionics, the reported strategy to enhance cyclability can be easily extrapolated to other systems relying on ion transport mechanisms, such as iontronics, sensors, or neuromorphic computing.

EXPERIMENTAL SECTION

Sample Fabrication. Co_3O_4 thin films of 40 nm thickness were grown at room temperature by reactive sputtering in a high-vacuum chamber (with a base pressure of $<8 \times 10^{-8}$ Torr) on nondoped (100)-oriented Si wafers previously coated with a 20-nm-thick titanium adhesion layer and 60-nm-thick copper seed layer. Prior to growing Co_3O_4 , the Cu seed layers were partly masked to leave enough space for the electric contact (*i.e.*, to later serve as a working electrode). The Co_3O_4 films were subsequently coated with Ta protective layers of variable thickness, ranging from 5 to 50 nm, which were left unprotected to self-passivate in air. Two reference films were also prepared to serve as references: uncoated Co_3O_4 and Co_3O_4 coated with Pt with the same range of thicknesses as Ta. The growth of Co_3O_4 was carried out in a mixed Ar and O_2 atmosphere using an oxygen partial pressure of 50% and a total working pressure of 3×10^{-3} Torr. The distance between the substrate and targets was around 10 cm, and the growth rate was approximately 0.6 \AA s^{-1} . Ti, Cu, Ta, and Pt layers were grown under 3×10^{-3} Torr Ar. The gun power to grow Ta was 100 W.

Magneto-ionic Characterization and Cyclic Voltammetry Curves. Room-temperature magneto-electric measurements were performed using a commercial vibrating sample magnetometer from Micro Sense (LOT, Quantum Design), with a maximum applied in-plane magnetic field of 2 T. The samples were electrolyte-gated using an external Agilent B2902A power supply, applying voltage between the counter electrode (a Pt wire) and the working electrode (*e.g.*, the investigated Si/Ti/Cu/ Co_3O_4 /Ta thin films) in a homemade electrolytic cell (see Figure 2(b)). The electrolyte consisted of anhydrous propylene carbonate with Na^+ and OH^- solvated species (10–25 ppm), formed by immersing small pieces of metallic sodium that were able to react with any possible traces of water.¹¹ Negative voltages in this work indicate the accumulation of negative charges at the working electrode (and *vice versa* for positive voltages). The magnetization (M) was obtained by normalizing the magnetic moment to the sample volume exposed to the electrolyte. Note that the linear slopes in the hysteresis loops at high fields (arising from diamagnetic or paramagnetic contributions) were subtracted by correcting the background signal (*i.e.*, at fields always significantly larger than the saturation fields).

Cyclic voltammetry curves for all the surfaces involved in the main magneto-ionic setup were also recorded. For these experiments, a scan speed of 10 mV/s and a potential sweep range from 0 V to -2 V to $+1.4$ V and to 0 V vs Pt were selected. The exposed surface was 0.5 cm^2 , and the distance between the reference and working electrode was 4 mm, thus mimicking the conditions utilized during the magneto-ionic experiments. Here, however, we used three electrodes (including a reference electrode), whereas magneto-ionic experiments were performed in a two-electrode configuration. Thus, all voltages in the CV curves are given with respect to a reference electrode, in this case Pt (99.99% Goodfellow), known to act well in organic solvents. The global cell (two-electrode) potential has been measured during these CV experiments to be on the order of 4 to 6 V depending on the system. Further potential could not be applied during the CV curves due to the limitations of the utilized potentiostat (VSP Biologic). However, the curves obtained in this potential range are already representative of the electrochemical behavior of the system.

Structural and Compositional Measurements. $\theta/2\theta$ XRD patterns were collected on a Materials Research diffractometer from Malvern PANalytical Company, equipped with a PIXcel^{1D} detector, using Cu $K\alpha$ radiation. HRTEM, HAADF-STEM, and EELS were

carried out on a TECNAI F20 HRTEM/STEM microscope operated at 200 kV. Cross-sectional lamellae were prepared by focused ion beam, placed onto a copper transmission electron microscopy grid, and topped with a protective platinum layer.

Doppler Broadening Variable Energy Positron Annihilation Spectroscopy and Variable Energy Positron Annihilation Lifetime Spectroscopy. DB-VEPAS measurements were conducted at the setup for *in situ* defect analysis (AIDA)⁵⁵ of the slow positron beamline (SPONSOR).⁶² Positrons were accelerated and mono-energetically implanted into samples in the range of $E_p = 0.05\text{--}35$ keV, which allows for depth-sensitive analysis. The mean positron implantation depth was approximated using a simple material density (ρ)-dependent formula: $\langle z \rangle = 36/\rho \cdot E_p^{1.62}$.⁶³ Since at the annihilation site thermalized positrons have very small momentum compared to the electrons, a broadening of the 511 keV line is observed mostly due to momentum of the electrons, which is measured with a high-purity Ge detector (overall energy resolution of 1.09 ± 0.01 at 511 keV). This broadening is characterized by a parameter S defined as a fraction of the annihilation distribution in the middle (511 ± 0.93 keV). The S -parameter is a fraction of positrons annihilating with low-momentum valence electrons and represents vacancy-type defects and their concentration.⁵⁸ VEPALS measurements were conducted at the monoenergetic positron source (MePS) beamline, which is an end station of the radiation source ELBE (Electron Linac for beams with high Brilliance and low Emittance) at Helmholtz-Zentrum Dresden-Rossendorf (Germany).⁵⁶ A digital lifetime CeBr₃ scintillator detector was used, with a homemade software employing an SPDevices ADQ14DC-2X with 14-bit vertical resolution and 2 GS s^{-1} (gigasamples per second) horizontal resolution and with a time resolution function down to about 0.230 ns.⁶⁴ The resolution function required for spectrum analysis uses two Gaussian functions with distinct intensities depending on the positron implantation energy, E_p , and appropriate relative shifts. All spectra contained at least 1×10^7 counts. The spectra were deconvoluted using the PALSfit fitting software into discrete lifetime components, which directly confirm different defect types (*i.e.*, sizes).⁶⁰ Typical lifetime spectrum $N(t)$ is described by $N(t) = \sum (I_i/\tau_i) \exp(-t/\tau_i)$, where τ_i and I_i are the positron lifetime and intensity of the i th component, respectively ($\sum I_i = 1$).

The corresponding relative intensities (I_i) reflect to a large extent the concentration of each defect type, and positron lifetimes (τ_i) are directly proportional to defect size (*i.e.*, the larger the open volume, the lower the probability and the longer it takes for positrons to be annihilated with electrons). The positron lifetime and its intensity were probed as a function of positron implantation energy E_p or, in other words, implantation depth (thickness). The average positron lifetime τ_{av} is defined as $\tau_{av} = \sum \tau_i \cdot I_i$, which is the weighted average of the defect size. The shortest lifetime component ($\tau_1 < 0.32$ ns) represents positron annihilation inside vacancy clusters (likely within grains) and/or at the grain boundaries, depending on the film's microstructure. The intermediate lifetime ($0.35 < \tau_2 < 0.90$ ns) accounts for annihilation at larger vacancy clusters (linked to grain boundaries and their intersections), surface states, and small voids/pores (0.28–0.37 nm in diameter, calculated based on the shape-free model for pore-size estimation of Wada *et al.*;⁵⁹ the longest lifetime component ($2.3 < \tau_3 < 3.3$ ns) indicates contributions of larger voids (0.58–0.74 nm in diameter).

ASSOCIATED CONTENT

Supporting Information

The Supporting Information is available free of charge at <https://pubs.acs.org/doi/10.1021/acsnano.3c01105>.

Cyclic voltammetry curves of the basic investigated layer structures (PDF)

AUTHOR INFORMATION

Corresponding Authors

Enric Menéndez – Departament de Física, Universitat Autònoma de Barcelona, 08193 Cerdanyola del Valles, Spain; orcid.org/0000-0003-3809-2863; Email: enric.menendez@uab.cat

Jordi Sort – Departament de Física, Universitat Autònoma de Barcelona, 08193 Cerdanyola del Valles, Spain; Institució Catalana de Recerca i Estudis Avançats (ICREA), E-08010 Barcelona, Spain; orcid.org/0000-0003-1213-3639; Email: jordi.sort@uab.cat

Authors

Zhengwei Tan – Departament de Física, Universitat Autònoma de Barcelona, 08193 Cerdanyola del Valles, Spain

Zheng Ma – Departament de Física, Universitat Autònoma de Barcelona, 08193 Cerdanyola del Valles, Spain

Laura Fuentes – Institut de Ciència de Materials de Barcelona, CSIC, 08193 Bellaterra, Barcelona, Spain; Centre Nacional de Microelectrònica, Institut de Microelectrònica de Barcelona-CSIC, 08193 Bellaterra, Barcelona, Spain; orcid.org/0000-0002-8799-2369

Maciej Oskar Liedke – Institute of Radiation Physics, Helmholtz-Zentrum Dresden - Rossendorf, Dresden 01328, Germany; orcid.org/0000-0001-7933-7295

Maik Butterling – Institute of Radiation Physics, Helmholtz-Zentrum Dresden - Rossendorf, Dresden 01328, Germany

Ahmed G. Attallah – Institute of Radiation Physics, Helmholtz-Zentrum Dresden - Rossendorf, Dresden 01328, Germany; orcid.org/0000-0002-7759-0315

Eric Hirschmann – Institute of Radiation Physics, Helmholtz-Zentrum Dresden - Rossendorf, Dresden 01328, Germany

Andreas Wagner – Institute of Radiation Physics, Helmholtz-Zentrum Dresden - Rossendorf, Dresden 01328, Germany

Llibert Abad – Centre Nacional de Microelectrònica, Institut de Microelectrònica de Barcelona-CSIC, 08193 Bellaterra, Barcelona, Spain

Nieves Casañ-Pastor – Institut de Ciència de Materials de Barcelona, CSIC, 08193 Bellaterra, Barcelona, Spain; orcid.org/0000-0003-2979-4572

Aitor F. Lopeandia – Departament de Física, Universitat Autònoma de Barcelona, 08193 Cerdanyola del Valles, Spain; Catalan Institute of Nanoscience and Nanotechnology (ICN2), CSIC and BIST, 08193 Barcelona, Spain

Complete contact information is available at:

<https://pubs.acs.org/doi/10.1021/acsnano.3c01105>

Author Contributions

The manuscript was written through contributions of all authors. All authors have given approval to the final version of the manuscript.

Notes

The authors declare no competing financial interest.

ACKNOWLEDGMENTS

Financial support by the European Union's Horizon 2020 Research and Innovation Programme ("BeMAGIC" European Training Network, ETN/ITN Marie Skłodowska-Curie Grant No. 861145), the European Research Council (2021-ERC-Advanced "REMINDS" Grant No. 101054687), the Spanish Government (CEX2019-000917-S y PID2021-123276OB-I00, PID2020-116844RB-C21, and PDC2021-121276-C31), and

the Generalitat de Catalunya (2021-SGR-00651) is acknowledged. J.S. thanks the Spanish “Fábrica Nacional de Moneda y Timbre” (FNMT) for fruitful discussions. E.M. is a Serra Hünter Fellow. Parts of this research were carried out at ELBE at the Helmholtz-Zentrum Dresden - Rossendorf e. V., a member of the Helmholtz Association. We would like to thank the facility staff for assistance. This work was partially supported by the Impulse-und Net-working fund of the Helmholtz Association (FKZ VH-VI-442 Memriox) and the Helmholtz Energy Materials Characterization Platform (03ET7015).

REFERENCES

- (1) Shalf, J. M.; Leland, R. Computing Beyond Moore's Law. *Computer* **2015**, *48*, 14–23.
- (2) Ramesh, R.; Manipatruni, S. Electric Field Control of Magnetism. *Proc. R. Soc. A* **2021**, *477*, 20200942.
- (3) Žutić, I.; Fabian, J.; Das Sarma, S. Spintronics: Fundamentals and Applications. *Rev. Mod. Phys.* **2004**, *76*, 323–410.
- (4) Wolf, S. A.; Awschalom, D. D.; Buhrman, R. A.; Daughton, J. M.; von Molnar, S.; Roukes, M. L.; Chtchelkanova, A. Y.; Treger, D. M. Spintronics: A Spin-Based Electronics Vision for the Future. *Science* **2001**, *294*, 1488–1495.
- (5) Kawahara, T.; Ito, K.; Takemura, R.; Ohno, H. Spin-Transfer Torque RAM Technology: Review and Prospect. *Microelectron. Reliab.* **2012**, *52*, 613–627.
- (6) Brataas, A.; Kent, A. D.; Ohno, H. Current-Induced Torques in Magnetic Materials. *Nat. Mater.* **2012**, *11*, 372–381.
- (7) Han, X.; Wang, X.; Wan, C.; Yu, G.; Lv, X. Spin-Orbit Torques: Materials, Physics, and Devices. *Appl. Phys. Lett.* **2021**, *118*, 120502.
- (8) Gambardella, P.; Miron, I. M. Current-Induced Spin-orbit Torques. *Philos. Trans. R. Soc. A* **2011**, *369*, 3175–3197.
- (9) Shiota, Y.; Nozaki, T.; Bonell, F.; Murakami, S.; Shinjo, T.; Suzuki, Y. Induction of Coherent Magnetization Switching in a Few Atomic Layers of FeCo Using Voltage Pulses. *Nat. Mater.* **2012**, *11*, 39–43.
- (10) Song, C.; Cui, B.; Li, F.; Zhou, X.; Pan, F. Recent Progress in Voltage Control of Magnetism: Materials, Mechanisms, and Performance. *Prog. Mater. Sci.* **2017**, *87*, 33–82.
- (11) Quintana, A.; Menéndez, E.; Liedke, M. O.; Butterling, M.; Wagner, A.; Sireus, V.; Torruella, P.; Estradé, S.; Peiró, F.; Dendooven, J.; Detavernier, C.; Murray, P. D.; Gilbert, D. A.; Liu, K.; Pellicer, E.; Nogués, J.; Sort, J. Voltage-Controlled ON–OFF Ferromagnetism at Room Temperature in a Single Metal Oxide Film. *ACS Nano* **2018**, *12*, 10291–10300.
- (12) Bauer, U.; Yao, L.; Tan, A. J.; Agrawal, P.; Emori, S.; Tuller, H. L.; Van Dijken, S.; Beach, G. S. D. Magneto-ionic Control of Interfacial Magnetism. *Nat. Mater.* **2015**, *14*, 174–181.
- (13) Gilbert, D. A.; Grutter, A. J.; Arenholz, E.; Liu, K.; Kirby, B. J.; Borchers, J. A.; Maranville, B. B. Structural and Magnetic Depth Profiles of Magneto-ionic Heterostructures Beyond the Interface Limit. *Nat. Commun.* **2016**, *7*, 12264.
- (14) Rojas, J.; Quintana, A.; Lopeandia, A.; Salguero, J.; Costa-Krämer, J. L.; Abad, L.; Liedke, M. O.; Butterling, M.; Wagner, A.; Henderick, L.; Dendooven, J.; Detavernier, C.; Sort, J.; Menéndez, E. Boosting Room-Temperature Magneto-ionics in a Non-Magnetic Oxide Semiconductor. *Adv. Funct. Mater.* **2020**, *30*, 2003704.
- (15) Martins, S.; De Rojas, J.; Tan, Z.; Cialone, M.; Lopeandia, A.; Herrero-Martín, J.; Costa-Krämer, J. L.; Menéndez, E.; Sort, J. Dynamic Electric-field-induced Magnetic Effects in Cobalt Oxide Thin Films: Towards Magneto-ionic Synapses. *Nanoscale* **2022**, *14*, 842–852.
- (16) Dasgupta, S.; Das, B.; Knapp, M.; Brand, R. A.; Ehrenberg, H.; Kruk, R.; Hahn, H. Intercalation-driven Reversible Control of Magnetism in Bulk Ferromagnets. *Adv. Mater.* **2014**, *26*, 4639–4644.
- (17) Vasala, S.; Jakob, A.; Wissel, K.; Waidha, A. I.; Alff, L.; Clemens, O. Reversible Tuning of Magnetization in a Ferromagnetic Ruddlesde-Popper-Type Manganite by Electrochemical Fluoride Ion Intercalation. *Adv. Electron. Mater.* **2020**, *6*, 1900974.
- (18) Tan, A. J.; Huang, M.; Avci, C. O.; Büttner, F.; Mann, M.; Hu, W.; Mazzoli, C.; Wilkins, S.; Tuller, H. L.; Beach, G. S. D. Magneto-Ionic Control of Magnetism Using a Solid-State Proton Pump. *Nat. Mater.* **2019**, *18*, 35–41.
- (19) Ye, X.; Singh, H. K.; Zhang, H.; Geßwein, H.; Chellali, M. R.; Witte, R.; Molinari, A.; Skokov, K.; Gutfleisch, O.; Hahn, H.; Kruk, R. Giant Voltage-Induced Modification of Magnetism in Micron-Scale Ferromagnetic Metals by Hydrogen Charging. *Nat. Commun.* **2020**, *11*, 4849.
- (20) Chen, G.; Ophus, C.; Quintana, A.; Kwon, H.; Won, C.; Ding, H.; Wu, Y.; Schmid, A. K.; Liu, K. Reversible Writing/deleting of Magnetic Skyrmions Through Hydrogen Adsorption/desorption. *Nat. Commun.* **2022**, *13*, 1350.
- (21) Lu, N.; Zhang, Z.; Wang, Y.; Li, H.-B.; Qiao, S.; Zhao, B.; He, Q.; Lu, S.; Li, C.; Wu, Y.; Zhu, M.; Lyu, X.; Chen, X.; Li, Z.; Wang, M.; Zhang, J.; Tsang, S. C.; Guo, J.; Yang, S.; Zhang, J.; Deng, K.; Zhang, D.; Ma, J.; Ren, J.; Wu, Y.; Zhu, J.; Zhou, S.; Tokura, Y.; Nan, C.-W.; Wu, J.; Yu, P. Enhanced Low-Temperature Proton Conductivity in Hydrogen-Intercalated Brownmillerite Oxide. *Nat. Energy* **2022**, *7*, 1208–1216.
- (22) De Rojas, J.; Quintana, A.; Lopeandia, A.; Salguero, J.; Muñiz, B.; Ibrahim, F.; Chshiev, M.; Nicolenco, A.; Liedke, M. O.; Butterling, M.; Wagner, A.; Sireus, V.; Abad, L.; Jensen, C. J.; Liu, K.; Nogués, J.; Costa-Krämer, J. L.; Menéndez, E.; Sort, J. Voltage-Driven Motion of Nitrogen Ions: A New Paradigm for Magneto-Ionics. *Nat. Commun.* **2020**, *11*, 5871.
- (23) De Rojas, J.; Salguero, J.; Ibrahim, F.; Chshiev, M.; Quintana, A.; Lopeandia, A.; Liedke, M. O.; Butterling, M.; Hirschmann, E.; Wagner, A.; Abad, L.; Costa-Krämer, J. L.; Menéndez, E.; Sort, J. Magneto-ionics in Single-layer Transition Metal Nitrides. *ACS Appl. Mater. Interfaces* **2021**, *13*, 30826–30834.
- (24) De Rojas, J.; Salguero, J.; Quintana, A.; Lopeandia, A.; Liedke, M. O.; Butterling, M.; Attallah, A. G.; Hirschman, E.; Wagner, A.; Abad, L.; Costa-Krämer, J. L.; Sort, J.; Menéndez, E. Critical Role of Electrical Resistivity in Magnetoionics. *Phys. Rev. Appl.* **2021**, *16*, 034042.
- (25) Tan, Z.; Martins, S.; Escobar, M.; De Rojas, J.; Ibrahim, F.; Chshiev, M.; Quintana, A.; Lopeandia, A.; Costa-Krämer, J. L.; Menéndez, E. From Binary to Ternary Transition-metal Nitrides: A Boost Toward Nitrogen Magneto-ionics. *ACS Appl. Mater. Interfaces* **2022**, *14*, 44581–44590.
- (26) Tan, Z.; De Rojas, J.; Martins, S.; Lopeandia, A.; Quintana, A.; Cialone, M.; Herrero-Martín, J.; Meererschaut, J.; Vantomme, A.; Costa-Krämer, J. L.; Sort, J.; Menéndez, E. Frequency-dependent Stimulated and Post-stimulated Voltage Control of Magnetism in Transition Metal Nitrides: Towards Brain-Inspired Magneto-ionics. *Mater. Horiz.* **2023**, *10*, 88–96.
- (27) Navarro-Senent, C.; Quintana, A.; Menéndez, E.; Pellicer, E.; Sort, J. Electrolyte-gated Magneto-electric Actuation: Phenomenology, Materials, Mechanisms, and Prospective Applications. *APL Mater.* **2019**, *7*, 030701.
- (28) De Rojas, J.; Quintana, A.; Rius, G.; Stefani, C.; Domingo, N.; Costa-Krämer, J. L.; Menéndez, E.; Sort, J. Voltage Control of Magnetism with Magneto-Ionic Approaches: Beyond Voltage-Driven Oxygen Ion Migration. *Appl. Phys. Lett.* **2022**, *120*, 070501.
- (29) Zehner, J.; Wolf, D.; Hasan, M. U.; Huang, M.; Bono, D.; Nielsch, K.; Leistner, K.; Beach, G. S. D. Magnetoionic Control of Perpendicular Exchange Bias. *Phys. Rev. Mater.* **2021**, *5*, L061401.
- (30) Martins, S.; Ma, Z.; Solans-Monfort, X.; Sodupe, M.; Rodriguez-Santiago, L.; Menéndez, E.; Pellicer, E.; Sort, J. Enhancing Magneto-ionic Effects in Cobalt Oxide Films by Electrolyte Engineering. *Nanoscale Horiz.* **2022**, *8*, 118–126.
- (31) Zhang, Q.; Luo, X.; Wang, L.; Zhang, L.; Khalid, B.; Gong, J.; Wu, H. Lithium-Ion Battery Cycling for Magnetism Control. *Nano Lett.* **2016**, *16*, 583–587.
- (32) Quintana, A.; Firme, A. A.; Jensen, C. J.; Zheng, D.; Liu, C.; Zhang, X.; Liu, K. Hydroxide-Based Magneto-ionics: Electric-Field

- Control of Reversible Paramagnetic-to-Ferromagnetic Switch in α -Co(OH)₂ films. *J. Mater. Chem. C* **2022**, *10*, 17145.
- (33) Walter, J.; Voigt, B.; Day-Roberts, E.; Heltemes, K.; Fernandes, R. M.; Biorol, T.; Leighton, C. Voltage-induced Ferromagnetism in a Diamagnet. *Sci. Adv.* **2020**, *6*, eabb7721.
- (34) Molinari, A.; Hahn, H.; Kruk, R. Voltage-control of Magnetism in All-solid-state and Solid/liquid Magnetoelectric Composites. *Adv. Mater.* **2019**, *31*, 1806662.
- (35) Pachat, R.; Ourdani, D.; Syskaki, M.; Lamperti, A.; Roy, S.; Chen, S.; Pietro, A. D.; Largeau, L.; Juge, R.; Massouras, M.; Balan, C.; Van Der Jagt, J. W.; Agnus, G.; Roussigné, Y.; Gabor, M.; Chérif, S. M.; Durin, G.; Ono, S.; Langer, J.; Querlioz, D.; Ravelosona, D.; Belmeugeni, M.; Herrera Diez, L. Magneto-Ionics in Annealed W/CoFeB/HfO₂ Thin Films. *Adv. Mater. Interfaces* **2022**, *9*, 2200690.
- (36) Zhou, X.; Yan, Y.; Jiang, M.; Cui, B.; Pan, F.; Song, C. Role of Oxygen Ion Migration in the Electrical Control of Magnetism in Pt/Co/Ni/HfO₂ Films. *J. Phys. Chem. C* **2016**, *120*, 1633–1639.
- (37) Herrera Diez, L.; Kruk, R.; Leistner, K.; Sort, J. Magnetoelectric Materials, Phenomena, and Devices. *APL Mater.* **2021**, *9*, 050401.
- (38) Chen, G.; Mascaraque, A.; Jia, H.; Zimmermann, B.; Robertson, M.; Lo Conte, R.; Hoffmann, M.; González Barrio, M. A.; Ding, H.; Wiesendanger, R.; Michel, E. G.; Blügel, S.; Schmid, A. K.; Liu, K. Large Dzyaloshinskii-Moriya Interaction Induced by Chemisorbed Oxygen on a Ferromagnet Surface. *Sci. Adv.* **2020**, *6*, eaba4924.
- (39) Chen, G.; Robertson, M.; Hoffmann, M.; Ophus, C.; Fernandes Cauduro, A. L.; Lo Conte, R.; Ding, H.; Wiesendanger, R.; Blügel, S.; Schmid, A. K.; Liu, K. Observation of Hydrogen-Induced Dzyaloshinskii-Moriya Interaction and Reversible Switching of Magnetic Chirality. *Phys. Rev. X* **2021**, *11*, 021015.
- (40) Huang, M.; Usama Hasan, M.; Klyukin, K.; Zhang, D.; Lyu, D.; Gargiani, P.; Valvidares, M.; Sheffels, S.; Churikova, A.; Büttner, F.; Zehner, J.; Caretta, L.; Lee, K.-Y.; Chang, J.; Wang, J.-P.; Leistner, K.; Yildiz, B.; Beach, G. S. D. Voltage Control of Ferrimagnetic Order and Voltage-assisted Writing of Ferrimagnetic Spin Textures. *Nat. Nanotechnol.* **2021**, *16*, 981–988.
- (41) Zehner, J.; Huhnstock, R.; Oswald, S.; Wolff, U.; Soldatov, I.; Ehresmann, A.; Nielsch, K.; Holzinger, D.; Leistner, K. Nonvolatile Electric Control of Exchange Bias by a Redox Transformation of the Ferromagnetic Layer. *Adv. Electron. Mater.* **2019**, *5*, 1900296.
- (42) Lecuyer, S.; Quemerais, A.; Jezequel, G. Composition of Natural Oxide Films on Polycrystalline Tantalum Using XPS Electron Take-Off Angle Experiments. *Surf. Interface Anal.* **1992**, *18*, 257–261.
- (43) Levine, B. R.; Sporer, S.; Poggie, R. A.; Della Valle, C. J.; Jacobs, J. J. Experimental and Clinical Performance of Porous Tantalum in Orthopedic Surgery. *Biomaterials* **2006**, *27*, 4671–4681.
- (44) Stella, K.; Burstel, D.; Franzka, S.; Posth, O.; Diesing, D. Preparation and Properties of Thin Amorphous Tantalum Films Formed by Small e-beam Evaporators. *J. Phys. D: Appl. Phys.* **2009**, *42*, 135417.
- (45) Dalla Torre, J.; Gilmer, G. H.; Windt, D. L.; Kalyanaraman, R.; Baumann, F. H.; O'Sullivan, P. L.; Sapjeta, J.; DiAz De La Rubia, T.; Djafari Rouhani, M. Microstructure of Thin Tantalum Films Sputtered onto Inclined Substrates: Experiments and Atomistic Simulations. *J. Appl. Phys.* **2003**, *94*, 263–271.
- (46) Liu, Q.; Wu, F.; Mu, D.; Wu, B. A Theoretical Study on Na⁺ Solvation in Carbonate Ester and Ether Solvents for Sodium-ion Batteries. *Phys. Chem. Chem. Phys.* **2020**, *22*, 2164–2175.
- (47) Weisheit, M.; Fähler, S.; Marty, A.; Souche, Y.; Poinsignon, C.; Givord, D. Electric Field-Induced Modification of Magnetism in Thin-Film Ferromagnets. *Science* **2007**, *315*, 349–351.
- (48) Silva, C.; Vovk, A.; Da Silva, R. C.; Strichovanec, P.; Algarabel, P. A.; Gonçalves, A. P.; Borges, R. P.; Godinho, M.; Cruz, M. M. Magnetic Properties of Co–N Thin Films Deposited by Reactive Sputtering. *Thin Solid Films* **2014**, *556*, 125–127.
- (49) Li, Z. L.; Du, B. X.; Yang, Z. R.; Li, J. Effects of Crystal Morphology on Space Charge Transportation and Dissipation of Sic/Silicone Rubber Composites. *IEEE Trans. Dielectr. Electr. Insul.* **2017**, *24*, 2616–2625.
- (50) Krikorian, E.; Sneed, R. J. Deposition of Tantalum, Tantalum Oxide, and Tantalum Nitride with Controlled Electrical Characteristics. *J. Appl. Phys.* **1996**, *37*, 3674–3681.
- (51) Gerstenberg, D.; Calbick, C. J. Effects of Nitrogen, Methane, and Oxygen on Structure and Electrical Properties of Thin Tantalum Films. *J. Appl. Phys.* **1964**, *35*, 402–407.
- (52) De Vries, J. W. C. Temperature and Thickness Dependence of the Resistivity of Thin Polycrystalline Aluminium, Cobalt, Nickel, Palladium, Silver and Gold Films. *Thin Solid Films* **1988**, *167*, 25–32.
- (53) Zubler, E. G. The Gettering Properties of Tantalum. *J. Electrochem. Soc. Jpn.* **1963**, *110*, 1072.
- (54) Bean, C. P.; Fisher, J. C.; Vermilyea, D. A. Ionic Conductivity of Tantalum Oxide at Very High Fields. *Phys. Rev.* **1956**, *101*, 551.
- (55) Liedke, M. O.; Anwand, W.; Bali, R.; Cornelius, S.; Butterling, M.; Trinh, T. T.; Wagner, A.; Salamon, S.; Walecki, D.; Smekhova, A. Open Volume Defects and Magnetic Phase Transition in Fe₆₀Al₄₀ Transition Metal Aluminide. *J. Appl. Phys.* **2015**, *117*, 163908.
- (56) Wagner, A.; Butterling, M.; Liedke, M. O.; Potzger, K.; Krause-Rehberg, R. Positron Annihilation Lifetime and Doppler Broadening Spectroscopy at the ELBE Facility. *AIP Conf. Proc.* **2018**, *1970*, 040003.
- (57) Tuomisto, F.; Makkonen, I. Defect Identification in Semiconductors with Positron Annihilation: Experiment and Theory. *Rev. Mod. Phys.* **2013**, *85*, 1583–1631.
- (58) Clement, M.; De Nijs, J. M. M.; Balk, P.; Schut, H.; Van Veen, A. Analysis of Positron Beam Data by the Combined Use of the Shape-and Wing-Parameters. *J. Appl. Phys.* **1996**, *79*, 9029–9036.
- (59) Xu, Q.; Popov, E.; Troev, T.; Zhang, J.; Dai, Y. Positron Lifetime Calculation of Vacancy Clusters in Tantalum Containing Hydrogen and Helium. *J. Nucl. Mater.* **2018**, *506*, 71–75.
- (60) Olsen, J. V.; Kirkegaard, P.; Pedersen, N. J.; Eldrup, M. PALSfit: A New Program for the Evaluation of Positron Lifetime Spectra. *Phys. Status Solidi* **2007**, *4*, 4004–4006.
- (61) Wada, K.; Hyodo, T. A Simple Shape-Free Model for Pore-Size Estimation with Positron Annihilation Lifetime Spectroscopy. *J. Phys. Conf. Ser.* **2013**, *443*, 012003.
- (62) Anwand, W.; Brauer, G.; Butterling, M.; Kissener, H. R.; Wagner, A. Design and Construction of a Slow Positron Beam for Solid and Surface Investigations. *Defect Diffus. Forum.* **2012**, *331*, 25–40.
- (63) Dryzek, J.; Horodek, P. GEANT4 Simulation of Slow Positron Beam Implantation Profiles. *Nucl. Instruments Methods Phys. Res. Sect. B Beam Interact. with Mater. Atoms.* **2008**, *266*, 4000–4009.
- (64) Hirschmann, E.; Butterling, M.; Hernandez Acosta, U.; Liedke, M. O.; Attallah, A. G.; Petring, P.; Görler, M.; Krause-Rehberg, R.; Wagner, A. A New System for Real-time Data Acquisition and Pulse Parameterization for Digital Positron Annihilation Lifetime Spectrometers With High Repetition rates. *J. Instrum.* **2021**, *16*, 08001.

Supporting Information

Regulating oxygen ion transport at the nanoscale to enable
highly cyclable magneto-ionic control of magnetism

*Zhengwei Tan,[†] Zheng Ma,[†] Laura Fuentes,^{‡, #} Maciej Oskar Liedke,[¥] Maik Butterling,[¥] Ahmed
G. Attallah,[¥] Eric Hirschmann,[¥] Andreas Wagner,[¥] Llibert Abad,^{‡, #} Nieves Casañ-Pastor,[‡] Aitor
F. Lopeandia,[†] Enric Menéndez,^{*, †}, Jordi Sort^{*, †, □}*

[†]Departament de Física, Universitat Autònoma de Barcelona, 08193 Cerdanyola del Vallès,

Spain

[‡]Institut de Ciència de Materials de Barcelona, CSIC, Campus UAB, 08193 Bellaterra,

Barcelona, Spain

[#]Centre Nacional de Microelectrònica, Institut de Microelectrònica de Barcelona-CSIC, Campus

UAB, 08193 Bellaterra, Barcelona, Spain

[¥]Institute of Radiation Physics, Helmholtz-Zentrum Dresden - Rossendorf, Dresden 01328,

Germany

Barcelona, Spain

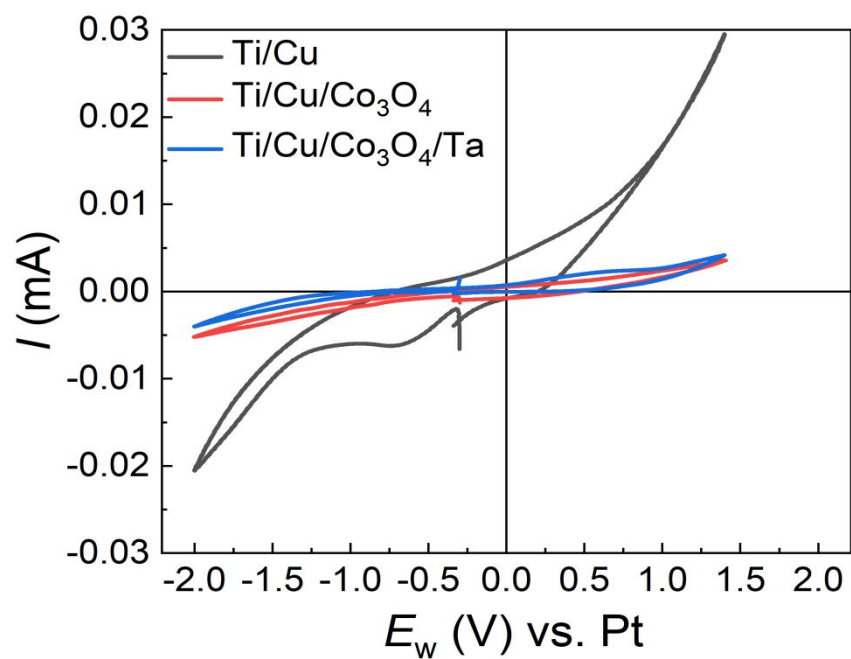


Figure S1: Cyclic voltammetry curves corresponding to the bare Ti/Cu conductive layers, the Ti/Cu/Co₃O₄ system and the Ti/Cu/Co₃O₄/Ta system.

4 General discussion

In the following, we emphasize the essential findings derived from the research presented in this Thesis. By placing these results within a broader context, we aim to provide a comprehensive understanding of the significance of this study in the realm of practical applications, particularly in emerging fields like magnetism-based memory and processing technologies, as well as the recently proposed neuromorphic computing paradigms.

This Thesis centers on “structural-ion” systems, providing a robust foundation for fundamental scientific exploration and practical applications. These systems inherently possess mobile ions originating from their structural elements, either oxygen (as in Co_3O_4) or nitrogen (as in CoN , CoMnN). As evidenced by our findings, in these systems one can induce ferromagnetism in ambient conditions with the application of just a few volts, demonstrating both energy efficiency and adaptability for room temperature operations. In addition to these advantages shared with most typical magneto-ionic systems, “structural-ion” materials offer distinctive benefits. Notably, they exhibit an innate and complete OFF state characterized by paramagnetic M vs. H curves. Achieving such a state remains a challenge for many systems that focus on single magnetic metals, largely due to their difficulty to be fully oxidized. In addition, they provide readily accessible lattice sites that facilitate ion diffusion. In terms of the fabrication process, all these magnetic target materials were grown at room temperature by magnetron sputtering on Si wafers, which is cost-effective and ensures compatibility with the well-established semiconductor industries. For these reasons, the magneto-ionic systems studied in this Thesis are not only technologically significant but also commercially viable, fostering advancements in magnetism control, energy efficiency, and data storage.

We have explored methods to enhance the electric field effect within magneto-ionics, paving the way for more efficient systems. Employing a liquid electrolyte, specifically the anhydrous propylene carbonate with Na^+ and OH^- solvated species, has allowed for the generation of strong electric fields at the interface between the magnetic material and the liquid electrolyte. However, material engineering offers avenues for further enhancement of magneto-ionic effects. For example, the partial substitution of Co by Mn in the thin-film composition transforms CoN films from metallic-like to semiconducting, extending the electric field's influence further into the film. This change increases N-ion transport channels, as verified by HAADF-STEM and EELS (Figure 3 in section 3.2 on page 106) and improves magneto-ionic

behavior. Moreover, decreasing the thickness of CoN films from 200 nm to 5 nm yields a remarkable 7.4-fold increase in ion motion rate. Visualizing the system as a parallel plate capacitor offers a way to explain these results: the electric field intensity is inversely related to the active dielectric thickness. Consequently, thinner films generate stronger electric fields, propelling ion diffusion more effectively. Broadly, these advancements in the electric field effect, achieved through elemental substitution and device miniaturization, have implications beyond magneto-ionics, including in fields like electrochemical catalysis, batteries, solar cells, and spintronics.

Furthermore, our research broadens the application of magneto-ionic systems to neuromorphic computing, with a particular focus on innovative brain-inspired functionalities. Neuromorphic computing, inspired by the brain's architecture, pioneers the development of synaptic devices with memory and processing capabilities, moving away from the limitations imposed by traditional von Neumann computing. In artificial neural networks, the concept of synaptic weight is of utmost importance as it symbolizes the impact of applied stimuli, such as electric fields in terms of their strength and polarity, on the physical properties of synaptic devices, including resistance and magnetization. The ability to adjust these synaptic weights is a fundamental requirement for achieving synaptic plasticity, which facilitates learning and enhances prediction accuracy. So far, the progress in magneto-ionics has made it a suitable approach for low-power hardware that minimizes Joule heating effects, promising energy-efficient artificial synaptic devices. The inherent vector nature of magnetization introduces an additional dimension, allowing for the direct programming of both positive and negative synaptic weights without the need for additional electronic components. Indeed, like other neuromorphic systems, the adjustment of synaptic weights through successive voltage pulses has become possible. Consequently, we can mimic controlled processes such as information processing, memory retention, and recovery. However, in conventional neuromorphic systems, the subsequent states after voltage stimuli cease can be unpredictable due to inherent relaxation effects. This unpredictability presents a significant challenge when attempting to accurately replicate essential brain-inspired functions, such as maintaining learning efficiency during deep sleep. In contrast, our magneto-ionic systems exhibit a noteworthy distinction. Once voltage stimuli are removed, magnetization can autonomously either decrease or increase without the need for additional energy input. This behavior depends on the interplay between film thickness and prior voltage actuation protocols. This post-stimulated control sets our magneto-ionic

system apart by providing more than just enhanced energy efficiency; it introduces a novel logical function. For instance, it enables the emulation of neuromorphic learning even during deep sleep, a capability unattainable with existing neuromorphic materials like resistive switching or spintronic materials. This distinctive feature offers a promising glimpse into a future where technology is not just faster or smaller but also smarter and more aligned with natural processes.

One of the pivotal accomplishments of this work is the optimization of switching speed in magneto-ionic materials—a field where considerable progress had been previously made, but our study took it a step further. Before our study, notable progress had been achieved in this magneto-ionic aspect. For example, in the case of very thin cobalt films with PMA, which are commonly studied magneto-ionic materials, researchers have successfully enhanced the switching speed to milliseconds by optimizing factors like device design, film thickness, and gate oxide materials. A significant advancement has been made in racetrack devices, where ferrimagnetic spin textures like domain walls and skyrmions are efficiently produced using hydrogen gating in a short 50 μs duration. More recently, the speed of manipulation in magneto-ionic devices has reached impressive levels, as fast as 100 nanoseconds, using a structure involving ferroelectric switching and oxygen ion movement in certain materials. (details can be seen in section 1.5.2). However, these advancements often relied on ultrathin metal layers, which have their drawbacks, such as susceptibility to oxidation, limited control over their magnetic properties, and challenges in achieving precise electrical control over their magnetic behavior. While transitioning to other materials like transition metal oxides or nitrides has been proposed to address these issues, it has typically led to switching speeds in the range of minutes, which is not practical for many applications. In this Thesis, as discussed in Section 3.1, we have achieved an impressive ion motion speed of $0.8 \text{ emu cm}^{-3} \text{ s}^{-1}$ for 5 nm CoN films, which is the highest within the self-contained magneto-ionic approach, marking a significant advancement. Furthermore, all CoN films in our study exhibited a sub-1s response. It is important to note that we could not determine the maximum possible switching speed due to limitations in our measurement techniques; our VSM equipment had a time resolution of 1 second, which means our values are still underestimated. Faster rates could only be assessed through cumulative effects arising from fast voltage-pulse actuation experiments. This demonstrates the feasibility of our approach as a framework for spintronics and emerging concepts like synaptic function simulations.

Another important aspect we tackled is the cyclability (endurance) of magneto-ionic effects, which greatly determines their suitability in different application scenarios. Within the context of this Thesis, we have introduced several innovative approaches with the primary aim of enhancing this critical aspect. To begin, our investigation focused on 25 nm-thick CoN films, which demonstrated an effective cyclability attributed to a delicate balance between magnetization generation and recovery (as depicted in Figure 2e in Section 3.1). In contrast to most other magnetization switching systems, which require varying voltage polarities for signal generation and recovery, our system exhibits partial cyclability without the requirement of opposing biases. This unique cyclability is achieved through a voltage-controllable N ion accumulation effect at the outer surface of CoN films interfacing with a liquid electrolyte. Notably, this effect can be tailored by adjusting both the CoN film thickness, which predominantly governs ion motion speed, and the frequency of pulsed voltage actuation. Consequently, this system offers an energy-efficient and robust means of cycling without the typical degradation associated with the repeated switching of voltage polarities. In addition, we have demonstrated that the incorporation of appropriate transition-metal elements into binary nitride compounds can significantly enhance cyclability and endurance. To be more specific, the substitution of Mn greatly favors the recovery process of CoN films and substantially improves high-frequency cyclability, as illustrated in Figure 2d and e in Section 3.2. When alternating pulsed voltages of -25 V and $+25$ V at 20-second intervals, CoMnN exhibits a consistent and reversible cycling behavior. In comparison, CoN films exhibit no sustained magneto-ionic effects after merely two cycles and only achieve stable cyclability with extended pulse durations. This phenomenon is substantiated by *ab initio* calculations, which indicate that the energy barrier in CoMn-N is consistently smaller than that in Co-N. Furthermore, we propose an innovative nanoscale-engineered magnetoionic architecture, featuring a thin solid electrolyte in contact with a liquid electrolyte, which brings about a remarkable enhancement in cyclability. By simply introducing a nanostructured Ta layer with suitable thickness and electric resistivity between the Co_3O_4 layer and the liquid electrolyte, we have achieved a significant increase in magneto-ionic cyclability, elevating it from less than 30 cycles to more than 800 cycles. Collectively, these findings represent a significant advancement in improving the endurance of magneto-ionic devices, thereby enhancing their viability and competitiveness for future applications.

Although this Thesis underscores key breakthroughs in magneto-ionic control within structural-ion systems, it is essential to recognize that much of the work in this domain remains at the preliminary research stage. To push this approach forward, especially in terms of realizing functional and scalable devices, there remain many open questions, such as:

- The concern regarding switching speeds and cyclability must be a focal point for future research endeavors. While our work has made notable advancements in these aspects, bringing them closer to the performance of other advanced systems utilizing H^+ or Li^+ (with switching speeds $\ll 1s$ and cyclability > 2000 cycles), there remains a substantial gap when compared to state-of-the-art technology, which boasts stability over 10^{15} cycles and switching speeds ranging from 10 ms (HDD) to 10 ns (STT-MRAM). To enhance switching speed, it is worth exploring interface and defect engineering as a promising avenue to optimize ion transport pathways and kinetics, a strategy akin to successful concepts in the realm of memristive systems. To boost cyclability, efforts should be directed towards mitigating strain-related fatigue or irreversible microstructure changes. Consequently, minimizing the affected volume, particularly at surface and interface regions, or employing nanoparticulate morphologies with weaker ionic bonding, could represent promising routes toward achieving high cyclability.
- Efforts in research aimed at transitioning from solid/liquid systems to all-solid-state magneto-ionic systems are strongly encouraged. While in this Thesis, the utilization of a liquid electrolyte has yielded benefits in certain aspects, such as the generation of substantial electric fields through electric double layer (EDL) formation and the controlled accumulation of ions, the pursuit of practical device applications necessitates the integration of a solid-state dielectric sublayer for gating the films. So far, several solid electrolytes have demonstrated remarkably high ionic mobility, exemplified by oxygen and hydrogen transport in materials like $SrCoO_{2.5}$ or GdO_x , as well as lithium intercalation in LiPON. However, in the case of nitrogen-based magneto-ionics, creating solid-state structures will require investigating potential sources of nitrogen reservoirs. These sources, which could include zirconium oxide, tantalum oxide, or GdN_x , should facilitate the insertion and extraction of nitrogen ions within transition metal nitride layers. This approach holds the promise of unlocking extensive application potential for solid-state nitrogen magneto-ionic devices.

- Further dimensional scaling of our structural-ion systems will provide an expanded platform to showcase their versatility. In our study, the magneto-ionic control of ON-OFF ferromagnetic switching is primarily demonstrated at the macro-scale. It remains to be explored how these effects will modify magnetic properties observable only at the micro- or even nano-meter scale, such as in Skyrmions, DMI, and the topological Hall effect. One approach to address this limitation is to employ lithography techniques to pattern our film into nanolines or nanodots. By doing so, one could investigate and fine-tune these intriguing phenomena through structural-ion methods, leading to a wealth of exciting fundamental scientific discoveries and extensive potential applications.

In conclusion, this Thesis explores the potential of magneto-ionics to revolutionize magnetism-based memory and processing technologies. It addresses key challenges including generating strong electric fields, improving magneto-ionic rates and cyclability, and advancing into neuromorphic computing. By choosing compatible materials and fabrication methods, the research aligns with semiconductor industries, ensuring commercial viability. Impressive achievements in ion motion speed and response times, coupled with innovative nanoscale architectures, enhance system performance, making practical applications closer to realization, particularly in neuromorphic computing. Challenges persist, such as increasing switching speed and cyclability, transitioning to all-solid-state systems, and exploring dimensional scaling through lithography techniques. These avenues offer promising directions for future research, ultimately positioning magneto-ionics as a driver of energy-efficient, commercially viable technology with broad implications for memory and computing applications.

5 Conclusions

The research conducted in this Thesis has led to the following conclusions:

- **Controllable ion accumulation effect:** The research demonstrates a novel controllable ion accumulation effect at the interface between CoN films and the adjacent liquid electrolyte. This effect is achieved by carefully selecting the thickness of CoN films and the frequency of voltage pulses. When CoN film thickness is below 50 nm, and the voltage is DC or with a pulse frequency is at least 100 Hz, a trade-off between ferromagnetism generation (voltage ON) and partial depletion (voltage OFF) through magneto-ionics occurs. This allows for precise control of magneto-ionic properties during and after voltage pulse actuation, enabling the emulation of post-stimulated neuromorphic functions.
- **Enhanced magneto-ionics through Mn introduction:** The addition of low percentages of Mn to CoN films significantly enhances magneto-ionic effects. Mn plays a pivotal role in modifying the microstructure and electrical transport properties of CoN films, resulting in a transition to an amorphous microstructure and semiconducting behavior. Consequently, this enhancement leads to a remarkable 6.7-fold increase in saturation magnetization and improved magneto-ionic cyclability. Ab initio calculations reveal that the formation energy for CoMn-N is lower than that for Co-N, indicating more efficient N-ion motion. These findings have broad applications in diverse technological areas, including electrochemical catalysis, batteries, solar cells, and spintronics.
- **Enhanced cyclability combining a liquid electrolyte with a thin solid ionic conductor:** The study highlights the beneficial effect of incorporating a thin solid ionic conductor, particularly an amorphous Ta interlayer, into Co₃O₄ films immersed in liquid electrolytes. Contrary to initial expectations, the thin Ta interlayer significantly enhances magneto-ionic cyclability, increasing it from less than 30 cycles in uncoated Co₃O₄ to over 800 cycles for a Ta thickness of 25 nm. This enhancement is attributed to the role of TaO_x layer in preventing the release of O²⁻ ions into the liquid electrolyte, effectively limiting oxygen ion transport within the Co₃O₄/TaO_x layers. This strategy extends beyond magneto-ionics and can be applied to other systems relying on ion transport mechanisms, including iontronics, sensors, and neuromorphic computing.

Overall, the Thesis contributes to the advancement of magneto-ionics by introducing novel methods to control ion accumulation, enhance magneto-ionic effects, and improve cyclability. These findings have far-reaching implications across various technological domains, offering innovative solutions for energy-efficient spintronics, neuromorphic computing, and ion-based devices.

6 Outlook

Moving forward, the research on magneto-ionic control in “structural-ion” systems and devices, however, is in its early stages. Consequently, many potential research directions remain to further advance this field, such as:

- To enhance ion insertion and extraction processes by strategically tailoring ionic pathways, such as through ion irradiation of the target films using He, Ar, or Xe ions, thus improving durability and ionic rates.
- To do further dimensional scaling, such as employing methods like lithographic techniques for patterned nano-lines and nano-dots, or even more sophisticated electrodeposited designs. Such approaches can offer opportunities to modulate magnetic properties based on the large-scale geometry of the system.
- To integrate the “structural-ion” approach with the emergent research directions in the magnetism community, such as voltage-controlled phenomena, e.g., exchange bias, Skyrmions, DMI and topological Hall effect.
- To draw inspiration from parallel fields like batteries, noble metal catalysis, and supercapacitors, where a wealth of knowledge and innovative concepts can pave the way for pioneering magneto-ionic devices.
- To replace the liquid electrolyte by solid-state alternatives like HfO_x , GdO_x or TaN, marking a step towards all solid-state “structural-ion” devices.
- To explore new ions responsive to voltage, potentially offering benefits over currently studied ions.

Curriculum vitae

ZHENGWEI TAN

Universitat Autònoma de Barcelona (UAB)
08193 Bellaterra (Barcelona), Spain

Tel: (+34) 605769754
justtzw@163.com
[Google Scholar](#)

EDUCATION

- ◆ 2020.11-present (**Ph.D**) Universitat Autònoma de Barcelona, Spain
Supervisors: Prof. Jordi Sort and Dr. Enric Menéndez
Research topic: Voltage control of magnetism with magneto-ionic approaches for energy efficient information technologies.
Financial support: **The Marie Skłodowska-Curie grant** agreement # 861145.
- ◆ 2023.2-2023.3 (Secondment) Georgetown University, United states
Supervisor: Prof. Kai Liu
Research topic: Control of exchange bias through magneto-ionic approaches
- ◆ 2017.09-2020.06 (M.S.) South China Normal University, China
Supervisors: Prof. Zhen Fan
Research topic: Dielectric, ferroelectric, and photovoltaic properties of perovskite oxides
- ◆ 2013.09-2017.07 (B.S.) Wuhan University of Science and Technology, China

RESEARCH INTERESTS

- ◆ Synthesis and experimental investigation of nanostructured functional materials, particularly in nanomagnetism of materials and electronic properties of ferroelectric materials.
- ◆ Involved topics: voltage-driven nitrogen and oxygen ion migration to control the magnetic properties of nitride and oxide films; Fine-tuning of ferroelectric photovoltaic and resistivity switching in ferroelectric materials.
- ◆ Expertise in (i) creating high-quality thin films, multilayers, and nanostructures using techniques like pulsed laser deposition (PLD), magnetic sputtering, and electron beam lithography (EBL); (ii) Analyzing materials structurally and compositionally through methods such as X-ray diffraction (XRD), electron microscopy; (iii) Evaluating magnetic and electronic properties with tools like Magneto-Optic Kerr Effect (MOKE) microscopy, Vibrating Sample Magnetometry (VSM), Atomic force microscopy (AFM), Ferroelectric workstation; (iv) Utilizing large-scale facilities, especially synchrotron X-rays (XAS and XMCD).

ACADEMIC TRACK

- ◆ Contributed to over 12 peer-reviewed publications, including *ACS Nano*, *Nature Communications*, *Material Horizons*, *Advanced Materials* and others.

- ◆ Over 6 oral talks in international workshops or conferences, such as MMM2022, JEMS 2023 and Joint workshop of the BeMAGIC/MagnEFi ITN networks.

PUBLICATIONS

- ◆ **Z. Tan**, Z. Ma, L. Fuentes, M. O. Liedke, M. Butterling, A. G. Attallah, E. Hirschmann, A. Wagner, L. Abad, N. Casañ-Pastor, A. F. Lopeandia, E. Menéndez and J. Sort. Regulating oxygen ion transport at the nanoscale to enable highly cyclable magneto-ionic control of magnetism. [ACS Nano 2023,17,6973](#). **I.F.=18.027**
- ◆ **Z. Tan**, J. De Rojas, S. Martins, A. Lopeandia, A. Quintana, M. Cialone, J. Herrero-Martín, J. Meersschaut, A. Vantomme, J. L. Costa-Krämer, J. Sort and E. Menéndez. Frequency-dependent stimulated and post-stimulated voltage control of magnetism in transition metal nitrides: towards brain-inspired magneto-ionics. [Mater. Horiz. 2023,10, 88](#). **I.F.=15.717**
- ◆ **Z. Tan**, S. Martins, M. Escobar, J. De Rojas, F. Ibrahim, M. Chshiev, A. Quintana, A. Lopeandia, J. L. Costa-Krämer, E. Menéndez and J. Sort. From binary to ternary transition-metal nitrides: a boost toward nitrogen magneto-ionics. [ACS Applied Materials & Interfaces, 2022,14, 44581](#). **I.F.= 10.383**
- ◆ **Z. Tan**, L. Hong, Z. Fan, J. Tian, L. Zhang, Y. Jiang, Z. Hou, D. Chen, M. Qin, M. Zeng, J. Gao, X. Lu, G. Zhou, X. Gao, and J.-M. Liu. Thinning ferroelectric films for high-efficiency photovoltaics based on the Schottky barrier effect, [NPG Asia Mater. 2019, 11, 20](#). Featured Article **I.F.= 10.761**
- ◆ **Z. Tan**, J. Tian, Z. Fan, Z. Lu, L. Zhang, D. Zheng, Y. Wang, D. Chen, M. Qin, M. Zeng, X. Lu, X. Gao, and J.-M. Liu. Polarization imprint effects on the photovoltaic effect in Pb(Zr,Ti)O₃ thin films. [Appl. Phys. Lett. 2018,112, 152905](#). **I.F.= 3.971**
- ◆ D. Gao, **Z. Tan (contribute equally)**, Z. Fan, M. Guo, Z. Hou, D. Chen, M. Qin, M. Zeng, G. Zhou, X. Gao, X. Lu, and J.-M. Liu. All-inorganic flexible Ba_{0.67}Sr_{0.33}TiO₃ thin films with excellent dielectric properties over a wide range of frequencies, [ACS applied materials & interfaces 2019, 11, 27088](#). **I.F.= 10.383**
- ◆ Z. Ma, L. Fuentes-Rodriguez, **Z. Tan**, E. Pellicer, L. Abad, J. H. Martín, E. Menéndez, N. Casañ-Pastor and J. Sort. Wireless magneto-ionics: voltage control of magnetism by bipolar electrochemistry. [Nat. Commun. \(Accepted\)](#) **I.F.= 17.694**
- ◆ B. Cui, Z. Fan, W. Li, Y. Chen, S. Dong, **Z. Tan**, S. Cheng, B. Tian, R. Tao, G. Tian, D. Chen, Z. Hou, M. Qin, M. Zeng, X. Lu, G. Zhou, X. Gao and J.-M. Liu. Ferroelectric photosensor network: an advanced hardware solution to real-time machine vision. [Nat. Commun. 2022,13,1707](#). **I.F.= 17.694**
- ◆ H. Fan, **Z. Tan**, H. Liu, L. Zhang, F. Zhang, W. Du, Z. Fan, X. Gao, F. Pan, D. Yu and Y. Zhao. Enhanced ferroelectric and piezoelectric properties in graphene-electroded Pb(Zr,Ti)O₃ thin films. [ACS Applied Materials & Interfaces, 2022,14,17987](#). **I.F.= 10.383**
- ◆ S. Martins, J. De Rojas, **Z. Tan**, M. Cialone, A. Lopeandia, J. Herrero-Martín, J. L. Costa-Krämer, E. Menéndez and J. Sort. Dynamic electric-field-induced magnetic effects in cobalt oxide thin films: towards magneto-ionic synapses. [Nanoscale 2022,14, 842](#). **I.F.= 8.307**
- ◆ J. Tian, Z. Tan, Z. Fan, D. Zheng, Y. Wang, Z. Chen, F. Sun, D. Chen, M. Qin, M. Zeng, X. Lu, X. Gao, and J.-M. Liu. Depolarization-field-induced retention loss in ferroelectric diodes. [Phys. Rev. Appl. 2019, 11, 024058](#). **I.F.= 4.7**

- ◆ J. Tian, H. Wu, Z. Fan, Y. Zhang, S. J. Pennycook, D. Zheng, Z. Tan, H. Guo, P. Yu, X. Lu, G. Zhou, X. Gao, and J.-M. Liu, Nanoscale topotactic phase transformation in SrFeO_x epitaxial thin films for high-density resistive switching memory. [Adv. Mater. 2019, 1, 1903679](#). **I.F.= 32.086**

AWARDS

- ◆ The funding of Marie Skłodowska-Curie Action (European Union)
- ◆ National scholarship of China
- ◆ The First Prize Scholarship

REFERENCES

- ◆ **Dr. Enric Menéndez**. Tenure-track Professor (Serra Húnter Fellow), Department of Physics, Sciences Faculty, Building Cc (office C5-246), Universitat Autònoma de Barcelona, 08193 Bellaterra (Barcelona), Spain; Email: Enric.Menendez@uab.cat; Tel. +0034 935814358. https://Enric_Menendez-scholar.google.com
- ◆ **Prof. Jordi Sort**. ICREA Professor, Gnm³ Group, Department of Physics, Sciences Faculty, Building Cc (office C5-114), Universitat Autònoma de Barcelona, 08193 Bellaterra (Barcelona), Spain; Email: jordi.sort@uab.cat; Tel. +0034 935812085. <http://jsort-icrea.uab.cat/>

